1-1-2016

Bio-Inspired Synthesis Of Nanostructured Materials On Substrates For Environmental And Energy Applications

Xinghua Meng Meng
Wayne State University,

BIO-INSPIRED SYNTHESIS OF FUNCTIONAL MATERIALS ON SUBSTRATES FOR ENVIRONMENTAL AND ENERGY APPLICATIONS

by

XINGHUA MENG

DISSERTATION

Submitted to the Graduate School

of Wayne State University,

Detroit, Michigan

in partial fulfillment of the requirements

for the degree of

DOCTOR OF PHILOSOPHY

2016

MAJOR: MATERIALS SCIENCE AND ENGINEERING

Approved By:

_____

Advisor Date

_____

_____

_____

_____

DEDICATION

Dedicated to my wife Jun Zhang, my parents Yu Meng & Ying Liu.

ACKNOWLEDGEMENTS

First of all, I would like to genuinely thank my advisor, Dr. Da Deng, for his guidance, patience, tolerance, support and encouragement. I got trained in all aspects of scientific research with him, which makes it possible to form this dissertation. His enthusiasm for research and his creative ideas across different fields have always been a source of inspiration for me. He not only shared with me his novel ideas, provided with me critical and constructive comments but also taught me the soft skills required to do research, including doing research scientifically based on hypothesis, scientific communication, drafting manuscripts logically and rigorously and thinking out of the box. Besides research, I also gratefully appreciate the experience and philosophy he shared with me and the freedom he provided for me to pursue my personal interests. He always encourages me to challenge myself and to be my best.

I want to sincerely thank my dissertation committee members, Prof. Caisheng Wang, Prof. Charles Manke, and Prof. Howard Matthew, for their valuable time and constructive suggestions and insightful comments. I also want to thank Prof. Charles Manke as the chair of the department for his help, and thank Prof. Guangzhang Mao as the MSE program director for her help.

I would like to thank Dr. Zhi Mei at the Lumigen Instrument Center for technical training and support. I am grateful to all my colleagues in the lab and department, especially Jian Zhu and Ayad M. Nacy, for enthusiasm and friendship.

I would like to express my sincere gratitude to my beloved wife Jun Zhang and my parents, without their support I would not be able to finish this dissertation. They are always supporting my life and research abroad. They encouraged me and helped me to overcome many difficulties during my Ph.D. studies. They are always there to support me whenever I need. I love you so much.

TABLE OF CONTENTS

LIST OF FIGURES

CHAPTER 1 INTRODUCTION

Nanomaterials have been intensively studied in materials science. Since they possess unique size and shape dependent physical and chemical properties, nanomaterials are significantly different from conventional materials in macro scale. The special size, morphologies and structures of nanomaterials systematically determine their properties and can find important applications in numerous fields.[1] Advanced nanostructures are being developed, leading to an increase in the performances of many devices using those nanomaterials.[2] Numerous inorganic materials, particularly, transit metal hydroxides, oxides, sulfides, have attracted much attention. Due to their unique size-dependent optical, electrochemical, magnetic and catalytic properties, these materials have potential applications in energy storages,[3] catalysis[4] and magnetic storage,[5] and so on. With the incredible development of nanotechnology, these functional materials are being re-designed. To understand the thermodynamics and kinetics process of formation of their nanostructures could not only reveal fundamental mechanisms involved but also can help researchers to design and fabricate improved functional materials effectively. However, traditional methods are not so satisfactory to apply them in manufacturing. The synthesis of nanomaterials is mainly studied in lab and applied in limited small-scaled production in some industrial fields. Thus, the development of innovative approaches to synthesize nanostructured materials is one of the most important research areas. It is of scientific and economic importance to develop nanomaterials via different and facile methods to not only dramatically improve their performances in applications but also reduce the cost of production. Taking energy and environmental applications for example, it is always critically important to develop advanced nanomaterials for those applications to make our world a better place.

The goal of this dissertation is to explore bio-inspired methods to synthesize controllably nanomaterials on different substrates and apply them in energy storage and

environment protection. This dissertation contains several different topics, but they are all involving some bio-inspired ideas. At the beginning, Chapter 2 presents some essential background and literature review from different perspectives: (1) Traditional methods to prepare nanomaterials, (2) advantages of synthesizing nanomaterials on substrates, (3) the history of bio-inspired methods for synthesizing materials, and (4) current progress of studying bio-inspired methods in nanomaterials for energy storage and environmental applications. Chapter 3 firstly introduces bio-inspired eggshell system to prepare $Co(OH)_2$ nanorods on eggshell membrane and corresponding CoO nanorods on carbonization eggshell membrane after mild heat treatment. Potential applications in lithium-ion batteries and supercapacitors are evaluated. Chapter 4 demonstrates the universal deposition capability of eggshell system on different substrates. To prove the extraordinary performance of as-prepared amorphous $Co(OH)_2$ nanorods on Ni foam, its electrochemical characterization is carried out. Chapter 5 describes the deeply integration eggshell membrane and nanomaterials via eggshell system and thermal treatment. More functions of eggshell membrane are studied. The hierarchical composite materials of CoO-Co@C on carbonized eggshell membrane are suitable for developing advanced anode materials for lithium-ion batteries and possess potential applications in other fields. Chapter 6 starts to think about transfer natural eggshell system to similar artificial system. It describes bio-inspired synthesis $Mn_3(PO_4)_2 \cdot 3H_2O$ nanoflakes on flexible cation-exchange membrane (Nafion N117). The properties of $Mn_3(PO_4)_2 \cdot 3H_2O$ are characterized. Controllable underwater wettability of as-deposited membrane is studied for potential applications for environment protection. Chapter 7 demonstrates the diffusion-assisted synthesis α-$Ni(OH)_2$ in the similar artificial Nafion system. By using bio-inspired mechanism, α-$Ni(OH)_2$ nanobristles on various substrates is conveniently achieved. The special wettability and electrochemical performance for supercapacitors are tested. Chapter 8 describes the results of optimized the synthesis conditions and performances by regulating Ni^{2+}

and Co^{2+} ions in Nafion system. Different nanostructured Ni-Co hydroxides are prepared and characterized. Chapter 9 demonstrates the advantages of combining eggshell membrane and Nafion system to synthesize nanomaterials. 3D networks of nanostructured NiO-Ni on carbonized eggshell membrane are developed. These composite materials reveal the importance of structure and composition of nanomaterials. Chapter 10 summarizes the general conclusions in this dissertation and suggestions for the future work. The overall conclusion is that bio-inspired synthesis via diaphragm-assisted system is a powerful tool to develop nanomaterials on substrates. With different substrates, the performances of different nanomaterials will be enhanced.

CHAPTER 2 LITERATURE REVIEW

2.1 Traditional Chemical and Physical Methods for Preparation of Nanomaterials

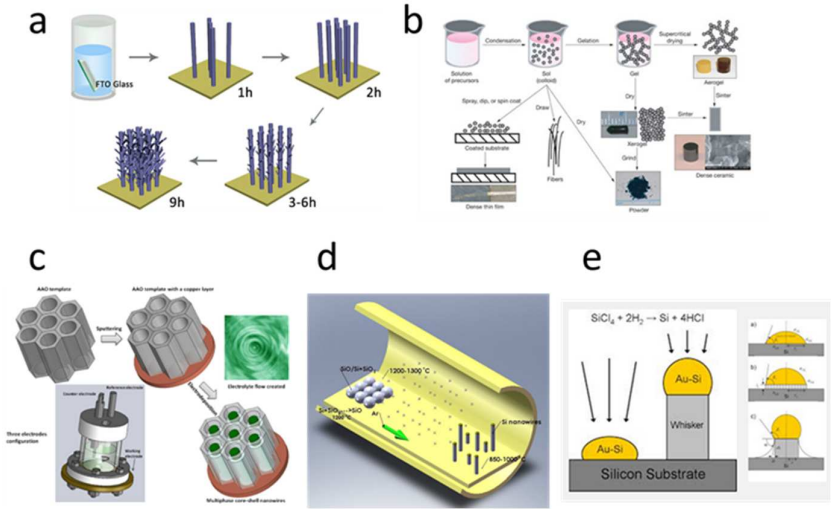

Figure 2.1. Schematic of the typical traditional methods for preparation of nanomaterials: a) hydrothermal method; b) sol-gel method; c) electrochemical method; d) CVD method; (e) VLS method.[1, 6]

After more than 20 years in the studies of nanomaterials, varieties of synthesis methods have been developed. There are some typical methods as follows (Figure 2.1): (1) Hydrothermal method is the most common route in forming inorganic nanomaterials in aqueous solutions under high pressure and high temperature. The method emulates the universal methods in geography.[7] The advantages of it over other types of synthesis methods include simple procedures, low cost, controllable crystalline phases and homogeneous nanostructures from it. For example, via hydrothermal method, the formation of metal hydroxides nanostructures from metal salt solutions under following steps: First, initial metal hydroxides forms by hydrolyzing metal ions. Then, metal hydroxides precursors trend to reform nano nucleus under high temperature and high pressure. Finally, they slowly grow into nanostructures.[8] However, the drawbacks of this method are also inevitable. The requirements of specific autoclaves, high-temperature ovens, dangerous potential leakage of high pressure and the impossibility of observing the process as crystal grows together hinder its large-scale

commercialization; (2) Sol-gel method is based on a wet chemical technique commonly used to synthesize a wide variety of nanomaterials from solutions. The method is widely applied for synthesizing nanoparticles in the lab. In the reaction process, monomers can convert into a colloidal solution as some precursors for forming integrated 3D network of distributed nanoparticles.[9] Typical precursors include metal alkoxides, oxyhydroxides, and hydroxides. However, its uncontrollable direct process, low productivity, and difficulties of preparing complex hierarchical structures trouble the development of it in large scale; (3) Electrochemical methods are a series of ways to develop nanomaterials such as metal hydroxides and oxides. On one hand, in the electrodeposition of oxides, various methods can be adopted.[10] For example, the electrodeposited metal film on electrodes can be polarized in alkaline solution (such as KOH). And then, the metal is dissolved in an electrochemical process. Finally, the chemical process initiates, leading to the deposition of hydroxides or oxides on the surface of substrates. Hydroxides or oxides films prepared by this method possess high adherence and controllable thickness with a large surface area. Nitrates are used to prepare metal hydroxides on the conductive substrates. Here, the hydroxyl ions are created by reducing nitrate ions in solution. Metal oxides (NiO, Co_3O_4, Fe_2O_3, CuO etc) have been electrodepositioned from an aqueous acidic solution containing the related nitrate salts of the metals. The advantage of this method is that all the reactions can be precisely controlled through potential or current. Besides, by introducing the AAO template, various metal hydroxides or oxides could be produced in 1D or 3D shapes conveniently. On the other hand, the anodization technique is another commonly chemical electronic method for forming unique nanostructures on a metal surface.[1] Since the breakthrough in the anodic formation of self-ordered porous hydroxides or oxide films, the anodization technique has attracted considerable attention.[11] However, the disadvantages of electrochemical methods are that expensive electronic facilities and specific electrolytes have to be involved, and researchers have to have

background of electrochemistry; (4) Methods based on high temperature. Firstly, chemical vapor deposition (CVD) is an artificial traditional bottom-up fabrication of inorganic nanomaterials through decomposition of molecular precursors on heated surfaces.[12-13] Various carbon-based or silicon-based nanomaterials often use this strategic process on the basis of a lot of applications. By carefully selecting the experimental conditions (e.g. temperature, reaction atmosphere, pressure, flow rates, precursors, etc.), CVD enables the obtainment of nanomaterials with expected components and morphologies. Secondly, vapor-liquid-solid growth (VLS) has been well understood to prepare one dimension (1D) nanomaterials. Metal catalysts melt, and liquid alloy droplets form at high temperature. Under some conditions such as temperature and vapor pressure, the alloy droplets for their components are supersaturated.[14] Therefore, the components tend to precipitate from their liquid-solid interface, in order to decrease surface free energy. Gradually, the 1D nanostructure starts to grow as the vapor components are provided continuously. Also, thermal decomposition is the third traditional methods based on high temperature, which has been proven to be universal and reliable. Many uniform nanoparticles with controllable sizes and morphologies can be prepared by it. However, the disadvantages of the methods above by heating are mainly related to energy consuming, special instruments as well as the expensive supply of precursors.

Although, via these varieties of methods, nanomaterials with ideal properties are massively achieved, many of these have inherent drawbacks such as energy consuming, complex/expensive facilities, lengthy and involved multiple steps, high pressure and high temperature, which means that we cannot afford the large-scale production of them based on current situation. Therefore, more green, facile, and efficient synthetic methods for nanomaterials are desirable to apply them in our daily life.

2.2 Nanostructures on Various Substrates and Their Potential Applications

Nanomaterials possess excellent performances and multiple applications. The primary stage of developing nanomaterials is merely focused on nanomaterials themselves. 0D, 1D, 2D as well as hierarchical 3D nanostructured materials were successfully prepared with different methods. Most of nanomaterials are used solely without substrates. Take lithium-ion batteries (LIBs) as an example. Many nanomaterials for LIBs have to mix with conductive additives and binder and then are spread on current collectors to make them as electrodes. This traditional method is widely applied in current industrial manufacture. However, there are several disadvantages in using these nanomaterials without substrates for LIBs directly: (1) complex procedures and limitations of preparation. The separation and clean of products are necessary, which might company with inevitable loss; (2) potential toxicity of nanomaterials. In some research, nanomaterials such as carbon nanotubes have been proved to be harmful to human bodies and even related to carcinogenicity; (3) difficulty stable storage. Due to the ultra large specific surface area and high surface energy, they tend to aggregate together during storage, which will destroy the merits of them; (4) Difficulty recycle. It is almost impossible to collect all the materials after the test because they are irreversibly combined with other parts of electrodes and have to waste much time to separate them manually. Moreover, without substrates, some more advantages of nanostructures of 1D, 2D or 3D cannot be demonstrated. For instance, 1D nanostructured materials grown on substrates could resist more large volume change in usage and controllable loading and conductivity in one direction and could process other applications such as superhydrophobic surface, water treatment or catalysts at the sample time, which could integrate different applications in the one-time synthesis of nanomaterials. It is another shortcut to increase productivity and decrease the energy consuming.

2.3 Bio-Inspired Methods to Synthesize Nanomaterials

We are living in an exciting period for materials scientists and engineers, in which new advanced technologies bring us the capability to control structures and properties in nano scale.

Meanwhile, new experimental discoveries in nature give us the insight and principles of how materials and structures in life achieve their remarkable properties.[15] Nature has some secrets in producing materials under environment-friendly conditions, without harsh conditions such as high temperature, high pressure, and dangerous chemicals.[16] In contrast, human beings develop traditional materials as well as advanced nanomaterials under these critical conditions. Though someone tends to call all the mild conditions limits, nature manages to prepare sophisticated structures and functional materials in nano scale that are much better than ours. For instance, the inner shell of abalone is twice as tough as existed advanced ceramics. The natural bone provides us exceptional protection daily, but much lighter than all the artificial ones. Eggshell is porous and thin, but cannot be broken easily. The hierarchical feature of these materials is organized by ordered nano-micro scale structures, which is Nature's another secret. From the atomic level to the macroscopic level, precision, strength, and flexibility are all achieved. Therefore, although we are still at the initial stage of preparing nanomaterials, Nature has mastered it for more than 3.8 billion years, which is reliable enough for us to imitate or take inspiration from those designs to improve our materials.

In practice, the idea of developing artificial materials to intimate nature has companied with the whole history of human beings at a low level for thousands of years. It can be taken as low-level biomimicry. The term “biomimicry” means directly mimicking biological objects to design artificial object with desirable properties.[17] Recently, another term “bio-inspired” raised, which included more combination of direct or indirect mimicry. Bio-inspired concept might be taken as a bridge to connect natural ideas with human ideas. Therefore, it is broader and more flexible. We could investigate the formation process, structures or function of materials in nature and learn the mechanism behind to synthesize similar materials. If we would like to continue to improve the methods of fabricating nanomaterials, we have to ask Nature again. After all, nanoscale is masterly operated by Nature to build massive biological

structures, such as microtubules, microfilaments, and chromatin.[18] Moreover, recently, the impact of human activities has gradually changed the normal situation of our earth. Climate change, industrial pollution as well as energy crisis have being inhabit the steps of us. Our previous methods to build our word have to be changed. Thus, the calling for biomimicry/bio-inspired strategy is highly focused by scientists, government as well as the public. All the people are wishing "green" manufacturing in future.

To observe the process how Nature makes materials is an excellent strategy to develop nanomaterials. There are three levels of bio-inspired design from elementary biological processes, biological unit process, to higher life processes in vitro.[19] Figure 2.2 demonstrate as-known processes in nature. For example, in nature, organic components control the whole process of nucleation and growth of inorganic structures and the self-assembly of inorganic building blocks in order. to form complex structures.[20] The highly organized structures from the molecules demonstrate special hierarchical characteristics, which meets the requirements of various functions in biology. There are two important principles behind the production of natural nanomaterials: bottom-up principle and self-assembly principle.

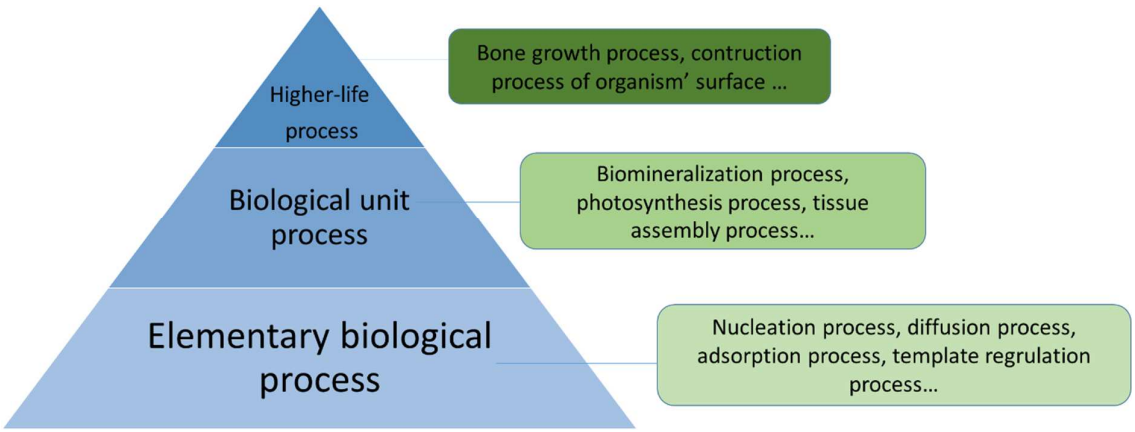

Figure 2.2. Illustration to show the overall biological process in nature.

2.3.1 Bottom-Up Principle.

This principle takes use of the interaction between molecules/ions to initiate nucleation. It controls those building blocks of small crystals to form hierarchical structures or composite materials. The advantages of this bottom-up strategy are valuable for Nature. Firstly, the innumerable chemical possibility is an attractive point. The surface of biological structures contains many active function groups, molecules. They are used as linkers among different building blocks. As a result, the special structures could be built up gradually. In contrast, the top-down strategy mainly shapes materials mechanically without considering these interactions. As a result, it 's hard to keep the inside orders or remove some useless parts of the raw materials. Secondly, the building blocks are so many that we can imagine producing complex structures that form exactly defined structures organized over vast areas in space. This highly controlled level is impossibly superable by other strategies. Nature is indeed a master of building complex structures. Thirdly, the bottom-up route takes use of energy efficiently. It just masters the smallest force to move atoms, molecules or ions to achieve different levels of organization. In comparison, the top-down strategy has to consume a significant amount of energy to build structures by moving many useless parts from bulk structures and bring about much waste as well. Thus, instead of using tools of higher precision and spending more money, we should follow this strategy to build nanomaterials from the bottom-up according to these reasons.

2.3.2 Self-Assembly Principle

The crucial tool to build natural nanostructures from bottom-up is self-assembly. By well-organizing atoms, ions, molecules and other colloidal building blocks, the high-level biological process can be achieved. Nature is a magician of mastering self-assemble skills. The large scaled molecular recognition makes it possible to self-assembly, which is the hidden trick of biological nanostructures. It learned all the interactions between biomolecules and ions. For example, two complementary strands of DNA will pair all the base-pairs form a special double

helix. The formation of DNA suggests two features of self-assembly. The interaction is strong enough to attract each other, forming a well-defined structure during association.[18] The whole process is entirely automatically once the orders are defined.[21]

Jump from the body of cells, another most important self-assembly case is biomineralization. The mineralization process is highly and precisely controlled according to physical and chemical principles and processes of self-assembly.[22] In principle, the special biomacromolecules is capable of guiding nucleation and growth of the inorganic materials in biology. However, much more details are still not clear. Some researchers suggested that the protein's acidic groups provide templates for the formation of $CaCO_3$ crystals. But now, it looks overly simplistic.[23-24] The self-assembly of inorganic structures is not only related to control the growth surface of organic parts and its shapes, but also it demands that conditions of nucleation are met. In somewhere, the solution is supersaturated with specific salt[25]. The degree of supersaturation of the precursor solution plays a central role. Its concentration, pH value as well as temperature all could control supersaturation. When natural nanomaterials' growth occurs by tiny particle absorption, the degree of supersaturation highly related to the properties of the forming particles and following deposited structures.

In specific, eggshell and seashell et al are composed of $CaCO_3$. The membrane inside them plays an important part in forming ordered inorganic structures.[23] It is expected to control the release of Ca^{2+} and CO_3^{2-}. Disordered precipitation of calcite crystals is prevented by this kind of controllable release. Besides, the membrane may provide the suitable nucleation sites at the surface of it. This model is a practical natural strategy to prepare inorganic materials by bottom-up, self-assembly and supersaturation.

In conclusion, the central tenet of Nature' preparation of hierarchy inorganic nanomaterials is that how to control the combination of molecules/ions, nucleation, growth, self-assembly of the inorganic crystals from bottom-up level by controlling the experimental

conditions, chemicals and devices under similarly mild conditions in nature. A bio-inspired strategy based on these principles could create new methods in synthesizing more inorganic nanomaterials. To direct the growth of sophisticated structures in nano scale like that in nature, researchers have been motivated to develop novel methods that mimic or exploit the existed natural inorganic nanomaterials.

2.4 Bio-Inspired Methods of Fabricating Hierarchical Materials on Substrates

2.4.1 Low-Level Bio-Inspired Synthesis of Nanomaterials

There are more than thousands years for human beings to get inspiration from Nature to design functional materials and tools. In past, researchers are used to be inspired by natural structures and their functions within the scope of the naked eye, focused on emulating or directly copy the existed ones in Biosystems by using mostly synthetic materials such as polymers and following traditional top-down approaches. Even in the field of nanotechnology, the traditional idea is still on work, which is called template method. For example, Eggshell membrane (ESM) is a common natural material, which has been served as an ideal template for developing hierarchical nanomaterials. Because ESM is organized by tens thousands of protein fibers with massive active dots, a lot of inorganic nanomaterials have been developed on ESM structure. The porous 3D networks formed by depositing nanoparticles of ZnO, TiO_2, CuO, Co_3O_4 and CeO_2 are successfully obtained, which is an expedient solution to take advantages of this biological structure to support original nanostructures and their applications.[26-30]

2.4.2 High-Level Bio-Inspired Synthesis

However, to use existed natural structures is not the whole story of bio-inspired synthesis for nanomaterials. To understand and follow the principles discussed above are more important. The first classic exploration of inorganic artificial nanomaterials based on bottom-up and self-assembly principles is the preparation of hydroxyapatite (HAP) from simulated

body fluid (SBF) by Kokubo.[31] By simulating the inorganic components in human blood under the same pH and temperature, the artificial supersaturation was created. This condition is suitable for depositing HAP on the specific substrates with functional groups.

Except providing the similar environment in nature, some researchers are also considering to select complementary biological molecules to fabricate complex structures based on inorganic building blocks. DNA has been taken as the template and director for hierarchical nanomaterials. Nanocrystals are aggregated by using DNA base pairs, uracil. Nanonetwork of gold nanoclusters and iron oxides is obtained by using dithiol connectors and biotin-streptavidin connectors respectively.[32] In this case, some proteins could be employed to control the morphology of oxides. For another example, egg albumin has been used as the template and controller to regulate the growth of Fe_3O_4 via a rolling mechanism.[33] Proteins present a significant advantage in attracting metal ions, therefore, the particles will intercalate metal oxides' precursors efficiently. Comparing with the conventional template methods, these biomacromolecules (DNA, protein, peptide, long chain polyamine) possess the ability to induce the growth and arrangement of inorganic crystals rapidly under mild conditions, which is called high-level bio-inspired synthesis. It is close to what Nature is doing.

Note that most of biomaterials are formed on substrates, especially all kinds of active membranes. By this way, special nanostructures and functions might be achieved at the same time. Therefore, to use some active membranes might make bio-inspired synthesis more flexible and practical, considering the advantages of nanomaterials with substrates. Someone employed natural membrane such as ESM to grow special nanostructured crystals on it. Instead of copying the original structure of ESM as related above, the porous structures of ESM and surface active sites can in further be used to control the grow nanomaterials such as nanorods,[34] nanotubes,[35] and spiral-like structures.[36]

Considering low controllable structures of natural materials, artificial membrane is another solution to carry out high-level bio-inspired synthesis. By simulating the natural membrane technology, Iijima et al firstly introduced cation-exchange membrane to mineralize octacalcium phosphate (OCP) to explore the formation of tooth enamel in vitro. Here, the membrane can control the diffusion of ions.[37] As a result, they obtained ribbon-like OCP. In fact, the growth was adjusted by diffusion of ions and the substrate at the same time. In the absence of the crucial substrates, OCP tended to grow along the ionic inflow. Recently, Takiguchi et al[38] attempted to crystallize $CaCO_3$ on cation-exchange membrane. Similarly, one of the roles of the membrane is to control the transportation of calcium ions. Besides, the surface of it affected the nucleation of $CaCO_3$. The composition and structure of the membrane may affect the growth of crystals. In contrast, two solutions separately containing cations and anions directly mixed cannot obtain similar nanostructures. Recently, the sea cucumber-like HAP is fabricated via the same artificial membrane.[39]

Therefore, the methods follow Nature's principles are more attractive and flexible to prepare artificial nanomaterials than straightforward "biomimic" synthesis. More and more exploration attempts to provide an understanding of the growth mechanisms from small molecules to final nanostructures. To make use of substrates such as active membranes to control similar process in nature such as diffusion, absorption, nucleation and regulation is important. These nanostructured materials or even achieved some special functions can be closer to bio-inspired purpose.

2.5 Bio-Inspired Methods to Develop Nanostructured Materials for Energy and Environmental Applications

Energy crisis and environment protection are two of most urgent problems to human society. The purpose of applying bio-inspired nanomaterials can be to store energy, increase energy efficiency, prevent pollution, and so on. Researchers are adopting massive bio-inspired ideas to apply nanotechnology in these areas.

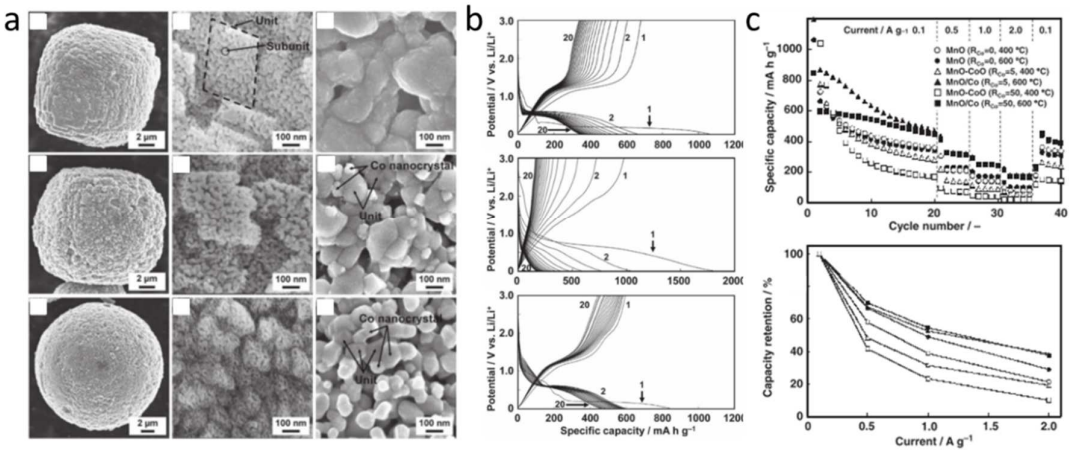

Figure 2.3. The morphologies and electrochemical performance of Mn-Co oxides composite prepared by using biomimetic solid solutions for lithium-ion batteries.[40]

Takao et al developed Mn-Co oxides composite material by using biomimetic solid solutions of $MnCO_3$ and $CoCO_3$.[40] The different structures of the metal oxides/composites (MnO, MnO-CoO, MnO and MnO/Co) with porous morphologies were synthesized by following thermal treatments in a reduction atmosphere. The contents of Co can be regulated by the concentration of it in $MnCO_3$-$CoCO_3$. The MnO/Co nanostructure possesses the best enhanced rate performance and cycling stability as anode materials for lithium-ion batteries.

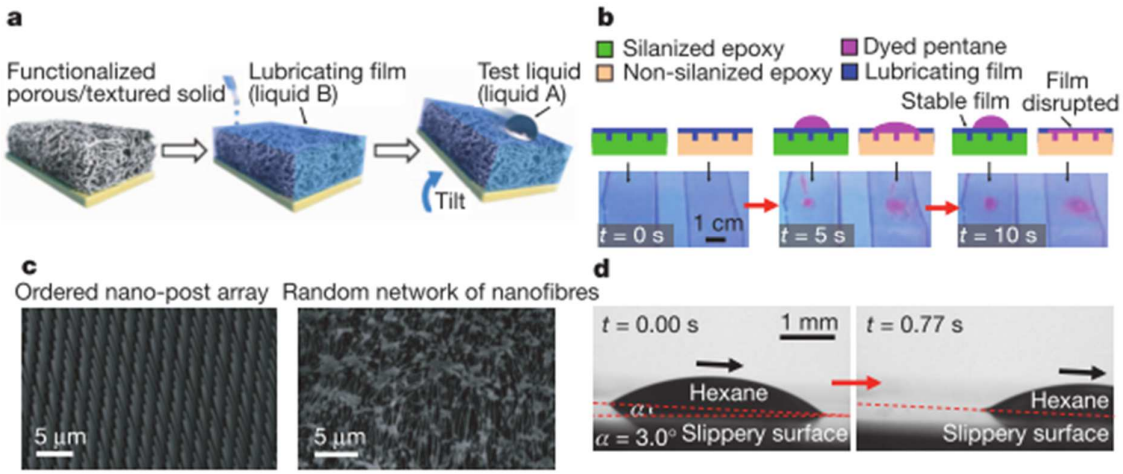

Figure 2.4. The illustration of the formation structures, morphologies and self-cleaning effects of novel bio-inspired surface materials.[41]

Wong et al[41] are inspired by the Nepenthes pitcher plant. Through locking-in an intermediary liquid in the extreme rough surface, the surface with 3D roughness performs its natural liquid-repellent surface. Various liquids such as water, hydrocarbons and crude oil can be repelled. Moreover, it maintained low contact angle hysteresis, restorable liquid-repellency and resisted ice adhesion. These functions were kept under high pressures. The bio-inspired strategy provides the alternative solution for achieving self-cleaning.

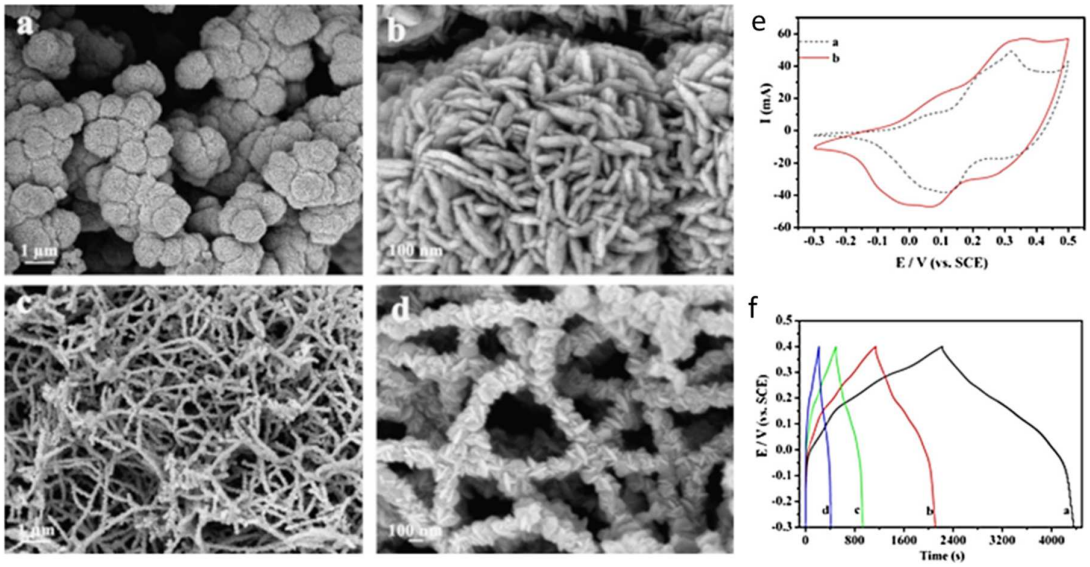

Figure 2.5. The morphologies and electrochemical performance of CoS prepared by introducing biomolecules for supercapacitors.[42]

L-cysteine (one kind of amino acid) was employed in hydrothermal method.[42] Cobalt sulfide (CoS) with the network structure was synthesized here. The biomolecule is used as the sulfide source and controller of the well-organized growth of CoS at the same time. The CoS network self-assembled by nanowires was prepared as electrodes for supercapacitor. It delivered the specific capacitance of 508 F g^{-1}. This biomolecule assisted method provides a bio-inspired strategy to synthesize other metal sulfides.

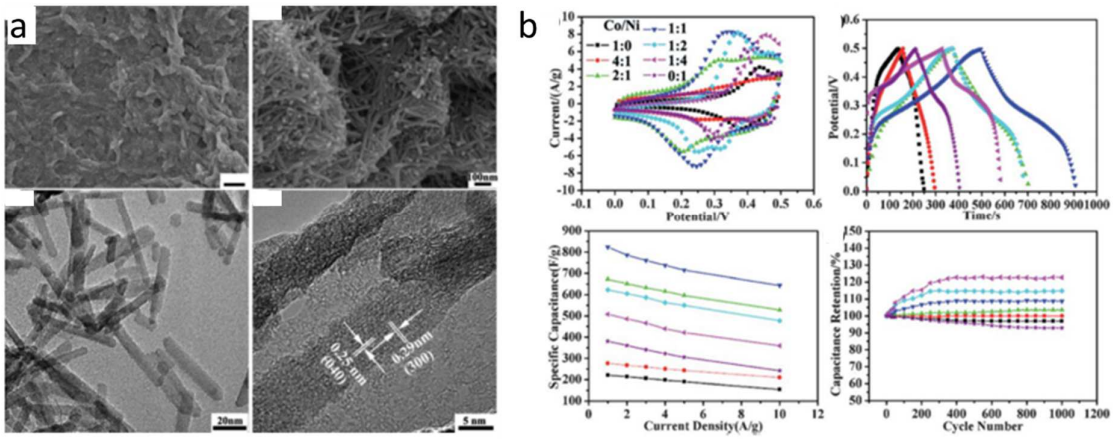

Figure 2.6. (a) The morphologies and (b) electrochemical performance of $Co_xNi_{1-x}O$ nanorods synthesized by biomimic biomineralization for supercapacitors.[43]

Xiao et al[43] made direct use of graphene oxide that consists the functional groups (carboxyl and hydroxyl) as an organic substrate to attract the nanostructures, which is similar to that in the biomineralization process. By directly dispersing $Co_xNi_{1-x}O$ nanorods on reduced graphene oxide (RGO) sheets, it is possible to regulate the molar ratio of Co and Ni. $Co_{0.45}Ni_{0.55}O$/RGO nanostructured electrode delivered a high specific capacitance of ~823.0 F g^{-1}. After 1000 cycles, only < 4% capacity is lost at 2 A g^{-1}.

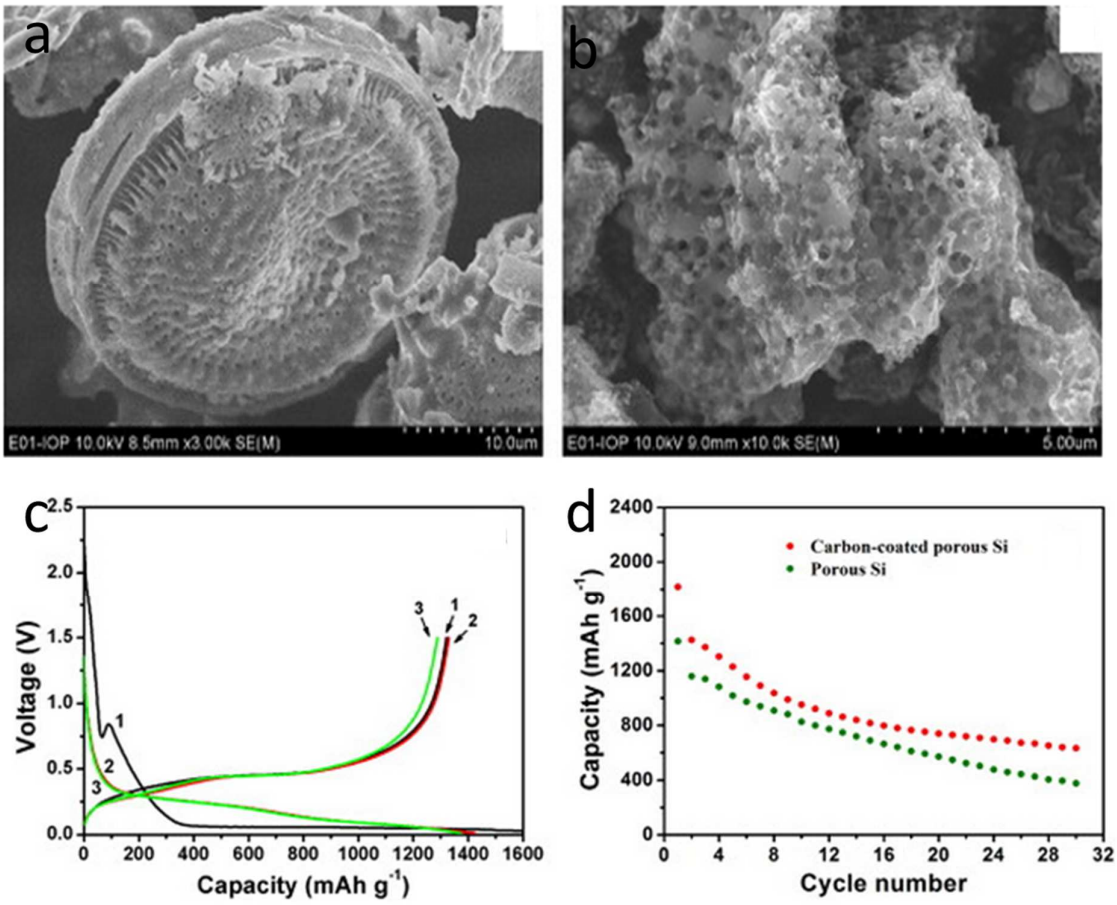

Figure 2.7. The morphologies and electrochemical performance of bio-template silicon electrodes for lithium-ion batteries.[44]

The skeletal shells of diatoms are made of the hydrated amorphous SiO_2. It has ordered nanopores. One step of magnesiothermic reduction method converted diatoms into highly porous silicon.[44] This silicon material successfully remained the original well-dispersed nanopores, which was used as anode materials for LIBs. The porous silicon electrode delivered 1321 mAh g^{-1} and 1818 mAh g^{-1}, respectively in the initial charge-discharge process. A stable capacity of 633 mAh g^{-1} is maintained after 30 cycles in cycling test.

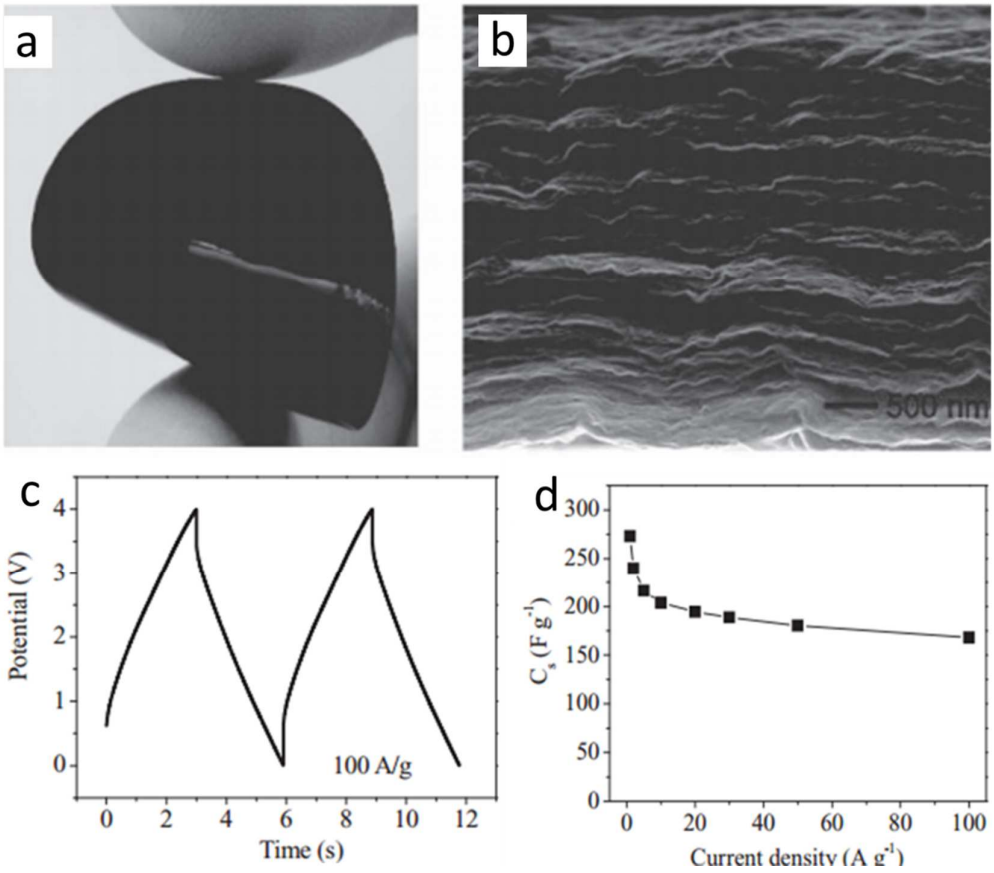

Figure 2.8. Optical and SEM images of the graphene/water hybrid structure and electrochemical performance for supercapacitors.[45]

Hydration forces are commonly existed in biologic processes. They are crucial factors that control the structure and biologic activities. Here, a balance between repulsive interactions and the intersheet π-π attractions facilitated to develop the special graphene and water hybrid structure.[45] The robust multi-layered graphene film has a highly porous structure, which allows the high efficient transportation of electrolyte on the surface of single graphene sheet. The power density of 150.9 Wh kg^{-1} and energy density of 8 kW kg^{-1} are high enough in graphene-based supercapacitors.

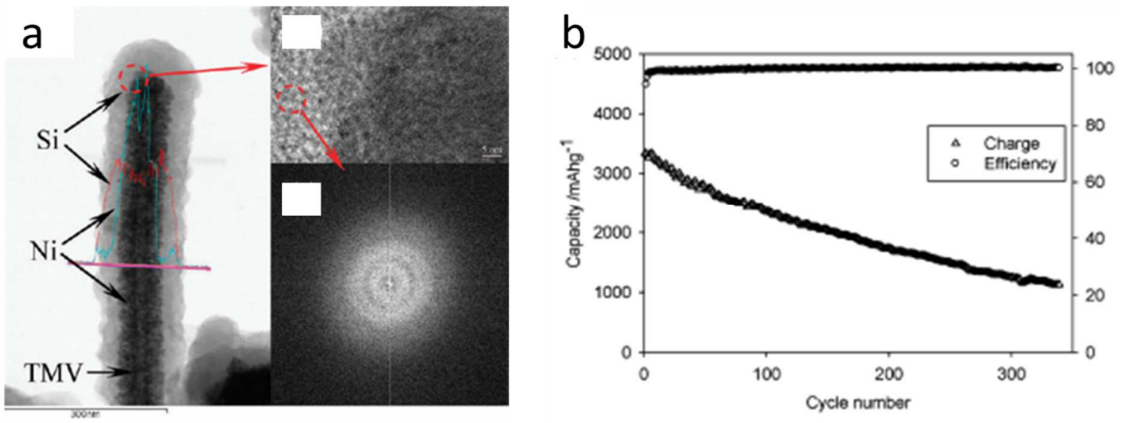

Figure 2.9. The structures and electrochemical performance of Ni-Si nanorods prepared by TMV virus for lithium-ion batteries.[46]

Genetically modified TMV virus was introduced cysteine residues with thiol groups in order to fix it on the metal surface.[46] The unique 1D nanostructure of the virus was coated with Nickel due to the existence of strong covalent interaction between the thiol groups and the metal ions. In this way, living-organism was transformed into active template to prepare silicon electrodes for LIB. This composite silicon anode delivered the high specific capacities of 3300 mAh g^{-1} at 1 C. Only 0.2 % capacity is lost in every cycle, indicating the excellent stability. The specially designed bio-template is effective to develop nanostructured materials with particular composition.

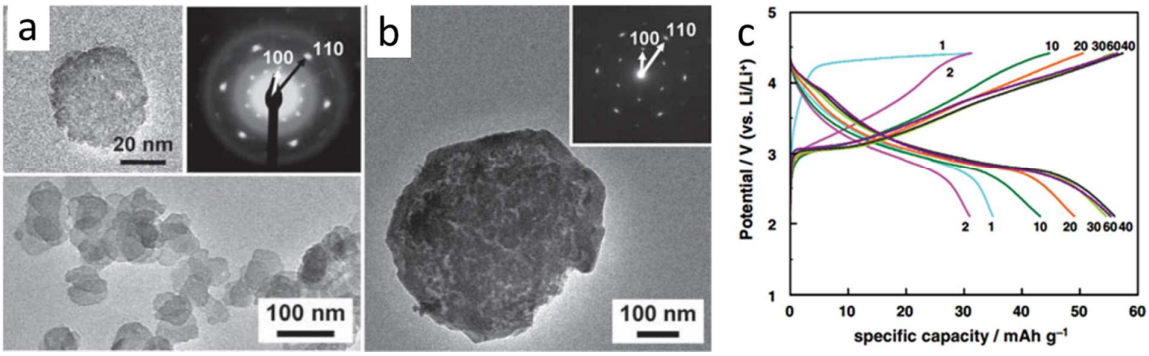

Figure 2.10. The structures and electrochemical performance of Ni-Si nanorods prepared by TMV virus for lithium-ion batteries.[47]

Oba et al obtained inspiration from the microbial mineralization of transition metal oxides.[47] The nanostructured $Mn(OH)_2$, β-MnOOH, and $Na_{0.55}Mn2O_4$ were synthesized in solution under room temperature. These nanostructures have different oxidation states. The $Mn(OH)_2$ could transfer into β-MnOOH and birnessite with the same morphology. The as-prepared β-MnOOH can be applied as a cathode material for LIBs. The organic molecules involved play a crucial role in controlling of the oxidation states and morphologies.

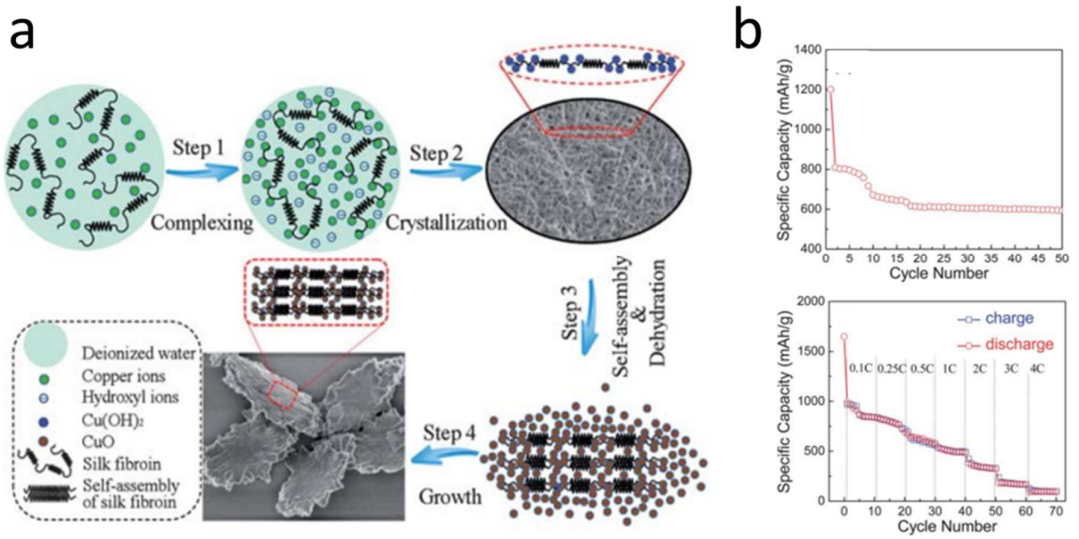

Figure 2.11. The illustration of the formation process, SEM images and electrochemical performance of CuO via special bio-template for lithium-ion batteries.[48]

The solution filled with specific protein could achieve to control the self-assembly of inorganic structures. Here, Fei et al [48] made use of silk fibroin solution as soft template to help form the hierarchy nanostructures of CuO and meanwhile combine them with biomimic mineralization under room temperature. The almond-like structures with branched edges will be transformed from $Cu(OH)_2$ nanowires. The size of CuO could be tuned by the concentration of precursor solution. The almond-like CuO was prepared as an anode material, which delivered 1200 mAh g^{-1} in the first irreversible reaction and kept a reversible capacity of 820 mAh g^{-1} at a rate of 0.3 C. The rate performance is stable from 0.1 - 4 C.

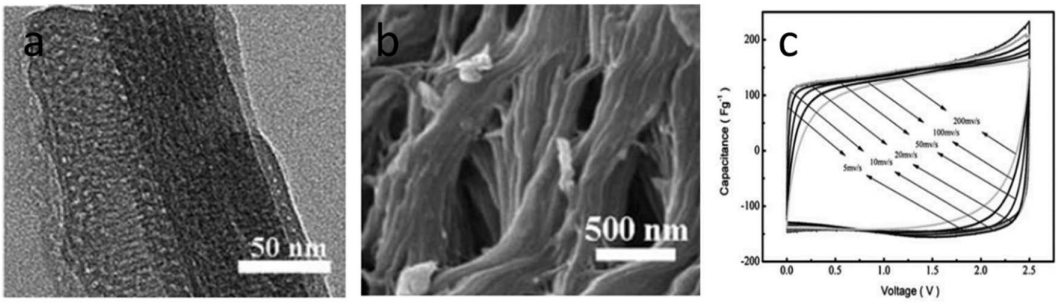

Figure 2.12. The morphologies and electrochemical performance of carbonized carb shell as carbon electrodes for supercapacitors.[49]

Existed biological templates have sophisticated hierarchy structures. Hai et al took the carb shell as the template to prepare mesoporous carbons with large specific surface area.[49] The surfactant-templating self-assembly of organic resols are used as the precursors. The carbonized product remained the original structures of the carb shell, which could be taken as the idea supercapacitors and fuel cells. The specific capacity of it is close to 145 F g^{-1}. The rectangle symmetry of the CV curve is kept well at 200 mv s^{-1}. The cycling performance is still good after 1000 cycles.

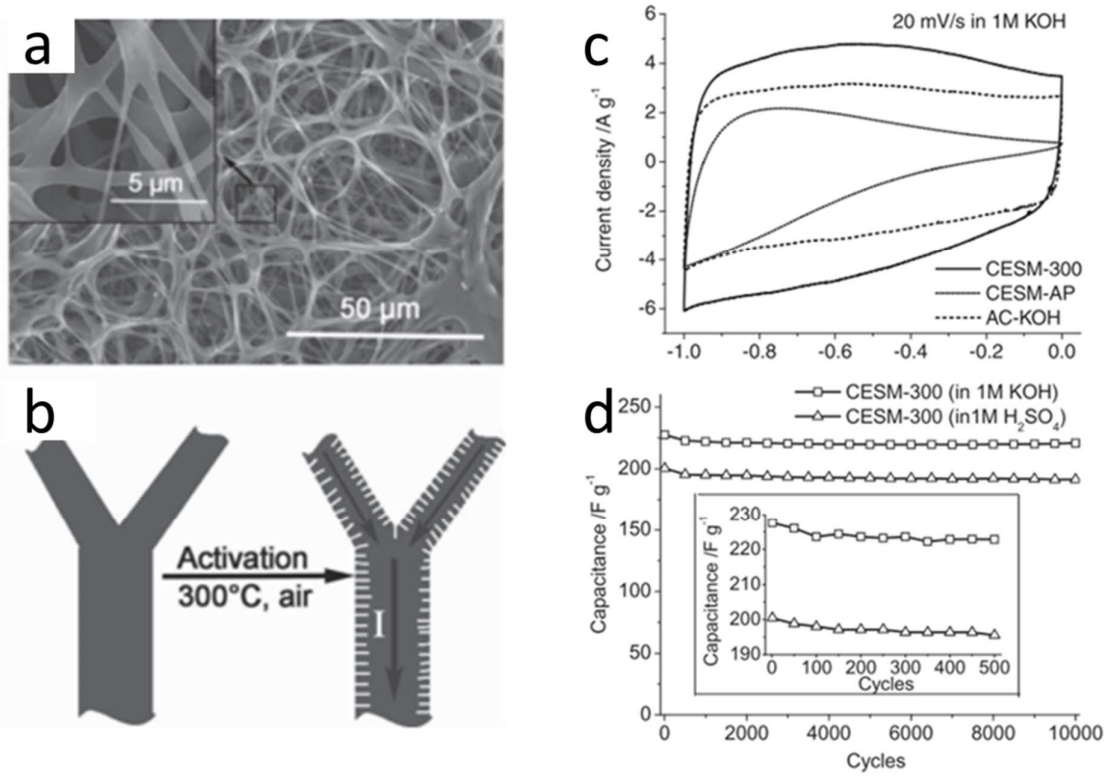

Figure 2.13. The illustration of the formation process, SEM image and electrochemical performance of carbonized eggshell membrane electrodes for supercapacitors.[50]

Sometimes, merely the simple treatment of existed nature nanostructures could bring a new application. Li et al[50] made use of a useless eggshell membrane as this kind of precursor. Novel carbon-based material with hierarchical porous 3D networks is used as supercapacitors. Although the surface area is only 221 m^2 g^{-1}, specific capacitances could be as high as 297 F g^{-1}. Moreover, the eggshell membrane electrode possesses excellent cycling performance, and only 3 % capacitance loss is observed after 10000 cycles at 4 A g^{-1}.

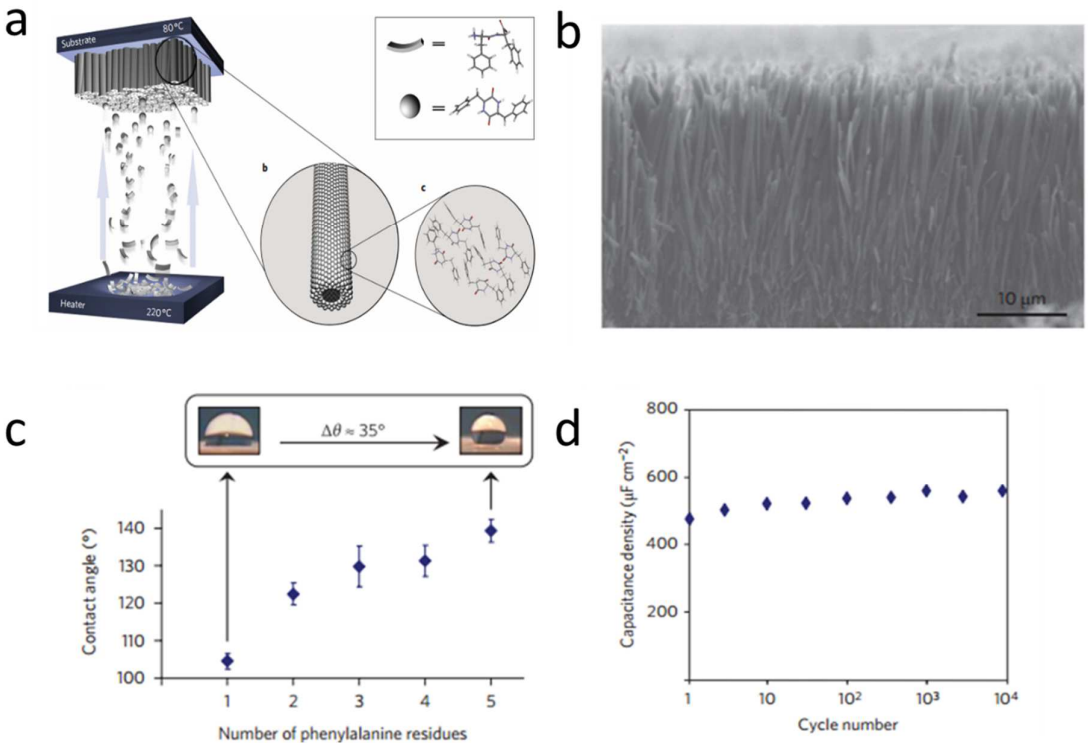

Figure 2.14. The illustration of the formation structures, SEM images and self-cleaning effect of aromatic peptide nanotubes.[51]

Self-assembly is one of the central ideas of biomimic method. Recently, Li et al[51] invented an artificial self-assembly method to fabricate large scale arrays of aromatic peptide nanotubes by a controllable vapor deposition method. The nanotubes were easily controlled. Furthermore, the nanotube arrays can be used as electrodes for supercapacitors. The cycling performance of it is excellent. It keeps more than 500 uf cm^{-2}. Its highly hydrophobic self-cleaning surface and function as microfluidic chips are obtained at the same time.

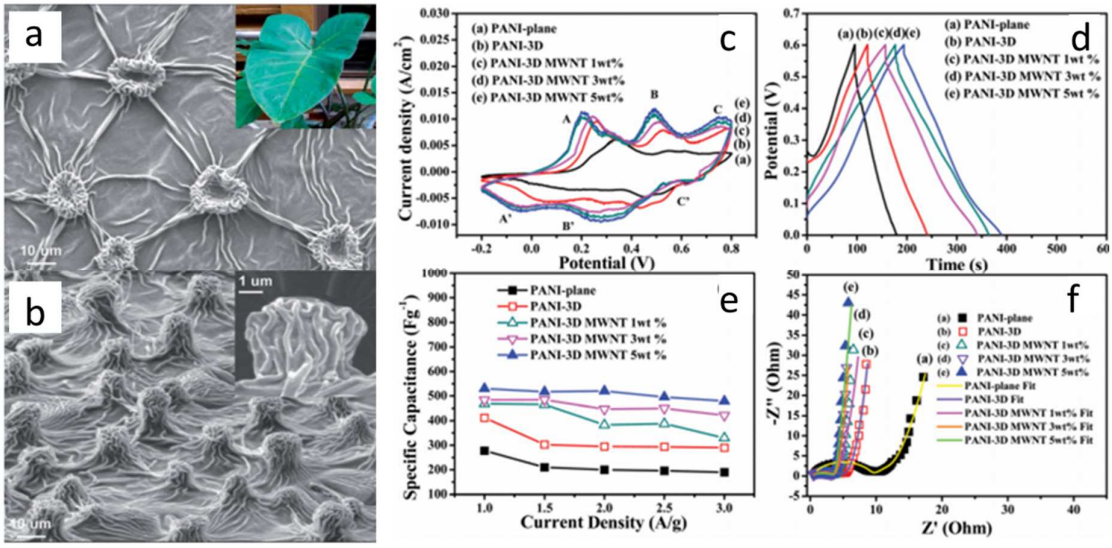

Figure 2.15. The morphologies and electrochemical performance of biomimetic PANI nanocomposite electrodes for lithium-ion batteries.[52]

Fresh Xanthosoma sagittifolium leaves were used as a template to fabricate the PANI/MWNT composite material by the simple casting technique.[52] The surface structure of PANI nanocomposite is similar to the template, which demonstrated that both papilla-like and nanostructured texture were replicated. MWNTs are well-dispersed in the surface and the hierarchical structure formed a highly rough nanocomposite of PANI/MWNT. Due to the large surface area, high specific capacitance of 535 F g^{-1} at 1 A g^{-1} was achieved. The stable nanostructure helped it to maintain good cyclability during the charge-discharge process.

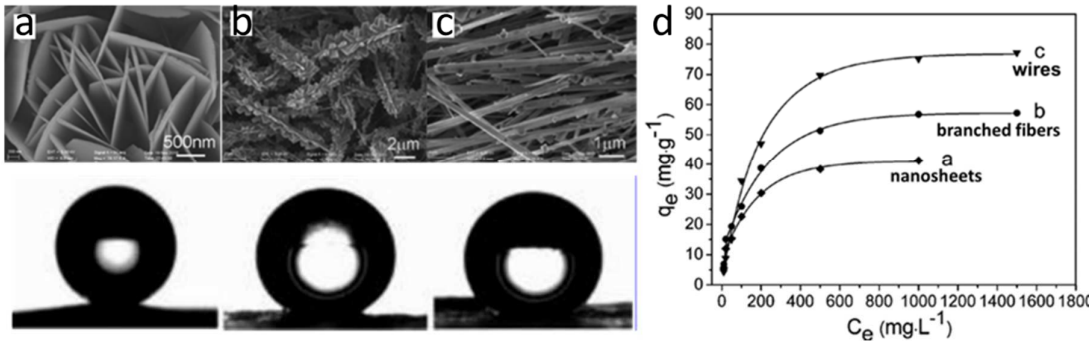

Figure 2.16. Morphologies and related wettability of FeOOH hierarchical structures controlled by different concentrations of PAA in precursor solution (left). Absorption capability of Cd^{2+} based on different nanostructures (right).[53]

Bio-inspired gas-liquid diffusion mechanism was used to fabricate hierarchical FeOOH array films from bottom up by self-assembling the building blocks at the air-water interface.[53] In this method, poly(acrylic acid) (PAA) as the organic part could mediate the morphology and structure of FeOOH. By changing PAA's concentration, the structures of FeOOH can be regulated among nanosheets, rice spikes, branched fibers and nanowires. The wettability of hierarchical FeOOH could be adjusted by controlling the structures. Moreover, the absorption capability for heavy metal ions varies according to different morphologies.

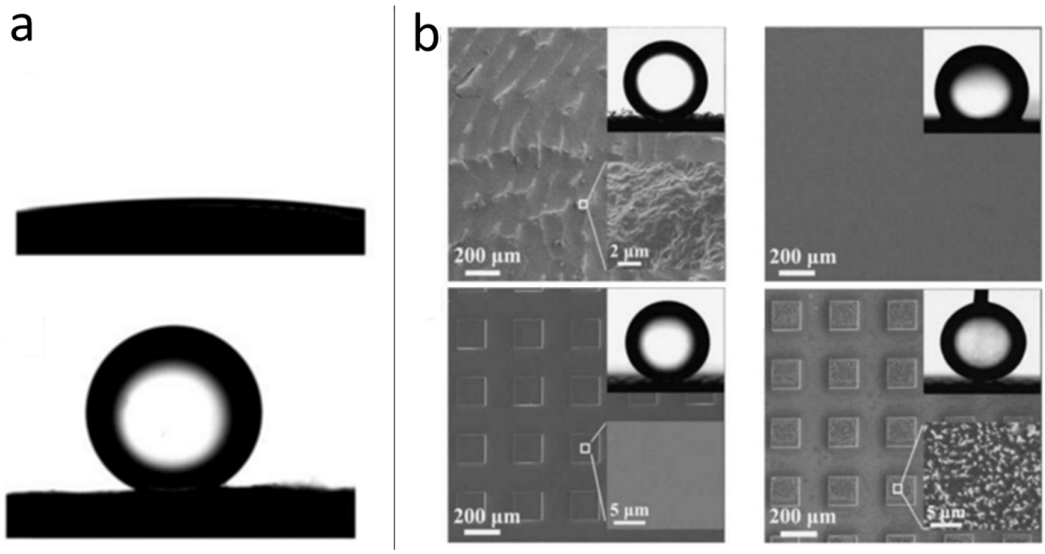

Figure 2.17. Wettability of fish scale's inspired nanostructures on surface.[54]

Recently, researchers found that fish scales is both superoleophilic and underwater superoleophobic.[54] Inspired by this special wettability, various functions of biomimic structures with superoleophilicity and superoleophobicity were synthesized. The potential environmental applications are related to anti-fouling, water/oil separation and self-cleaning. Although the study of underwater oil wettability is at the early stage, its development is fasting growing.

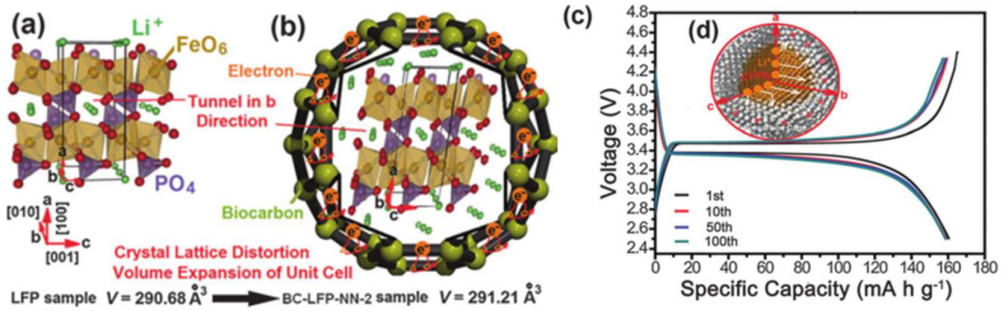

Figure 2.18. The illustration of the formation structures, TEM images and electrochemical performance of cell-derived $LiFePO_4$ electrodes for lithium-ion batteries.[55]

Negative function groups of biomacromolecules can improve the hydrophilic on the cell wall. As a result, biomineralization ability of them could be regulated artificially. Zhang et al[55] presented a facile and low-cost method for preparing carbon-coated $LiFePO_4$. The yeast cells can be taken as both the bio-template in biomineralization and the carbon source after the following thermal treatment. By calcination under 750 ^oC, the yeast cells were carbonized and carried out a reducing atmosphere that can prevent the oxidation of Fe^{2+}. The carbonized structure as the shell effectively restricted the growth of $LiFePO_4$ and increased the conductivity of it. Excellent discharge capacity (160.4 mAh g^{-1} at 1 C) and cycling performance (0.9 % loss from the initial value) were achieved.

CHAPTER 3 NOVEL EGGSHELL DIRECTED BIOMIMIC SYNTHESIS OF CoO NANOROD CLUSTERS ON CARBONIZED EGGSHELL MEMBRANE AS ELECTRODE MATERIALS FOR LITHIUM-ION BATTERIES AND SUPERCAPACITORS

3.1 Introduction

Nanotechnology is an exciting field and attracts more and more attention. The development and innovation of strategies for developing nanostructured materials have been one of the hottest research topics. Due to their unique physical and chemical structures (large surface area/volume, high catalytic activity, controllable morphologies, etc.), they are different from related conventional bulk materials. In the vast domain of energy storage, it is valuable to develop nanotechnology to synthesize materials. It is well known that size, morphologies, and structures of nanomaterials systematically influence their electrochemical properties and in further applications in this area. Massive novel nanomaterials have being developed, leading to improve dramatically their performances in energy storage.[56] To consider nanomaterials in practical energy storage, it is crucial to develop nanomaterials via varieties of facile but "green" methods to accelerate their commercialization.

In the past decades, a series of methods have been developed to prepare various hydroxides/oxides nanomaterials, which could be promising candidates for energy storage.[2, 57-58] Among the transition metal hydroxides and oxides, Co-related hydroxides and oxides (e.g., $Co(OH)_2$, CoO and Co_3O_4) are particularly interesting because of the potential applications in lithium-ion batteries[59-63] and supercapacitors.[64-69] By now, various traditional methods like hydrothermal methods,[65] solvothermal processes,[70] sol-gel,[62] thermal decomposition,[62, 71] electrochemical methods,[43, 72] chemical precipitation,[68] spray-pyrolysis[73] have been used to fabricate $Co(OH)_2$, CoO or Co_3O_4 nanomaterials. However, most of them are companied with limits such as energy consuming process, expensive facilities, complicated preparation steps, and high pressure/temperature. In a sense, it means that we cannot afford the large-scale

production of their nanomaterials based on current methods. Therefore, more environment-friendly, convenient and energy-efficient methods for preparing nanomaterials are of interest and realistic to apply them in our daily life.

Bio-inspired synthesis also referred to biomimetic synthesis are paid much attention.[40, 43, 45, 74] Although we are still at the early stage of synthesizing nanomaterials, nature has mastered it for almost 4 billion years, which is reliable for us to imitate or take inspiration from its designs and processes to improve our fabricating nanomaterials.[16] Moreover, in most cases, these natural materials are developed under mild conditions and no harmful impact to the earth. In contrast, human activities in manufacture have gradually changed the normal situation of our earth such as greenhouse effect, industrial pollution and energy crisis, which have being inhabit the steps of us recently. Thus, there is a growing call for biomimic synthesis for researchers and surging public interest in "green" manufacturing next-generation materials-nanomaterials.

Even if most of bio-inspired methods followed the principles of biologic methods or used natural materials directly, [40, 75-76] few, as if, reported more interesting strategy that combines these two ideas together to simulate the synthetic progress in nature. For eggshell membrane (ESM), there have been many reports of preparing functional materials by taking it as a hard template but no attractive nanostructures of these materials, except small nanoparticles, are created on it.[26, 28] Thus, these results are still far away from ideal biomimic synthesis. These studies did not consider the biologic principles of synthesizing nanomaterials. Alternatively, the beneath mechanism of biomineralization could be considered to grow controllable nanostructures.[77-79]

Herein, we demonstrate a novel strategy for facile synthesis of amorphous $Co(OH)_2$ precursor with nanorod clusters based on the biomimic mineralization principles and decomposed it into CoO under relatively low temperature. Eggshells are firstly introduced as

natural reactors. Meanwhile, ESM is not only taken as an active substrate for biomimic mineralization but also good conductive carbon matrix as a part of CoO@CESM electrode materials. To our best knowledge, this structure is first found here due to our unique biomimic strategy. This strategy can be considered as a new solution of taking advantages of the characteristics of Eggshells with ESM and the principles of biomineralization at the same time. It could help us to explore bio-inspired technology for nanomaterials and energy storage. The precursors of CoO@CESM were easily prepared under mild conditions in eggshells. The hierarchical structures of CoO@CESM possess both a high specific surface area and shorter path for ions and electrons transportation, which is essential for enhancing electrochemical reactions. For LIBs, the results show that nanostructured CoO clusters in CoO@CESM electrodes exhibit stable more than 900 mAh g^{-1} at 0.1 A g^{-1} after 120 cycles and the cycling performance is excellent without any fading. Similarly, CoO@CESM electrodes perform good electrochemical performances as SCs. They deliver ~605.3 F g^{-1} after 1000 cycles at the current rate of 2 A g^{-1}.

3.2 Experimental Section

Materials Synthesis. In a typical synthesis procedure, fresh hen eggs purchased in a local supermarket were gently opened at the blunt end with air cell and were taken off all the contents. The eggshells with ESM were washed with DI water totally. Typically, 30 ml 1 M $CoSO_4$ solution with 10 mM CTAB was gently injected into an eggshell with ESM, then 30 ml 1 M NaOH solution was slowly injected into the outside of this eggshell in a beaker. The treated ESM in a beaker can be taken as an "eggshell" reactor. Finally, several eggshell reactors were sealed by Para films and placed in an oven. All the reactors were incubated at 50 ^oC for different reaction periods (12 h, 24 h, 48 h and 96 h, respectively). After the reaction, all the eggshell reactors were emptied and cleaned with DI water thoroughly. All the eggshells were dried in vacuum oven at 50 ^oC for 24 h. Then, as-deposited ESMs were easily separated from the

eggshells and heat treated in argon or air at different temperature (350 °C or 650 °C) for 2 h. The ramping rate was set at 10 °C min^{-1}. The schematic of the reaction route of preparing CoO@CESM is shown in Figure 1.

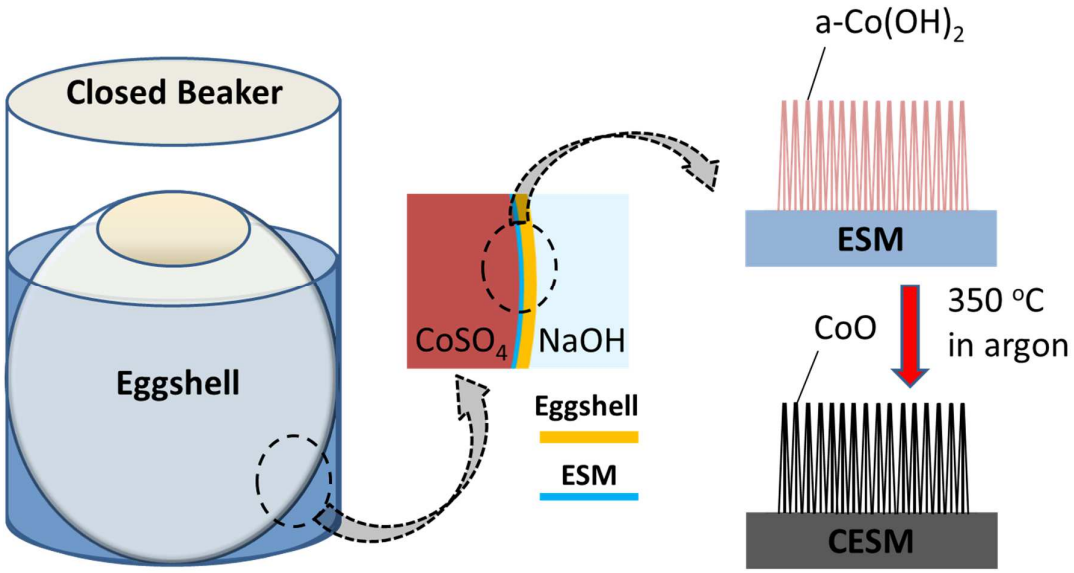

Figure 3.1. Schematic of this reaction route.

Materials Characterization. X-ray diffraction analysis of the samples was carried out by XRD machine (Rigaku RU 200B with Cu Kα radiation). The surface of as-prepared ESM and related products after heat treatment with gold coating were observed via a field-emission scanning electron microscopy (FESEM/EDX JEOL-7600, operating at 15 kV). Transmission electron microscopy (TEM JEOL-2010, with accelerating voltage of 200 kV) was used to determine the size, morphology and structure. The thermo-gravimetric measurement was performed on Perkin-Elmer TGA Q600 thermal analyzer in air from room temperature to 1000 °C (heating rate is 10 °C min^{-1}). XPS Data was acquired by X-ray photoelectron spectrometer (Perkin-Elmer 5500).

Electrochemical Analysis. The electrochemical properties of CoO@CESM electrodes for LIBs were characterized in 2032 coin cells. The homogeneous slurry was prepared by well mixing the as-synthesized CoO@CESM, super C65 and polyvinylidene fluoride (PVDF)

binder in a weight ratio of 8:1:1 in N-methylpyrrolidone (NMP). The slurry was then coated on Cu foil current collectors and dried in vacuum oven at 100 ^{o}C overnight to prepare the binder contained electrodes. The assembly of electrochemical test cells were operated in an argon-filled glove box, using the coated Cu foil as the working electrode, metallic lithium foil as the counter and reference electrode. 1 M solution of $LiPF_6$ in a 50:50 (wt%) mixture of ethylene carbonate (EC) and diethyl carbonate (DEC) are used as the electrolyte, and PP/PE/PP trilayer membranes (Celgard 2320) are used as the separator. Cyclic voltammetry (CV) of CoO@CESM electrodes were tested by an electrochemical workstation (CHI 660D) at a potential between 0.01 - 3 V at room temperature. The scanning rate is 0.2 mV s^{-1}. The assembled coin cells were charged and discharged galvanostatically at room temperature in the voltage window of 0.01 - 3 V at different current densities (0.1 to 1 A g^{-1}) on a Neware battery tester. At the same time, CoO@CESM electrodes were evaluated as supercapacitors. The same slurry was coated on cleaned Ni foam as the working electrode and characterized with a three-electrode system, which consisted of Pt mesh counter electrode and Ag/AgCl reference electrode in 1M KOH aqueous solution. CV and galvanostatic charge-discharge cycling of CoO@CESM electrodes were tested by CHI 660D at a potential between 0.1 - 0.5 V and 0 - 0.48 V, respectively at room temperature. For CV measurement, the scanning rate is ranging from 2 to 50 mV s^{-1}. For galvanostatic measurement, the current densities are ranging from 1 A g^{-1} to 16 A g^{-1}. The specific capacitances of the electrodes were calculated according to the equation of $C = I \times \Delta t / \Delta V$, where I is the constant discharge current, Δt is the discharging time and ΔV is the voltage window for the galvanostatic measurement.

3.3 Results and Discussion

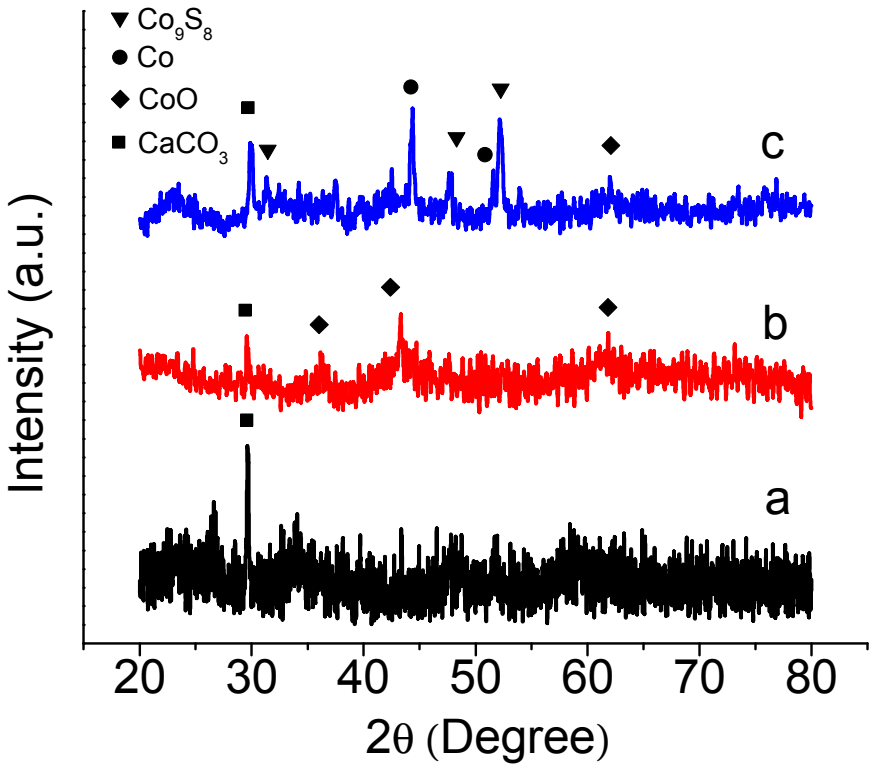

Figure 3.2. XRD patterns of (a) a-$Co(OH)_2$@ESM and related products after calcination in argon for 2 h at (b) 350 ºC and (c) 650 ºC.

The main products derived the as-deposited ESM after 96 h reaction and related decomposed products after calcination in argon were characterized by powder XRD measurement. As shown in Figure 3.2a, there are no obvious peaks of crystalline $Co(OH)_2$ after biomimic mineralization though ESM became brown from white color. It indicates that the as-deposited $Co(OH)_2$ on ESM is amorphous. To our best knowledge, only a few reports are related to amorphous $Co(OH)_2$ (a-$Co(OH)_2$).[71, 80] The obvious peak marked is $CaCO_3$ (104), which is the impurity from eggshell itself. The cubic phase CoO (JCPDS Card No. 89-7099) can be obtained by decomposition of a-$Co(OH)_2$ at 350 ºC in argon for 2 h. There are three peaks of CoO located at 36º, 43º and 62.5º, respectively. However, the intensity of peaks are very weak, and they are broad. This phenomenon reveals that crystal size of CoO might be

very small or the existence of some amorphous structure inside. Since the low intensity and the background noise, the exact size cannot be calculated from XRD here. If we increase the heating temperature to 650 °C, typical peaks of metallic Co (JCPDS Card No. 89-7093) and Co_9S_8 (JCPDS Card No. 86-2273) are detected. This transformation from CoO to Co and Co_9S_8 suggests that ESM processes reducibility after calcination at 650 °C in argon due to the release of mixture reduction gas (such as H_2S, CH_3S and NH_3).[81-82] To our best knowledge, this interesting phenomenon has not been reported before. The properties of Co-Co_9S_8 composites are being studied currently. To be sure of the high content of CoO in anode materials for more specific capacity, we chose 350 °C as the temperature of preparing CoO@CESM anode materials, at which the precursor a-$Co(OH)_2$ has already decomposed to CoO without Co and Co_9S_8. Although there are always impurity peaks of $CaCO_3$, the content of it is relatively low and can be ignored according to EDS and TGA results in Figure 3.3.

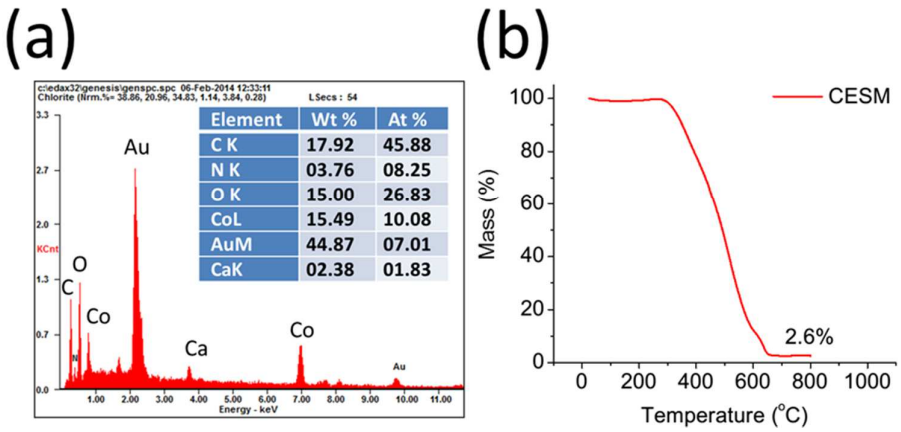

Figure 3.3. Content of impurity $CaCO_3$ in pure ESM: (a) EDS analysis results and (b) TGA analysis results.

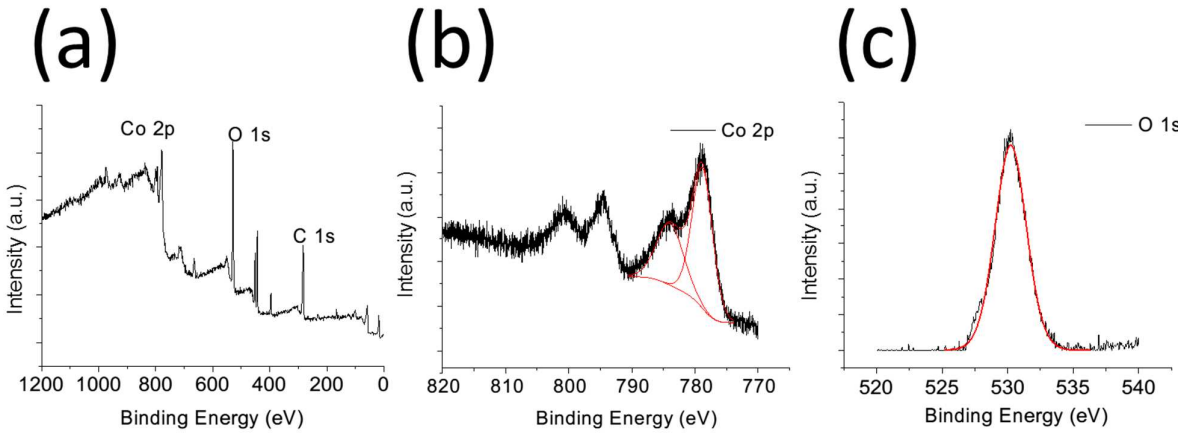

Figure 3.4. (a) XPS spectra of CoO nanorods on the surface, and related high-resolution spectra of (b) Co and (c) O.

To in further confirm the chemical composition of decomposed product in argon at 350 ^{o}C, XPS was employed. In Figure 3.4a, multi-peaks of Co, O and C were all detected. C peak is used to index Co. Figure 3.4 shows the Co 2p and O 1s XPS spectra of typical CoO@CESM sample. As shown in Figure 3.4b, there are two main Co 2p peaks, which locate at binding energy (BE) 795 eV (Co $2p_{1/2}$) and 779.1 eV (Co $2p_{3/2}$) with shake-up satellite peaks.[83] It is difficult to determine directly the oxidation state in cobalt oxides by means of XPS because of similar Co 2p spectra of Co, CoO and Co_3O_4.[84-85] In general, the gap energy between two main peaks and satellites of Co is the variable used to clarify its oxidation states. When the distinct satellites peaks are located ~6 eV above the corresponding main peaks, the spectrum could be indexed to Co^{2+} in CoO. Only if the distance is approximately 10 eV, the spectrum can be indexed to Co^{3+}.[86] If it is pure metallic Co, there are few satellites.[85] Therefore, as-synthesized product after calcination is indexed CoO, which is consistent with its XRD pattern.

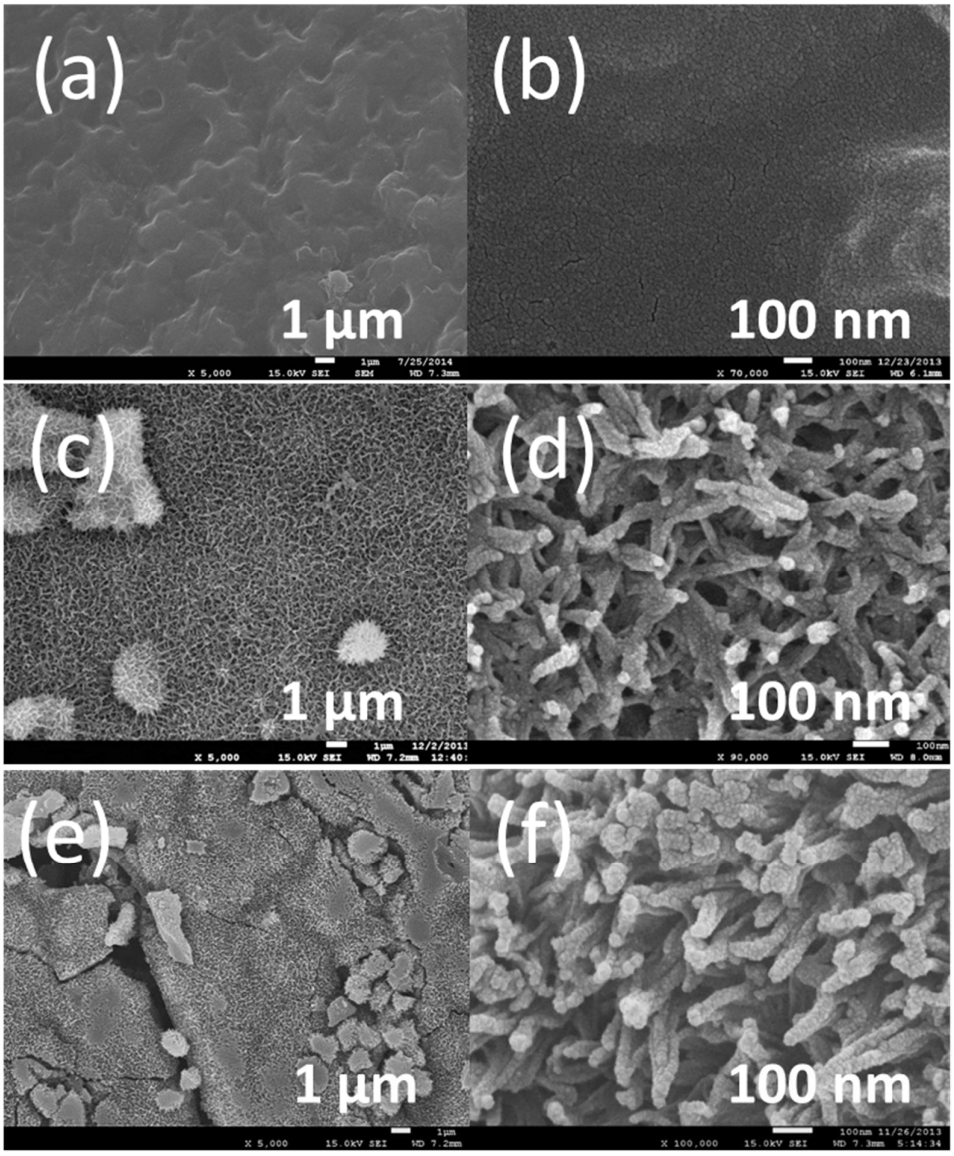

Figure 3.5. FESEM images of the related products at different reaction stages: (a, b) original ESM before reaction; (c, d) a-Co(OH)@ESM precursors after reaction under 50 ^{o}C for 96 h at different magnifications; (e, f) CoO@CESM after calcination under 350 ^{o}C in argon for 2 h at different magnifications.

FESEM images revealed all the details of the surface of ESM at different stages of synthesis. The initial structure and morphology of ESM facing to $CoSO_4$ solution are shown in Figure 3.5a and Figure 3.5b. The surface of it is smooth and no any nanostructures except some specific dot structures from ESM itself. After 96 h reaction at 50 ^{o}C, the surface of all the membrane was covered by nanostructures (Figure 3.5c). At higher magnification in Figure

3.5d, the average diameter of nanorods is less than 50 nm and the length is up to 200 nm. Interestingly, these unique nanorods do not stand independently. All of them are agglomerated into clusters and then connected with each other to form porous hierarchical networks. In specific, the roots of them are separated, but the tips of them are attached. We would like to highlight that this kind of structure of Co-related hydroxides and oxides has not been reported before while there was the similar structure of nickel hydroxide carbonate prepared.[87] The potential applications for it will be studied later. For Figure 3.5e and 5f, after calcination at 350 ^{o}C in argon, the nanostructures were kept well but some cracks in CESM (Figure 3.5e). These broken areas are due to the brittle nature of CESM. As showed in Figure 3.4f, the surface of nanorod clusters became rough.

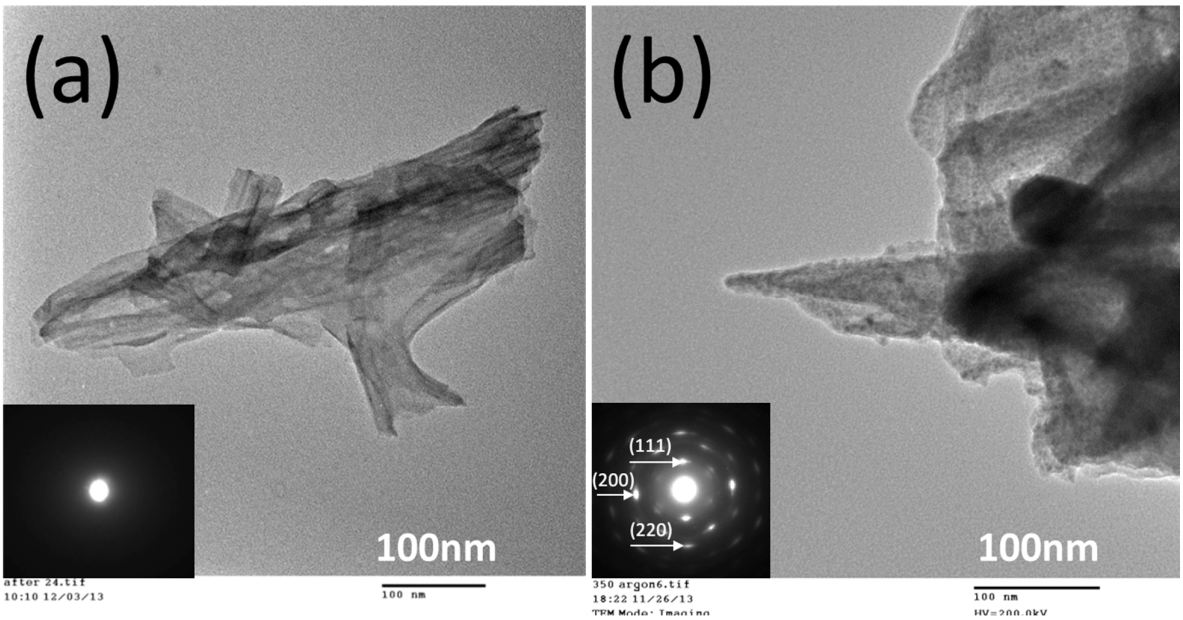

Figure 3.6 TEM images of (a) as-prepared a-$Co(OH)_2$ nanorod clusters and (b) CoO nanorod clusters after calcination at 350 ^{o}C in argon for 2 h. The insets in (a) and (b) are the corresponding electron diffraction patterns, respectively.

The morphologies and structures characterization of a-$Co(OH)_2$ and CoO nanorod clusters separated from ESM/CESM were also performed in detail by TEM and SAED. In Figure 3.6a, the as-prepared a-$Co(OH)_2$ nanorod clusters show a smooth texture. These

nanorods attach each other and some places are linked by sheets-like structure, which is different from the traditional single nanorod/nanowires of $Co(OH)_2$.[63, 88] The nanorod is 200 - 350 nm in length and around 50 nm in diameter, which is agreed with the observation in FESEM images (Figure 3.5c). The SAED inset suggests that it is amorphous, which is consistent with the XRD analysis above. In contrast, Figure 3.6b shows CoO nanorods clusters after calcination at 350 ^oC in argon. The surface of nanorods become rough and some aggregated tiny particles could be noticed. However, its morphology as a whole is not changed. The three sets of diffraction spots in SAED patterns along with Figure 3.5b are indexed as (111), (200) and (220) planes of cubic CoO.[89] To be noticed here, it is hard to separate CoO from CESM since they are connected each other firmly after calcination.

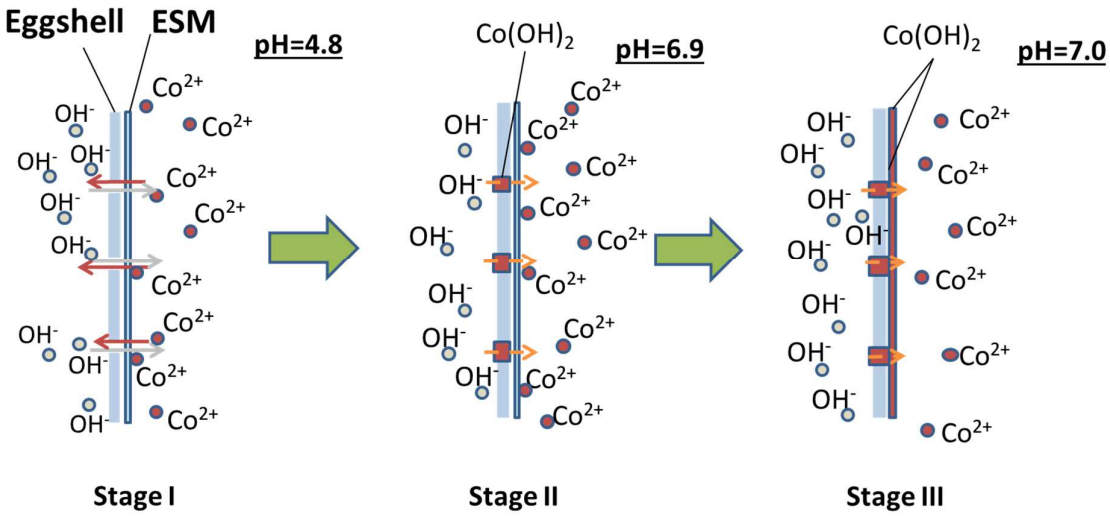

Figure 3.7. The proposal mechanism of the formation of nanostructured a-$Co(OH)_2$@ESM.

Although the mechanism of formation of these interesting nanostructures is still not totally clear, some existed information could help us to understand it roughly. Figure 3.7 presents the hypothesis of it based on related experimental observation. Here, there are two main parts in reaction: one is eggshell, the other is ESM. On one hand, eggshell is taken as a solid separator, which could separate NaOH and $CoSO_4$ solutions mechanically. However, unlike full isolation, the natural air pores on eggshell allow OH^- and Co^{2+} ions to freely

transport at the early stage of reaction (Stage I). Initially, the pH value of $CoSO_4$ solution is 4.8. Then, with the increase of pH value (4.8 to 6.9), at Stage II, a-$Co(OH)_2$ could initially deposit and accumulate around the pores[90] and lead to blocking the exchange of ions and hinder their fast transportation. Although OH^- ions could not pass eggshell freely, it still can slowly diffuse via blocked nanopores.[90] The slight increase of pH value (from 6.9 to 7.0) of $CoSO_4$ solution confirms it. During the formation of nanostructured a-$Co(OH)_2$, there might be different degrees of supersaturation for a-$Co(OH)_2$ in $CoSO_4$ solution due to the pH change. This change is also involved in natural biomineralization.[91] On the other hand, ESM provides a large number of active sites to accelerate the heterogeneous nucleation of a-$Co(OH)_2$ on ESM.[92-93] The functional groups such as -COOH, -NH_2 and -OH can attract Co^{2+} ions. Meanwhile, the diffusion of OH^- ions supports the continuous supersaturation of $Co(OH)_2$ in the whole process. As a result, a-$Co(OH)_2$ nucleus forms on ESM. Following the mechanism of biomineralization, these nucleus could continue to grow (Stage III) on ESM. The self-assembly of nanostructured a-$Co(OH)_2$ on ESM could be spontaneously controlled in the closed eggshell system, involving a change of pH value, ESM substrate, anions, temperature, CTAB surfactant and so on. Finally, a-$Co(OH)_2$ nanorod clusters are successfully developed. Note that $CoSO_4$ solution is just a typical case to make use of this proposal mechanism, other metal salt solutions might be applied to expand this biomimic protocol to mineralize various metal hydroxides or even oxides. The following studies are undergoing.

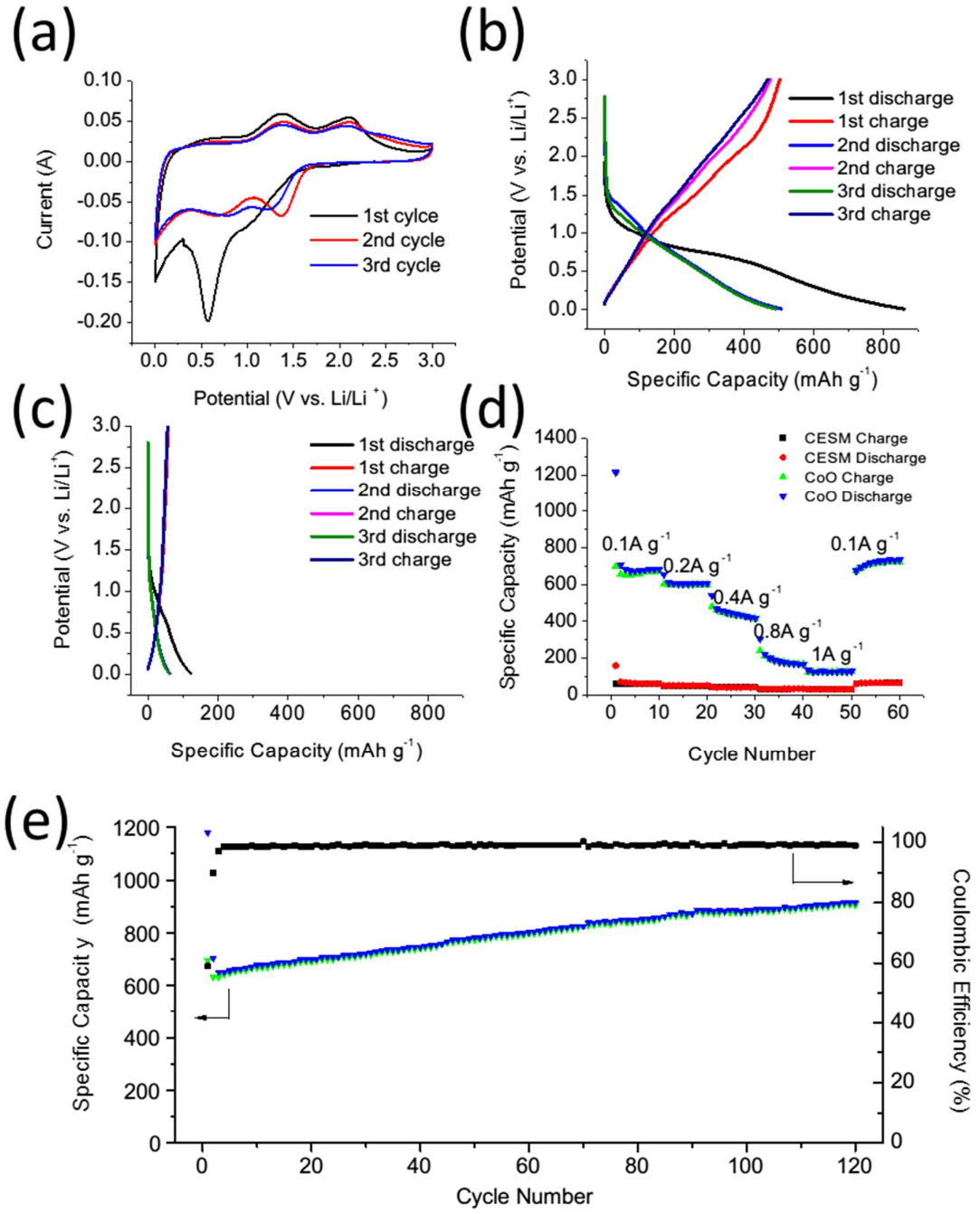

Figure 3.8. Electrochemical properties of CoO@CESM anode materials: (a) typical charge-discharge profiles of the first 3 cycles at a current rate of 0.1 A g-1; (b) CV curves of the first 3 cycles at the scanning rate of 0.2 mV s-1; (c) charge-discharge profiles of the first 3 cycles of pure CESM as a control at a current rate of 0.1 A g-1; (d) rate performance and (e) cycling performance of CoO nanorod clusters after normalization.

Recently, nanostructured CoO and its composites employed as advanced energy storage materials have been intensively studied.[7, 15, 37, 48-58] These tailored nanostructures could improve the electrochemical properties via increasing surface area, improving conductivity or stabilizing the volume change during the charge-discharge process. The electrochemical properties of CoO@CESM as anodes for LIBs were first evaluated in half-cell assembly here. The CV curves of the first three cycles are shown in Figure 3.8a at a scan rate of 0.2 mV s^{-1}. It can be noticed that CoO@CESM electrodes have a strong peak at 0.5 - 0.75 V in the first cathodic scan, which indicates the composition of CoO into Co and the formation of Li_2O and the SEI.[83, 94] The broad peaks located at about 1.3 and 2.2 V in the following anodic scan curves may be attributed to the partial decomposition of the SEI and oxidization of Co.[94-95] The related redox reactions of CoO are listed below.

$$CoO + 2Li + 2e^- \rightleftharpoons Co + Li_2O \text{ (Discharge)} \quad (1)$$

$$Co + Li_2O \rightleftharpoons CoO + 2Li^+ + 2e^- \text{ (Charge)} \quad (2)$$

In the 2nd and 3rd cycles, the cathodic peaks shift due to the influence of irreversible formation of SEI and the decomposition of electrolyte.[83]

The initial three discharge-charge cycling curves of CoO@CESM electrodes are shown in Figure 3.8b. For the first discharge process, the potential plateau is not clear as pure CoO for the existence of CESM. Instead, there still is a slow slope curve from ~1.2 to 0.75 V, following by another slow slope curve down to cut-off voltage 0.01 V. The initial discharge capacity and charge capacities are 858.1 and 502.9 mAh g^{-1}, corresponding to a Coulombic efficiency of 58.6%. This relatively low Coulombic efficiency might be related to the irreversible formation of SEI and electrochemical reaction in the first cycle.[96] Then the second and third cycle curves of discharge and charge are highly overlapped, suggesting the good cycling property. Comparing with the pure CESM in Figure 3.8c, CoO@CESM electrodes' enhanced reversible capacity (60 mAh g^{-1} for CESM and 507 mAh g^{-1} for CoO@CESM) is

contributed to nanostructured CoO network on the surface. To understand the practical value of the specific capacity of CoO nanorods itself in CoO@CESM electrodes, we normalized the obtained specific capacity by deducting the contribution of CESM inside. Figure 3.8d shows the normalized electrochemical performance of the CoO nanorods at various current densities from 0.1 to 1A g^{-1} and the control of CESM. The normalized specific capacity of CoO nanorod clusters in CoO@CESM suggests the high capacity of it. At 0.1A g^{-1}, nanostructured CoO clusters deliver a capacity of 683 mAh g^{-1} at the 10^{th} cycle. The following capacities of the electrodes are 606 mAh g^{-1} at the 20^{th} cycle at 0.2 A g^{-1}; 416 mAh g^{-1} at the 30^{th} cycle at 0.4 A g^{-1}; 167 mAh g^{-1} at the 40^{th} cycle at 0.8 A g^{-1}; 127 mAh g^{-1} at the 50^{th} cycle at 1 A g^{-1}, respectively. At the first three current densities, the performance is stable, which can be attributed to this hierarchical nanostructure and the integration with carbonized substrate, which improves the contact area of electrode/electrolyte and facilitate the diffusion of ions. However, at the higher current densities (> 0.4 A g^{-1}), the performance is poor. The possible reason might be the degree of carbonization of CESM. After all, 350 ^{o}C is not high enough to carbonize ESM well to achieve better conductivity. Further studies are in progress to improve the properties at the high current rate. The capacity retention property of CoO@CESM electrodes at a current density of 0.1 A g^{-1} is presented in Figure 3.8e. The CoO@CESM electrodes exhibit pretty good cycling stability during 120 cycles, corresponding to a Coulombic efficiency of 99.7%. The interlocked nanostructured CoO clusters demonstrate high electrochemical activity. They deliver 914.9 mAh g^{-1} at 0.1 A g^{-1} at 120^{th} cycle without any decay. The stable cycling performance may be attributed to the stable nanostructures of CoO as well as the 3D porous network integrated on conductive CESM. Moreover, with the increase of cycles, the specific capacity has slightly increased, which might be ascribed to the reversible formation of a polymeric gel-like film.[97]

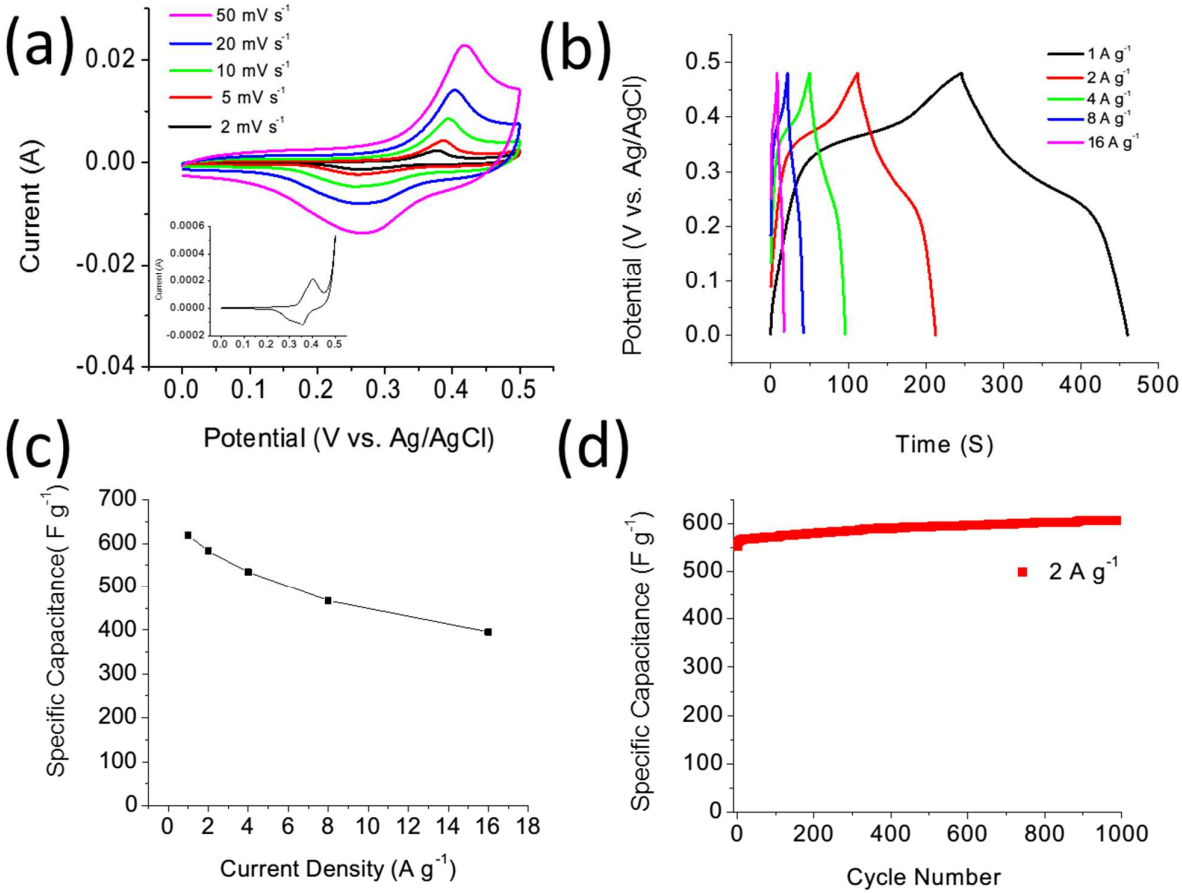

Figure 3.9. Electrochemical characterization of CoO@CESM electrodes: (a) CV curves at various scan rates from 2 mV s^{-1} to 50 mV s^{-1}; (b) Galvanostatic charge and discharge curves at various current densities from 2 A g^{-1} to 16 A g^{-1}; (c) Specific capacitance at various current densities; (d) Cycling performance at 2 A g^{-1}.

Because of the extremely large specific surface area and electrochemical activity of nanostructured CoO clusters. The electrochemical properties of CoO@CESM were also characterized as electrodes for supercapacitors. Figure 3.9a shows the CV curves of CoO@CESM electrodes in 1 M KOH at different scanning rates of 2, 5, 10, 20, 50 mV s^{-1}. A pair of redox peaks in every curve is observed, which indicates the typical faradic reactions in equations below:

$$CoO + OH^- \leftrightarrow CoOOH + e^- \quad (3)$$

$$CoOOH + OH^- \leftrightarrow CoO_2 + H_2O + e^- \quad (4)$$

Besides, with the increase of scanning rate from 2 mV s^{-1} to 50 mV s^{-1}, the peak currents increase as well, suggesting fast kinetics of electrochemical reaction sites on the surface.[98-99] Note that the pure Ni foam has tiny peak currents as shown in the insert, which can be ignored.

In Figure 3.9b, the galvanostatic charge-discharge curves of CoO@CESM electrodes were characterized in a potential range of 0 - 0.48 V at different current densities, ranging from 1 to 16 A g^{-1}. The profiles of charge-discharge curves with obvious plateau suggest the feature of pseudo-capacitance, which is agreed with the results of CV curves above. Even if the mass of CESM is taken into account, the calculated specific capacitances of CoO@CESM are 619.2, 582.8, 533.9, 467.8, 395.6 F g^{-1} at different current densities of 1, 2, 4, 8, 16 A g^{-1}, respectively. The relationship between these capacitances and current densities are plotted in Figure 3.9c. This curve suggests that about 64% of the specific capacitance at 1 A g-1 is still kept even if the current density is multiplied 16 times. This good result could be ascribed to the porous network of CoO nanorod clusters on CESM. The large specific surface area results in easily contacting with electrolyte, boosting the transportation of ions.[99-100] The cycling performance was evaluated over 1000 cycles at the current density of 2 A g^{-1}. The CoO@CESM electrodes exhibit excellent long-term stability here, delivering 605.3 F g^{-1} after 1000 cycles with a slightly rising tendency. This outstanding stability could be attributed to the uniformed distribution of CoO nanorod clusters on conductive CESM firmly. Therefore, CoO@CESM electrodes could have promising applications in supercapacitors as it in LIBs. However, the function of incorporated CESM will be focused on the next step.

3.4 Conclusion

In conclusion, CoO nanoclusters on CESM were successfully prepared from amorphous $Co(OH)_2$ precursors on ESM under mild conditions by using biomimic mineralization followed by heat treatment. These unique compositions and structures were

firstly characterized by XRD, XPS, FESEM, and TEM. The possible mechanism of the formation of nanorod clusters on ESM in eggshells has been proposed. The eggshell reactor could spontaneously control the morphology and amount of precursors by merely adjusting reaction periods. After calcination in argon at 350 ^{o}C, the electrochemical properties of the CoO@CESM electrodes for LIBs and supercapacitors were evaluated. The satisfactory rate performance and cycling performance can be attributed to the special hierarchical structures of CoO nanorod clusters and their natural integration with conductive CESM. This novel biomimic approach is promising in fabricating other hydroxides and oxides as well.

CHAPTER 4 EGGSHELL-ASSISTED SYNTHESIS OF AMORPHOUS $Co(OH)_2$ NANOROD NETWORKS AS BINDER-FREE ELECTRODES FOR HIGH-PERFORMANCE SUPERCAPACITORS

4.1 Introduction

Amorphous materials possess short-range within several atoms without long-range atomic order. They are totally different from crystalline ones, regarding crystal structures as well as physical and chemical properties.[101-103] Amorphous materials are the important parts of the natural world and our society. Surprisingly, nature has developed varieties of amorphous structures with unique nanostructures.[104-107] These amorphous materials play an important part in biological activities. However, for human beings, most of artificial amorphous materials are still limited to bulk materials such as glass, rubber, and plastic. Since we have not easily understood the internal structures of amorphous materials and mechanism of fabrication. As a result, we have limited capabilities to design nanostructured amorphous materials in contrast of massive crystalline nanomaterials. Even if researchers have reported some interesting applications of amorphous materials, the low specific surface areas of conventional bulk structures hinder their potential applications.[108]

Amorphous materials at the nanoscale are promising for developing advanced materials for energy storage. In the past decades, amorphous nanomaterials have been explored as electrodes for secondary batteries. For example, amorphous $FePO_4$ nanomaterials have been reported as compromising cathodes for LIBs and sodium-ion batteries (SIBs).[109-111] Nanostructured amorphous carbon are another electrode materials to improve the performance of LIBs and potential candidates for SIBs.[112-113] Recently, amorphous nanomaterials such as TiO_2,[114] red phosphorus[115] and V_2O_5[116] also were studied as potential electrodes for SIBs. Supercapacitors (SCs) are another potential candidates for energy storage. By now, most of amorphous materials for SCs are focus on carbon-based materials[117-119] and metal oxides.[120-122] For carbon materials, they are based on double-layer theory. Thus, the specific capacitance

is mainly limited by its surface properties even if nanostructures could improve their performances by increasing surface area. For metal oxides, based on redox reactions, amorphous RuO_2 demonstrated excellent electrochemical performance. Its amorphous property played an important part in its performance to prevent the rigid lattice structure from limiting redox reaction.[122] However, the low reserve, high cost as well as high toxicity hinder amorphous RuO_2's commercialization.[123-124]

Hydroxides such as $Co(OH)_2$ have been intensively studied to replace RuO_2 as high-performance pseudocapacitors due to cheap cost and high theoretical capacitance (3460 F g^{-1}).[125-127] By now, most hydroxides for supercapacitors are crystalline. Previously, amorphous hydroxides performed poorly.[128-129] However, recently, some researchers have approved that amorphous $Co(OH)_2$ could achieve the commeasurable performance of the crystalline one.[80] Not only electrode materials, but also the fabrication process of electrodes affect electrochemical performance. Traditionally, electrodes have to be prepared by slurry-coating methods,[127, 130-131] which requires additional steps to combine active materials with the current collector and inevitably suffer relatively poor performance. In contrast, more and more studies are focusing on binder-free strategy, which is more facile and makes electrochemical performances better. Electrochemical methods are convenient to prepare binder-free $Co(OH)_2$ electrodes.[128, 132-137] However, these methods require well designed electrochemical apparatus or dangerous high potential. Hydrothermal method is another common solution to prepare binder-free $Co(OH)_2$ electrodes, but it requires high pressure and well-designed autoclaves. Researchers are still looking forward alternatives to make binder-free $Co(OH)_2$ electrodes via low-cost but facile approaches.

Herein, we demonstrate a bio-inspired method for controllable synthesis of amorphous $Co(OH)_2$ (a-$Co(OH)_2$) from $CoSO_4$ solution directly under mild conditions without any special devices. Abundant waste eggshells were introduced as "natural" reactors to separate simply

two reactant solutions, NaOH, and $CoSO_4$. After 4 days, a-$Co(OH)_2$ nanorod networks formed on immersed Ni foam in $CoSO_4$ solution. As-deposited Ni foam as binder-free electrodes possessed both high specific surface area and good conductivity, which is excellent for supercapacitors. To our best knowledge, These amorphous nanorod networks of $Co(OH)_2$ are firstly fabricated and possess the highest electrochemical performance for supercapacitors, comparing with existed amorphous $Co(OH)_2$. The results showed that the obtained nanostructured a-$Co(OH)_2$ binder-free electrodes exhibited a stable specific capacitance of ~1371 F g^{-1} at 2 A g^{-1} and 666.7 F g^{-1} at 20 A g^{-1}, the cycling performance is excellent as well. After 3000 cycles, they retained 991.7 F g^{-1} at a current density of 10 A g^{-1} without any capacitance loss. More surprisingly, the facile bio-inspired routine can be applied to varieties of substrates to expand the potential applications of amorphous nanostructured $Co(OH)_2$. The proposed mechanism also inspired us to explore controllable diffusion route to develop other amorphous nanomaterials.

4.2 Experimental Section

Materials Synthesis. In a typical synthesis procedure, large-sized hen eggs obtained from a local market were carefully broken at the blunt end and were emptied of their contents. Eggshells with eggshell membrane (ESM) were washed with DI water totally to remove the remaining albumen to be taken as the reactors. Then 30 ml 1 M $CoSO_4$ solution with 10 mM CTAB was gently injected into eggshells with ESM, then 1 M NaOH solution was slowly injected into the outside of eggshells in beakers. Pieces of pre-cleaned Ni foam were placed in the eggshell reactors. Finally, the reactors were sealed by Para films and kept in the oven. All the reactors were incubated at 50 ^oC for different reaction time (1, 2, 3, and 4 days, respectively). After reaction, all the reactors were emptied and the as-deposited Ni foam and ESM separated from eggshells were cleaned with DI water thoroughly. All the samples were dried in vacuum oven at 80 ^oC for 24 h. The schematic of the reaction route is shown in Figure

4.1. To test the universal applications, other substrates such as glass, Cu foil, and Ti foil were also used. The control was set by mixing the same reactant solutions directly and followed by the same procedure.

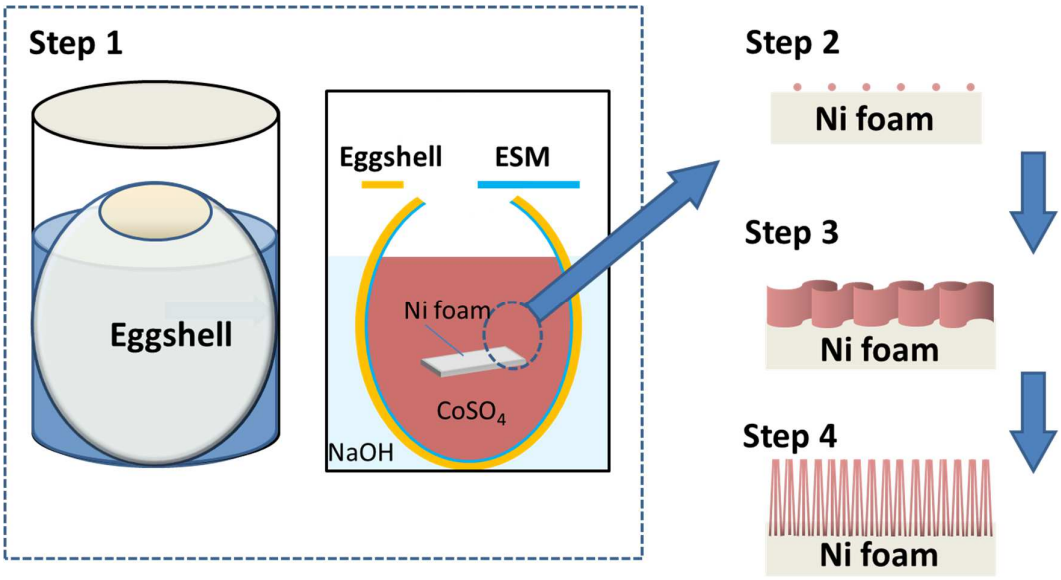

Figure 4.1. Schematic of eggshell-assisted synthesis of a-$Co(OH)_2$ nanorod networks on Ni foam: Step 1, all the reactant solutions and Ni foam are placed in home-made reactors; Step 2, nucleation is initiated on Ni foam; Step 3, nanosheets precursors are self-assembled on Ni foam; Step 4, nanorod networks of a-$Co(OH)_2$ are finally formed on Ni foam after 4 days.

Materials Characterization. X-ray diffraction analysis of the samples was carried out under Rigaku Smart Lab X-ray Diffractometer with Cu Kα radiation. The as-prepared Ni foam and ESM were observed with a FESEM (JEOL JSM-7600 coupled with EDX). Transmission electron microscopy (JEOL 2010 TEM instrument, with accelerating voltage of 200 kV) was used to determine the size, morphologies and structures. Fourier transform infrared spectrophotometer IRAffinity-1S was employed to detect FTIR spectra of a-$Co(OH)_2$.

Electrochemical Analysis. Electrochemical properties were characterized with a three-electrode system, which consisted of the $Co(OH)_2$ working electrode, Pt mesh counter electrode and Ag/AgCl reference electrode in 1M KOH aqueous solution with a three-port glass cell. Cyclic voltammetry (CV) and galvanostatic charge-discharge (GCD) cycling of the

a-$Co(OH)_2$ electrode was tested by a CHI660D electrochemical workstation at 0.1 - 0.5 V and 0 - 0.45 V, respectively. The capacitances of the electrodes were calculated according to the equation of $C = I \times \Delta t / \Delta V$, where I is the constant discharge current, Δt is the discharging time and ΔV is the voltage window for the galvanostatic measurement. The loading mass of a-$Co(OH)_2$ was ~0.51 mg/cm^2.

4.3 Results and Discussion

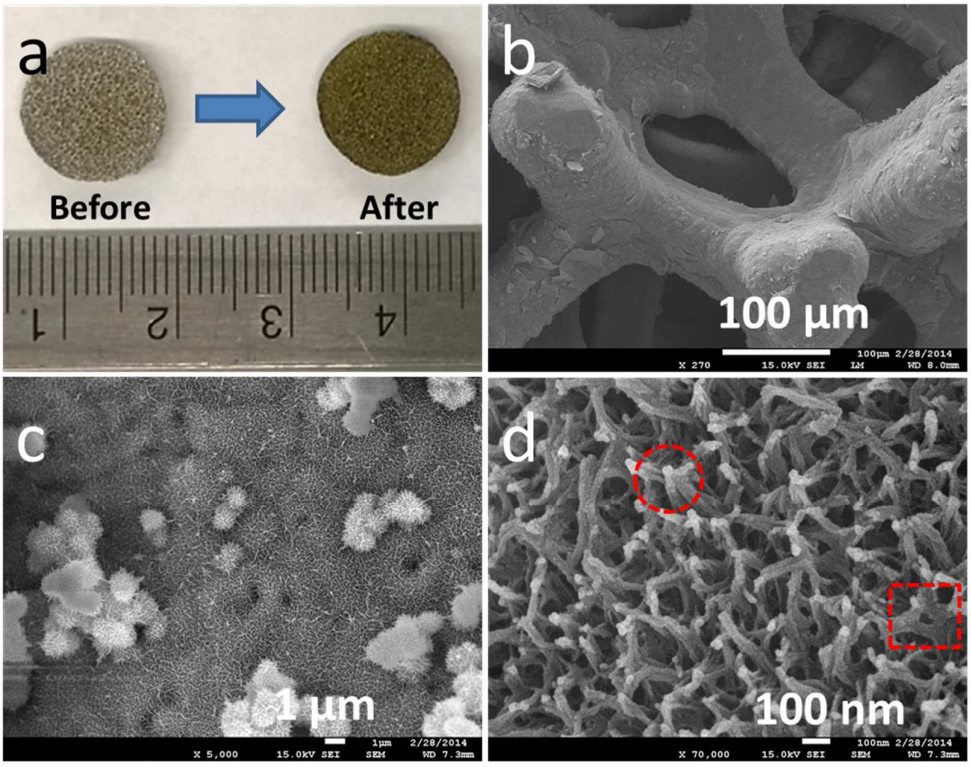

Figure 4.2. (a) Optical image of Ni foam before and after eggshell-assisted deposition in $CoSO_4$ solution at 50 ºC for 4 days, (b, c, d) FESEM images of as-deposited Ni foam at different magnifications.

Figure 4.2a shows the optical differences between original Ni foam and as-deposited one. The color totally changed from metallic silver to brown. All the surface of Ni foam was covered by brown color, which indicates the uniformed coating. In the past, most of $Co(OH)_2$ have two colors, pink for β-$Co(OH)_2$ and blue for α-$Co(OH)_2$.[138] The special matte brown color suggests the different crystal structure of our deposited $Co(OH)_2$. The typical FESEM images

of as-deposited Ni foam clearly show the morphologies of the surface after reaction at different magnifications. In Figure 4.2b, the 3D porous structure of Ni foam itself was observed. The surface is covered by as-deposited $Co(OH)_2$ and looks rough. At higher magnification in Figure 4.2c, the surface of the well deposited Ni foam is highly rough, all the surface of Ni foam was covered by the network-like nanostructured coating. Moreover, some sphere clusters, which is resulted by the slight abnormal deposition of $Co(OH)_2$. Figure 4.2d provides more details in nano-scale. The rough coating is well organized by uniformed nanorod networks. In a surprise, these nanorods are not vertically and individually standing on the surface of Ni foam. Instead, they are connected with each other (marked by a circle). The tips of nanorods are prone to attach each other as marked by a circle. To be noticed here, some bodies of nanorods are connected with sheet-like structures (marked by a square), which suggests some relationship between each other. The average diameter and length of the nanorods are estimated to be about 40 nm and more than 100 nm, respectively.

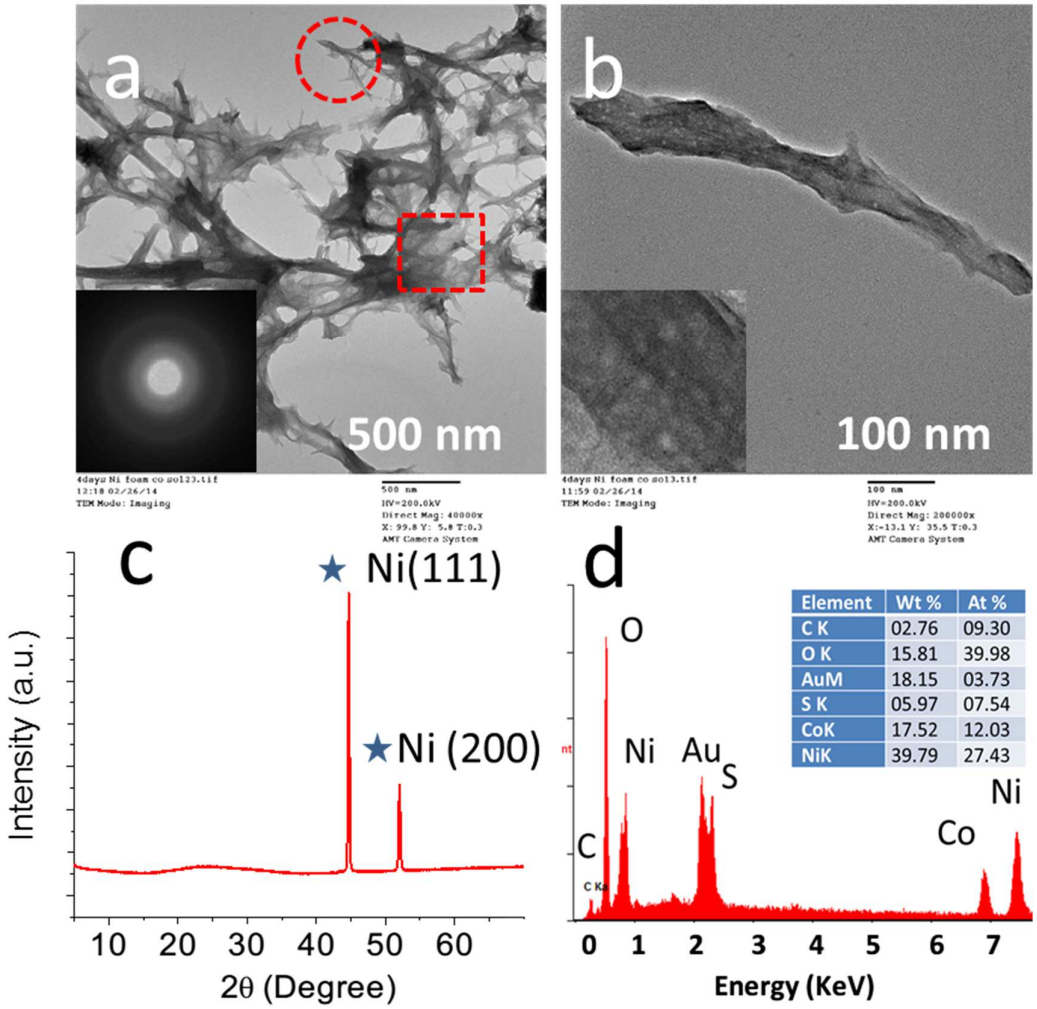

Figure 4.3. TEM images of (a) a-$Co(OH)_2$ nanorod networks and (b) a single nanorod. (c) XRD pattern and (d) EDS analysis of a-$Co(OH)_2$ nanorod networks on Ni foam after reaction in $CoSO_4$ solution at 50 ºC for 4 days. The insets in (a) and (b) are the corresponding SAED pattern and enlarged details of a single nanorod, respectively.

TEM images in Figure 4.3 further confirmed the details of the structure by presenting nanorod networks. Figure 4.3a shows the overall networks of a-$Co(OH)_2$. They are self-assembled by many nanorods. These nanorods are aggregated randomly. Some parts of them are attached each other and some are merged into sheets-like structure as described in FESEM images above (marked by the same shapes as that in Figure 4.2d). The varying dark-image contrasts in some areas suggest either the changeable thickness or folded parts of networks.

The diffuse rings of SAED pattern without obvious rings or dots confirms that they are amorphous. As shown in Figure 4.3b, a single rod's diameter is ~35 nm with a length of ~500 nm. Interestingly, the edges of this rod are not smooth with a little change in diameter. The sheet-like edge could be easily observed in some areas. Besides, the color of it is not uniform, which indicates the different densities of it. By the enlarged inset image, we can notice some porous structures on the surface, which was used to observe in amorphous structures.[110, 139] These observations above indicate that the growth of these nanorods is different from direct growth along one direction as discovered nanorods or nanowires of $Co(OH)_2$ based on existed methods.[140-147] According to the shape of the nanorod and whole networks, we could conclude that there is some special relationship between sheet-like structure and nanorods. The further study has to be focused on this. XRD pattern in Figure 4.3c suggests the amorphous nature of $Co(OH)_2$ as well. Only strong peaks of Ni (111) and Ni (200) from Ni foam were detected. This result is consistent with the SAED pattern in Figure 4.3a. EDS results in Figure 4.3d present the typical elements of $Co(OH)_2$ and the substrate. The existence of sulfur reveals the intercalation of SO_4^{2-} in $Co(OH)_2$.

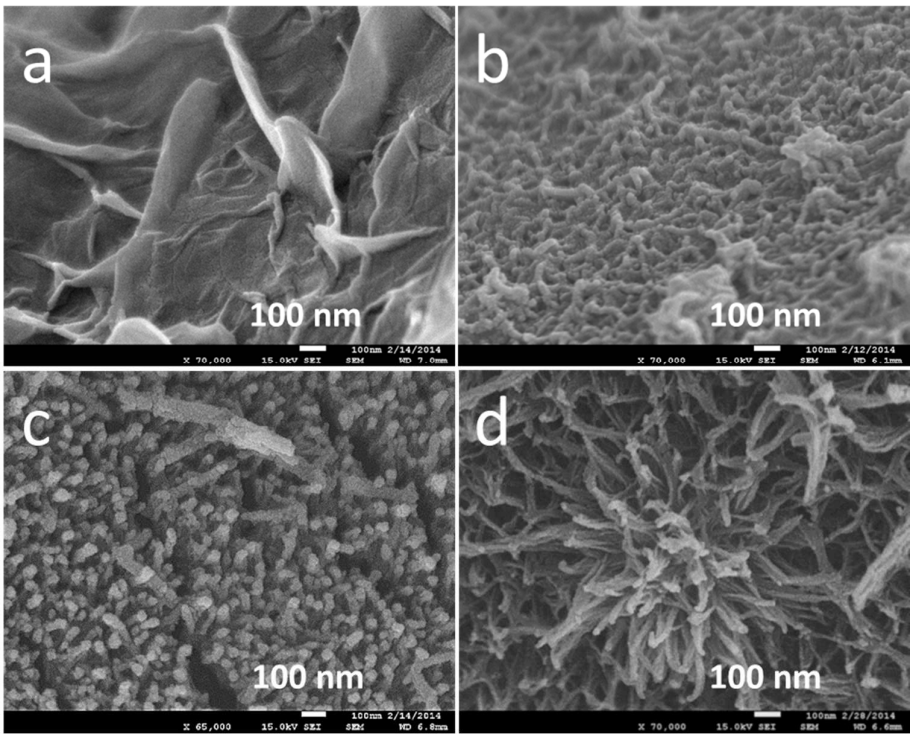

Figure 4.4. FESEM images of a-$Co(OH)_2$ on Ni foam after (a) 1 day, (b) 2 days, (c) 3 days, and (d) 4 days reaction.

To investigate the detailed process of the growth process of nanorod networks, a series of time-dependent experiments were carried out from 1 day to 4 days. After 1 day reaction (Figure 4.4a), the surface of Ni foam is covered by nanosheets and they are interconnected with each other. The average height of them is lower than 100 nm and the thickness is only 10 nm. The sheets-like structure is the typical morphology of $Co(OH)_2$ due to the layered crystal structure of it.[148] However, after 2 days (Figure 4.4b), these nanosheets have disappeared and massive networks lie on the surface of Ni foam. Then, with the increase of reaction time, the short nanorods were observed grown on the surface after 3 days. Finally, the length of nanorods increased in further (Figure 4.4d), which is more than 100 nm after 4 days and the diameter is ~40 nm. In some places, clusters organized by nanorods were also observed. In contrast of nanorods formed after 3 days reaction, the bodies of nanorods after 4 days prone to attach and partly sheet-like edges were noticed, indicating the different growth path from existed 1D

nanostructures of $Co(OH)_2$ and relationship between nanosheets and nanorods again. To our best knowledge, this is the first time to observe this transformation process in $Co(OH)_2$ on Ni foam under mild conditions. Surprisingly, there are the same morphologies inside Ni foam, which suggests the uniformly deposition of $Co(OH)_2$ on Ni foam from outside to inside.[140]

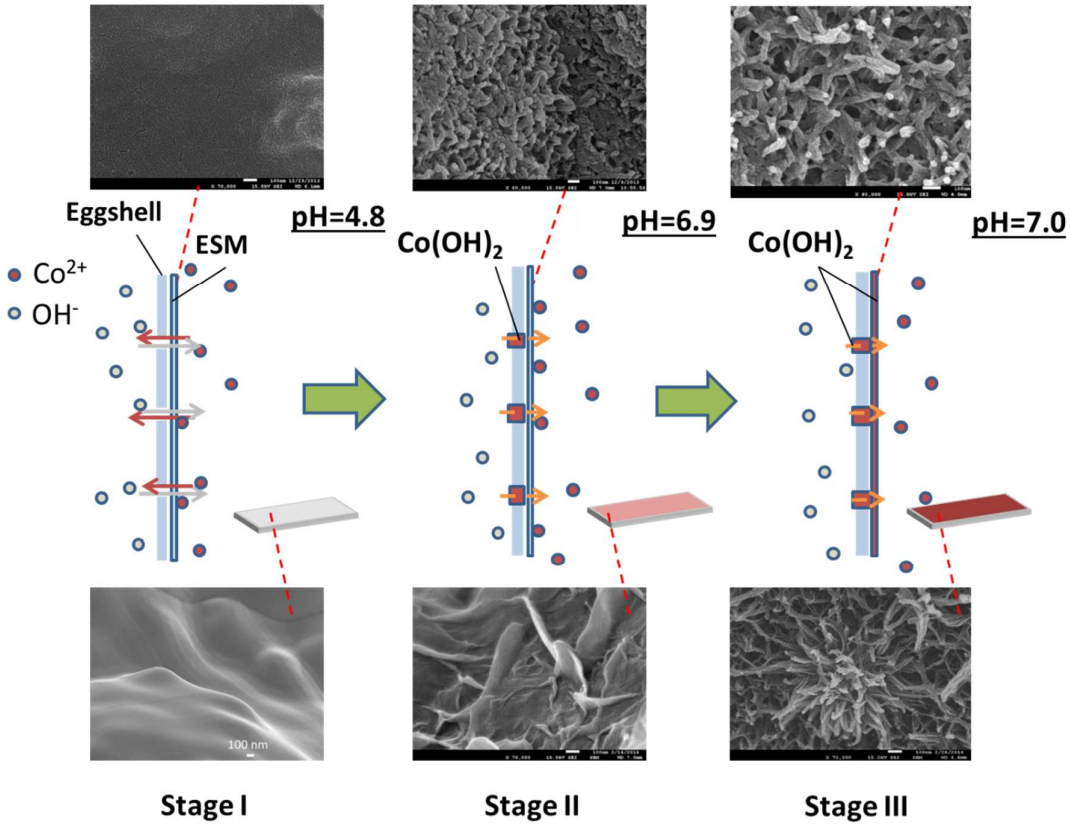

Figure 4.5. The proposal mechanism of the formation of a-$Co(OH)_2$ nanorods on Ni foam.

Although the mechanism of formation of this interesting nanostructure is still not totally clear, some experiment results and studies reported could help us to understand it roughly. Figure 4.5 presents the hypothesis of the formation of a-$Co(OH)_2$ nanorods on Ni foam. Here, there are two key parts in reaction: one is the eggshell with ESM, contacting NaOH and $CoSO_4$ solution at the same time, the other is a substrate, Ni foam, in $CoSO_4$ solution. For the eggshell with ESM, it is taken as a natural separator, which could separate NaOH and $CoSO_4$ solutions

mechanically. However, unlike full separation, with the massive air pores, the eggshell allows to exchange OH^- and Co^{2+} ions freely at the early stage of reaction (Stage I). At this moment, ESM and Ni foam still keep smooth surface without deposition as shown in Figure 4.5. The pH value of $CoSO_4$ will start to increase fast from the original 4.8 with the transportation of OH^- through pores in the eggshell. Then, as initial $Co(OH)_2$ is gradually aggregating around the pores, these pores will be finally blocked, hindering the fast transportation of OH^-. At this point (Stage II), the pH value has increased to 6.9. As a result, ESM attached on the eggshell and Ni foam in solution are both deposited by a little amount of $Co(OH)_2$ after nucleation and growth of initial $Co(OH)_2$ in this supersaturated solution. Notably, the morphologies of them are different, which suggests the different microenvironment around ESM and Ni foam in the same $CoSO_4$ solution. Since ESM itself is a semipermeable membrane, the movement of ions could be limited, so these different microenvironment is reasonable. Undefined networks on ESM and nanosheets on Ni foam were observed, respectively. Although OH^- could not pass eggshell directly, it still continues to diffuse toward $CoSO_4$ solution slowly via pores filled by initial $Co(OH)_2$. Consequently, there is always continuous supersaturation for forming $Co(OH)_2$ from $CoSO_4$ solution with the osmosis of OH^- in the following process. The balance between supersaturation and growth rate of $Co(OH)_2$ is kinetically controlled by the whole reaction system. Under this situation, the pH value of $CoSO_4$ keeps stable at this stage (Stage III). Meanwhile, structure transformation occurs. Nanorod networks both appear on ESM and Ni foam finally. During the whole process, some crucial steps of reaction might be similar to natural biomineralization, such as controllable ions transportation, supersaturation, moderated pH value, mild temperature, heterogeneous nucleation, and typical nucleation-growth mechanism of natural nanostructures.[149-15031,32]

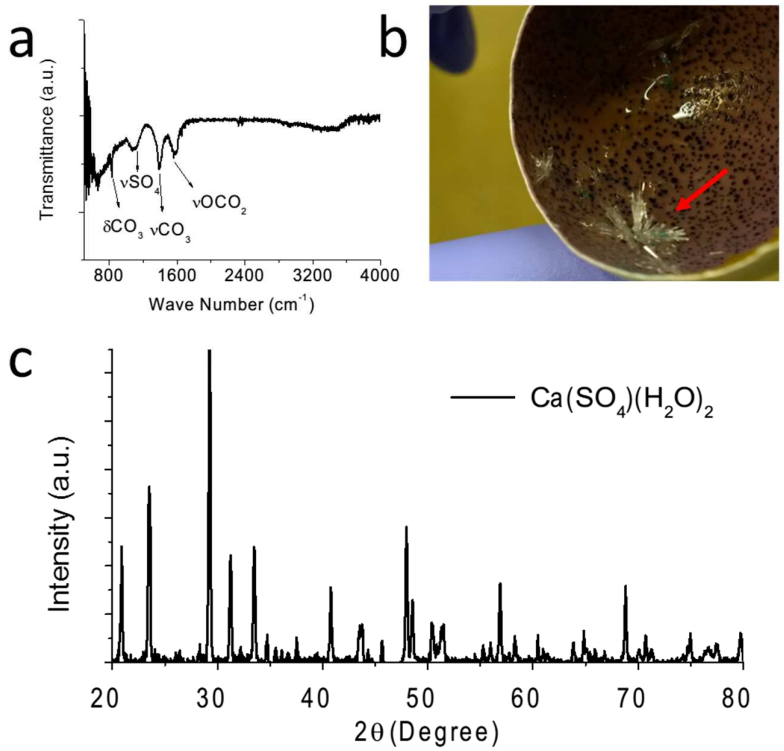

Figure 4.6. (a) FTIR spectra of a-$Co(OH)_2$ nanorod networks, (b) optical image and XRD pattern of $Ca(SO_4)(H2O)_2$ crystals on ESM after 10 days reaction.

To be noticed here, there are a lot of factors might affect the formation of nanorod networks. Among them, CO_3^{2-} might play an important role in it. According to IR spectra of a-$Co(OH)_2$, we found strong peaks regarding CO_3^{2-} in Figure 4.6a. However, we don't have any carbonate groups in all the regents. Therefore, the most possible source of them is the eggshell itself. After all, the initial pH is just 4.8, which is possible to dissolve parts of the eggshell. In order to confirm our hypothesis, we extended our reaction time to 10 days. Reasonably, big crystals of $Ca(SO_4)(H_2O)_2$ was identified in Figure 4.6b and 6c. Eggshell indeed is able to dissolve. In previous studies, carbonate anions always existed in fabricating cobalt hydroxide/cobalt hydroxide carbonate nanorods.[141, 143-144, 147] Carbonate ions were verified to inhibit the lateral growth of $Co(OH)_2$ crystals.[141, 144] For our products, nanosheets and nanorods were both detected during forming nanorod networks. This transformation from 2D to 1D nanostructures was reported before.[144-145, 147, 151-152] But all of them are based on crystalline

structures. In our experiments, carbonate and sulfate anions are coexisting in $CoSO_4$ solution. Considering the low pH value here for developing $Co(OH)_2$, there are a large amount of OH^- defects between interlayers of a-$Co(OH)_2$. Sulfate anions have big anionic radii, which will affect the crystalline after intercalation.[153] In addition, there might be an interaction between carbonate and sulfate anions such as anion exchange in forming nanorod networks.[143, 153] EDS results and IR spectra confirmed the existence of these two anions (Figure 4.3d and Figure 4.6a). Therefore, this metastable amorphous structure is able to exist stably. It might be taken as a transit status between well crystalline nanosheets and nanorods under the effect of anions and pH value. This hypothesis also might explain why we got this amorphous structure and sheet-like edges in nanorods as well as networks. The further experiments have to be focused on understanding this special formation mechanism. Notably, the pH value keeps nearly unchanged after Stage I. This phenomenon is different from direct co-precipitation reaction to form common $Co(OH)_2$ nanopellets. Moreover, not only were ESM and Ni foam covered by a-$Co(OH)_2$ nanorod networks, but also other substrates such as glass, Cu foil, and Ti foil (Figure 4.7) can be easily deposited. More potential applications of a-$Co(OH)_2$ based on our environmentally friendly, facile and energy-efficient method can be explored in future. Previously, if someone would like to obtain organized 1D structures, higher temperature, and additional pressure are necessary.[60, 141, 146, 15414,33,34] Our bio-inspired strategy is interesting and compromising to develop for fabricating other nanomaterials in future only if the mechanism could be understood totally.

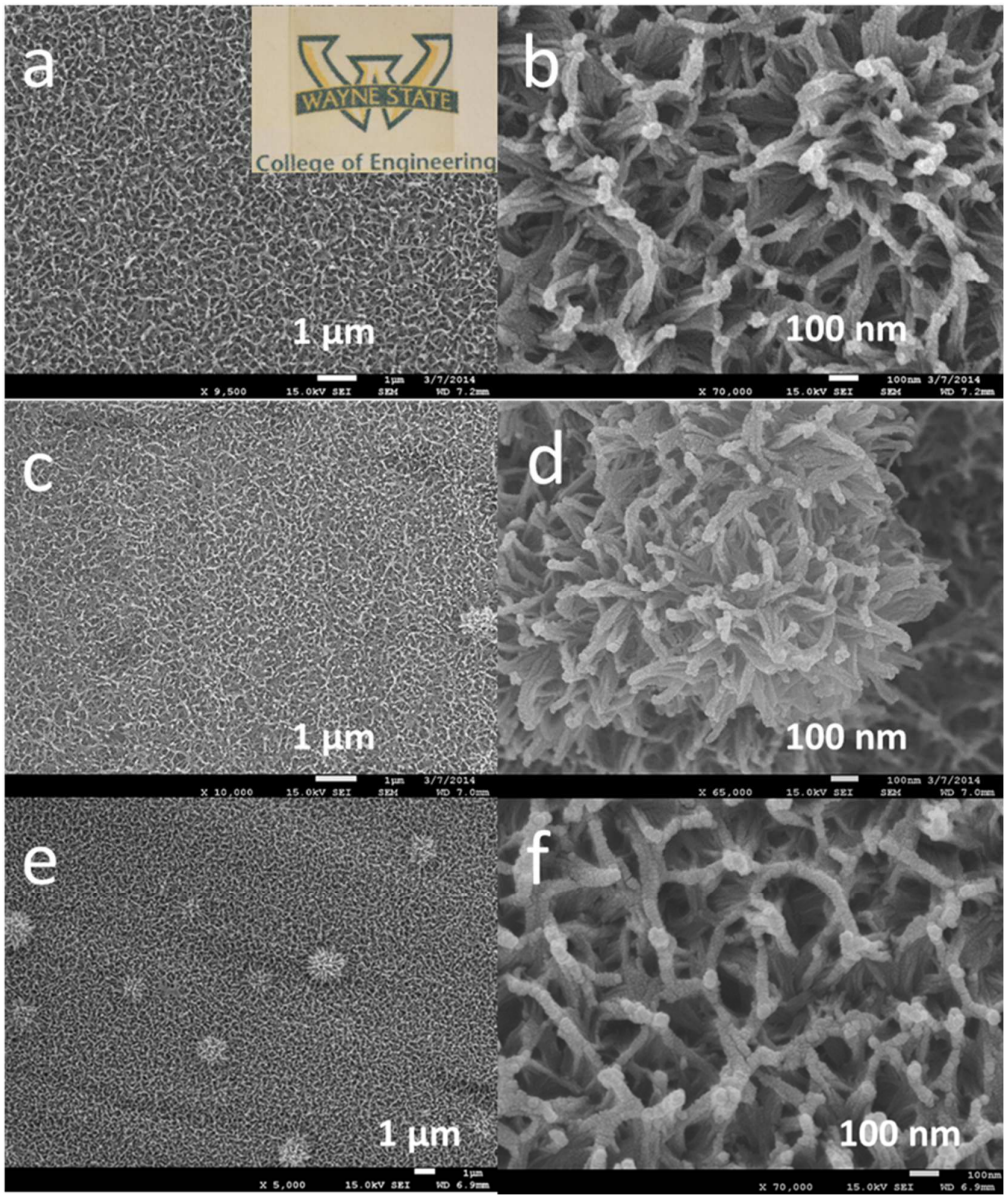

Figure 4.7. FESEM images of a-$Co(OH)_2$ nanorods on different substrates: (a, b) glass, (c, d) Ti foil, and (e, f) Cu foil. The inset of (a) is the optical image of an as-deposited glass to demonstrate the transparency.

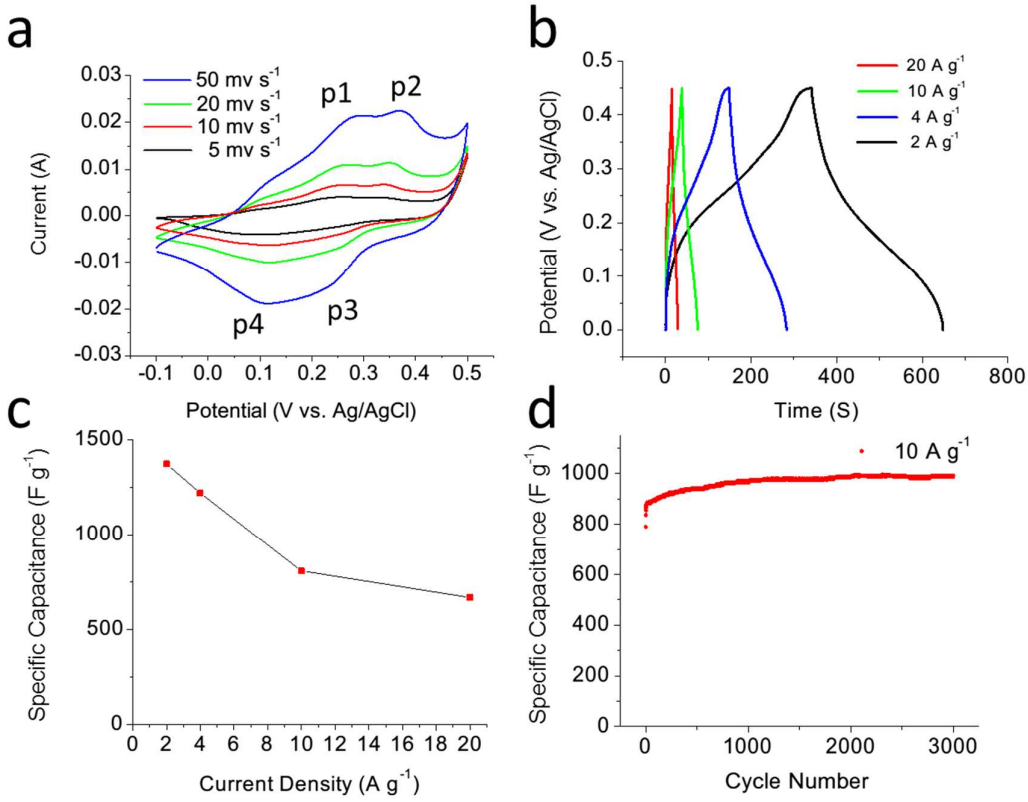

Figure 4.8. Electrochemical characterization of the a-$Co(OH)_2$ nanorod networks electrodes: (a) CV curve at various scan rates from 5 mv s^{-1} to 50 mv s^{-1}, (b) GCD profiles at various current densities from 2 A g^{-1} to 20 A g^{-1}, (c) graph of charge-discharge current dependent specific capacitance at various current densities from 2 A g^{-1} to 20 A g^{-1}, (d) cycling performance within 3000 cycles at 10 A g^{-1}.

Unique nanostructured a-$Co(OH)_2$ possess large specific area, which is suitable for developing supercapacitors. we directly took as-deposited Ni foam after 4 days as binder-free electrodes in a three-electrode configuration with 1 M KOH as the electrolyte. The CV curves of a-$Co(OH)_2$ are shown in Figure 4.8a. The CV curves involve unique reversible redox peaks (marked as P1, P2, P3 and P4) without non-rectangular shape, indicating that the measured capacitances of a-$Co(OH)_2$ derived from stable Faradaic reactions on the surface. These two pairs of large redox peaks can be clearly identified, indicating that the a-$Co(OH)_2$ nanorod networks are already electrochemically active in the as-grown state. According to the positions of the reaction peaks, the primary reaction equations should follow the listed below:[126, 155]

$$Co(OH)_2 + OH^- \leftrightarrow CoOOH + H_2O + e^- \quad (1)$$

$$CoOOH + OH^- \leftrightarrow CoO_2 + H_2O + e^- \quad (2)$$

The color change of as-deposited Ni foam was noticed during CV scan from brown to black periodically. Such color change also confirmed the reversible reactions of a-$Co(OH)_2$. Also, the shape of the CV curves has no significant change with the increase of scan rates from 5 mV s^{-1} to 50 mV s^{-1}. It suggests the improved mass transportation, electron exchange as well as limited equivalent series resistance due to the 3D networks of $Co(OH)_2$ nanostructure.[156] The existed shifts of the potential of the redox peaks are mainly attributed to inevitable internal resistance of the electrodes.[156-157] Notably, the shifts are pretty limited, suggesting the fast ions/electrons diffusion in this process. These results could be contributed to advantages of binder-free connection and the special amorphous nanostructures.

Figure 4.8b shows the galvanostatic charge-discharge (GCD) profiles under different current densities ranging from 2 to 20 A g^{-1}. No distinct plateau region can be observed during the process, in contrast of typical crystalline $Co(OH)_2$.[128, 155, 158] The nearly symmetrical capacitance of charging and discharging curve replies the excellent reversibility. In Figure 4.8c, the specific capacitance (SC) of the a-$Co(OH)_2$ electrodes was calculated from discharge time based on the chronopotentiometry curves. The binder-free electrodes delivered high SCs of 1371.6, 1218.3, 807.6 and 666.7 F g^{-1} at current densities of 2, 4, 10 and 20 A g^{-1}, respectively. The SC gradually decreased with the increase of current densities, which could be attributed to the incremental voltage drop and insufficient active materials involved in redox reaction at higher current densities.[159] However, at a high current density of 20 A g^{-1}, the a-$Co(OH)_2$ electrodes still possess a high capacitance of 666.7 F g^{-1}. The results imply a good rate capacity of a-$Co(OH)_2$ electrodes. Such high SC at large current density further proves the merits of the a-$Co(OH)_2$ nanostructures and the good connection between the active materials and the current collector without binder. Note that the specific capacitance is even much better than

that of amorphous $Co(OH)_2$ currently reported under corresponding different current densities.[80] This improvement might be contributed to the controllable nanorod networks. Moreover, the loading mass of reported one is only 0.124 mg/cm^2,[80] which might be the limitation of this electrochemistry technique.[80, 160 161] For our method, it is easy to load more than 1 mg/ cm^2 active materials on Ni foam.

Furthermore, the a-$Co(OH)_2$ electrodes present excellent electrochemical stability. The cycling performance is plotted in Figure 4.8d. During the first 1000 cycles at 10 A g^{-1}, the specific capacitance keeps obviously increasing without any decrease. This phenomena could be attributed to the activation process.[162-164]. The activation process might be highly related to electrode structures such as crystal structures and morphologies[162, 165-166]. Previously, amorphous $Co(OH)_2$ reported also involved the activation process during the first 1000 cycles.[80] We speculate that amorphous structures with defects might be easy to trap ions to demonstrate the activation phenomenon at the beginning. Besides, our a-$Co(OH)_2$ have special nanostructures, which might boost this activation. After consecutive 1000 cycles the performance of it is stable with a slight increase in 3000 cycles. After 3000 cycles, the a-$Co(OH)_2$ electrodes are still stable, further demonstrating that they indeed have excellent cycling stability.

In general, the electrochemical properties of supercapacitors are determined by structures and conductivity of electrode materials. For a-$Co(OH)_2$ binder-free electrodes, there are three main factors to the outstanding performances. The first point relates to the nature of amorphous structure. For conventional crystalline $Co(OH)_2$ electrodes,[167 65] the diffusion of electrons and ions are limited, and the expected volume change during diffusion possibly destroy the stability of active materials on the surface. In contrast, amorphous $Co(OH)_2$ involves includes massive defects and under-coordinated atoms.[168] It might trend to keep faster ions/electrons diffusion to improve its electronic conductivity[161] and endure volume change

during rapid change-discharge process.[169] In addition, its loose-packed interlayer structure is beneficial for fast de/intercalating charges ($Co(OH)_2 + OH^- \leftrightarrow CoOOH + H_2O + e^-$). Here, CoOOH has better conductivity, in comparing with $Co(OH)_2$.[170] Secondly, the special hierarchical nanostructures formed by controllable biomimic mineralization. Although $Co(OH)_2$ is amorphous, it has hierarchical nanorod networks. These 3D nanostructures increase the contact area between electrolyte and electrodes, and boost the transportation of ions/electrons. Thirdly, the amorphous nanostructure was deposited on Ni foam directly and covered the whole surface of it from outside to inside. Therefore, this binder-free design combined large surface area of active materials improve the conductivity and the stability of connection between a-$Co(OH)_2$ nanomaterials and electrodes.

4.4. Conclusion

In conclusion, amorphous $Co(OH)_2$ nanorod networks were fabricated on Ni foam via a bio-inspired method under mild conditions. We observed the growth and the structure transformation of $Co(OH)_2$ on Ni foam from nanosheets to nanorod networks during different reaction periods. The possible mechanism of formation of amorphous $Co(OH)_2$ nanorod networks is illustrated according to the theory of nucleation and growth based on biomineralization as well as the special reaction conditions. As-prepared amorphous binder-free electrodes possess porous large active specific surface area, demonstrating significantly good electrochemical performances. The rate test presented their SC of 1371.6 F g^{-1} at 2 A g^{-1} and even 666.7 F g^{-1} at 20 A g^{-1}, suggesting a good ability to deliver large SCs at different current densities. In addition, the cycling performance is extraordinary during 3000 continuous charge - discharge cycles at 10 A g^{-1}. Amorphous nanostructures and binder-free feature together achieved the excellent electrochemical performances for supercapacitors. Due to this low-cost but facile bio-inspired method as well as the satisfactory electrochemical properties of a-$Co(OH)_2$ binder-free electrodes, these nanostructured amorphous supercapacitors may

help us to increase energy storage efficiency and decrease the consumption of energy at the same time. Moreover, the present interesting structure-controllable bio-inspired strategy and the unclear principles behind it offer a compromising route to deposit nanomaterials on any substrates for any possible applications.

CHAPTER 5 TRASH TO TREASURE: POMEGRANATE-LIKE CoO-Co@C PREPARED BY NOVEL EGGSHELL SYSTEM AS COMPOSITE MATERIALS FOR LITHIUM ION BATTERIES

5.1 Introduction

Currently, Lithium-ion batteries (LIBs) have been taken as main energy storage solutions, ranging from portable electronic devices to electric vehicles as well as emerging renewable energy storage. Thanks to researchers' and engineers' endeavors, the performances of LIBs have been dramatically improved since they were commercialized by Sony.[171] However, with the increase of surging demands for high-performance LIBs, current LIBs have not been satisfactory. New materials and structures aroused considerable attention to meet consumers' expectations. The traditional anode materials are made of graphite, which is stable, but only yields 372 mAh g^{-1}. Poizot firstly discovered the potential applications of metal oxide as anode materials for LIBs in 2000.[172] After that, metal oxides have been paid more and more attention as electrodes due to their high theoretical specific capacities.[2, 173] Among them, cobalt oxides (Co_3O_4 and CoO) are a group of typical materials possess better initial electrochemical performances than other metal oxides such as iron oxides and nickel oxides.[172] Unfortunately, they are still suffering inherent poor rate performance and capacity retention during the long-term charge-discharge process.[174] During reacting with Li ions, the large volume change, poor conductivity and formation of a solid electrolyte interface (SEI) all severely deteriorate the practical performance and hinder their commercialization. For typical nanostructured CoO, there are two main ways to improve it: (1) To combine them with other components such as metal and carbon to improve conductivity, buffering the volume change and increase chemical stability.[175-176] To partly reduce Co_3O_4 or heating cobalt-based precursors were investigated to form CoO-Co composite structures.[97, 177] CVD and hydrothermal methods are widely employed to create carbon coating on CoO;[94, 147, 178-179] (2) To redesign their inherent structures. Porous hierarchical nanostructures have been widely proven to improve the properties of

conventional bulk structures of CoO.[180-181] The larger active areas for electrochemical reaction, stable nanostructures and faster ions/electrons transportation rate can be achieved after improvement. By now, from nanoparticles to 1D, 2D, and 3D hierarchical structures, rational design of CoO or its composite materials was developed to enhance electrochemical properties.[95, 180, 182-183] Although these involved strategies could be considered to improve the electrochemical performance of CoO, the practical effect is finally determined by the stability of structures and components of electrode materials at the same time.[179] The limitations of existed synthesis methods are conspicuous such as high temperature, high pressure, and complicated devices. It is important to integrate conveniently useful components with suitable structures to achieve the ideal properties for CoO electrodes.[3] To fabricate controllable structures and combine them with effective components for improving electrochemical properties is still challenging.

Eggshell (ES) with eggshell membrane (ESM) is one of largest waste products in the world. American consume more than 263 eggs per person in 2014 according to American egg board. The total number is still increasing. In regular, these ESs with ESMs are taken as useless wastes and thrown away directly. However, more and more researchers are being attracted by the special chemical and physical properties of ES and ESM.[184-186] For example, ESM's potential applications have involved biomedical field,[187] environmental protection,[188] energy storage,[55] photocatalyst[189] and so on. Previously, ESM was applied as an ideal bio-template to develop nanomaterials due to its unique interwoven network structure and large amounts of active groups on the surface. Duplicated networks of TiO_2, ZnO, NiO, Co_3O_4, Mn_3O_4, PdO, PbSe, PbS, CdS, and $Sm_{0.5}Sr_{0.5}CoO_3$ were successfully prepared via ESM bio-template.[26, 190] Biomimic mineralization principles were partly applied in these studies. However, all of them are simply coated on micrometer-sized fibers of ESM, and ESM is only used as a hard template. Good control of ions diffusion, nucleation, and growth of crystals on the surface haven't been

introduced. In contrast, Eggshell is successfully mineralized on ESM by Nature expertly based on these elementary biological process.[191] Therefore, how to make use of ESM currently are limited.

Herein, we introduce a bio-inspired method to synthesize pomegranate-like CoO-Co@C on CESM as composite materials by fully taking advantages of ES and ESM together. Original ES with ESM was directly taken as a natural reactor to control the formation of highly crystalline $Co_2(OH)_3Cl$ precursors on ESM by biomimic mineralization. Then, as-deposited ESM was used sequentially as conductive support, reductant and carbon source to transform $Co_2(OH)_3Cl$ to CoO-Co@C after calcination at 450 ^oC in argon. As a result, uniformed C shells covered nanostructured CoO-Co cores. We employed the nanostructures, C shells/substrates (CESM) and metallic Co simultaneously to improve the electrochemical properties of CoO as anode materials for LIBs. The rate and cycling performances of them were both improved by systematically integrating the merits of structures and components. To our best knowledge, this is the first time to explore the functions of carbon coating and reducibility of ESM. Moreover, ES with ESM was successfully transferred from waste materials to important parts in developing composite materials for LIBs.

5.2 Experimental Section

Materials Synthesis. Several large-sized hen eggs from the same company were purchased from a grocery store. The yolk and albumen were poured out from the broken blunt end. The empty ESs were thoroughly rinsed with DI water to remove the remaining albumen. Thin ESM was kept well inside. In fact, ESM is made of two main kinds of membrane. The outer layer membrane (OLM) is organized by the interwoven fibrous proteins and the inner layer membrane (ILM) has no special structures as shown in Figure 5.1b. After cleaning the ESs with pristine ESM, 30 ml 1 M $CoCl_2$ solution with 10 mM surfactant CTAB was carefully injected inside every ES. And then every portion of 30 ml 1 M NaOH solution was filled in

several 100 ml beakers. The ESs finally were placed in beakers and sealed by parafilm tightly. We call these home-made reactors “natural ES system”. The system was placed in an oven at 50 ^{o}C for different reaction periods. After the reaction, the system was taken out and the ESs with ESMs were emptied again and rinsed by DI water. The ESs with ESM were dried in a vacuum oven at 100 ^{o}C overnight, and ESM was separated by tweezers gently. Next, as-prepared ESM was calcined under an argon atmosphere at 450 ^{o}C for 2 h. The ramping rate was 10 ^{o}C min^{-1}. The illustrated natural ES system, reaction process, and a typical ES after biomimic mineralization are schematically shown in Figure 5.2. After carbonization, some products were treated by 2.5 M HCl to remove CoO-Co cores. In comparison, the control without natural ES system was set by mixing the same volume of $CoCl_2$ and NaOH solutions directly.

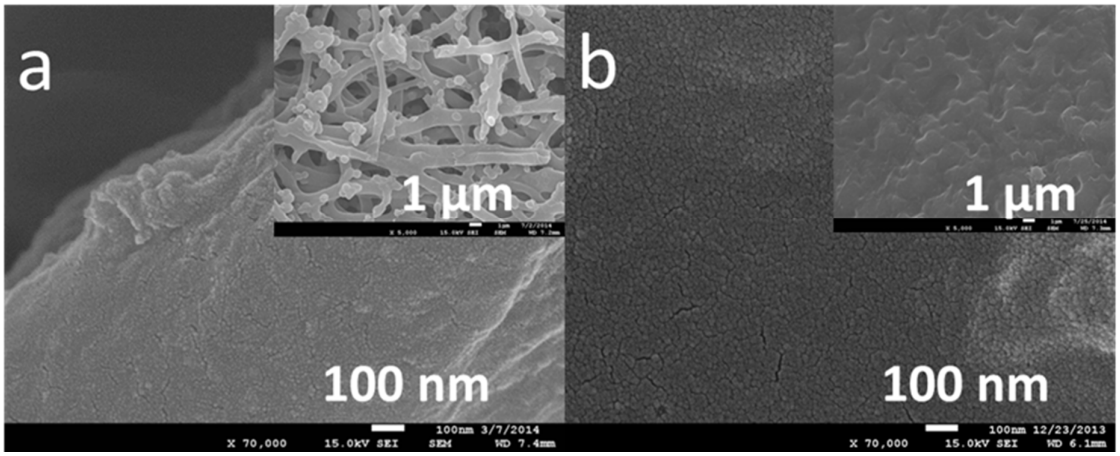

Figure 5.1. FESEM images of (a) the OLM of ESM, and (b) the ILM of ESM at different magnifications.

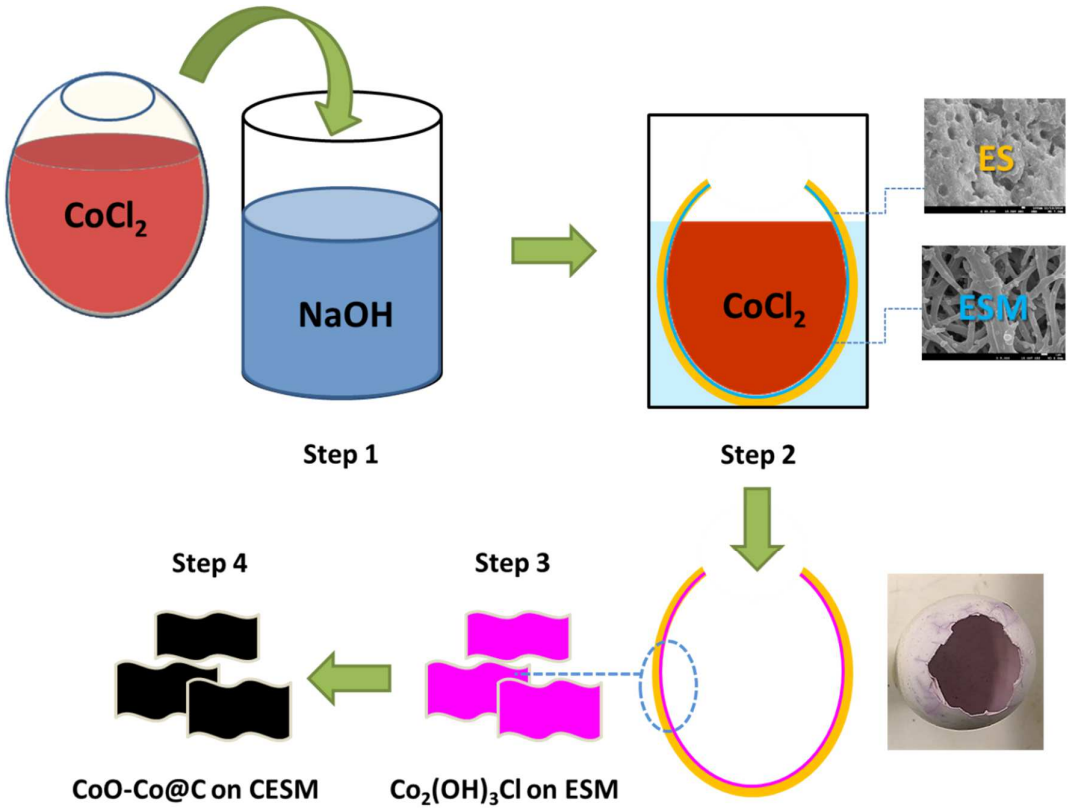

Figure 5.2. Schematic of the preparation of pomegranate-like CoO-Co@C on CESM and optical image of an as-prepared eggshell with a lavender color coating ($Co_2(OH)_3Cl$) in it.

Materials Characterization. X-ray diffraction analysis of the samples was carried out by Rigaku Smartlab XRD instrument with Cu Kα radiation. The structures of the $Co_2(OH)_3Cl$ precursors and related calcined products were examined by a field-emission scanning electron microscopy coupled with the energy dispersive analysis of X-rays (FESEM/EDAX JEOL-7600, operating at 15 KV). Transmission electron microscopy (JEOL 2010 TEM instrument with accelerating voltage of 200 KV) was used to determine the size, morphologies and structures of products at different stages. The thermo-gravimetric measurement was employed on a Perkin-Elmer TGA Q600 thermal analyzer in air at a heating rate of 10 °C min^{-1} from room temperature to 800 °C.

The electrochemical properties were characterized in CR2032 coin-type cells. The calcined products (CoO-Co@C on CESM), Super C65 and PVDF binder in NMP were

homogenously mixed in weight ratio of 8:1:1. The slurry was later spread on a clean copper foil and dried in vacuum oven at 100 ^{o}C overnight to prepare the binder-contained electrodes. Coin-type half cells were assembled by using the coated copper foil as the working electrode, metallic lithium foil as the counter and reference electrode, 1 M solution of $LiPF_6$ in a mixture of EC and DEC (1:1, wt. %) as the electrolyte, and Celgard 2320 as the separator in an argon-protected glove box. The cells were discharged and charged galvanostatically at room temperature in the voltage window of 0.01 - 3 V at different current densities ranging from 0.1 to 1 A g^{-1} on a MTI BST8-WA battery tester. If not mentioned, all reported capacities are based on the total mass of CoO-Co@C on CESM. The CoO control derived from $Co_2(OH)_3Cl$ precipitated in mixed same $CoCl_2$ and NaOH solutions was tested based on the same conditions.

5.3 Results and Discussion

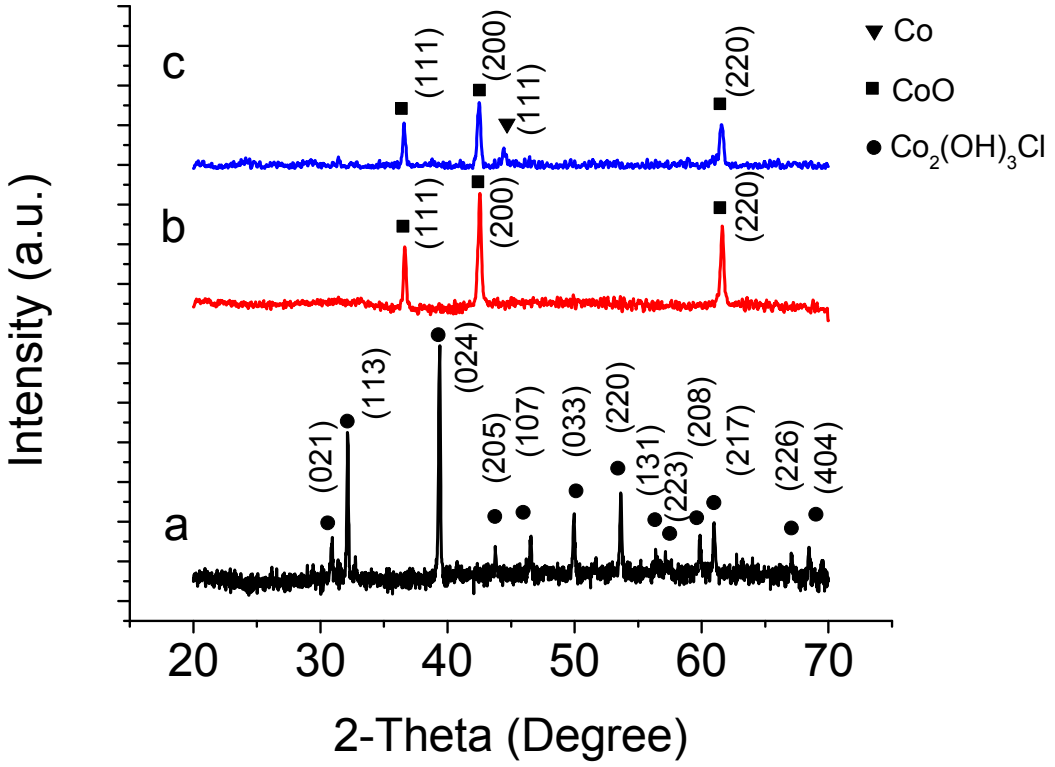

Figure 5.3. XRD patterns of (a) the as-prepared $Co_2(OH)_3Cl$ precursors on ESM after biomimic mineralization for 5 days, (b) the CoO control after calcination at 450 °C in argon for 2 h, (c) pomegranate-like CoO-Co@C on CESM after calcination at 450 °C for 2 h.

Figure 4.3a shows the XRD patterns of as-prepared ESM with $Co_2(OH)_3Cl$ precursors. The main peaks indexed are agreed well with $Co_2(OH)_3Cl$ (JCPDS No. 73-2134). The control via mixing reaction solutions directly has the same compound. $Co_2(OH)_3Cl$ always is derived from $CoCl_2$ solution after reaction with alkali. The structure is approaching a S=1/2 pyrocholore lattice (a = 6.8420 Å, c = 14.504 Å),[192] which makes it studied as an interesting partial ferromagnetic material.[193-194] Recently, Co_2OH_3Cl was introduced to energy fields such as supercapacitors and lithium-ion batteries.[195-197] After calcination at 450 °C in argon, the control was decomposed and the typical peaks of pure CoO (JCPDS No. 78-0431) appeared in Figure 5.3b. In contrast, the as-prepared CoO-Co@C on CESM (Figure 5.3c) has extra small peak marked in Figure 5.3c, which could be assigned to Co (111) of metallic Co (JCPDS No. 89-7093). No graphite peaks were detected, suggesting the carbon structures involved were amorphous. As-prepared CoO-Co@C on CESM could be attracted by the magnet and released some bubbles after soaking in 2.5 M HCl. Both of these experimental results indirectly indicate the existence of metallic Co.

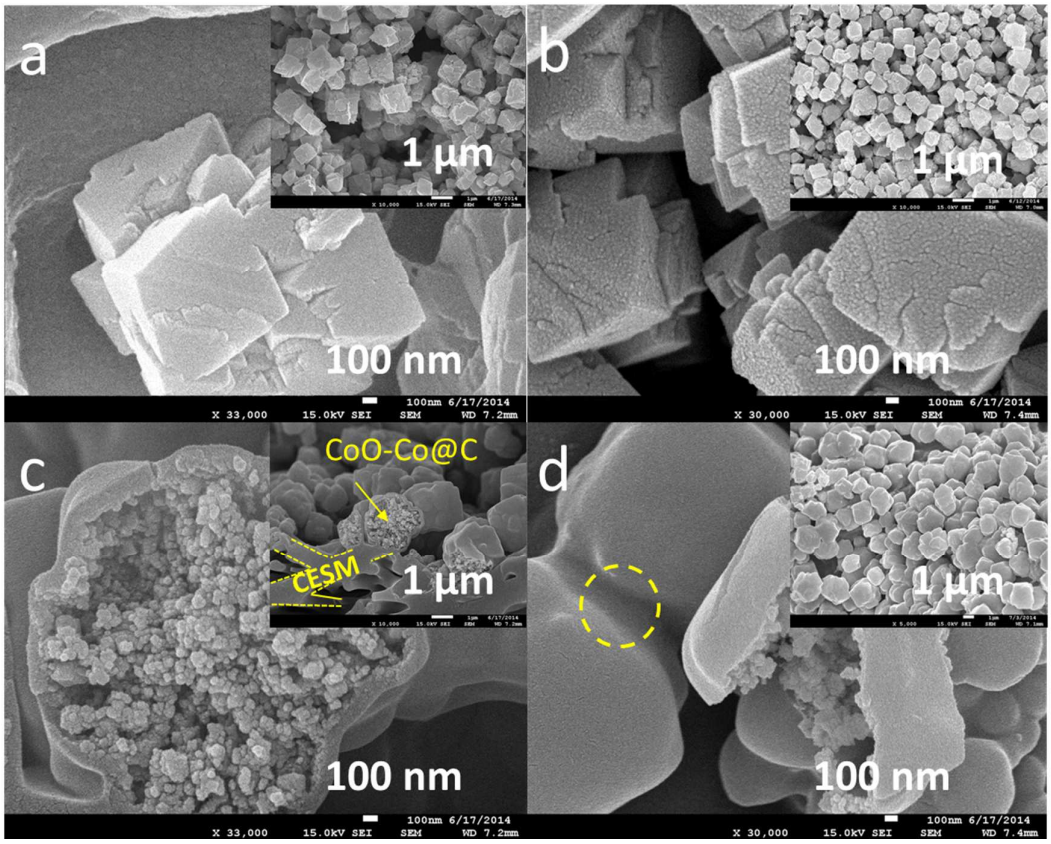

Figure 5.4. FESEM images of (a, b) the as-prepared $Co_2(OH)_3Cl$ precursors on both sides of ESM after biomimic mineralization for 5 days, (c, d) pomegranate-like CoO-Co@C on both sides of CESM after calcination at 450 °C in argon for 2 h.

FESEM images demonstrate the typical morphologies of as-prepared $Co_2(OH)_3Cl$ precursors on ESM after biomimic mineralization for 5 days and CoO-Co@C on CESM after calcination. Both of the panoramic and partly enlarged FESEM images are presented in Figure 5.4. After reaction in the ES system, the interwoven fibers of the OLM (see Figure 5.1a) are covered by a large amount of $Co_2(OH)_3Cl$ particles, which overspread the original structures of ESM (Figure 5.4a). Typical structures of $Co(OH)_2$ and related intercalated structures with other anions (CO_3^{2-}, SO_4^{2-}, NO_3^-) tend to form 2D sheet-like structures or 1D oriented structures according to previous studies.[153, 198] In comparison, there are scarce reports regarding the morphologies of $Co_2(OH)_3Cl$, though its crystal structure was discussed.[193-194, 197, 199-200] It can be taken as deformed pyrochlore structure regarding to a solid solution of $CoCl_2$ and

$Co(OH)_2$.[197] It might be the reason why it has no orderly morphology.[195] Here, as shown in Figure 5.4a, the $Co_2(OH)_3Cl$ particles are self-assembly by deformed octahedral sub-structures with a lot of defects. Some broken edges and stacking lamellar structures are noticed. The size is not uniformed, ranging from 500 nm to 2 μm. In Figure 5.4b, the similar particles are distributed randomly on the surface of the other side of ESM (ILM). In Figure 5.4c and Figure 5.4d, the special core-shell structure is presented. A host of nanoparticles are encapsulated by thin and smooth C shells tightly. The thickness of C shells is ~100 nm. Besides, massive voids are left among nanoparticles inside C shells. To our best knowledge, this pomegranate-like structure has not be reported yet. Only similar other structures related to nanoparticles encapsulated by shell structures were reported.[201-204] As depicted in the inset of Figure 5.4c, a lot of "pomegranates" of CoO-Co@C are grown on branch-like structures of CESM seamlessly, suggesting the inherent connection between them. Surprisingly, the C shells do not only cover the CoO-Co nanoparticles but also tend to interconnect with each other as marked in Figure 5.4d. As a result, all the carbon structures (CESM and C shells) are linked to form a big carbon network in these composite materials.

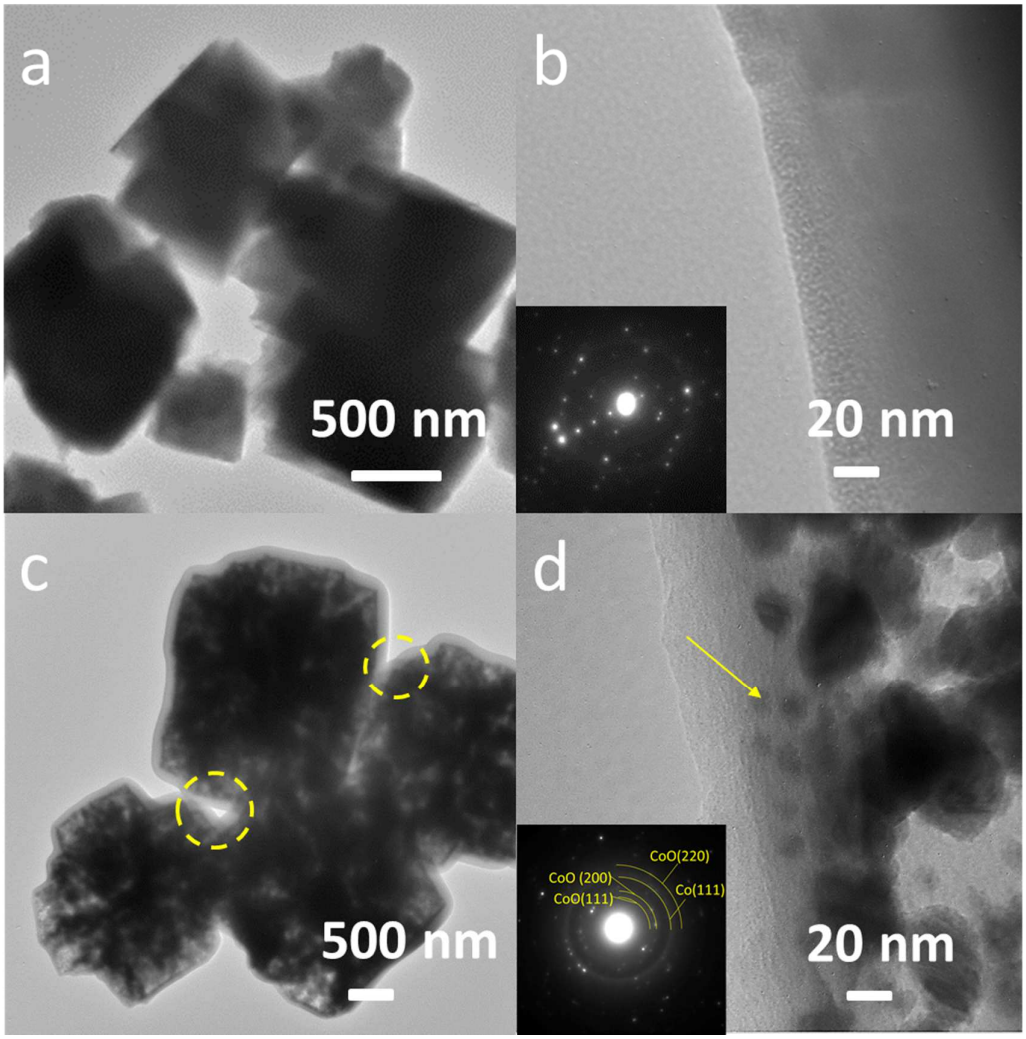

Figure 5.5. TEM images of (a, b) as-prepared $Co_2(OH)_3Cl$ precursors after biomimic mineralization for 5 days at 50 ^oC, (c, d) pomegranate-like CoO-Co@C after calcination at 450 ^oC in argon for 2 h. The insets are corresponding SAED patterns.

To confirm the different structures before and after calcination, TEM images at different magnifications of as-prepared $Co_2(OH)_3Cl$ precursors and final pomegranate-like CoO-Co@C are revealed in Figure 5.5. Figure 5.5a shows the solid particles of $Co_2(OH)_3Cl$ with irregular shapes and sizes as we described in FESEM observation (Figure 5.4a, b). The surface of them compacts well at higher magnification in Figure 5.5b. No more details could be detected. The discrete diffraction spots in SAED pattern (the inset in Figure 5.5b) confirm the highly ordered crystal structure of $Co_2(OH)_3Cl$. In contrast, unique pomegranate-like core-

shell particles are presented in Figure 5.5c, which is consistent with the result in Figure 5.4c. The porous cores indicate the existence of voids as well. To be noticed here, some parts of C shells are integrated as a whole (marked by yellow circles in Figure 5.5c) is also recorded in Figure 5.4d. The local details between C shells and the nanoparticles are demonstrated in Figure 5.5d. The average size of nanoparticles is ~20 nm. Noticeably, some tiny nanoparticles marked by a yellow arrow are even totally embedded in C shells. Consequently, C shells and cores aggregated by CoO-Co nanoparticles are firmly linked. Lattice planes of CoO (111), CoO (200), CoO (220), and Co (111) are confirmed by SAED patterns, which also corresponds well to XRD pattern in Figure 5.3c.

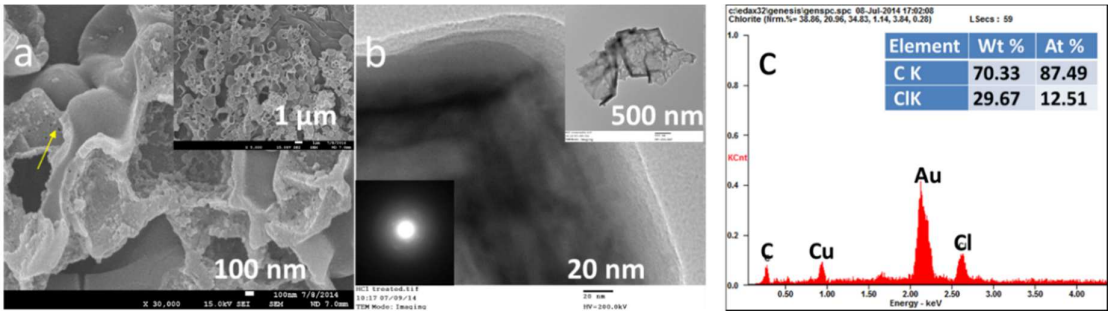

Figure 5.6. (a) FESEM images, (b) TEM images, and (c) EDS analysis of C shells left after soaking in 2.5 M HCl for 24 h. The insets in (a) and (b) are the corresponding images at lower magnifications and SAED pattern, respectively.

To clarify the components of cores and shells in this pomegranate-like structure. Final product was treated with 2.5 M HCl. FESM, TEM, and EDS were employed to characterize the structure after HCl treatment. Reasonably, all the CoO-Co nanoparticles were dissolved due to the reaction with HCl and the C shells were kept well in Figure 5.6a. The outer surface of shells is smooth. In contrast, the rough texture inside and several holes (marked by yellow arrow) are clearly recorded, which might explain why the nanoparticles could combine with the shells firmly. TEM images in Figure 5.6b indicate that the C shells are layering based on the different darkness of it. The inset SAED pattern reveals the amorphous nature of C shells in accord with XRD results above. The inset image shows the rough texture and the networked

connection inside and outside C shells, which is favorable to support nanoparticles in pomegranate-like structure. As shown in Figure 5.6c, the EDS results suggest that C shells are mainly made of carbon (87.5%), and light chloride element (12.5%) was detected. Note that the detected Cl is interesting. Whether it is doped in carbon structure and how it react with carbon will be studied in further. Thus, we could conclude that the final pomegranate-like product is composed of CoO-Co cores and interlinked C shells. Such ingenious core-shell structure of CoO-Co@C has not be reported before.

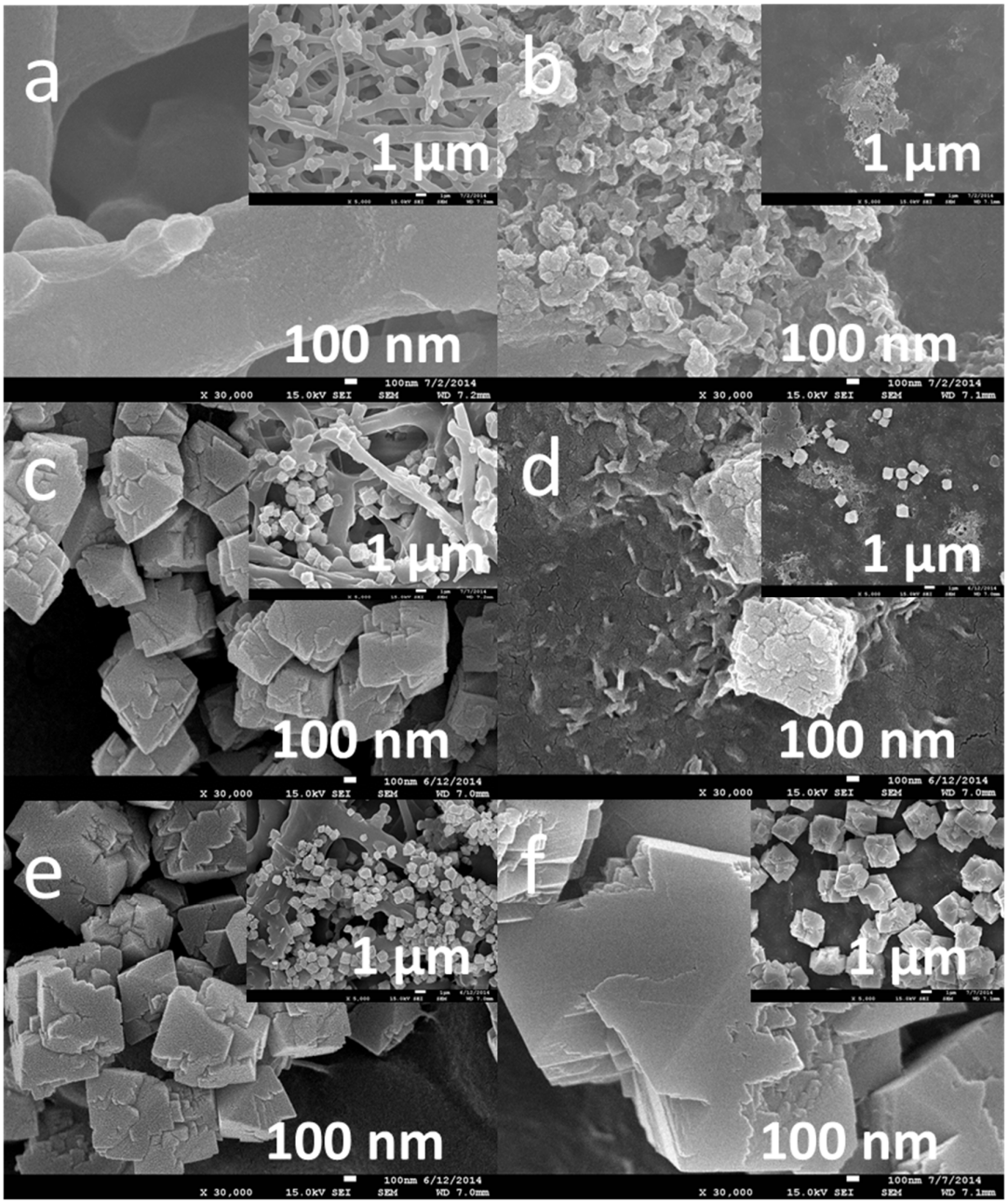

Figure 5.7. FESEM images of $Co_2(OH)_3Cl$ on ESM after biomimic mineralization for (a, b) 6 h, (c, d) 1 day and (e, f) 3 days.

To investigate the effect of biomimic mineralization periods, Figure 5.7 presents the FESEM images of as-prepared samples on both sides of ESM after 6 h, 1 day and 3 days, respectively at different magnifications. After 6 h mineralization, there is no deposition on the fiber-like OLM. However, some porous nanosheets and small nanoplates are observed on some

areas of the ILM. When the mineralization time increased to 1 day, both sides of ESM are deposited by a few particles and their size is between 500 nm and 1 μm. Notably, the big particles on the ILM is compacted by tiny nanoparticles, and some nanosheets are also observed around them. This distribution suggests that the particles might be derived from these nanosheets via recrystallization. After 3 days reaction, a large amount of particles started to occupy the surface of ESM. The particles on the ILM are slightly larger than that of on the OLM, and they are organized by the similar structures. The differences between them might be attributed to the microenvironment around them in the ES system during diffusion process. The smooth surface of the ILM and direct contact with $CoCl_2$ solution might facilitate the crystal growth of $Co_2(OH)_3Cl$ and combination of particles. Note that with the increase of mineralization periods, the amount of $Co_2(OH)_3Cl$ between ES and ESM increased. As a result, it became easier and easier to separate ESM from eggshells and some lavender-colored powders detached from the surface of ESM.

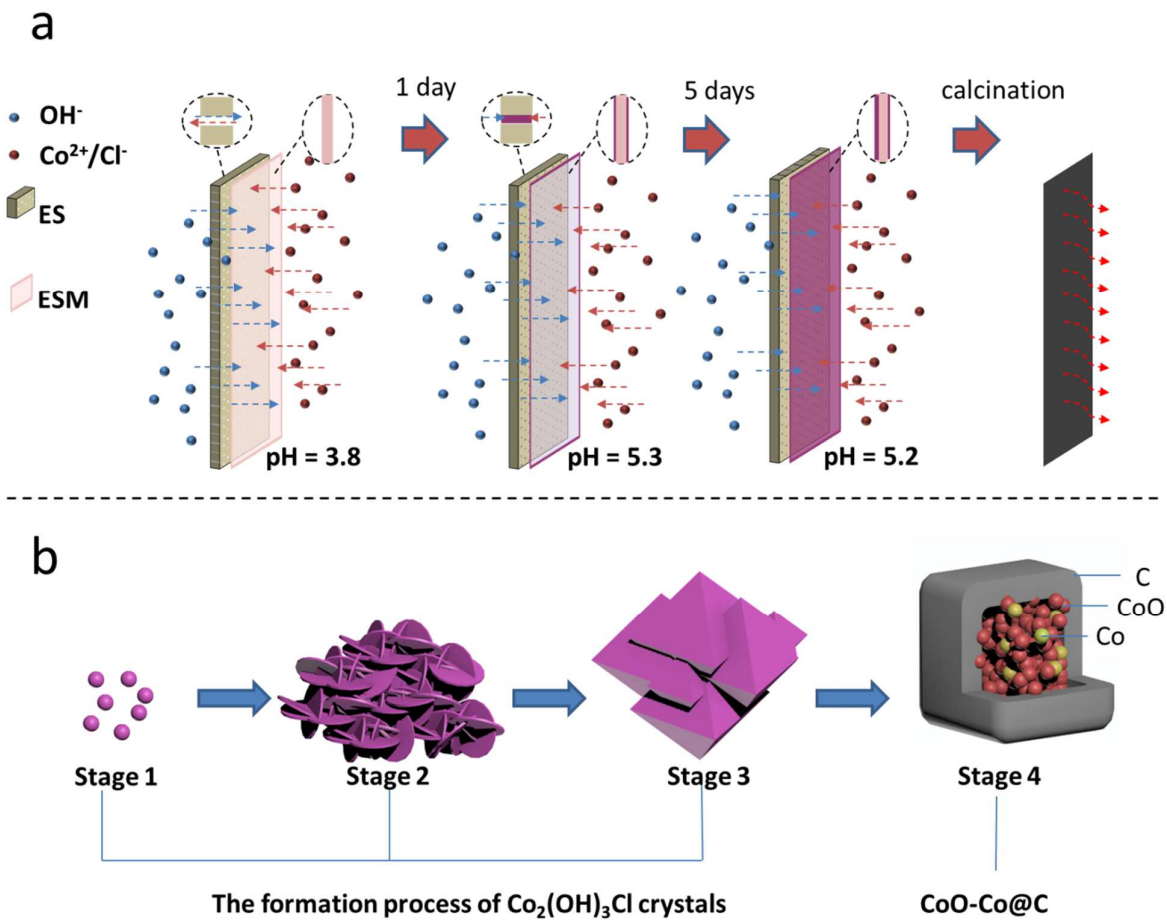

Figure 5.8. (a) Illustration of the possible growth mechanism of $Co_2(OH)_3Cl$ precursors in the ES system, and (b) structures evolution of pomegranate-like CoO-Co@C during the whole reaction process.

Currently, the mechanism of the formation of $Co_2(OH)_3Cl$ precursors and final CoO-Co@C after heat treatment is still being studied. The existed experimental results and related studies could help us to learn it in general. The biomimic mineralization process with crucial steps is shown in Figure 5.8a. Controllable ions diffusion via ES determines the formation of $Co_2(OH)_3Cl$ precursors. Firstly of all, when ES is filled by $CoCl_2$ (pH = 3.8) and placed in NaOH solution, ES nearly separate two solutions. However, they are not totally isolated by ES. ES possesses a lot of gas pores and bubble pores.[205] Therefore, solutions are still able to contact with each other, but this contact has been largely limited by ES. Since OH^- ions could elevate the pH value of $CoCl_2$ solution, nucleation firstly occurs around pores to form initial

$Co_2(OH)_3Cl$ (stage 1). After 1 days, the pH value increased from 3.8 to 5.3, and the pores gradually are blocked by $Co_2(OH)_3Cl$ deposition as the reaction goes. Even if the pores are filled up by $Co_2(OH)_3Cl$, the diffusion of ions is still undergoing due the concentration difference. At this time, the pH value is not high enough to fast precipitate $Co_2(OH)_3Cl$ in solution via homogeneous nucleation and growth. Instead, heterogeneous nucleation and growth of it on ESM is applicable due the special structures of ESM and the relatively high pH value (stage 2 and stage 3). ESM is made of protein that is in rich of functional groups such as -COOH and $-NH_2$, the nucleus of $Co_2(OH)_3Cl$ initiates on it at the beginning of diffusion process. After stage 3, the pH value will be controlled by the ES system and keep stable around 5.5. The stable pH value provides enough supersaturation for further growth of $Co_2(OH)_3Cl$. The diffusion process, controllable pH value, interaction between ions and proteins, local supersaturation on the surface of proteins as well as mild aqueous environment are similar to the conditions of biomineralization in biology.[90-91, 206] Thus, the formation of $Co_2(OH)_3Cl$ can be taken as a typical biomimic mineralization in ES system. After 1 day mineralization, the surface of ESM has been slightly deposited by $Co_2(OH)_3Cl$. Considering the local conditions of the OLM and ILM, The growth rate of $Co_2(OH)_3Cl$ on them is different. Irregular particles are randomly assembled by smaller defective octahedral units are firstly formed on the OLM. At the same time, fewer micrometer-sized particles and nanosheets aggregates are formed on the ILM. Then, the biomimic mineralization continues and the amount of deposition on both sides of ESM increases at the different rate. After 5 days, obvious $Co_2(OH)_3Cl$ coating with lavender color were noticed on the OLM after ESM was separated from ESs. The different lavender color existed on both sides, which is related to the different amount of deposition of $Co_2(OH)_3Cl$. To be noticed here, the concentration of $CoCl_2$ is important. By adjusting the concentration of it, we could get different structures on ESM, which is presented in Figure 5.9. The further studies to control the morphologies of precursors are undergoing. In addition, not

only could ESM be deposited crystalline $Co_2(OH)_3Cl$ by this biomimic mineralization, but also a piece of Ni foam placed in $CoCl_2$ solution could initiate another nanostructures on the surface after 10 days in Figure 5.10. Therefore, this biomimic mineralization might be applied to more substrates to fabricate other functional materials in future. However, how to accelerate the process of biomimic mineralization has to be studied to make it more efficient.

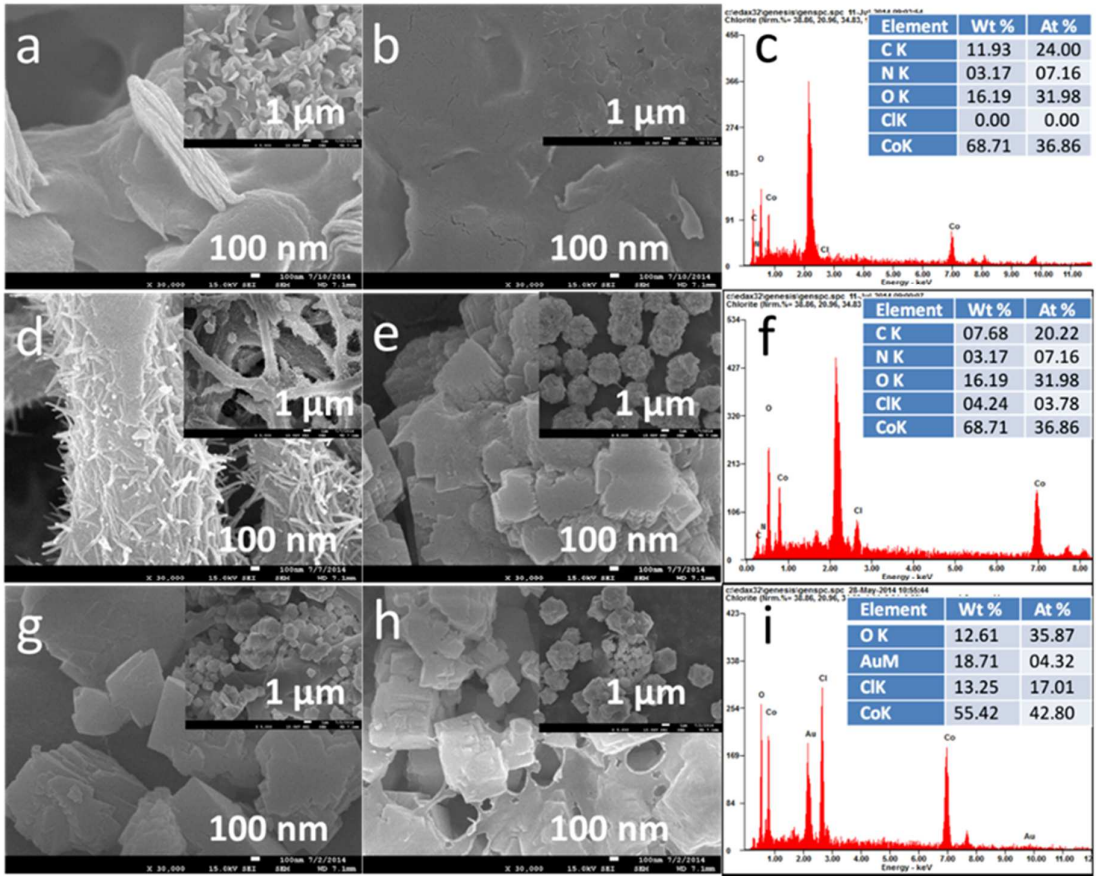

Figure 5.9. FESEM images and EDS results of $Co_2(OH)_3Cl$ on ESM after biomimic mineralization for 3 days based on (a, b, c) 0.01 M $CoCl_2$, (d, e, f) 0.25 M $CoCl_2$, (g, h, i) 1 M $CoCl_2$.

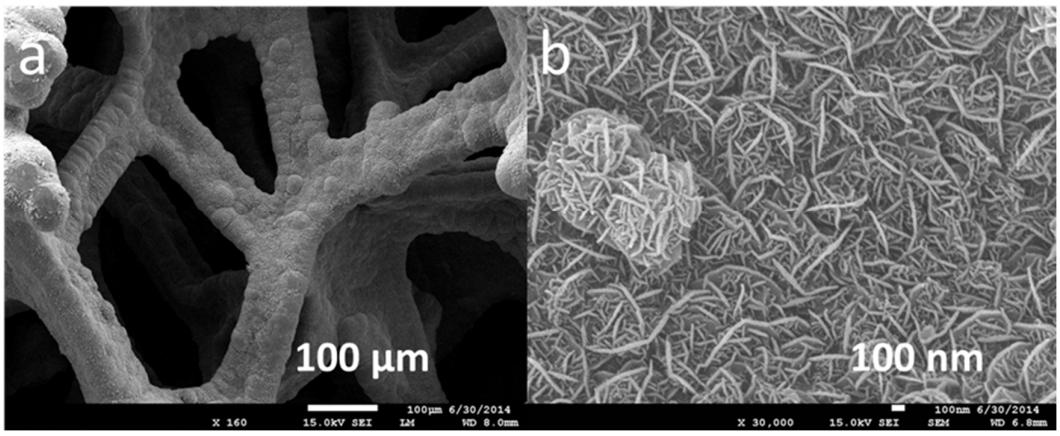

Figure 5.10. FESEM images of flower-like nanostructures on Ni foam after biomimic mineralization for 10 days at 50 ^{o}C.

Finally, ESM deposited by $Co_2(OH)_3Cl$ precursors are calcined at 450 ^{o}C in argon and converted into CoO-Co@C on CESM. Figure 5.8b demonstrates the overall evolution of pomegranate-like CoO-Co@C from $Co_2(OH)_3Cl$ crystals (Stage 1 to Stage 3 in nucleation and growth) and the unique core-shell structures of it (Stage 4) after calcination according to observation in FESM and TEM. Here, ESM not only is carbonized into CESM but also releases the reducing gases as the decomposition of protein-based ESM.[81] Some important amino acids in ESM were proven to release NH_3, H_2S, C_xH_y during heating treatment.[82, 207-208] Therefore, It is believed that ESM can generate these gases as well in heating process.

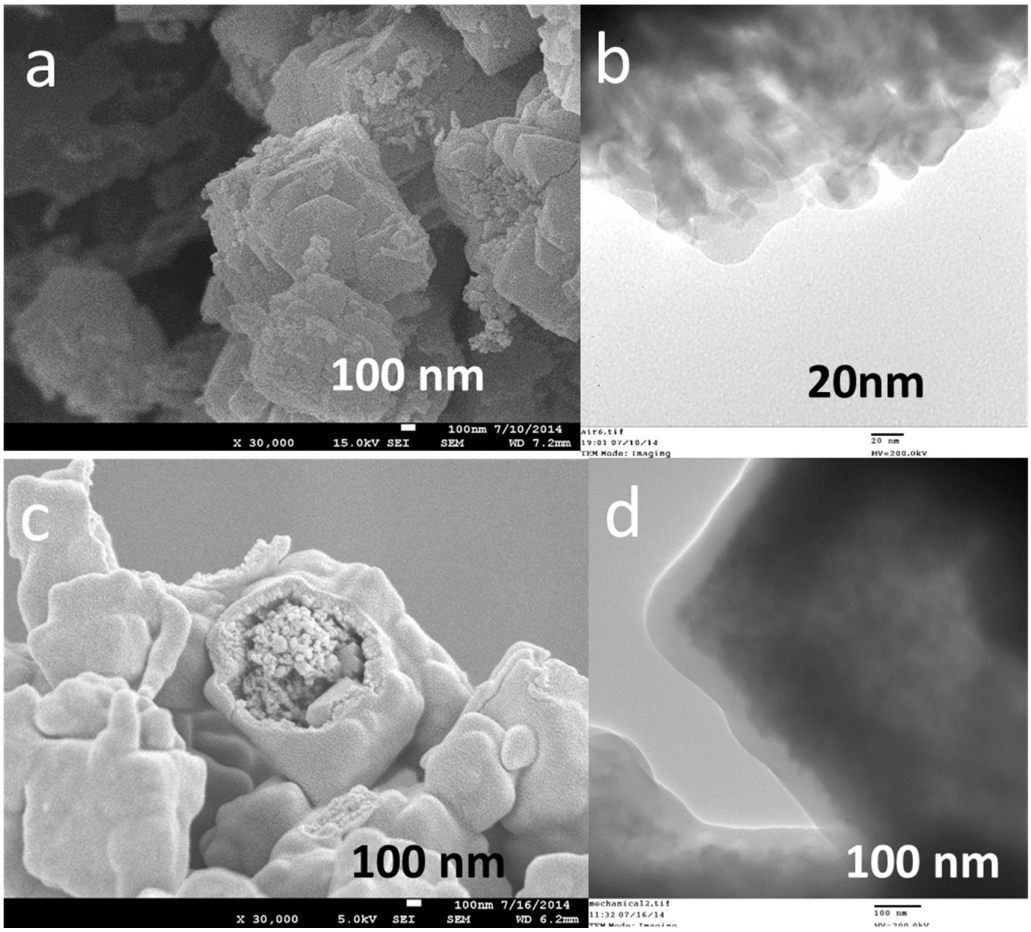

Figure 5.11. FESEM images and TEM images of (a, b) Co_3O_4 after calcination at 450 ^oC in air for 2 h, and (c, d) CoO-Co@C derived from separated $Co_2(OH)_3Cl$ powders after calcination with ESM at 450 ^oC in argon for 2 h.

We speculate that there might be two steps to form C shells. One is to partly reduce CoO to Co under autogenic gas environment during calcination. The other is to catalyze the formation of carbon layers on CoO-Co nanoparticles under this special gas environment. To confirm the importance of CESM and present inert atmosphere, $Co_2(OH)_3Cl$ powders were gently scraped from ESM and calcined in air independently. There are no any core-shell structures after calcination as present in Figure 5.11a and 5.11b. Surprisingly, even if $Co_2(OH)_3Cl$ powders were separated and only physically placed on the surface of an extra piece of ESM, we still can get the pomegranate-like structure (Figure 5.11c and Figure 5.11d). These evidences indicate that this bio-inspired carbon coating method might be applied directly to

coat carbon on various metal oxides particles easily. The mechanism of C shells formation has to be focused in the further studies. To encapsulate nanoparticles by C shells have been widely studied based different methods such as arc discharge,[209] hydrothermal methods,[210] chemical vapor condensation,[211] and solution phase chemical reduction.[212] However, by now, no other studies are related the ESM-derived carbon encapsulation. This carbon encapsulation route is facile and green, which can convert waste ESs with ESM into useful carbon source to fabricate core-shell nanomaterials.

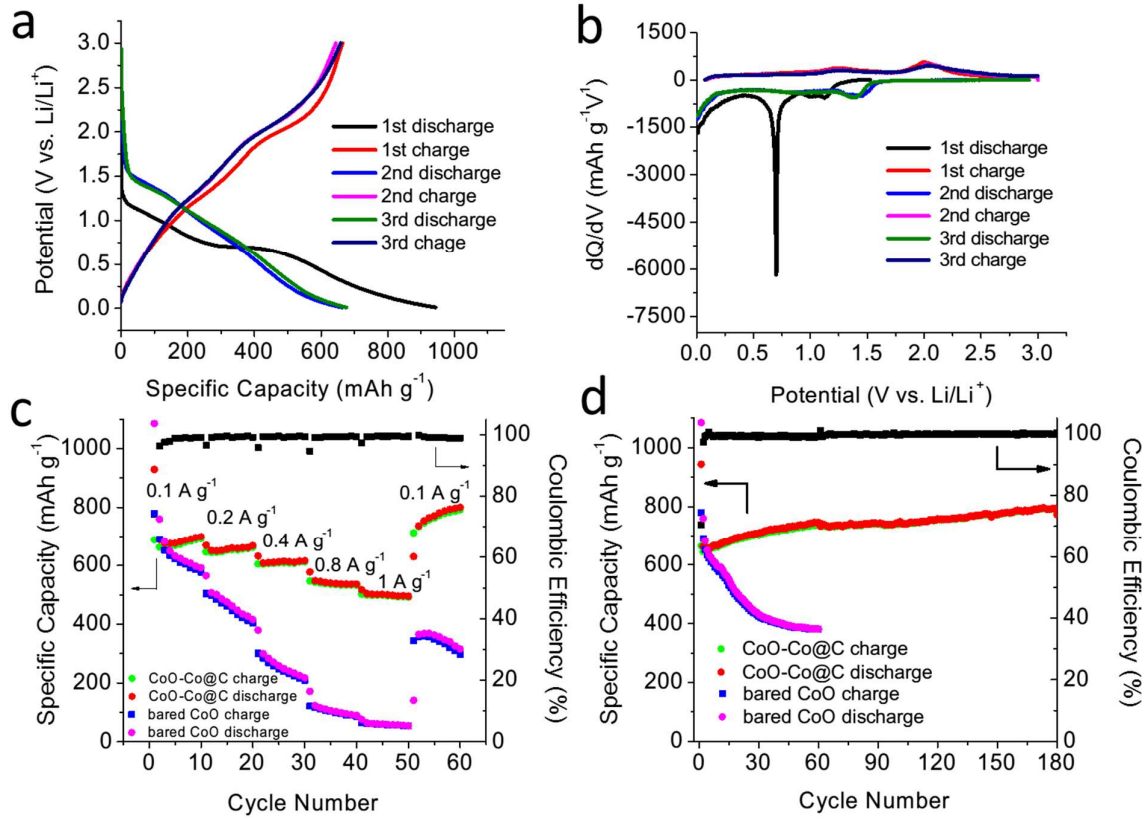

Figure 5.12. (a, b) Charge-discharge profiles and corresponding dQ/dV curves of the initial 3 cycles of the CoO-Co@C composite electrodes at a current density of 0.1 A g^{-1}, (c) rate performance of the CoO-Co@C and CoO control electrodes at different current densities ranging from 0.1 A g^{-1} to 1 A g^{-1}, (d) cycling capacity retention of the CoO-Co@C and bare CoO electrodes at a current density of 0.1 A g^{-1}.

The electrochemical characterization of pomegranate-like CoO-Co@C on CESM as composite electrodes for LIBs is shown in Figure 5.12. Firstly, Figure 5.12a presents the initial three charge-discharge profiles of it between 0.01 - 3.0 V at 0.1 A g^{-1}. There are three distinct parts of the first discharge process. From 1.2 V to 0.7 V, the slow slope curve is different from that in typical pure CoO anodes.[176, 180, 213] Instead, many CoO@C composite electrodes (especially combined with graphene) experience the similar curve.[94, 96, 183, 214] The integrated carbon might react with Li^+ ions based on traditional insertion reaction with C or other structures.[215-216] The second part of the first discharge curve is the stable plateau around 0.7 V, which is related to solid electrolyte interphase (SEI) formation and the redox reaction between CoO and Li^+ ($CoO + 2Li^+ + 2e^- \leftrightarrow Co + Li_2O$).[172] Finally, another slow slope curve is regarding the degradation of electrolyte and gel-like polymeric film.[176, 180, 217] The large irreversible specific capacity (943 mAh g^{-1}) is attributed to the formation of SEI and irreversible Li^+ trapped in composite structures during the first discharge. The initial Coulombic efficiency is ~70.1%. Then, the following charge and discharge curves are similar. The reversible specific capacity is ~700 mAh g^{-1}. Considering the existed of Co and CESM, the practical reversible capacity of CoO itself should be larger than its theoretical value of 715 mAh g^{-1}. To identify the electrochemical reactions clearly during change-discharge process, the related differential capacity is plotted in Figure 5.12b. The small peaks at ~1 - 1.2 V might be related to the C shells due to the formation of LiCl.[195] Another obvious peak at ~0.75 V could be attributed to the formation of SEI, reduction of CoO.[177, 214, 218] In the following charge and discharge curves, the reaction peaks located at ~2.0 and 1.5 V appear periodically and are highly overlapped, which suggested the reversible conversion reactions of CoO nanoparticles ($CoO + 2Li^+ + 2e^- \leftrightarrow Co + Li_2O$).

The rate performances of composite electrodes and the CoO control electrodes at the various current densities ranging from 0.1 A g^{-1} to 1 A g^{-1} are directly compared in Figure

5.12c. Although the trend of irreversible loss of specific capacity at the first cycle for both of them is almost same, the following performances demonstrate apparently different. For the CoO-Co@C composite electrodes, it delivered ~700, 661, 612, 532 and 493 mAh g^{-1} at 0.1, 0.2, 0.4, 0.8 and 1 A g^{-1}, respectively. At a current density of 1 A g^{-1}, the reversible capacity is 70.4% of that in the second cycle at 0.1 A g^{-1}. Then, it rapidly goes back to ~712 mAh g^{-1} when the current density decreased to 0.1 A g^{-1}. Under various current densities, the CoO-Co@C composite electrodes always kept stable. More importantly, when the current density was back to 0.1 A g^{-1}, the specific capacity gradually increased from 712 mAh g^{-1} to 791 mAh g^{-1} in 10 cycles, indicating the superior stability of their structure. FESEM and TEM images of composite electrodes after electrochemical characterization in Figure 5.13 confirmed this conclusion. In contrast, the control electrodes faded very fast under various current densities though it has high initial capacity. At 1 A g^{-1}, its capacity only retained at 53 mAh g^{-1} (15% of that in the second cycle at 0.1 A g^{-1}). Worse, it kept fading even if the current density went back to 0.1 A g^{-1}, and only 296 mAh g^{-1} was left under this current density after 10 cycles.

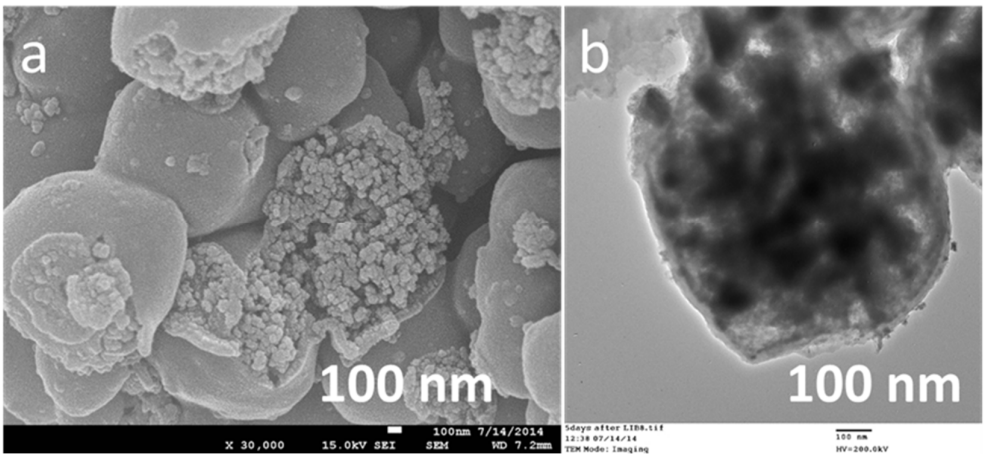

Figure 5.13. (a) FESEM images and (b) TEM images of CoO-Co@C after 60 cycles of rate performance test.

As expected, the cycling performance of CoO-Co@C composite electrodes is excellent. More than 793 mAh g^{-1} was retained in 180 cycles under 0.1 A g^{-1}. The slight increase of the capacity could be attributed to the decomposition of electrolyte and formation of gel-like polymeric film.[217] This phenomenon were reported in CoO anode materials.[180, 214] In comparison, the bared CoO control experienced obvious decay under the same condition and the specific capacity merely left 379 mAh g^{-1} after only 60 cycles.

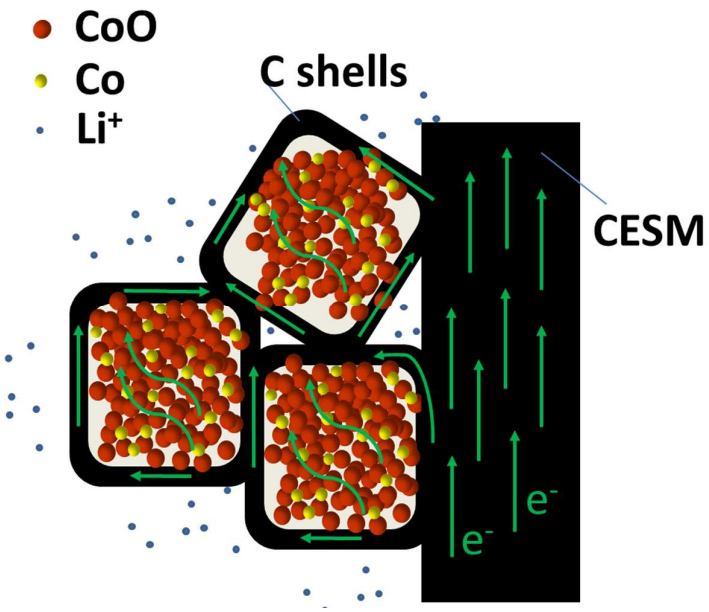

Figure 5.14. A schematic demonstrating the pomegranate-like CoO-Co@C on CESM are beneficial for electrochemical properties for LIBs.

The significant improvement of electrochemical properties of pomegranate-like CoO-Co@C composite electrodes in comparison with bared CoO control electrodes could be attributed to the unique hierarchical pomegranate-like structure and their special components. Figure 5.14 shows the schematic of composite electrodes. Firstly, interconnected C shells have several advantages. They form a highly conductive network and combine with nanoparticles inside and CESM outside naturally to support fast ions/electrons transportation in active materials.[94, 178, 180] Consequently, the rate capacity improves dramatically, compared with bare

CoO electrodes. They can tolerate the volume change during conversion reactions and prevent the detachment of active materials from the current collector.[94-96, 147, 182-183] The robust structure is a key point to maintain cycling capacity. Besides, the micrometer-sized C shell could hinder the formation of more SEI directly on CoO-Co nanoparticles with large surface area and aggregation of these nanoparticles during the charge-discharge reaction. Secondly, the structure and components of the CoO-Co cores are favorable to their performance. Large surface area of CoO-Co nanoparticles provides more active sites for electrochemical reactions with Li^+. ESM partly reduce CoO to Co, improving the conductivity among CoO-Co nanoparticles as the cores. The extra Co could facilitate the decomposition of Li_2O according to the electrochemical reaction equation.[97, 219] Third, the hierarchical pomegranate-like structure possesses widely distributed porosity in the cores encapsulated by C shells. This voids could accommodate the volume expansion of CoO during charge-discharge reaction. To our best knowledge, this is the first time to combine so much advantages of the hierarchical structure and the multicomponent composite materials to bring out the synergic effect for the final electrochemical performance. As a result, the synergetic effect of these features of pomegranate-like composite structure achieved the large specific capacity, rate performance, and excellent capacity retention. We would like to highlight that LIB is not the only one potential application of pomegranate-like CoO-Co@C. Since its special features in structure and composition, other energy and environmental applications could be expanded in future to demonstrate the merits of it. Other composite materials based on this pomegranate structure might have wide applications.

5.4 Conclusion

In conclusion, pomegranate-like CoO-Co@C on CESM as composite materials were prepared by bio-inspired eggshell system followed by calcination under relatively low temperature. Based on biomimic mineralization mechanism, under mild conditions, ESs with

ESM control the progress of reactions of ions in solutions to deposit irregular particles of $Co_2(OH)_3Cl$ on ESM. ESM not only affects the formation of the precursors but also changes the morphology and the compositions. The final products are self-assembled by C shells and nanostructured CoO-Co cores at one step. Due to the special composite structures and compositions, the rate performance and cycling performance were improved dramatically by comparing with the bared CoO control and overcome several typical disadvantages of nanostructured metal oxides. Such a facile protocol provides a new route to design the special core-shell structures of materials based on metal oxides for energy storage and other potential applications.

CHAPTER 6 BIO-INSPIRED FORMATION OF SINGLE CRYSTALLINE NANOFLAKE ARRAYS ON FLEXIBLE SUBSTRATES WITH SUPEROLEOPHOBICITY

6.1 Introduction

Functional nanostructured materials have attracted much attention in the past few decades. Nanostructured materials can find many important applications in various fields, including catalysis,[220] sensors,[221-222] energy storage,[56] self-cleaning surfaces,[223] drug delivery,[224] water splitting,[225] and solar cells.[226] Nanostructures are typically synthesized by hydrothermal methods,[227] co-precipitation,[228] chemical vapor deposition (CVD),[229] and template-assisted deposition. The existing methods have some restrictions, such as the need for extreme experimental conditions, expensive instruments and the lack of feasibility to synthesize nanostructures on flexible substrates (e.g., polymers) at room temperature on a large scale. For instance, hydrothermal methods require high temperature and high-pressure conditions;[230] CVD synthesis needs expensive CVD reactors and typically operates at high temperature;[231-232] it is difficult to fabricate high-order nanostructured arrays on substrates by co-precipitation methods in solution, and template-assisted synthesis requires the use of expensive sacrificial templates that have to be removed.[233-234] Therefore, it is always intellectually interesting and technically challenging to develop new approaches for the facile synthesis of ordered nanostructures on given flexible substrates at room temperature.

Nature, with nearly four billion years of evolution, offers many inspirations to develop facile approaches to synthesize nanostructures on substrates at room temperature. Numerous hierarchical nanostructures are synthesized by various species in nature, providing unique features. Few interesting examples are: self-cleaning lotus leaves,[235] the high visual efficiency of fly eyes,[236] the iridescent colors of butterflies,[237] the low drag of shark skin,[238] mechanically robust eggshells,[239] the strong surface adhesion of a gecko's feet,[240] bacterial biofilms with resistance to liquid wetting and gas penetration,[241] the water collection capability of a Namib

desert beetle,[242] the antifogging properties of mosquito compound eyes,[243] and robust eggshells. Bio-inspired synthesis of functional nanostructures has attracted much attention recently. Take eggshell for example – an inorganic eggshell is formed by a sophisticated strategy: the carbonate ions from the metabolism of an embryo could pass through the eggshell membrane and react with calcium ions from the uterus forming calcium carbonate structures only on the external surface of the eggshell membrane to form a protective eggshell made of calcium carbonate (~95%) stabilized by a protein matrix (~5%).[244-245] The robust shell can protect the embryo inside, and also controls the passage of air in and out of the egg through tiny pores. It will be interesting to learn from the sophisticated strategy of eggshell membrane-assisted synthesis of eggshell and develop an artificial membrane-assisted method of nanostructures on a large scale. Another interesting example would be fish scales with superoleophobicity that could provide protection against pollutants and toxins in rivers.[246] Artificial fish scales with superoleophobicity can find many applications, including antifouling coating, pollutant and toxin prevention, and oil spill recovery. However, bio-inspired membrane-assisted synthesis of functional nanostructures is still in its infancy. It would be interesting to learn the strategy from the eggshell formation mechanism to synthesize superoleophobic materials. There are only a few reports on the membrane-assisted synthesis of calcium-based materials.[39, 247] We believe that bio-inspired synthesis could be applied, in principle, to prepare many different kinds of nanostructures, beyond calcium-based materials, with unique morphologies, desired structures and compositions and therefore functional properties. It opens up opportunities for low cost and green production of nanostructures.

We have identified hydrated manganese(II) phosphate ($Mn_3(PO_4)_2 \cdot 3H_2O$) as the model to explore the general application of bio-inspired membrane-assisted synthesis of nanostructures on flexible substrates. $Mn_3(PO_4)_2 \cdot 3H_2O$ mineral, existing as Reddingite mineral in nature, is a functional material with many important applications. For example, it could be

used as a coating material to enhance wear resistance,[248] a precursor to synthesize $LiMnPO_4$cathode materials for lithium-ion batteries,[249-250] and an additive in flame retardant systems.[251] Additionally, it also demonstrated interesting ferromagnetic properties.[252] In the preparation of this manuscript, we also learned that $Mn_3(PO_4)_2 \cdot 3H_2O$ could be used as a catalyst for water oxidation.[253] Precipitation and solid state reactions are typically used to synthesize $Mn_3(PO_4)_2 \cdot 3H_2O$.[249, 252-253] Therefore, it will be fascinating to explore bio-inspired membrane-assisted methods to prepare $Mn_3(PO_4)_2 \cdot 3H_2O$ nanostructures at room temperature, in particular, forming nanoarrays on flexible substrates.

Herein, we present a bio-inspired membrane-assisted approach to fabricate $Mn_3(PO_4)_2 \cdot 3H_2O$ nanoflake arrays on flexible polymer substrates at room temperature for the first time. A cation-exchange membrane (Nafion N117) was selected as the semi-permeable membrane to control the diffusion direction of Mn^{2+} ions as well as the cation concentration for controlled crystallization to form a unique 2-D rectangle shape. At the same time, the hydrophilic groups on the Nafion membrane facilitate the nucleation and growth of $Mn_3(PO_4)_2 \cdot 3H_2O$ nanoflakes on the Nafion membrane, forming a robust nanoflake array-coated membrane as a piece of flexible material. The flake-like nanostructures formed on the substrate and the hydrophilic nature of the hydrate can achieve impressive underwater hydro/oleophobicity with an oil contact angle of ~170° and extremely low oil adhesion, which is similar to that of fish scales.

6.2 Experimental Section

Materials Synthesis. All chemicals were used as received. In a typical procedure, 0.1 M $MnSO4 \cdot H_2O$ aqueous solution and 0.1 M $H3PO_4$aqueous solution were first prepared in beakers. The pH value of the $H3PO_4$ solution was adjusted to 8 by using a LiOH aqueous solution. Then 8 ml of each of the two solutions was put into two chambers of the reactor separated by a piece of cation exchange membrane (Nafion N117) and sealed with two O-rings

in Figure. 6.1a. The membrane was rinsed and saturated in deionized water before use. The reactors were maintained at room temperature for different time intervals, ranging from 6 h, 24 h, 3 d, 5 d to 7 d. It was observed that $Mn_3(PO_4)_2 \cdot 3H_2O$ nanoflake arrays only formed on the side of the membranes exposed to the [PO_4^{3-}] solution, not on the side exposed to the [Mn^{2+}] solution.

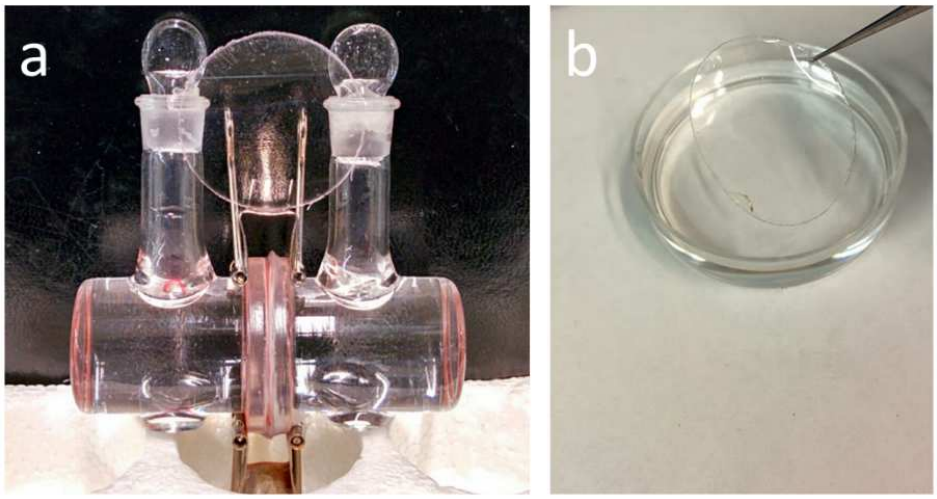

Figure 6.1. Optical images of (a) a reactor with two chambers with two precursor solutions separated by a piece of Nafion membrane sealed with two O-rings, and (b) a piece of transparent Nafion N117 membrane rinsed in water before use.

Materials Characterization. X-ray diffraction analysis was carried out on an XRD instrument (Rigaku with Cu Kα radiation). The morphology was characterized by using a field emission scanning electron microscope (FESEM, JEOL 7600) coupled with an energy dispersive X-ray spectrometer (EDS) for elemental analysis. A transmission electron microscope (TEM, JEOL 2010) was also used. Thermogravimetric analysis (TGA, TA Q600) was carried out at a ramp rate of 10 °C min^{-1} from room temperature to 700 °C in air. For underwater oil contact angle analysis, 1,2-dichloroethane ($C_2H_4Cl_2$) dyed with Oil Red O was selected as the model oil due to the fact that its density is higher than that of water. 5 μL of oil droplets was directly dropped onto the $Mn_3(PO_4)_2 \cdot 3H_2O$ nanoflake array-covered Nafion membrane underwater. The optical images of the bead-like oil droplets were taken by using a

camera with a micro lens (Nikon 85 mm f/3.5G). The static oil contact angles were measured based on the optical images using ImageJ software.

6.3 Results and Discussion

Figure 6.2 shows the optical image and the chemical composition characterization of the $Mn_3(PO_4)_2 \cdot 3H_2O$ nanostructures formed by bio-inspired membrane-assisted synthesis after 7 days of reaction at room temperature. Figure 6.2a is the optical image of a piece of Nafion membrane covered with white color $Mn_3(PO_4)_2 \cdot 3H_2O$ nanoflake arrays in water. The uniform white color suggests the even distribution of the $Mn_3(PO_4)_2 \cdot 3H_2O$ nanoflake arrays on the Nafion surface. Note that Nafion without the $Mn_3(PO_4)_2 \cdot 3H_2O$ nanoarrays is entirely transparent in water. The formation of $Mn_3(PO_4)_2 \cdot 3H_2O$ was observed only on the side of the Nafion exposed to the [PO_4^{3-}] solution. The other side of the Nafion membrane which was in contact with the [Mn^{2+}] solution remained clean without any solid formation. This phenomenon, as expected, might be attributed to the cation-exchange nature of the Nafion membrane.[39, 247, 254] Nafion has a unique structure of fluorocarbon backbones attached to a high concentration of negatively charged sulfonate groups ($-SO^{3-}$) at 1.13 mol L^{-1}.[255] The unique property of Nafion only allows cations to be exchanged but not anions or electrons.[254, 256] Thus, the Mn^{2+} cations transferred via Nafion can react with PO_4^{3-} anions forming insoluble $Mn_3(PO_4)_2 \cdot 3H_2O$ nanoarrays only on the side of the membrane exposed to the [PO_4^{3-}] solution. On the other side, the Li^+ cations transferred are fully dissolved without any solid formed such as Li2SO4 which is very soluble at room temperature in water.

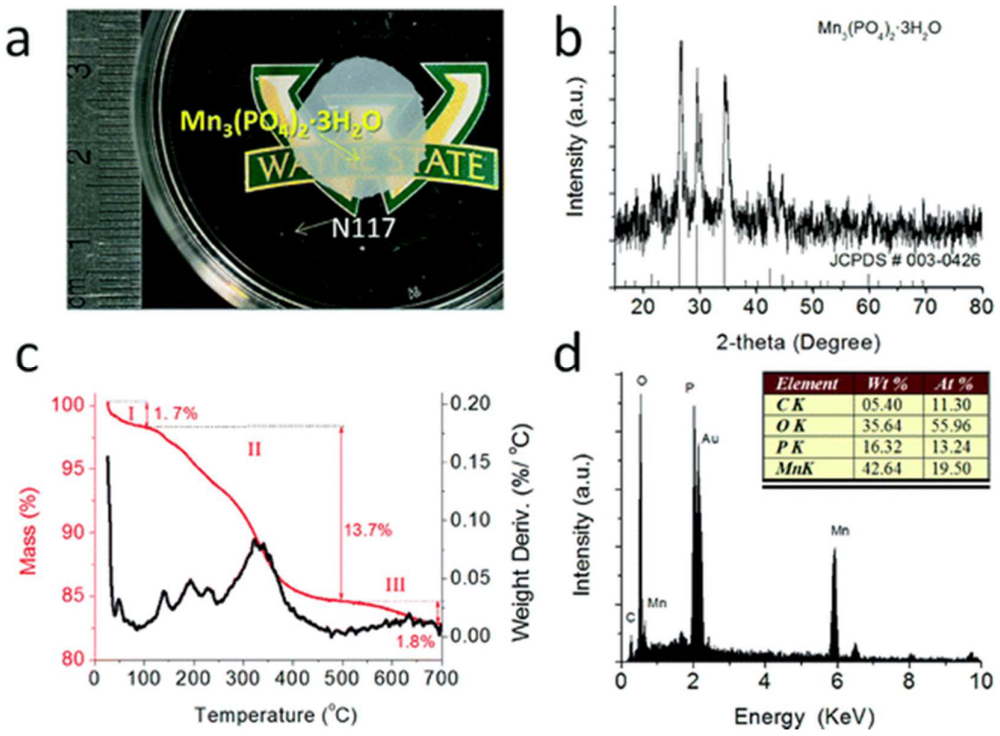

Figure 6.2. $Mn_3(PO_4)_2 \cdot 3H_2O$ nanostructures grown on Nafion N117 substrates: (a) optical image of white color $Mn_3(PO_4)_2 \cdot 3H_2O$ formed on a piece of Nafion membrane, (b) XRD pattern assigned to $Mn_3(PO_4)_2 \cdot 3H_2O$, (c) TGA profile, and (d) EDS analysis of the collected $Mn_3(PO_4)_2 \cdot 3H_2O$ to double confirm the chemical composition.

The optical image clearly shows that $Mn_3(PO_4)_2 \cdot 3H_2O$ forms a uniform white film on the Nafion membrane surface (Figure 6.2a). The part of the Nafion membrane not exposed to the reactants (covered by O-rings) is colorless. The XRD result (Figure 6.2b) confirms that the white sample is $Mn_3(PO_4)_2 \cdot 3H_2O$. The XRD diffraction peaks could be matched relatively well to those of $Mn_3(PO_4)_2 \cdot 3H_2O$ according to JCPDS #003-0426. $Mn_3(PO_4)_2 \cdot 3H_2O$ should have a triclinic crystal structure, and the lattice constants generally agreed with those in the literature.[253] Figure 6.2c shows the TGA profile of the as-prepared $Mn_3(PO_4)_2 \cdot 3H_2O$. There are three stages. Firstly, from room temperature to 87 °C, the 1.7 wt% mass drop could be attributed to the removal of physically adsorbed water molecules on the surface. Then, the weight loss continued to drop by 13.7 wt% up to 500 °C, which suggests the removal of structural water in the $Mn_3(PO_4)_2 \cdot 3H_2O$ crystals. The experimentally observed mass loss (13.7

wt%) agrees well with the theoretical value of structural water in $Mn_3(PO_4)_2 \cdot 3H_2O$ (13.2 wt%). Above 500 °C, there is still a slight decrease (1.8 wt%) from 500 to 700 °C, which could be assigned to the decomposition of trace impurities. The profile of the TGA curve is consistent with the references reported,[249, 251, 253] once again confirming its chemical composition as $Mn_3(PO_4)_2 \cdot 3H_2O$. Interestingly, the structural water in $Mn_3(PO_4)_2 \cdot 3H_2O$ can only be fully eliminated at a much higher temperature (500 °C) than other regular hydrated compounds, such as $FePO_4 \cdot 2H_2O$ at 200 °C, $CaHPO_4 \cdot 2H_2O$ at 165 °C, and $CaSO4 \cdot 2H_2O$ at 220 °C.[257-259] It could be attributed to the triclinic crystal structure of $Mn_3(PO_4)_2 \cdot 3H_2O$, which could form strong intermolecular interactions.[252-253] As shown in Figure 6.2d, EDS analysis shows the presence of Mn, P and O elements. The atomic ratio of Mn and P is 1.47, which is very close to the theoretical ratio of 1.5. Therefore, based on the TGA, XRD, and EDS analysis, the formation of $Mn_3(PO_4)_2 \cdot 3H_2O$ using our room temperature method is confirmed.

The structure of the $Mn_3(PO_4)_2 \cdot 3H_2O$ nanoflake arrays was characterized by both FESEM and TEM (Figure 6.3). The low-magnification overall view (Figure 6.3a) shows that the nanoflake arrays were formed on the surface of the Nafion substrates. The nanoflakes are interlaced and intercrossed with each other to form continuous 3D structures on the surface of the membrane substrate, with each nanoflake growing outwards against the Nafion substrate. The intercrossed network could enhance the mechanical stability of the nanoflakes standing on the substrate, forming arrays. The nanoflakes are rectangular in shape with widths of 500 nm to 2 μm and lengths of 1-3 μm. The thickness of the nanoflakes is about 80-100 nm (Figure 6.3b). The nanoflakes were formed by stacked layered-structures, as evidenced by the presence of thin layers on the surface of the nanoflake (highlighted by a yellow arrow in Figure 6.3b). Surprisingly, there are nanowires and branched nanowires linking the nanoflakes observed (Figure 6.3a and 6.3b). The Y-shaped nanowires connecting three nanoflakes are particularly interesting. The nanowire by-products might find potential applications utilizing their function

as linkers for electron, mass and energy transfer in the future. Our on-going effort is to further investigate the nanowire by-products. For the scope of this current paper, we will focus on the main products which are the nanoflake arrays. The rectangular shape of the as-grown $Mn_3(PO_4)_2 \cdot 3H_2O$ was double-confirmed by the TEM image (Figure 6.3c). The layered-structure is more clearly observed with a uniform projection of two layers with different contrasts at the upper right side as highlighted by the yellow arrow. Based on the SAED analysis, these rectangular flakes have extended their length along the [001] direction and their width along the [010] direction. The flakes have dominantly exposed {100} facets, which could be thermodynamically stable under the experimental conditions. Notably, the mouth-like defect in the top right of the flake highlighted by a yellow arrow suggests that an intercrossed flake was "locked" by it but was broken off under intensive mechanical vibration during the preparation of the sample for TEM. The interlocked nanoflakes could enhance their stability as an integrated piece of material on the macro scale. The SAED pattern shows the clear diffraction spots indicating good crystallinity and all the spots can be assigned to $Mn_3(PO_4)_2 \cdot 3H_2O$.

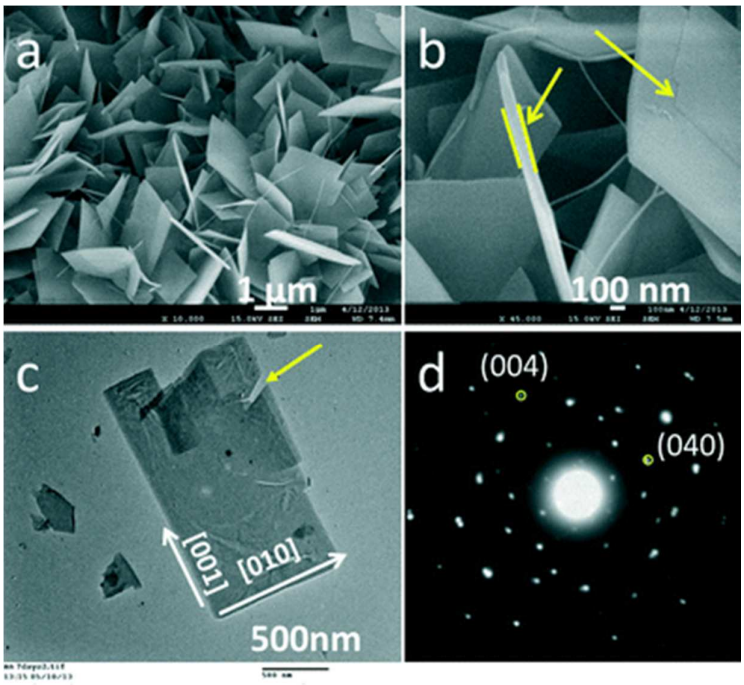

Figure 6.3. (a) Low-magnification FESEM image showing the overview morphology of the nanoflake arrays of $Mn_3(PO_4)_2 \cdot 3H_2O$ grown on the Nafion N117 membrane at room temperature after 7 days of reaction; (b) high-magnification FESEM image of few typical flakes tilted at different degrees, the "edge" and "face" are defined as highlighted, and nanowires and multilayers are observed; (c) TEM image of one typical rectangle flake; the yellow arrow highlights the edge where the defect and multilayers are observed; (d) the corresponding SAED pattern of a section of a typical flake shown in (c).

In order to explore the mechanism of formation of the nanoflake arrays of $Mn_3(PO_4)_2 \cdot 3H_2O$, the effect of different reaction times and temperatures on the nanoflakes was studied. The evolution of the morphologies of $Mn_3(PO_4)_2 \cdot 3H_2O$ over time is presented in Figure 6.4. After 6 h, a large number of flakes without regular shapes formed on the surface. The flakes were not yet rectangular at this stage (Figure 6.4a). When the reaction time was extended to 24 h, the size increased as compared to those obtained after 6 h of reaction. We also observed that, at 50 °C instead of at room temperature, nanobelt arrays instead of nanoflakes would be formed after 24 h of reaction (Figure 6.3d), which suggests that high temperature could significantly accelerate the oriented growth of the $Mn_3(PO_4)_2 \cdot 3H_2O$ arrays along the [001] direction. The formation of belts could be considered as the extended rectangle-

shaped flakes with faster growth in the [001] direction at higher temperature. Two factors, namely cation mobility in Nafion and crystallization rate, are significantly affected by temperature, leading to the formation of layered nanobelts on the flexible substrate (Inset of Figure 6.4d).

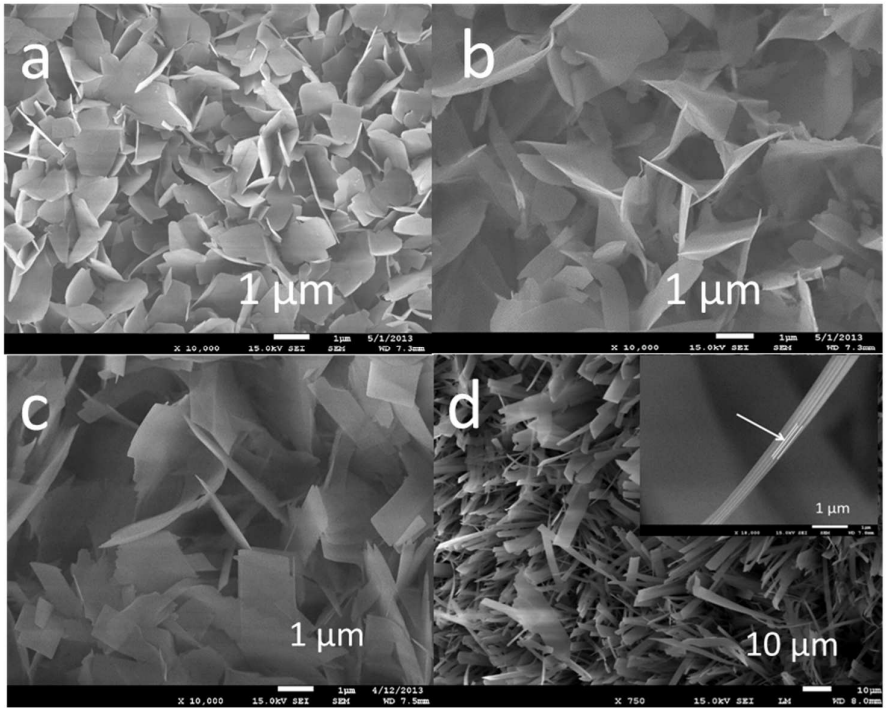

Figure 6.4. FESEM images of $Mn_3(PO_4)_2 \cdot 3H_2O$ formed on the Nafion N117 membrane after different reaction periods: (a) 6 h, (b) 24 h, and (c) 5 d, while keeping all other experimental parameters constant; (d) FESEM images of $Mn_3(PO_4)_2 \cdot 3H_2O$ nanobelt arrays prepared on Nafion N117 membrane after a reaction time of 24 h at 50 oC keeping other experimental conditions unchanged as those typical condition.

Based on our experimental evidence and understanding of the properties of Nafion, we propose a possible formation mechanism (Figure 6.5). At the beginning, Mn^{2+} ions are easily transferred from the [Mn^{2+}] solution chamber to the [PO_4^{3-}] solution chamber via the cation-exchange membrane.[254] At the same time, Li^+ and H^+ as counter ions are also carried from the [PO_4^{3-}] solution chamber and Nafion to the [Mn^{2+}] solution chamber to balance the charge. The Li^+ and H^+ ions in the [Mn^{2+}] solution chamber are fully dissolved in the presence of [SO_4^{2-}] anions without solid formation. In contrast, the transfer of Mn^{2+} ions toward the [PO_4^{3-}] solution

chamber could initiate nucleation due to the low solubility of $Mn_3(PO_4)_2 \cdot 3H_2O$ in water. Note: $Mn_3(PO_4)_2 \cdot nH_2O$ has a solubility product constant KSp = 6.13×10^{-32},[56] and $Mn_3(PO_4)_2$ has a KSp = $1 \times 10^{-27.45}$. The $Mn_3(PO_4)_2 \cdot 3H_2O$ crystals formed on the surface of Nafion might experience a typical nucleation and growth process. In this process, Nafion played an important role. Firstly, Nafion has ion channels,[260] which assist the continuous transfer of Mn^{2+} ions in the [PO_4^{3-}] solution side due to the presence of a concentration gradient between the two sides of the membrane. Secondly, Nafion provides a pre-existing interface, reducing the activation energy of the nucleation of $Mn_3(PO_4)_2 \cdot 3H_2O$ to initiate heterogeneous nucleation and growth. Thirdly, the large amounts of sulfonate groups with a negative charge can bind to Mn^{2+} ions to keep the initial heterogeneous nucleation of $Mn_3(PO_4)_2 \cdot 3H_2O$ on the surface.[261-262] Eventually, the nanoflake arrays were formed on the flexible substrate. However, the exact mechanism of formation is still not fully understood which will require additional studies.

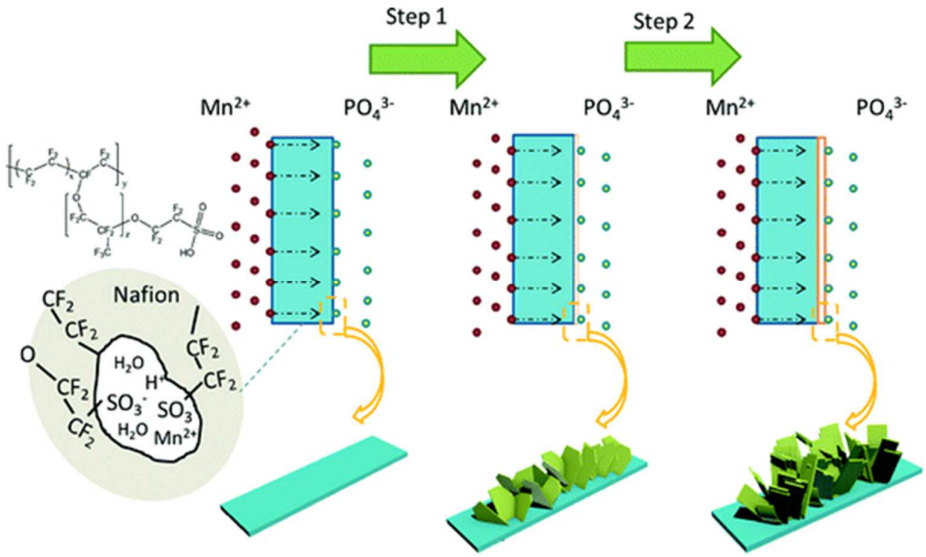

Figure 6.5. Schematic illustrating the formation of nanoflake arrays of $Mn_3(PO_4)_2 \cdot 3H_2O$ on a Nafion membrane.

To demonstrate the possible application of the as-prepared $Mn_3(PO_4)_2 \cdot 3H_2O$ nanoflake arrays on flexible Nafion, a unique surface property was investigated. $Mn_3(PO_4)_2 \cdot 3H_2O$ is a

typical oleophobic material due to its hydrate nature and the existence of hydrophilic groups. After introducing hierarchical nanostructures, its oleophobicity could transform into superoleophobicity underwater, like fish scales. To explore the effect of the structures on its wettability underwater, we measured the oil contact angles (OCAs) on the as-deposited Nafion membrane based on different reaction times (0 to 7 days). Bare Nafion membrane has an OCA of 113° (Figure 6.6a). Compared with the flattened surface of Nafion N117 in water, the bottom of Nafion detached from the glass slides and deformed slightly after being exposed to an oil droplet. The oil droplet was stuck to the Nafion surface. The observed phenomenon might be ascribed to the nature of the Nafion membrane. Nafion has a backbone of hydrophobic tetrafluoroethylene with hydrophilic sulfonic acid groups ($-H^+SO^{3-}$) in its side chain. .[254] Goswami et al. studied the behavior of the deformation of Nafion in contact with water and observed a transformation from hydrophobicity to hydrophilicity due to the movement of polar groups.49 Therefore, the slightly deformed surface observed could be caused by partial restructuring of the surface group in response to the changes in surface energy (from water to oil locally) and the induced mechanical stress. After the surface of the Nafion was covered with the $Mn_3(PO_4)_2 \cdot 3H_2O$ nanoflake arrays obtained after 6 h of reaction, the exposed surface in contact with the oil droplet is only from $Mn_3(PO_4)_2 \cdot 3H_2O$ and not from Nafion. Thus, as shown in Figure 6.6b, the OCA increased significantly to 146°, and the oil droplet easily moved around. No Nafion deformation was observed at the interface between the oil droplet and the Nafion, indicating that $Mn_3(PO_4)_2 \cdot 3H_2O$ arrays with hierarchical micro/nanostructures have isolated the surface of Nafion from the oil droplet. As the reaction time extended with further nanostructure growth, the OCA was higher at 166° after 5 days (Figure 6.6c). Finally, it was totally superoleophobic and oil adhesion was ultralow for the 7 d sample (Figure 6.6d). Here, the oil droplet demonstrates a nearly spherical shape (OCA = 171°). The extremely low oil adhesion was also achieved, where the oil droplets rolled off easily. The interesting

superoleophobicity underwater with the assistance of a hierarchical micro/nanostructure could find many applications, including pollutant and toxin prevention, oil/water separation and microscale transfer.[136, 263-265]

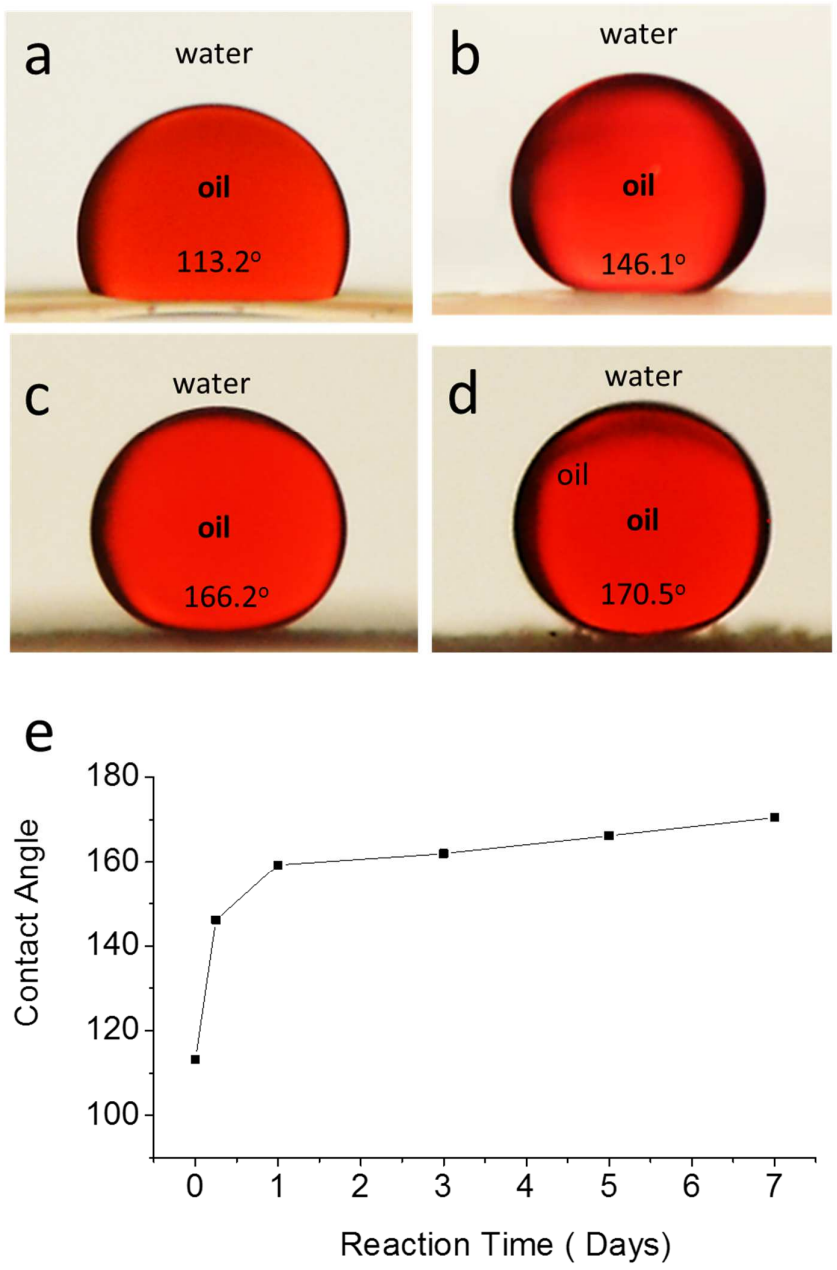

Figure 6.6. Shape change of an oil droplet (1,2-dichloroethane dyed with Oil Red O, 5 μL) underwater on the surface of (a) bare Nafion membrane, and as-deposited Nafion N117 membrane with $Mn_3(PO_4)_2 \cdot 3H_2O$ nanoflake arrays after reaction times of (b) 6 h, (c) 5 d, and (d) 7 d. (e) The underwater oil contact angles of the oil droplets sitting on $2Mn_3(PO_4)_2 \cdot 3H_2O$

covered Nafion membranes obtained after different reaction periods of 6 h, 24 h, 3 d, 5 d, and 7 d. The 0 h data is from bare Nafion membrane.

The observed superoleophobicity underwater can be interpreted by the Cassie model (Figure 6.7). The Cassie equation is:[54]

$\cos\theta_{OW'} = f\cos\theta_{OW} + f - 1$

where f is the area fraction of the solid, θ_{OW} and $\theta_{OW'}$ are the contact angles of the oil droplet sitting on a smooth and a rough surface, respectively, in water. When the rough surface was immersed in water, the space and voids between the hierarchical micro/nanostructures were occupied by water, or f is extremely small. Consequently, the nanoflake arrays filled with water could prevent the oil droplet from touching the Nafion membrane. The superoleophobicity, measured based on the oil droplet contact angle underwater, increases with the decrease in f or the increase in roughness at the micro/nanoscale induced by the $Mn_3(PO_4)_2 \cdot 3H_2O$ nanoflake arrays, as expected in Figure 6.5e.

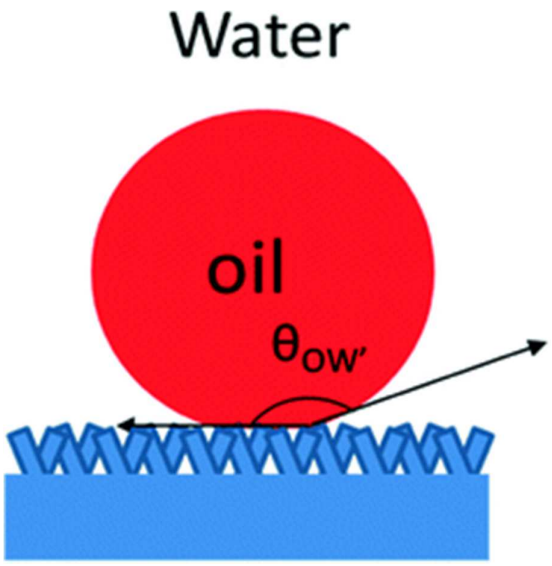

Figure 6.7. Schematic demonstrating the induced roughness and superoleophobicity of the nanoflake arrays underwater.

We would like to highlight that the self-assembled nanostructured $Mn_3(PO_4)_2 \cdot 3H_2O$ on the Nafion membrane as a robust and flexible material may find other applications, including

solid supercapacitors, water oxidation, electrochemical biosensors and battery positive electrodes.[67, 253, 266-268]

6.4. Conclusion

We demonstrated a bio-inspired membrane-assisted approach to fabricate nanoflake arrays on a flexible Nafion membrane at room temperature. The Nafion N117 membrane not only controlled the transport of ions and their reactions but also was used as a flexible substrate to support the growth of the $Mn_3(PO_4)_2 \cdot 3H_2O$ nanoflake arrays. We believe that our approach outlined in this paper could be applied to achieve room temperature and bio-inspired synthesis of many different kinds of functional nanostructures, including but not limited to metal hydroxides, metal phosphates, etc. The hierarchical nanostructures of the $Mn_3(PO_4)_2 \cdot 3H_2O$ nanoflake arrays demonstrated interesting superoleophobicity underwater similar to fish scales and they could find important applications.

CHAPTER 7 BIO-INSPIRED SYNTHESIS OF α-$Ni(OH)_2$ NANOBRISTLES ON VARIOUS SUBSTRATES AND THEIR APPLICATIONS.

7.1 Introduction

Layered nickel hydroxides, which can find many important applications, have attracted much attention recently. For example, nickel hydroxides can be employed as positive electrode materials for nickel metal hydride batteries,[269] as highly efficient catalysts for electrochemical water splitting,[270] as precursors for the facile preparation of NiO which can be used in lithium-ion batteries,[271] as electrodes for supercapacitors,[272]4 and for high-performance sensors.[273]5 Nickel hydroxide has two polymorphs, namely, α-$Ni(OH)_2$ and β-$Ni(OH)_2$. α-$Ni(OH)_2$ has anions and/or water molecules intercalated between the positively charged $Ni(OH)_{2-x}$ layers and the interlayer distance is about 0.7 nm; in contrast, β-$Ni(OH)_2$ has a hexagonal closest-packed structure without any intercalation between the layers with an interlayer distance about 0.46 nm. α-$Ni(OH)_2$ has more randomly oriented layers and disorder than β-$Ni(OH)_2$.[274] α-$Ni(OH)_2$ can be electrochemically and reversibly converted into the γ-NiOOH phase without any mechanical deformation. In contrast, β-$Ni(OH)_2$ is converted into β-NiOOH which is then converted into γ-NiOOH leading to irreversible damage.[269] The distinguished features enable α-$Ni(OH)_2$ to demonstrate superior electrochemical performances as compared to β-$Ni(OH)_2$.[269, 275] However, α-$Ni(OH)_2$ is unstable and can be transformed into β-$Ni(OH)_2$ in alkaline solution.[269] Therefore, it is very difficult, if not impossible, to prepare α-$Ni(OH)_2$ from alkaline solution.

Recently, many efforts have been focused on the facile preparation of α-$Ni(OH)_2$. It is critically important to manipulate and control the pH of the solution in order to avoid the formation of β-$Ni(OH)_2$. It is generally impossible to obtain phase-pure α-$Ni(OH)_2$ by a direct reaction between Ni^{2+} salts (e.g., $NiCl_2$) and alkali salts (e.g., NaOH) in solution. In many cases, urea was selected to control the pH at a relatively low level, instead of using alkali, and special

instruments were required to decompose urea. For example, the microwave-assisted hydrothermal method has been developed for the synthesis of α-$Ni(OH)_2$ with the assistance of urea.[274] The ultrasound radiation assisted synthesis of α-$Ni(OH)_2$ has been demonstrated with the presence of urea.[275] α-$Ni(OH)_2$ microspheres have been prepared by a solvothermal method using triethylene glycol and water as the solvents with the assistance of urea.[276] Chemical precipitation in the presence of sodium dodecyl benzene sulfonate and urea has been employed to prepare flower-like α-$Ni(OH)_2$.[277] The solvothermal method has been developed for the synthesis of α-$Ni(OH)_2$ hollow spheres with the assistance of oleylamine.[270] It is intellectually interesting and technically challenging to develop new methods for the facile preparation of α-$Ni(OH)_2$ under mild conditions. Particularly, it will be interesting to prepare α-$Ni(OH)_2$ nanostructure arrays directly on various substrates for applications.

One may find inspiration from the sophisticated biological systems to develop a facile method for the synthesis of α-$Ni(OH)_2$ nanostructures on substrates under mild conditions. Bio-inspired synthesis of functional materials has attracted much attention recently.[278] For example, eggshells are formed by a unique strategy: the carbonate ions from the metabolism of embryos could pass through the semipermeable eggshell membrane and react with calcium ions forming calcium carbonate based shells on the external surfaces of eggshell membranes.[244-245] The strong shell can protect the embryo from external infection, and also controls the passage of air in and out of the egg through the unique structures. It will be interesting to learn from this sophisticated strategy of eggshell membrane assisted synthesis and develop artificial membrane assisted synthesis of functional materials, including α-$Ni(OH)_2$. We understand that α-$Ni(OH)_2$ is metastable in alkaline solution. Therefore, it would be interesting to explore whether a semipermeable membrane could be selected to control the amount of OH^- anions in the solution to such a right level so that α-$Ni(OH)_2$ can be formed by the reaction between a common Ni^{2+} salt (e.g., $NiCl_2$) and a simple alkaline solution (e.g., NaOH).

Herein, we demonstrate an eggshell-inspired synthesis of α-$Ni(OH)_2$ nanobristles on various substrates with the assistance of a semipermeable Nafion membrane in two reaction chambers containing Ni^{2+} cations (from $NiCl_2$) and OH^- anions (from NaOH), separately. The selection of the Nafion membrane to mimic an eggshell membrane is based on our understanding that Nafion allows hydroxide ions (comparable to carbonate anions in the egg system) to be transferred.[254]13 The hydroxide ions will be controlled by the Nafion membrane with a low concentration in the opposite chamber and react with Ni^{2+} ions (comparable to calcium cations in the egg system) forming α-$Ni(OH)_2$. With the right reaction environment, α-$Ni(OH)_2$ nanostructures can form on various substrates, including glass, ITO glass and nickel foam, which can find interesting applications in superhydrophobic and superoleophobic surfaces, electrochromic devices, as well as supercapacitors.

7.2 Experimental Section

Materials Synthesis. Nickel(II) chloride hexahydrate ($NiCl_2 \cdot 6H_2O$), sodium hydroxide (NaOH) and cetyltrimethylammonium bromide (CTAB) were used as received from Sigma, USA. A piece of Nafion N117 membrane (DuPont, USA) was immersed in deionized water overnight to totally wet it before use. Typically, a water solution containing NiCl2·$6H_2O$ (1 M) and CTAB (5 mM) and a water solution of NaOH (1 M) were separately filled into two chambers separated by a piece of Nafion diaphragm (Figure 7.1). The basic experimental setup was very simple, using two glass chambers, a piece of Nafion membrane, sealed with O-rings, and fixed by two clamps. To form α-$Ni(OH)_2$ on Ni foams, a piece of cleaned Ni foam was placed in the $NiCl_2$ solution chamber for the formation of α-$Ni(OH)_2$ nanostructures on Ni foam. Various other substrates were inserted inside the chamber for growth of α-$Ni(OH)_2$ nanostructures on their surface, including glass, ITO glass, silicon wafer, copper foil and PET plastic. The reaction chambers were maintained at 50 °C for various periods of time. The α-$Ni(OH)_2$ nanostructures were observed to form only in the Ni^{2+} solution chamber and no solid

formed in the NaOH solution chamber. The substrates coated with α-$Ni(OH)_2$ nanostructures were washed with water and dried in a vacuum oven overnight.

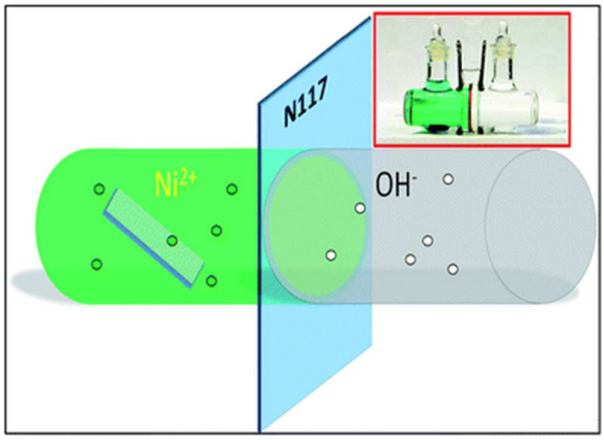

Figure 7.1. Schematic of the experimental setup with a pair of chambers separated by a Nafion membrane. A piece of substrate is inserted into one chamber to form nanostructures directly on the substrate. The inset is the optical image of the experimental setup.

Materials Characterization. The chemical composition and morphology of the as-obtained α-$Ni(OH)_2$ nanostructures were thoroughly characterized by XRD, SEM, TEM and SAED according to the previous procedure.[278] Two kinds of wettability tests were carried out, namely, the superoleophobic test in water and the superhydrophobic test in air. For the superoleophobic test, the underwater oil contact angle was measured. Typically, 1,2-dichloroethane ($C_2H_4Cl_2$) dyed with Oil Red O was selected as the model oil due to the fact that it has a high density of 1.25 g mL^{-1}. A 5 μL oil droplet was directly dropped on α-$Ni(OH)_2$ nanostructures coated glass underwater. The optical image of the bead-like oil droplets was taken by a camera with a micro lens (Nikon 85 mm f/3.5 G), and the static oil contact angle was measured by an image processing software.[278] For the superhydrophobic test, the water contact angle in air was measured. Typically, the α-$Ni(OH)_2$ nanostructures directly formed on a piece of glass were first treated by physical vapor deposition via exposure to the vapor of heated silicone oil to change the surface property of α-$Ni(OH)_2$ nanostructures from

hydrophilic to hydrophobic. A 5 μL water droplet was directly dropped on the treated α-$Ni(OH)_2$ nanostructure coated glass in air. The water contact angle was analyzed similarly.

Electrochemical Analysis. Electrochemical properties were characterized with a typical three-electrode setup, using α-$Ni(OH)_2$ formed on Ni foam as the working electrode, a platinum wire as the counter electrode, and a Ag/AgCl reference electrode in a 1 M KOH aqueous solution. Cyclic voltammetry (CV) and galvanostatic charge/discharge cycling were carried out on a CHI660D electrochemical workstation at a potential between 0 - 0.5 V and 0 - 0.45 V, respectively.

7.3 Results and Discussion

The successful formation of α-$Ni(OH)_2$ by diaphragm-assisted synthesis was confirmed by XRD (Figure 7.2). The results demonstrate that nickel hydroxide exists as α-$Ni(OH)_2 \cdot H_2O$ (JCPDS # 22-0444).[279-280] The XRD peaks can be assigned to diffraction from (001), (002), (110), (111), (104) and (300) planes of α-$Ni(OH)_2$. The slight shift in the positions could be attributed to the differences in species intercalated.[198, 281-284] No β-$Ni(OH)_2$ was detected by XRD.[285] The broad peaks suggest that the as-prepared α-$Ni(OH)_2$ is in the nanoscale. The as-obtained α-$Ni(OH)_2$ has a rhombohedral P3 structure.[286] The positively charged $Ni(OH)_{2-x}$ layers might be intercalated with Cl^- to achieve charge neutralization and structure stability as well as with H_2O.[287-289] The presence of intercalated Cl^- in the as-derived α-$Ni(OH)_2$ was confirmed by EDS result in Figure 7.2c. The absence of β-$Ni(OH)_2$ indicates that the as-prepared α-$Ni(OH)_2$ is highly phase-pure. TEM analysis shows that the nanoscale α-$Ni(OH)_2$ is in the form of 1-D nanobristles (Figure 7.2b and 7.2c). The SAED further confirms the phase-pure nature of nanobristles with the diffraction spots/rings assigned to α-$Ni(OH)_2$. The TEM analysis also reveals that the cross section of the nanobristles is not circular, which could be attributed to the layered nature of $Ni(OH)_2$.

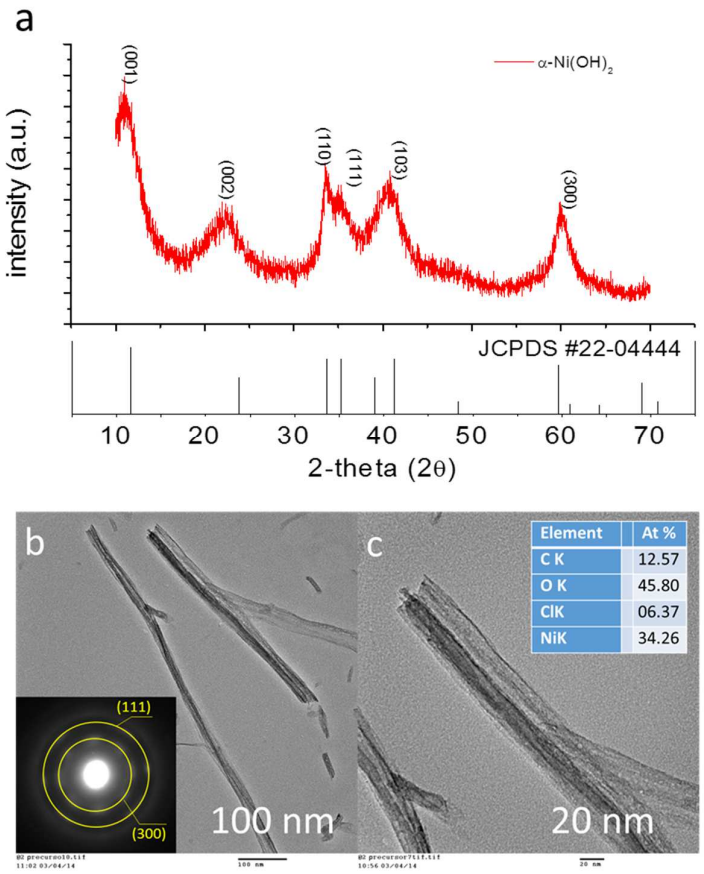

Figure 7.2. (a) XRD patterns of the as-synthesized α-Ni(OH)$_2$; TEM images of nanobristles: (b) low-magnification view of few α-Ni(OH)$_2$ nanobristles; the inset shows the SAED pattern; (c) high-magnification view of the tip of a nanobristle.

The membrane-assisted synthesis can grow α-Ni(OH)$_2$ nanobristles on various surfaces, including on the surfaces of glass (Figure 7.3a), as well as Ni foam, ITO glass, copper foil, silicon wafer and PET plastic. The optical image of the glass coated with α-Ni(OH)$_2$ nanobristles shows that it is translucent and light green (Figure 7.3a), in contrast to the transparent and clear glass substrate without any coating (Figure 7.3b). The uniform color also suggests that the α-Ni(OH)$_2$ nanostructures are evenly distributed on the glass, indicating that the coating is highly efficient. The low-magnification FESEM image clearly revealed that the α-Ni(OH)$_2$ nanobristles, in the form of a porous network, extensively covered the surface of the glass (Figure 7.3c). The zoom-in view reveals that the α-Ni(OH)$_2$ network is formed by aggregated nanobristle arrays on the surface (Figure 7.3d). The pores have diameters about few

micrometers which are formed by the tips of nanobristles self-assembled into circles. It is interesting to note that most of the circular pores are formed by left-hand curled nanobristles, as highlighted by two red circles in Figure 7.3d. Artificial coiled mesostructures built from nanoscale bristles are rarely reported.[290] The detailed arrangement of the α-$Ni(OH)_2$ nanobristles is more clearly revealed by the high-magnification view of a typical pore (Figure 7.3e). It shows that the self-assembly mainly occurred at the tips of nanobristles, and the other end of nanobristles attached on the flat glass substrate are not twisted into circles. A typical bundle of joined tips that has not yet formed into a full circle is shown in Figure 7.3f, which is also left-hand curled. Coiled, spiral and twisting configurations are commonly observed in nature, including shells of snails and galaxies. One of the possible reasons for those nanobristle tips to join into bundles is that the $Ni(OH)_{2-x}$ layers in the nanobristles are positively charged, which can attract the negatively charged anions attached on the surface of neighboring nanobristles. Van der Waals force may also contribute to the formation of the bundles from the aggregated tips of nanobristles, especially in the case of nanobristles with non-cylindrical shapes. The bended nanobristles also suggest that they have very good mechanical flexibility. It is still not clear why the curling nanobristles are left-handed, which will require further studies.

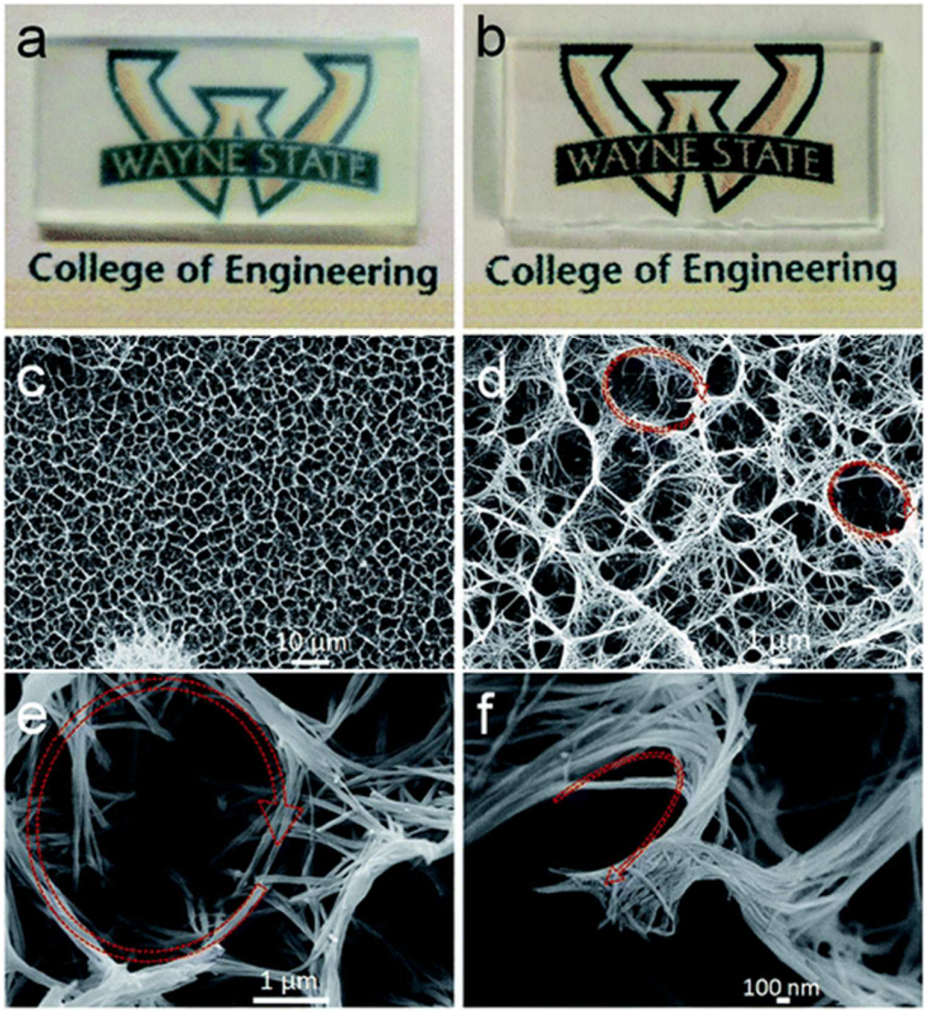

Figure 7.3. Optical images of (a) a piece of glass slide coated with α-$Ni(OH)_2$ nanobristle arrays in comparison with (b) a bare glass slide without any coating. The FESEM images reveal the microstructures of α-$Ni(OH)_2$ nanobristle arrays formed on the surface of glass: (c) low-magnification overall view showing its extensive coverage; (d) zoom-in view showing the nanobristle arrays aggregated forming a network; the red circles highlight the holes formed by self-assembled nanobristles; (e) zoom-in view of the "hole" formed by self-assembled nanobristle arrays; (f) zoom-in view of the "tip" formed by aggregated and self-assembled nanobristle arrays left-hand curled. Time of reaction: 3 days.

A plausible mechanism is proposed to explain the formation of α-$Ni(OH)_2$ nanobristles. Although Nafion is known for cation exchange,[279] anions can be transported under high concentration conditions.[291-292] Therefore, OH^- could diffuse via the membrane into the other chamber to meet and react with Ni^{2+} cations. The pH value in the Ni^{2+} chamber was monitored and was around 8 through the reaction process, which provides the right alkalescence

conditions (pH is between 7 and 10) for forming α-$Ni(OH)_2$, instead of β-$Ni(OH)_2$. Our system offers a unique way to maintain a right alkalescence environment under mild conditions, in contrast to that of using chemicals, such as urea and HMT.[287, 293] It is possible to synthesize α-$Ni(OH)_2$ under mild conditions via diaphragm regulation. At the same time, CTAB introduced as the cationic surfactant could control the morphology of the α-$Ni(OH)_2$ formed by selectively decreasing the surface energy of crystal planes[294-297] The 1-D nanobristle arrays could self-assemble into high-order mesostructures on the glass, forming an extremely rough surface. Double roughness with structures at both nano- and micro-scales was achieved. The double-rough surface can demonstrate interesting wettability caused by surface roughness, which is commonly observed in nature. For example, the lotus leaf surface has double roughness with nanohairs on microbumps and demonstrates superhydrophobicity. The lotus leaf surface has a water contact angle of more than 150° and can demonstrate self-cleaning capability due to surface roughness. Many efforts have been devoted to artificial double-rough and superhydrophobic surfaces. In another example, fish scales demonstrate underwater superoleophobicity which could provide protection towards pollutants and toxins in water.[246] An artificial surface with super-hydro/super-oleo phobic nature can find many important applications, including antifouling coating, pollutants and toxins prevention, and oil spill recovery. Here, we also try to preliminarily explore wettability of the obtained double-rough α-$Ni(OH)_2$ nanobristle covered rough glass surface. The hydrophilic terminal surface groups of α-$Ni(OH)_2$ nanobristles were easily converted into hydrophobic surface terminals by a simple physical vapor deposition procedure using heated silicone oil.[298] The presence of double-rough nano- and micro-structures and hydrophobic surfaces with alkylsiloxane coating lead to superhydrophobic surfaces at the macroscale on the α-$Ni(OH)_2$ nanobristle covered glass. The water contact angle measured is 156° in air (Figure 7.4a), indicating its superhydrophobic nature. Similarly, the as-synthesized α-$Ni(OH)_2$nanobristle covered glass

without any treatment demonstrated superoleophobicity in the water medium (Figure 7.4b). The oil droplet selected was 1,2-dichloroethane for its density is higher than that of water. The oil droplet was dyed with Oil Red O for enhanced visibility in water. The static oil contact angle measured is 161°, indicating that the surface is underwater superoleophobic. The interesting surface wettability demonstrated here suggest that the as-synthesized α-$Ni(OH)_2$ nanobristles as well as their derivatives formed on substrates may find many potential applications, including protection from pollutants and toxins, oil/water separation, and microscale liquid transfer[136, 263-265].

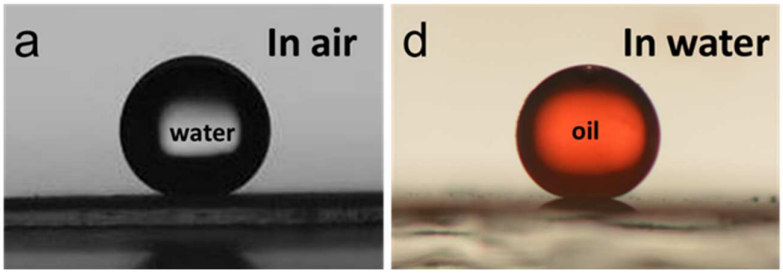

Figure 7.4. Optical images of (a) a water droplet in air and (b) an oil droplet (1,2-dichloroethane dyed with Oil Red O, 5 μL) in water sitting on a double-rough α-$Ni(OH)_2$ nanobristle covered glass. The nanobristles on glass in (a) were coated with silicone by physical vapor deposition and in (b) were synthesized without any post-synthesis treatment.

The observed superhydrophobic and superoleophobic properties can be explained by the Cassie–Baxter model, according to the following equation[54, 299]

$$\cos \theta_{L^*} = r_f f \cos \theta_L + f - 1$$

where r_f is the roughness ratio of the droplet wet area; f is the fraction of the projected area of the solid surface that is wet by the liquid of the droplet; θ_L and θ_{L^*} are the contact angles of the liquid droplet sitting on a smooth and rough surface, respectively. The environmental medium could be air in the case of a water droplet and water in the case of an oil droplet. In air, the micro- and nano-scale space and voids induced by the double-rough micro/nanostructures underneath the water droplet could be occupied by air. It could be attributed to the hydrophobic nature of the silicone coated α-$Ni(OH)_2$ nanobristles which prevents the water with high surface

tension to enter those microvoids. It is known that a smooth silicone surface has a contact angle of about 107° (or $\theta_L = 107°$).[300] Assuming that the roughness ratio of the water wet area is close to 1, the experimentally measured water contact angle $\theta_{L*} = 156°$. It is estimated that the fraction of the projected area of the solid surface that is wet by the water or f is about 0.1. In contrast, in the case of the underwater test, the space and voids between the double-rough micro/nanostructures underneath the oil droplet could be occupied by water instead. In this case, the bare α-$Ni(OH)_2$ nanobristles were hydrophilic which could be totally wetted by water and the microvoids could be filled by water due to capillary effects. Consequently, the oil droplet was essentially sitting on a film of water and the fraction of solid nanobristles wet by the oil droplet is small, achieving underwater superoleophobicity.

In another proof-of-concept demonstration, a piece of Ni foam was placed in the $NiCl_2$ solution chamber for the formation of α-$Ni(OH)_2$ nanobristles directly on Ni foam (Figure 7.5). The α-$Ni(OH)_2$ nanobristles formed on Ni foam can be used as electrodes for supercapacitors. As compared to the bare Ni foam with a metallic color with reflection spots (inset of Figure 7.5a), the α-$Ni(OH)_2$ nanobristle coated Ni foam is gray (inset of Figure 7.5c). The absence of any observable reflection spots in the coated Ni foam suggests that the Ni foam was thoroughly covered with α-$Ni(OH)_2$ nanobristles. The $Ni(OH)_2$ coating was stable even after it was treated by ultrasonic cleaning. The Ni foam with a 3-D network is commonly employed as the support for electrochemical evaluation (Figure 7.5a and 7.5b). The 3-D Ni foam could allow a large area to be exposed to the reactants for the formation of α-$Ni(OH)_2$ nanobristles on the surface of 3-D Ni foam. The FESEM image clearly reveals the uniform coating of α-$Ni(OH)_2$ nanobristles on the 3-D network (Figure 7.5c). The zoom-in view shows that the nanobristles aggregated at the tips and formed a network of nanowires (Figure 7.5d), similar to those observed on glass (Figure 7.3c). The 3-D network of metallic Ni frames can function as the current collector and the α-$Ni(OH)_2$ nanobristles formed on the

surface as active materials with a large area exposed to the electrolyte. Therefore, the as-coated Ni foam can be used as binder-free electrodes ready for use after material preparation for supercapacitors.

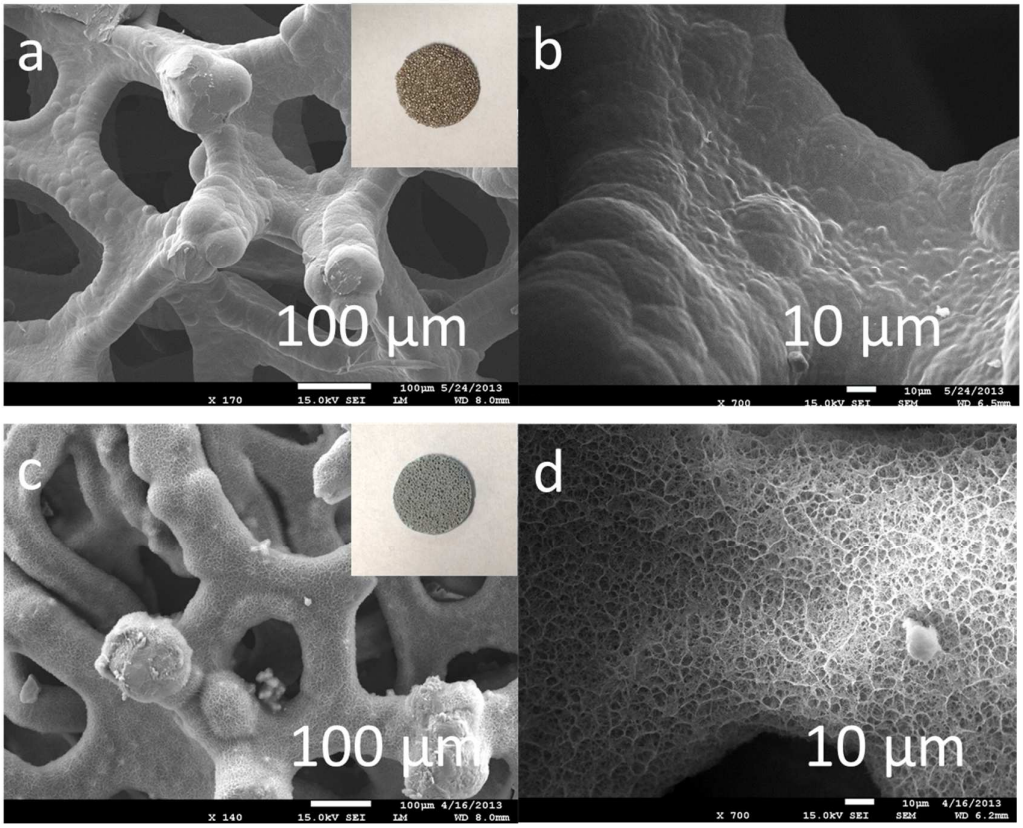

Figure 7.5. Optical and FESEM images to reveal the successful coating of α-$Ni(OH)_2$ nanobristle arrays on the surface of nickel foam: (a) low-magnification overall and (b) zoom-in view of bare Ni foam without any coating; (c) low-magnification overall and (b) zoom-in view Ni foam coated with α-$Ni(OH)_2$ nanobristle arrays showing the uniform and extensive coverage by α-$Ni(OH)_2$ nanobristles achieved. The insets in (a) and (c) are the optical images of bare and α-$Ni(OH)_2$ nanobristle covered Ni foam, respectively.

The as-synthesized electrodes were electrochemically evaluated. In conventional electrode preparation, the active materials are mixed with the binder and conducting agent to make a slurry which is then cast on Ni foam and dried.[301-302] In contrast, our electrode is free of those complicated procedures and additives. The α-$Ni(OH)_2$ nanobristles were formed directly on Ni foam as the active materials , forming a binder-free and integrated electrode. The cyclic voltammetry (CV) profiles obtained at different scanning rates show a pair of redox

peaks (Figure 7.6a), which is typically associated with $Ni(OH)_2$. The reversible electrochemical reactions involved could be:[272, 276, 303-304]

$$\alpha\text{-}Ni(OH)_2 + OH^- \longleftrightarrow \gamma\text{-}NiOOH + H_2O + e^-$$

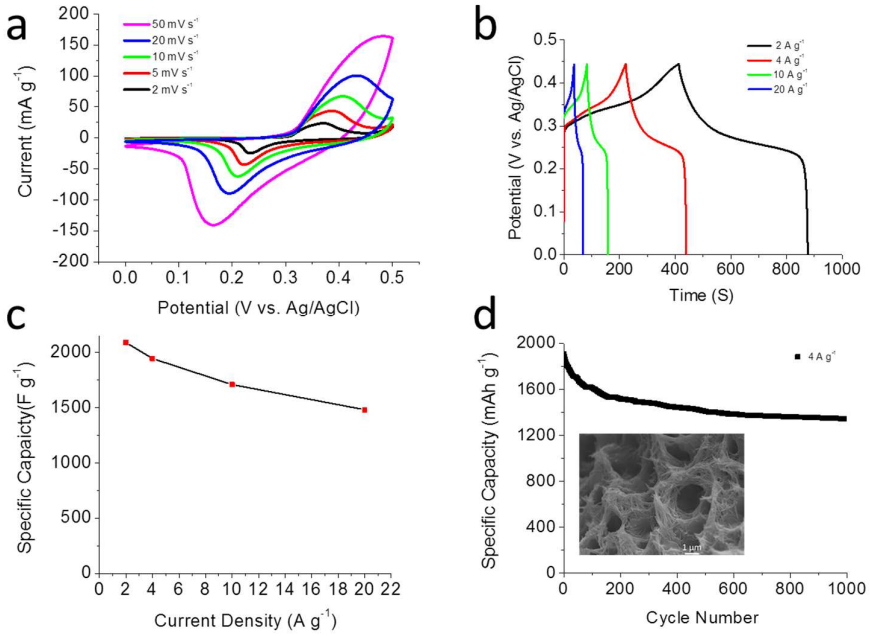

Figure 7.6. Electrochemical characterization of $Ni(OH)_2$ nanobristles formed on Ni foam as binder-free electrodes: (a) CV curves at various scan rates (from 2 to 50 mV s^{-1}); (b) galvanostatic charge and discharge profiles at different currents; (c) capacitances achieved at different testing currents; (d) cycling performance over 1000 cycles at a testing current of 4 A g^{-1}. The inset of (d) shows FESEM image of the surface of α-$Ni(OH)_2$ electrodes after 1000 cycles of electrochemical test as an electrode for supercapacitors.

The overall shapes of CV curves obtained at different scan rates (from 2 to 50 mV s^{-1}) show similar profiles, indicating that the integrated electrodes with 3-D nanobristles formed on the surface could improve electrochemical mass and electron transfer. Close examination shows that, with increasing rates, the current increased and the oxidation peaks shifted in the more positive direction while reduction peaks shifted to a more negative direction. This could be explained by the internal diffusion resistance increases within the active materials under high scan rates.4 Figure 7.6b shows the representative cycles of charge–discharge curves, which suggest relatively good cycle stability. The gravimetric capacitance based on the mass

of the active materials could be estimated (Figure 7.6c). The capacitances of the electrodes were calculated based on $C = I \times \Delta t/\Delta V$, where I is the constant discharge current; Δt is the discharging time; ΔV is the voltage window for galvanostatic measurements. The Ni foam coated with α-$Ni(OH)_2$ nanobristles could achieve a high capacitance of 2090, 1945, 1750 and 1481 F g^{-1} at various discharge currents of 2, 4, 10 and 20 A g^{-1}, respectively, indicating good rate performance. The theoretical specific capacitance of $Ni(OH)_2$ was estimated to be 2082 F g^{-1}.[305] The good electrochemical stability was demonstrated by cycling the electrodes over 1000 cycles at a current of 4 A g^{-1} (Figure 7.6d). The morphology of nanobristles was well maintained after cycling (Inset in Figure 7.6d). We believe that additional optimization can further improve performances.

7.4 Conclusion

In summary, we have demonstrated a facile bio-inspired method to prepare α-$Ni(OH)_2$ nanobristles on various substrates. The 3-D network of nanobristles formed on a glass substrate offers a double-rough surface, which demonstrated interesting roughness induced superhydrophobicity in air and superoleophobicity underwater. The as-prepared α-$Ni(OH)_2$ nanobristles formed on Ni foam could be used as integrated and binder-free electrodes directly. They demonstrated good electrochemical performances, and could be cycled for at least 1000 cycles. The α-$Ni(OH)_2$nanobristles formed on various substrates can also be used as precursors for making other functional materials, including metallic Ni and NiO based nanobristles. We believe that the methods and ideas outlined here can be used for the fabrication of various kinds of functional materials under mild conditions.

CHAPTER 8 BIO-INSPIRED SYNTHESIS OF ALPHA NICKEL-COBALT LAYERED DOUBLE HYDROXIDES AT ROOM TEMPERATURE AND APPLICATIONS

8.1 Introduction

Double layered hydroxides (LDHs) are a family of hydroxides with defined layered structures. They consist of positively charged brucite-like host layers and charge-balancing anions in the interlayers.[306] Among them, transitionmetal hydroxides such as $Ni(OH)_2$ and $Co(OH)_2$ are intensively studied.[307-309] Due to the rapid development of nanotechnology, nanostructured hydroxides have been widely reported as supercapacitors,[310-311] catalysts,[312-313] absorbers,[282, 314] magnetic materials[315] and functional coatings for superhydrophobic applications.[316-317] In energy storage field, especially for electrochemical supercapacitors, nanostructured $Ni(OH)_2$ is being taken as a promising candidate due to its high theoretical capacity (2358 F g^{-1}) and low cost compared with RuO_2.[318] However, the performance of $Ni(OH)_2$ is still unsatisfactory due to the low conductivity ($\sim 10^{-5}$ to 10^{-9} s cm^{-1})[319] and conventional procedure of preparing electrodes with additives.[320]

To enhance the performance of $Ni(OH)_2$, cobalt used to be introduced in its structure. There are several advantages by building nanostructured nickel-cobalt hydroxides (NCH): 1. It improves the electrical conductivity and raise the oxygen overpotential;[321-322] 2. The favorable interlayer spacing supports more redox reactions involved;[307] 3. Other interesting applications of NCH could be applied.[323-324] By now, the conventional methods of preparing nanostructured NCH is limited. There are four main routes: Hydrothermal methods,[325] electrodeposition,[326] sol-gel methods,[327] and chemical bath deposition.[328] However, each strategy has some inherent drawbacks. For hydrothermal methods, they require high pressure, high temperature and suffer from unobservable process during reaction. Extra hydrolysis agents such as urea and Hexamethylenetetramine (HMT) are necessary for initiating reaction.[325] CBD methods are also based on these hydrolysis agents, requiring an elevated

temperature.[328] For electrodeposition, special expensive devices such as an electrochemical workstation and conductive substrates have to be used.[329] For sol-gel methods, it is difficult to control precipitation, especially deposition on specific substrates. OH^- providers such as amonia have to be added in manually. To find better methods to prepare NCH nanostructure is still challenging, especially for the affordable large-scale production.

In this study, we demonstrate an improved controllable diffusion strategy to fabricate α-NCH on variable substrates. The whole reaction can be carried out at room temperature without any hydrolysis agents in simple salt metal solution. By controlling the diffusion of OH^- ions via cation exchange membrane, typical nucleation and growth process of α-NCH occurred on different substrates. Within 2 days, self-assembled nanosheets α-NCH were successfully formed on them. After deposition of nanostructured α-NCH, Ni foam could be used as a promising binder-free electrode for electrochemical supercapacitors. It delivered stable specific capacitance at different current densities, ranging from 4 to 20 A g^{-1} during 3000 cycles. After deposition on glass, superhydrophobicity in air (after silicone oil pretreatment) and superhydroleophobicity underwater were easily achieved. The ratio of Ni and Co, the structures of nanocomposites can be artificially regulated. Due to this powerful bottom-up coating ability and highly controllable synthesis, this facile strategy could be used to achieve various potential applications of α-NCH and its derived materials. It provides a proof of concept to prepare nanostructured coating in simple solution easily and economically for potential manufacture.

8.2 Experimental Section

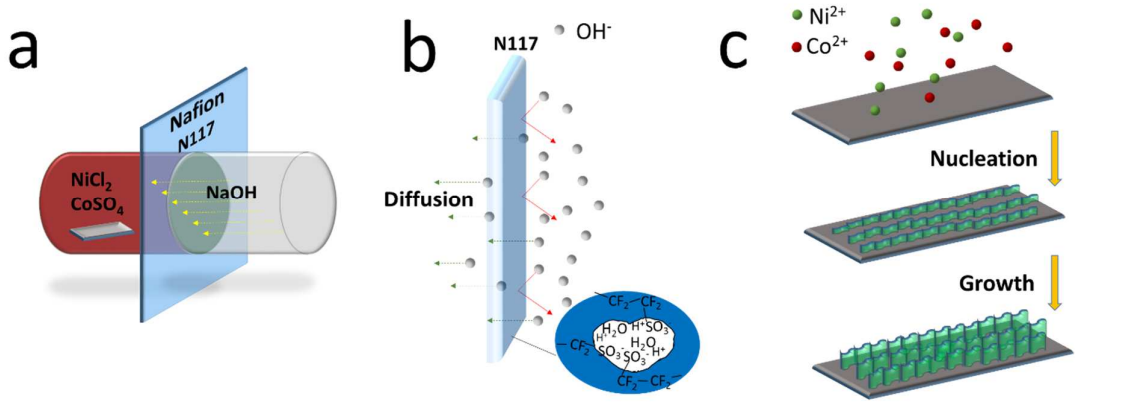

Figure 8.1. (a) Schematic of an installed side-by-side reactor, (b) controllable movement of OH^- ions in reaction, (c) typical procedure of growing α-NCH on substrates.

Materials Synthesis. Nickel chloride hexahydrate ($NiCl_2 \cdot 6H_2O$) and Cobalt sulfate heptahydrate ($CoSO_4 \cdot 7H_2O$), sodium hydroxide (NaOH) and cetyl trimethylammonium bromide (CTAB) were used as received from Sigma-Aldrich without purification. Cation exchange membrane (Nafion N117) was purchased from Ion Power, Inc. Nafion N117 was hydrated in water overnight before use. Typically, 0.25 M $NiCl_2 \cdot 6H_2O$, 0.5 M $CoSO_4 \cdot 7H_2O$, and 2 mM CTAB were dissolved together in DI water to prepare Ni-Co solution. Another 1 M NaOH solution was prepared at the same time. To deposit α-NCH nanosheets on Ni foam, several pieces of Ni foam were cleaned by acetone, 2.5 M HCl, and DI water, alternatively. These pieces of Ni foam were inserted as-setup side-by-side reactors. Different reaction periods, ranging from 1 day to 4 days, were chosen to study the effect of reaction time. A typical side-by-side reactor is shown in Figure 8.1a. Both of as-prepared solutions were slowly injected into two chambers of a side-by-side reactor separated by Nafion N117 membrane. Similarly, various other substrates (glass, Ti mesh and carbon fiber paper) were also used for deposition of α-NCH nanostructures. The reactors were kept at room temperature for various reaction periods. The α-NCH coatings were only found in the chamber of Ni-Co solution. No any change was observed in NaOH solution. The substrates coated with α-NCH were totally cleaned by DI water for several times and dried in a vacuum oven overnight.

The mechanism of formation of α-NCH based on two critical conditions found in our previous study.[330] One is the special feature of Nafion N117 membrane. Nafion N117 can limit the movement of ions. Under high concentration, OH^- can slowly diffuse via it. The other condition is the controllable self-assembly based classic nucleation and growth theory. With the controllable transportation of OH^- ions towards Ni-Co solution, pH could be elevated to achieve supersaturation status. The heterogeneous nucleation and following growth are able to initiate to assemble nanosheets on soaked substrates. CTAB, as a surfactant, in further control the reaction conditions of it.[325] The schematic process is shown in Figure 8.1b and Figure 8.1c.

Materials Characterization. Materials characterization: X-ray diffraction analysis of the samples was carried out under Rigaku X-ray diffractometer (XRD) with Cu Kα radiation. Transmission electron microscopy (JEOL-2010 TEM instrument, operating at 200 kV) was used to determine more details about their structures and compositions. The as-deposited NCH were coated with gold and examined by a field-emission scanning electron microscopy (FESEM/EDX JEOL-7600, operating at 15 kV).

Electrochemical Analysis. As-deposited Ni foam was used as binder-free electrode directly. Electrochemical properties for supercapacitors were characterized with a three-electrode cell, which consisted of the α-NCH working electrode, Pt mesh counter electrode, and Ag/AgCl reference electrode in 1 M KOH aqueous solution. Cyclic voltammetry (CV) and galvanostatic charge-discharge (GCD) cycling of the α-NCH electrode were tested by a CHI660D electrochemical workstation at 0.1 - 0.5 V and 0 - 0.45 V, respectively. Variable current densities between 2 to 20 A g^{-1} were applied. The specific capacitance of the electrodes was calculated according to the equation of $C = I \times \Delta t / \Delta V$, where I is the constant discharge current, Δt is the discharging time and ΔV is the voltage window for the galvanostatic measurement. The loading mass of α-NCH was ~0.63 mg/cm^2.

Wettability measurement: Two kinds of wettability (hydrophobicity and hydroleophobicty) measurements were applied. For hydrophobicity measurement, water contact angle in air was recorded. Typically, the α-NCH coated glass was pretreated by the facile physical vapor of heated silicone oil to switch the hydrophilic surface to hydrophobic one.[298] A water droplet (5 μl) was dropped on the surface of the pretreated glass in air. For hydroleophobicity measurement, oil contact angle in water was recorded. Typically, 1, 2-dichloroethane ($C_2H_4Cl_2$) dyed with Oil Red O was chosen as the model oil due to its relatively high density (1.25 g/ml, larger than water density). A 5 μL oil droplet was directly dropped on the directly deposited glass. The optical images were captured by a professional digital camera with macro lens (85 mm, 1.35G). The contact angles were measured by Image J software with drop analysis plugins.

8.3 Results and Discussion

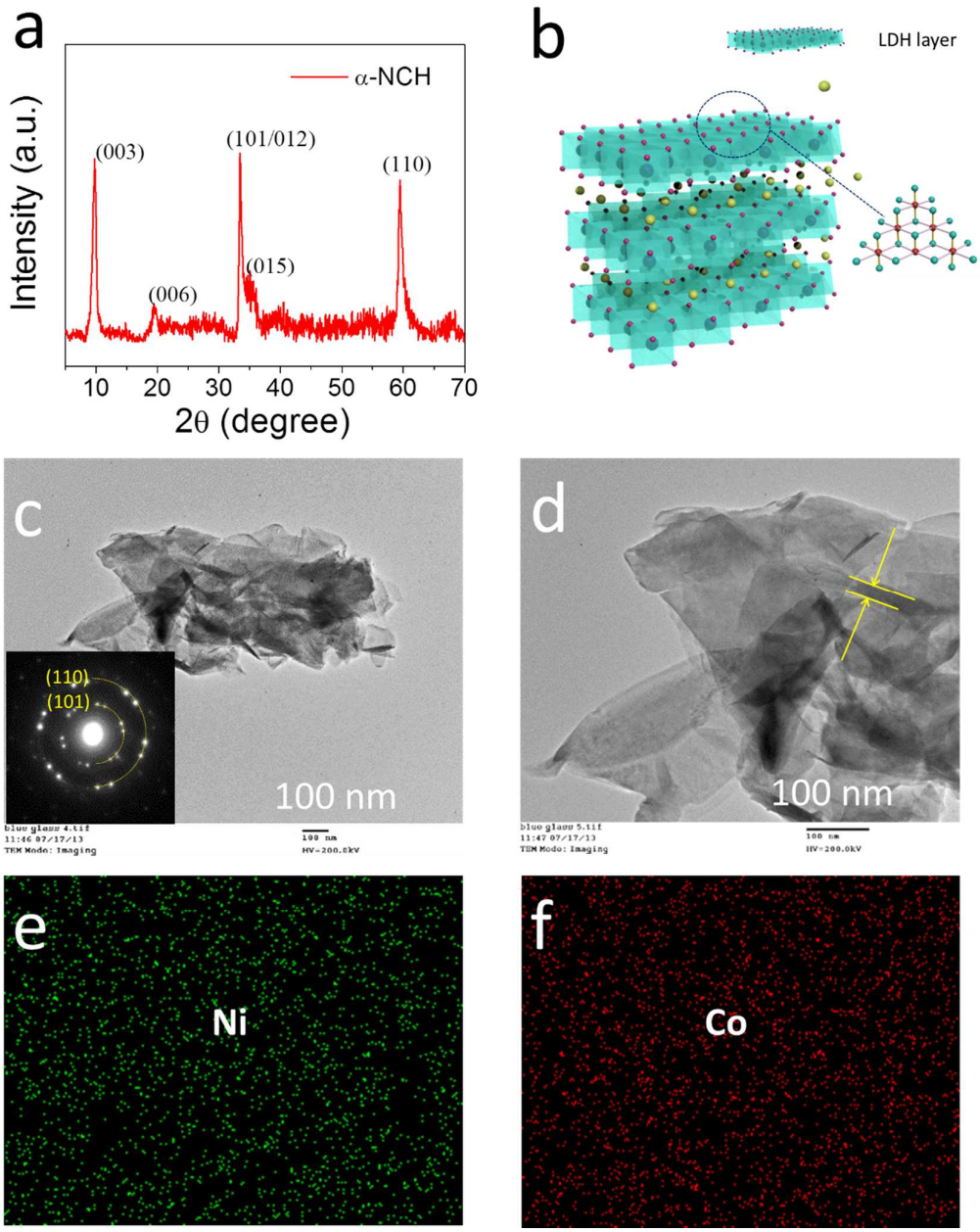

Figure 8.2. (a) XRD pattern of α-NCH collected from substrates, (b) illustrated 3D structure of LDH structures of α-NCH. (c, d) TEM images of collected α-NCH with different magnifications. EDS mapping of α-NCH on a piece of glass to demonstrate the distribution of Ni and Co elements in nanostructures. The inset of (c) is the indexed SAED pattern of α-NCH.

The crystal structure of as-deposited α-NCH coating was characterized by X-ray diffraction pattern. As shown in Figure 8.2a, distinct strong peaks of α-phase of NCH were detected. No peaks arising from β-phase impurities can be detected. The position of (003) peak

indicates the interlayer spacing of 9.08 Å. According to their changeable layered structures, there are two kinds of NCH, one is hydrotalcite-like α-NCH (usually, d(003) > 7 Å),[84, 328] the other is brucite-like β-NCH (usually, d(003) ≈ 4.6 Å).[331-332] They both are stacked by LDH layers as present in Figure 8.2b, which is ordered organized by edge-sharing Ni/CoO_6 octahedron but have distinguished interspacing.[331, 333] Here, as-prepared NCH has hydrotalcite-like structure, which contains a large amount of anions and/or water molecules between interlayers. For (003) peak, it is still symmetric, but with the increase of angle, the obvious asymmetry of peaks was noticed, which indicates that stacked layers are much loose and rich in defectives. This turbostratic phase observed in most of α phase hydroxides.[148] According to the previous study, this α phase structure has higher chemical activity than β-form.[334] Normally, mixed Ni-Co solution with NaOH cannot obtain any α phase structure. The sudden change of pH value is unfavorable to form unstable α-phase structure. Previously, only hydrolysis agents and electrochemical methods were applied to prepare α-NCH.[306, 325, 328, 335] To our best knowledge, this is the first time to use NaOH to fabricate directly α-NCH.

TEM images confirm the nanosheets structure of α-NCH. In Figure 8.2c, stacked nanosheets are observed, which is similar to graphene's 2D structures. These 2D nanosheets of α-NCH are hard to keep flat, the edges of them are partly curled. For the inset SAED pattern, its (110), (101) planes are indexed, which is consistent with those in XRD characterization. The interesting coupled dots are scarce, which indicates the special ordered organization of $Ni(OH)_2$ and $Co(OH)_2$ in our α-NCH. EDS mapping result confirms the uniform distribution of Ni and Co in Figure 8.2e-f. Under higher magnification (Figure 8.2d), the multiple layers of nanosheets are found as marked, the overall thickness is ~20 nm.

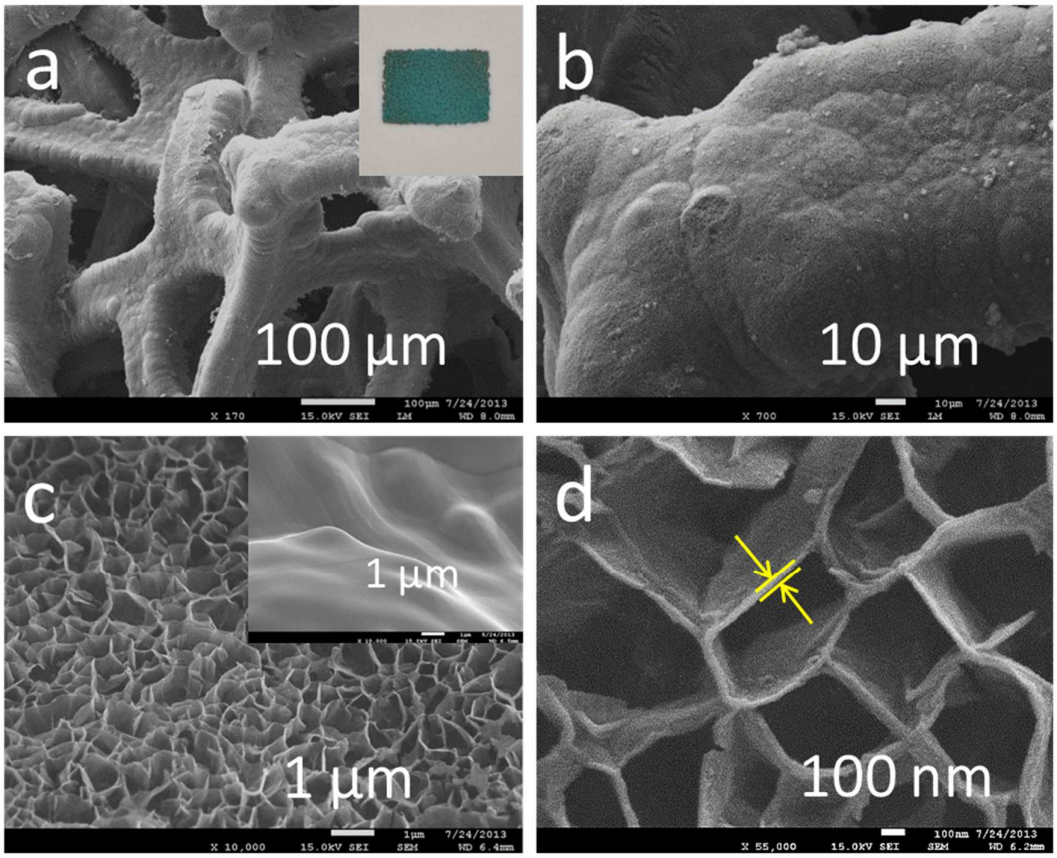

Figure 8.3. (a-d) FESEM images of as-deposited Ni foam after 2 days reaction. The insets of (a) and (c) are the corresponding optical image of as-deposited Ni foam and FESEM image of bared Ni foam, respectively.

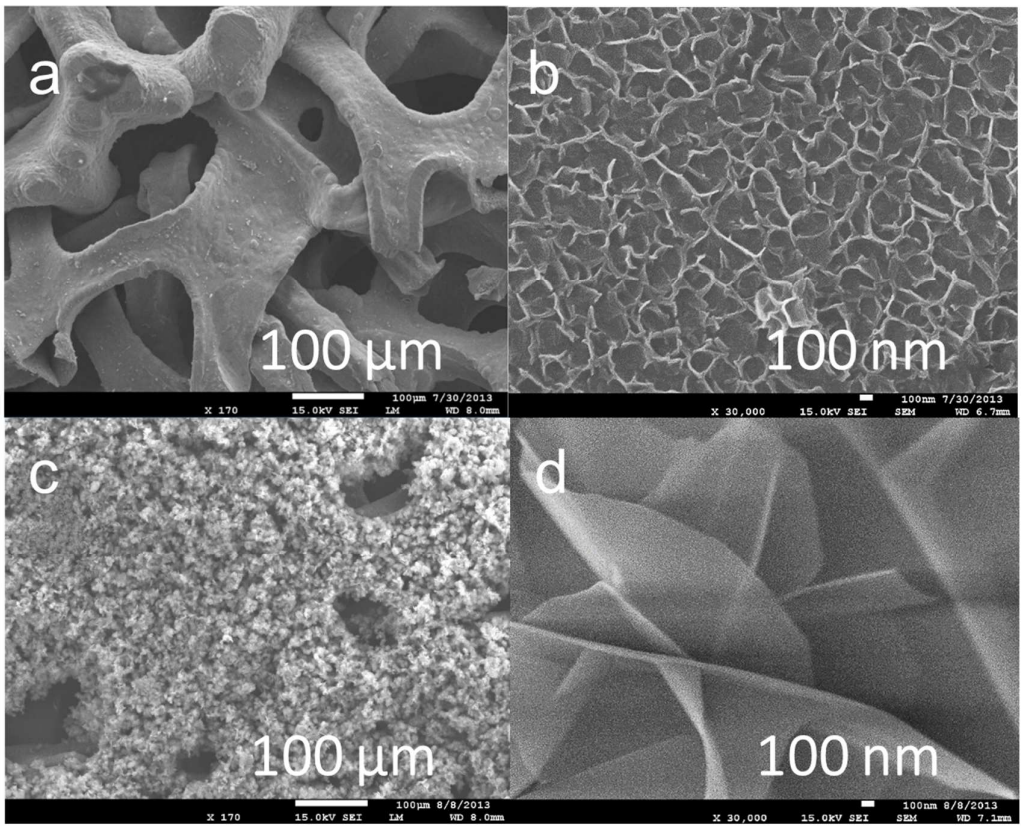

Figure 8.4. FESEM image of as-deposited Ni foam after different reaction periods: (a, b) 1 day, (c,d) 4 days

As shown in Figure 8.3a-3d, FESEM images reveal the morphology of as-deposited α-NCH on Ni foam. For Figure 8.3a, the overall 3D porous structure of Ni foam is clearly present. This kind of structure has been approved to enhance electrochemical performance of supercapacitors.[140, 336] No obvious co-precipitated nanostructures attached on the surface. The corresponding optical image of it shows the surface of Ni foam has been deposited by blue-green colored α-NCH. In Figure 8.3b, homogenous α-NCH has totally covered the surface of Ni foam, and massive tiny pores could be easily noticed. In zoom-in observation, the nanosheets α-NCH were self-assembled into honeycomb structure presented in Figure 8.3c, making the surface of Ni foam extremely rough. In contrast, bared Ni foam inset has no any special structures. Under higher magnification, the more details could be found. The “wall” of honeycomb is less than 30 nm, which is close to the nanosheets observed in TEM images. The

highly porous honeycomb structure with extremely thin "wall" is beneficial for providing a lot of active sites and fast diffusion paths of ions and electrons. The growth amount of α-NCH can be well controlled by the reaction time. Figure 8.4 shows the growth status of α-NCH within 1 day and 4 days, respectively. These different growth amounts also suggest the controllable loading mass on Ni foam.

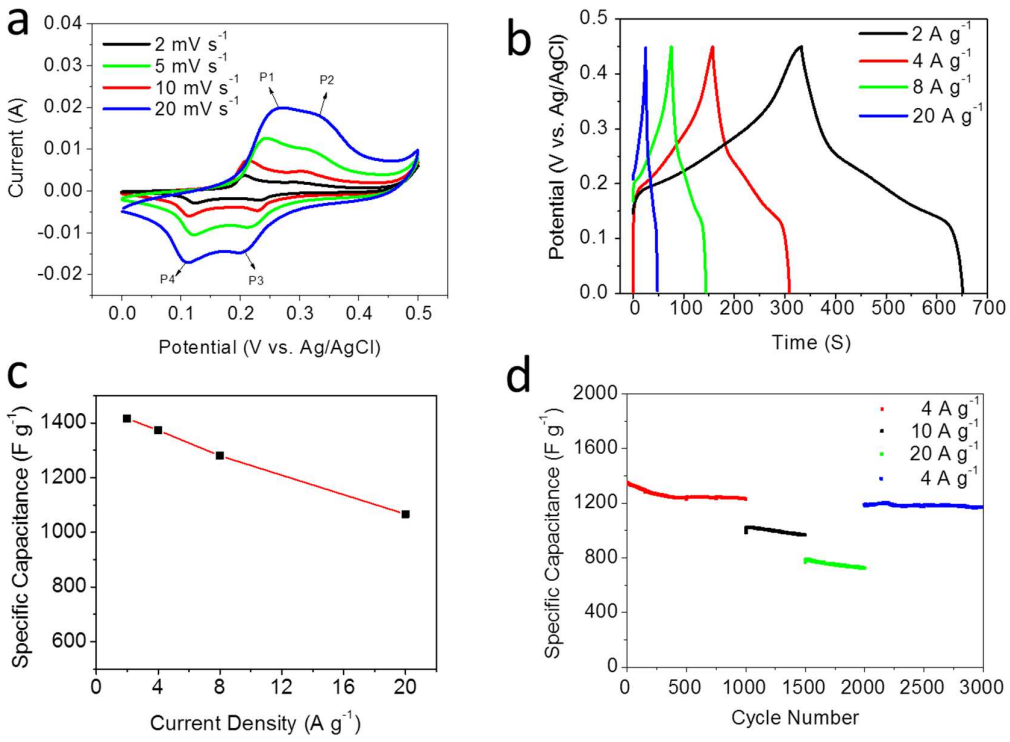

Figure 8.5. Electrochemical characterization of α-NCH electrodes: (a) CV curves of at various scan rates from 2 to 20 mV s^{-1}; (b) Galvanostatic charge and discharge curves at various current densities from 2 to 20 A g^{-1}; (c) Graph of charge-discharge current dependent specific capacitance at various current densities from 2 to 20 A g^{-1}; (d) Cycling performance at various current densities from 4 to 20 A g^{-1} within 3000 cycles.

The electrochemical properties of α-NCH were characterized in Figure 8.5. As-deposited Ni foam after 2 days was used directly as a binder-free electrode in a three-electrode configuration with 1 M KOH as the electrolyte. The CV curves under different scan rates are shown in Figure 8.5a. The reversible redox peaks marked were found, which suggests the stable

Faradaic reactions in electrodes, rather than common double layer supercapacitors with a rectangle shape. The primary reaction equations should follow the listed reactions below[337]

$$Ni(OH)_2 + OH^- \leftrightarrow NiOOH + H_2O + e^- \quad (1)$$

$$Co(OH)_2 + OH^- \leftrightarrow CoOOH + H_2O + e^- \quad (2)$$

$$CoOOH + OH^- \leftrightarrow CoO_2 + H_2O + e^- \quad (3)$$

The peaks slightly shift with the increase of scan rate. This phenomenon can be attributed to inevitable internal diffusion resistance of the electrodes.[338] Figure 8.5b demonstrates the galvanostatic charge-discharge profiles under different current densities ranging from 2 to 20 A g^{-1}. No distinct plateau region can be observed during the process, in consistence with reported NCH electrodes.[337, 339] The nearly symmetrical capacitance of charging and discharging curve replies the excellent reversibility.

In Figure 8.5c, the specific capacitances of α-NCH electrodes were calculated from discharge time based on the chronopotentiometry curves in Figure 8.5b. The binder-free electrode delivered as high as 1415.6, 1373.3, 1280.1 and 1066.7 F g^{-1} at current densities of 2, 4, 8 and 20 A g^{-1}, respectively. The specific capacitance gradually decreased with the increase of current densities, which could be attributed to the incremental voltage drop and insufficient active materials involved in redox reaction at higher current densities. However, even if the current density increased 10 folds, the capacitance was still 1066.7 F g^{-1} (75.4% of that at 2 A g^{-1}), which demonstrates the high performance of this α-NCH electrode. In previous studies, the binder-free design of electrodes supports the fast charge-discharge process.[335, 340-341]

In Figure 8.5d, the cycling performance of α-NCH electrodes under different current densities was evaluated. At the beginning, a current density of 4 A g^{-1} was applied. After a slight decrease of specific capacitance within the first 500 cycles, the electrodes kept stable

without decay. Increasing the current density to 10 A g^{-1} and 20 A g^{-1}, both of them experiences a similar trend. For 10 A g^{-1}, the capacitance gradually decreases from 982.2 to 967.7 F g^{-1} within 500 cycles (98.4 % of initial capacitance remained). For 20 A g^{-1}, the capacitance also decreased slowly from 764.4 to 724.4 F g^{-1} within 500 cycles (94.8 % of initial capacitance remained). When the current density came back to 4 A g-1, extremely stable performance within 1000 cycles was achieved again. No noticeable decay was observed.

To verify the stability of nanosheets, the sample after 3000 cycles test was examined via FESEM. As shown in Figure 8.6a, the nanosheets still remained, only the thickness of them increased slightly from 25 nm to 40 nm. The excellent electrochemical performance of α-NCH electrodes can be attributed to several advantages in this electrode. Unique porous nanostructures in-situ grown on 3D porous current collector possess extremely large surface area and electrochemical active sites for superior electrochemical performance. Electrons and ions were easily transported among nanopores (Figure 8.6b). These nanopores as well as loose crystal configuration of α-NCH also ensure the stability of nanostructures. In addition, the bimetallic hydroxides of Co and Ni were proved to have better electrochemical performance than monometallic hydroxides.[339] As a result, 3D porous binder-free design, stable nanostructures, and special chemical compositions synergically improved the conductivity and stability of α-NCH electrodes. In a recent study, we firstly fabricated α-$Ni(OH)_2$ nanobristles based on similar strategy.[330] However, the relative poor performance was recorded due to inherent drawbacks of $Ni(OH)_2$.[329] And the longer reaction period and heating condition is inevitable to fabricate them. Here, this α-NCH electrode achieved much better performance and can be developed at room temperature. Therefore, this diffusion controlled strategy is worthy of keeping explore in future to design high-performance electrodes for supercapacitors.

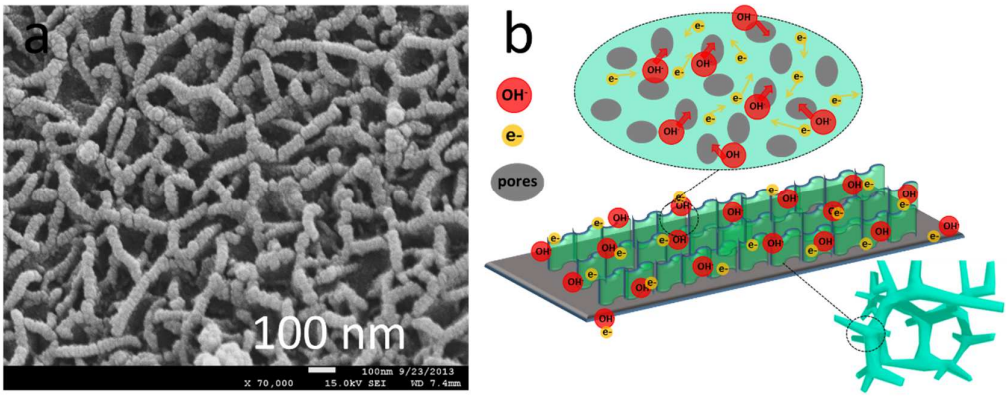

Figure 8.6. (a) FESEM image of the α-NCH electrode after cycling test, (b) schematic of the transportation of ions and electrons in porous α-NCH nanosheets during electrochemical reactions.

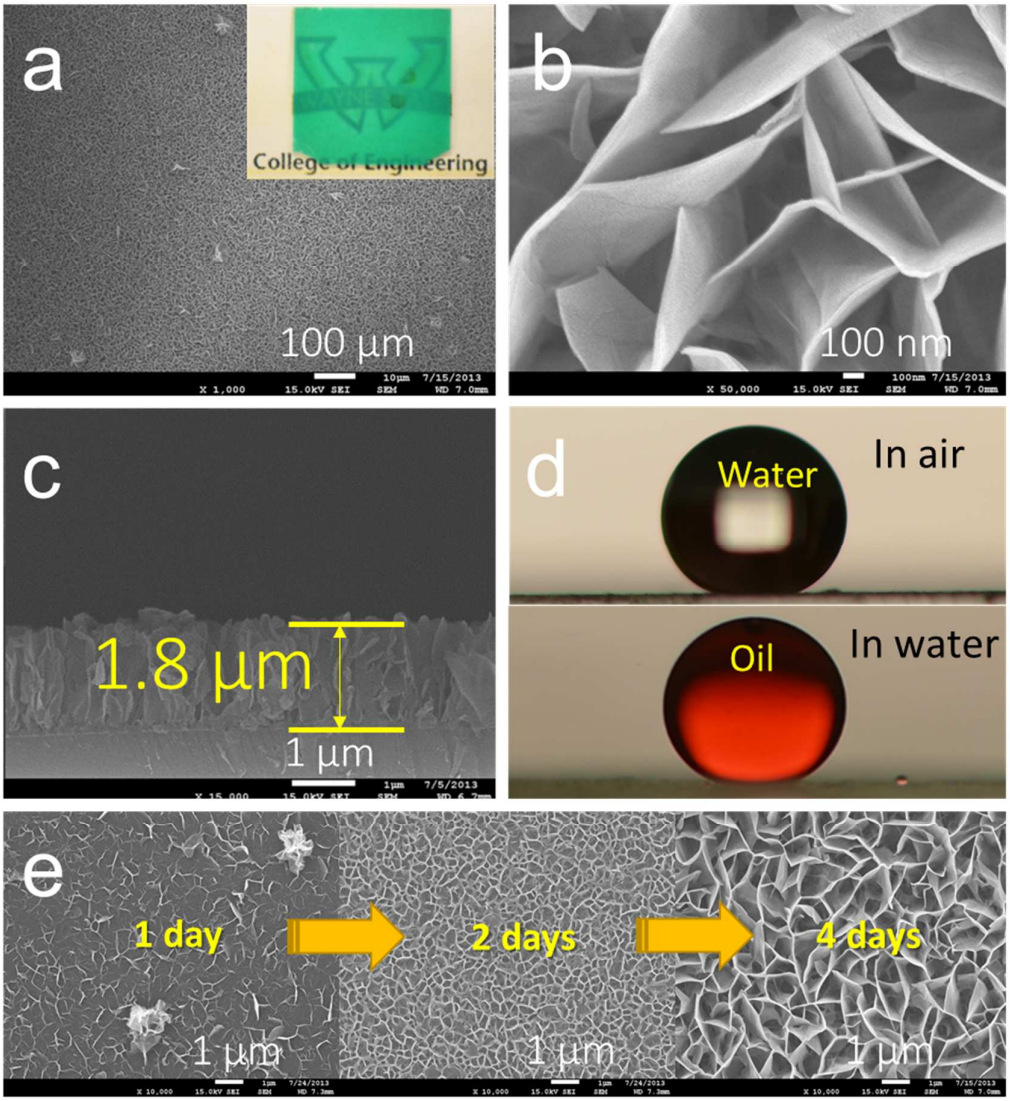

Figure 8.7. (a, b, c) FESEM images of nanosheets α-NCH on a piece of glass after 4 days reaction. (d) The wettability of as-deposited glass slides in air and water for water droplet and oil droplet, respectively. (e) The change of morphologies of nanosheets with an increase of reaction periods. Inset of (a) is the corresponding optical image.

Not only Ni foam, other substrates could be easily deposited by this diffusion-controlled strategy. In Figure 8.7, a piece of glass was used as another typical substrate to grow α-NCH nanosheets. Under the same conditions, the blue-green colored coating was uniformly formed on glass, making it semitransparent. Top-view FESEM image and optical image of it are shown in Figure 8.7a. The similar porous nanostructures are observed at higher magnification with decreased thickness of nanosheets, compared with those on Ni foam. As present in Figure 8.7c, the side-view FESEM image shows the morphology and height of coating. After 4 days, 1.8 μm coating of α-NCH was formed on glass. Consider the hierarchical roughness of nanostructured coating, some special wettability of the surface of glass could be found. After simply physical vapor deposition, superhydrophobicity was achieved in air. The water contact angle is around 154.1^{o}. In addition, bared α-NCH coating possesses oil contact angle underwater is 160.0^{o}. The special wettability suggests potential applications in various applications (water-oil separation, self-cleaning surface, etc.). Moreover, the nanostructures of α-NCH on glass are controllable. From 1 day to 4 days, different size of porous nanosheets coating was recorded in Figure 8.8. After 1 day, only sparse short nanosheets were observed. Two days later, a lot of relatively small porous nanosheets network formed. Then, extending to 4 days, bigger porous nanosheets network finally covered the surface of glass, which might be used to adjust the wettability of nanostructured coating.

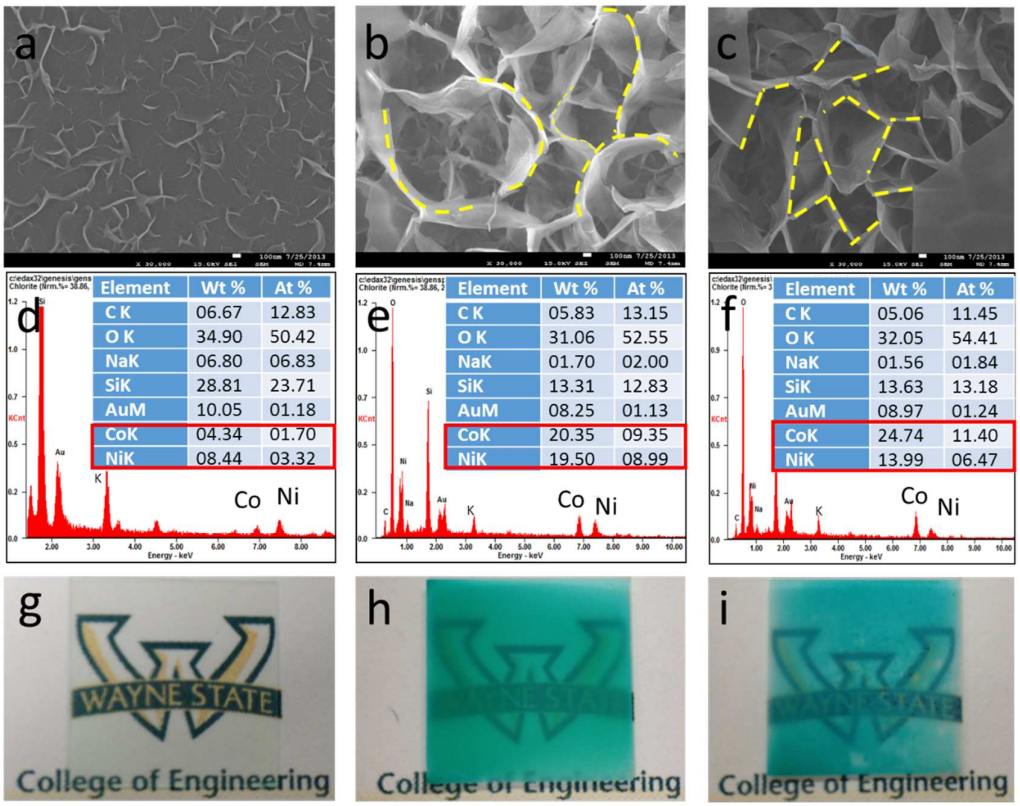

Figure 8.8. FESEM and optical images and EDS results of as-deposited glass slides after 2 days reaction with different ratio of Ni-Co solutions: (a, d, g) Ni/Co = 1, (b, e, h) Ni/Co = 0.5, (c, f, i) Ni/Co = 0.25.

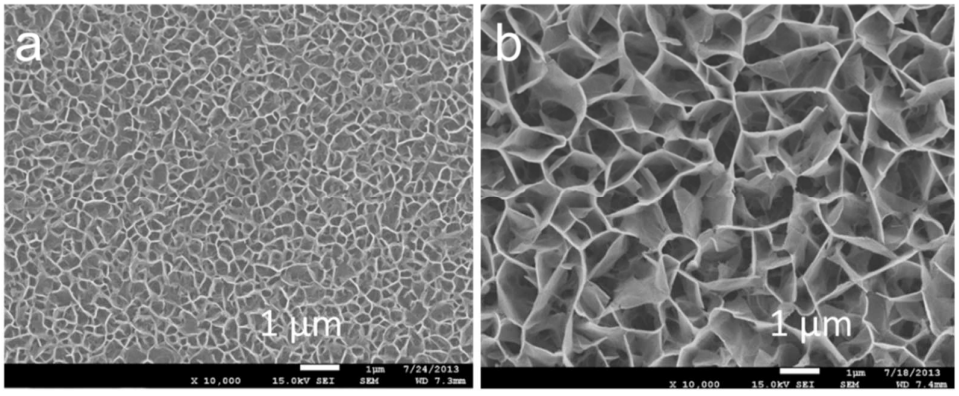

Figure 8.9. FESEM images of as-prepared samples under different temperature: (a) at room temperature; b. at 50 ^{o}C.

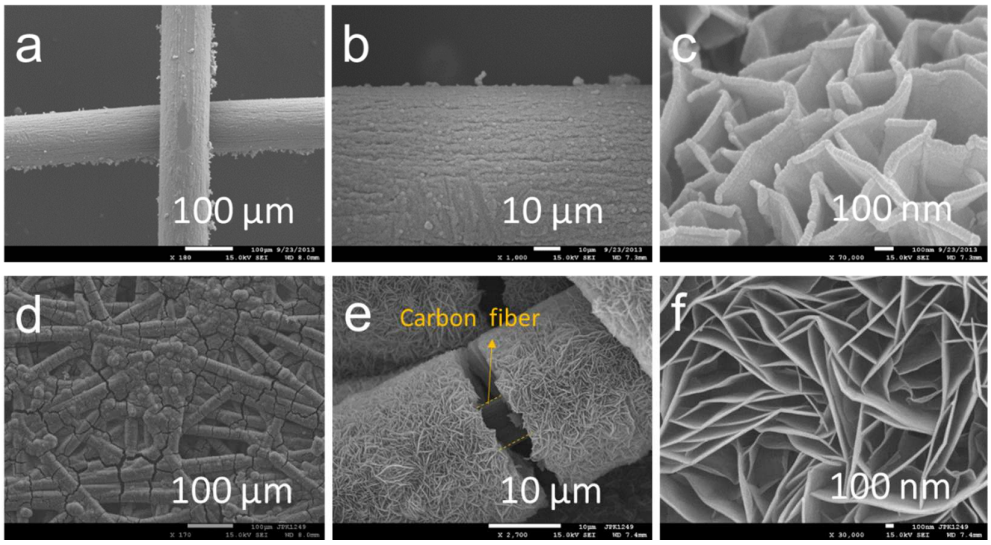

Figure 8.10. FESEM images of as-deposited (a-c) Ti mesh, (d-f) carbon paper after 2 days reaction under different magnifications.

Not only reaction time is able to control α-NCH's nanostructures, but also different initial molar ratios of $NiCl_2$ and $CoSO_4$ in Ni-Co solution can regulate their nanostructures and compositions in Figure 8.8. After two days, different values of Ni/Co affect the nanostructures significantly on the surface. When Ni/Co is 1, short and sparse nanosheets formed (Figure 8a), the corresponding ratio in α-NCH is around 2:1(Figure 8.8d). As the value of Ni/Co decreased to 0.5, large and curled nanosheets were observed (Figure 8.8b), and the final ratio of Ni and Co in α-NCH is around 1:1 (Figure 8.8e). If the value in further decreases to 0.25, more big and oriented nanosheets is obtained (Figure 8.8c), and the ratio of Ni and Co is around 1:2 (Figure 8.8f). Thus, the more cobalt involved in Ni-Co solution, the more oriented nanosheets were observed. Meanwhile, the as-deposited coating became more nonuniform as shown in optical images (Figure 8.8g-8i). This phenomenon suggests that the reaction system could spontaneously control the nanostructures and their chemical compositions. In addition, it is found that temperature is able to control the size of porosities as well as present in Figure 8.9. Therefore, this synthesis method is highly controllable for nanostructured α-NCH, which might be applied to adjust properties in different applications. More experiments for them are

undergoing. We have to highlight that there are no preferences for this coating strategy. Other substrates such as Ti mesh and hydrophobic carbon fiber paper were verified to be applied successfully. The slight different structures could form on them (Figure 8.10). These results suggest that this controllable deposition is universal to different shapes and different surface wettability. Therefore, it is speculated that this diffusion method could be applied to various substrates to make use of nanostructured α-NCH effectively. It is also noticed that nickel cobalt oxides and nickel cobalt sulfides have excellent properties in electrochemical devices.[342-345] α-NCH can be easily converted into oxides, sulfides for these applications, in further expanding the potential applications of this methods.

8.4 Conclusion

In summary, a diffusion-controllable synthesis method at room temperature was present to grow nanosheets alpha nickel-cobalt hydroxides on different substrates. After depositing on Ni foam, the prepared binder-free α-NCH electrodes delivered extremely stable high capacitance at different current densities for at least 3000 cycles. The highly rough surface of glass deposited by nanostructured α-NCH demonstrated special wettability such as superhydrophobicity in air and superoleophobicity in water. The controllable morphologies and compositions were also achieved by adjusting different parameters. This highly controllable synthesis strategy at room temperature suggests various potential applications of nanostructured α-NCH as well as oxides, sulfides derived from this hydroxide precursor.

CHAPTER 9 A BIO-INSPIRED SYNTHETIC ROUTE FOR THE ONE-STEP FORMATION OF NiO-Ni 3D NANOSTRUCTURES ON CARBONIZED EGGSHELL MEMBRANE AS ANODE MATERIALS FOR LITHIUM-ION BATTERIES

9.1 Introduction

NiO has been intensively studied as multifunctional materials in 3d transition metal oxides. Its applications involve a large number of potential fields such as catalysts,[346] magnetic materials,[347] gas sensors,[348] photovoltaic devices,[349] fuel cell electrodes,[350] electrochemical supercapacitors[351] and anode materials for LIBs.[352] Among them, energy storage field, especially LIBs are being accelerated by the urgent demand of customer electronics, electric vehicles, sustainable energy storage systems as well as energy crisis.

As a potential anode material for LIBs, NiO possesses satisfactory theoretical capacity (718 mAh g^{-1}) and highly safety, environmental benignity and low cost. As a result, it is attracting more and more researchers to devote themselves in studying NiO.[352-358] In the past decades, nanotechnology also was boosting the development of NiO materials. Compared with conventional bulk materials, nanostructured materials demonstrate exotic physical and chemical properties. For anode materials with nanostructures, there are main outstanding advantages: (1) the extremely large surface areas enhance the specific capacity and high-rate charge-discharge cycling performance due to the dramatic increase of the reaction interface between the active materials and electrolytes. (2) well controlled space among the nanostructures could accommodate the volume change of active materials on insertion/exertion of Li ions.[56]

Although nanomaterials demonstrate a lot of merits in contrast of bulk materials, the morphologies and compositions of them significantly influence their performances for LIBs. The initial nanomaterials are limited to nanoparticles. Thus, the inevitable disadvantages hinder the application of them.[359] For example, the most critical problem is the aggregation of nanoparticles, which result in poor cycling performances. In addition, here are other inevitable

issues that severely deteriorate the cycling performances, such as pulverization and detachment of active particles during charging and discharging process, and poor conductivity, especially for 3d transition metal oxides.[234] Therefore, the following 1D, 2D and 3D hierarchical structures are paid attention to.[360-362] Among them, 1D nanostructures and the ordered self-assembly of them have recently being become a hot topic due to the inherent advantages of 1D nanostructures and the self-assembly patterns.[363]

Various methods of preparing nanostructured NiO have been developed. These approaches include hydrothermal methods,[364] thermal decomposition,[365] template methods,[366] electrodeposition,[352] sol-gel methods,[367] chemical precipitation methods,[368] and so on. However, most of them are limited to the laboratory scale due to some unresolved problems, such as special reaction conditions, tedious procedures or complex apparatus, low yield, and high cost at different levels. Considering the urgent demand for nanostructured LIBs, it is still essential to explore facile, low-cost and environmentally friendly methods for large scale manufacture in the future. Bio-inspired methods may provide alternative routes. Although we are still in the initial stage of preparing nanomaterials, nature has mastered it for 3.8 billion years, which is reliable enough for us to imitate or get inspiration from these designs to improve our design.[369] Recently, a large number of bio-inspired strategies have been taken recently.[43, 190, 250, 356, 370-373] Unfortunately, by now, there is no report combines 3D hierarchical nanostructures and bio-inspired route to improve electrochemical properties of NiO.

In this paper, we demonstrate a facile bio-inspired strategy for preparing nanostructured NiO with 3D networks self-assembled by 1D nanowires. The controllable diffusion method can be considered as a creative technology with a large potential for fabricating nanomaterials. In the present work, Nafion N117, cation-exchange membrane, was chosen as the diaphragm to control the transportation of ions. Besides, the eggshell membrane (ESM) was introduced to be taken as a bio-active substrate to initiate self-assembly of $Ni(OH)_2$ precursors, conductive

carbonized substrate and a reductant for developing metallic Ni nanoparticles in NiO nanowires. By systematical integration of novel nanostructures and conductive components, the results show that as-prepared NiO-Ni@CESM composites exhibited excellent rate and cycling performance. The electrodes retained a highly stable capacity of ~815 mAh g^{-1} at 0.1 A g^{-1} and the properties are much better than the NiO control.

9.2 Experimental Section

Materials Synthesis. In a typical synthesis procedure is similar to our previous study,[373] nickel chloride hexahydrate ($NiCl_2 \cdot 6H_2O$) and sodium hydroxide (NaOH) were used directly without further purification. A cation-exchange membrane, Nafion N117, was purchased from Ion Power, Inc. The membrane is a perfluorosulfonic acid/PTFE copolymer, and the typical thickness is 183 μm. It was soaked in deionized (DI) water overnight before use. $NiCl_2 \cdot 6H_2O$ and NaOH were individually dissolved in DI water. The initial concentration of NaOH and $NiCl_2$ solutions was 1.0 M. 5 mM CTAB was added in the $NiCl_2$ solution. This concentration was arbitrarily adopted only to get a sufficient driving force for diffuse OH^- ions and reaching supersaturation of $Ni(OH)_2$ in $NiCl_2$. The fresh hen eggs with the same brand purchased from a local supermarket were carefully broken at the blunt end and were emptied of the contents. The eggshells with ESM were washed with DI water totally. 2.5 M HCl was used to separate ESM from the eggshells. And then, we cut a whole ESM into several small sheets (15 mm × 30 mm) and placed them in one chamber of a side-by-side crystallizer. Figure 9.1 shows the schematic of the crystallizer. The homemade crystallizer is also horizontally placed in Figure 9.1a. The practical crystallizer is composed of two cylindrical glass chambers, a piece of N117 membrane, silicon rubber sheets, and two clamps. The inner diameter of the glass cap is 20 mm. A piece of Nafion N117 membrane was tightly fixed on the middle of the glass caps by silicon rubber sheets and two clamps. NaOH and $NiCl_2$ solutions were injected into two chambers gently. The ESM sheets were kept in $NiCl_2$ solution. The crystallizer was placed in

an oven at 50 °C for 2 days to finish biomimic mineralization of $Ni(OH)_2$ precursors. Then, as-prepared ESM sheets were taken from $NiCl_2$ solution, and then gently rinsed by DI water totally, and dried in an oven at 50 °C for 1 day. The effect of reaction periods (12 h, 24 h and 36 h) and the surfactant (CTAB) were recorded as well. Finally, as-prepared ESM sheets were heated in argon at 350 °C for 2 h. The heating rate is 10 °C min^{-1}. The whole process is illustrated in Figure 9.1b below. To study the effect of heat treatment, 300 °C was also used. The NiO control was set to be annealed in air at 350 °C for 2 h.

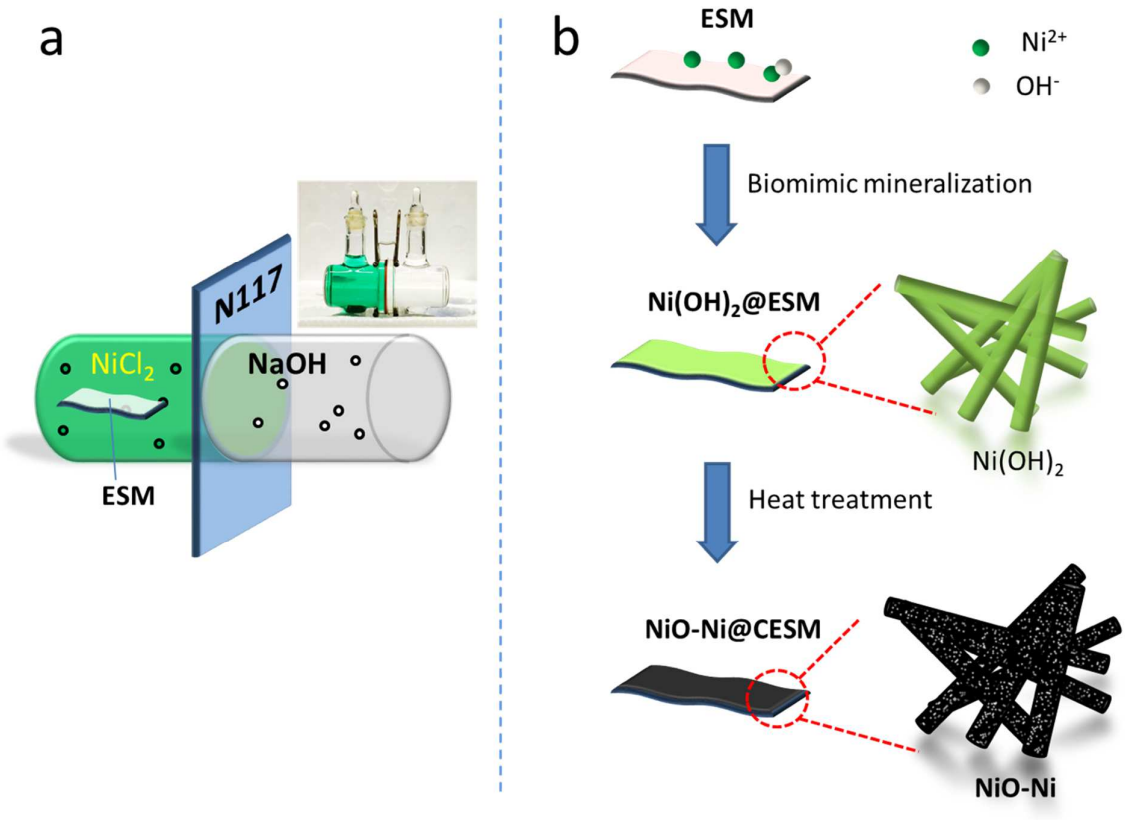

Figure 9.1. (a) Schematic of a homemade crystallizer, (b) illustration of the fabrication procedure of NiO-Ni@CESM. The inset of (a) is the optical image of the crystallizer.

Materials Characterization. X-ray powder diffraction of all the products was characterized by Rigaku Smartlab XRD instrument with Cu Kα radiation. The morphologies of as-prepared $Ni(OH)_2$ precursors and corresponding NiO-Ni products after heat treatment were examined by a field-emission scanning electron microscopy (FESEM/EDAX JEOL-

7600). Transmission electron microscopy (TEM JEOL 2010) was used to determine the sizes, morphologies and components of all the products.

Electrochemical Analysis. The electrochemical measurements were carried out in CR2032 coin-type cells. NiO-Ni@CESM slurries were prepared by well mixing with conductive additive, Super C65, and polyvinylidene fluoride (PVDF) binder (8:1:1, wt%) in N-methylpyrrolidone (NMP). The slurries were later spread on copper foils as current collectors and dried in vacuum oven at 100 ^{o}C overnight for preparing NiO-Ni@CESM electrodes. Coin-type cells were assembled in an argon protected glove box, using the coated copper foil as the working electrode, metallic lithium foil as the counter and reference electrode, 1 M solution of $LiPF_6$ in a mixture of ethylene carbonate (EC) and diethyl carbonate (DEC) as the electrolyte (1:1, wt%), and Celgard 2320 as the separator. The cells were tested on a MTI BST8-WA battery tester by charging and discharging galvanostatically at room temperature in the voltage window of 0.01 - 3 V at different current densities, ranging from 0.1 to 1 A g^{-1}. The NiO control electrodes were prepared and tested based on the same procedure.

9.3 Results and Discussion

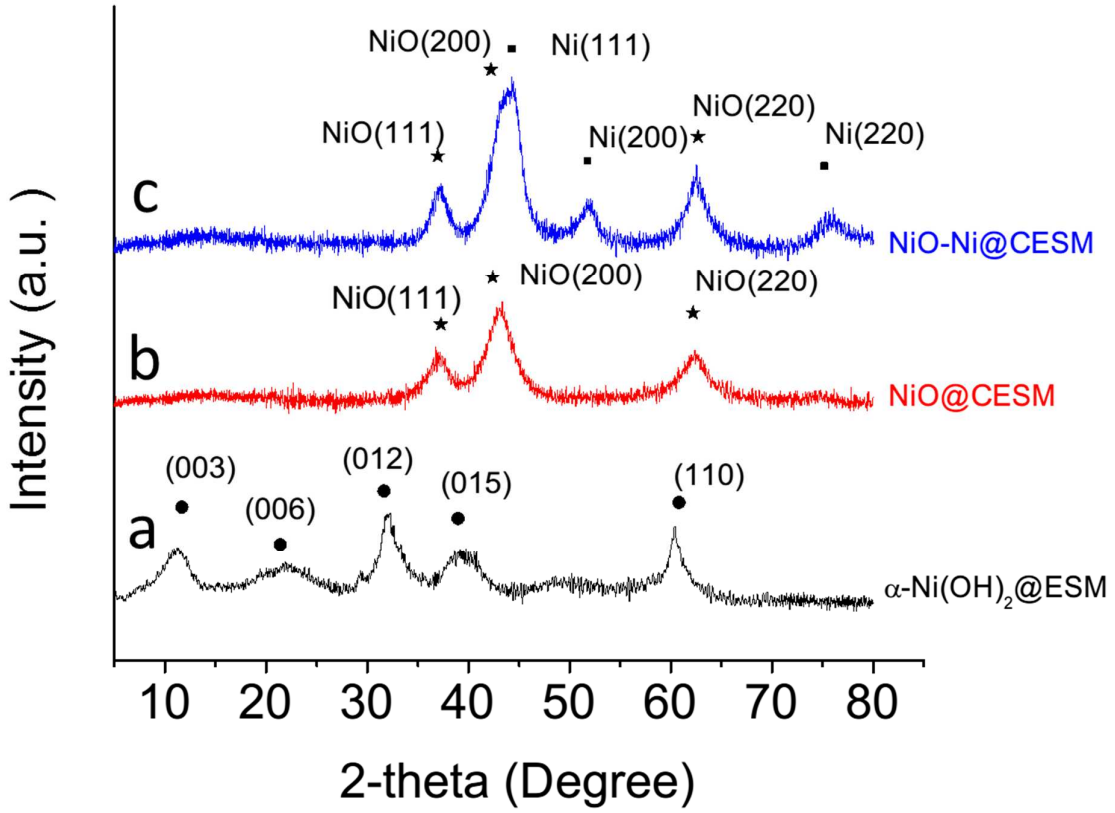

Figure 9.2. XRD patterns of (a) α-$Ni(OH)_2$@ESM after biomimic mineralization, (b) NiO@CESM and (c) NiO-Ni@CESM after calcination at 300 °C and 350 °C, respectively in argon for 2 h.

Figure 9.2 demonstrates different XRD patterns of as-prepared products at different stages. The $Ni(OH)_2$ precursors with ESM are shown in Figure 9.2a. The indexed (003), (006) planes of $Ni(OH)_{2-x}$ are agreed well with the hydrotalcite-like structures of α-$Ni(OH)_2$.[281, 374-376] There are two polymorphs for $Ni(OH)_2$. One is brucite-type β-$Ni(OH)_2$. It is stacked perfectly with hexagonal cells, with a small interlayer spacing (4.60 Å).[377-378] The other is hydrotalcite-like α-$Ni(OH)_2$ structure. It is indexed on randomly stacked triple-layered hexagonal cell due to the intercalation of anions and/or water molecules, with variable interlayer spacing (> 7 Å).[378-379] After calcination at 300 °C of temperature, NiO (JCPDS PDF No. 89-7130) can be detected after decomposition of $Ni(OH)_2$. There are three typical peaks of NiO located at 36°, 43° and 62.5°, respectively. They are indexed as (111), (200), (220) planes of NiO. The peaks are weak and broad. When we increased the temperature to 350 °C, the

intensity of peaks of NiO slightly increased. And then, at 350 °C, several peaks attributed to metallic Ni (JCPDS PDF No. 87-0712) were found. Notably, all the peaks are still weak and broad, which suggests their small grain size. According to Scherrer equation, the grain size of NiO and Ni is approximately 4.3 nm and 6.8 nm, respectively. The appearance of Ni suggests that NiO is partly reduced. Because NiO itself cannot transform into Ni under regular calcination in argon, the only possible reason for that is related to decomposition of ESM. ESM is mainly made of proteins. Thus, ESM might possess strong reducibility after calcination in argon due to the release of reduction gas such as NH_3 and H_2S.[81, 207] This "green" route to make use of waste ESM as reductant is attractive and could be extended to other metal oxides to get a series of metal oxide-metal composites easily. The related studies are undergoing.

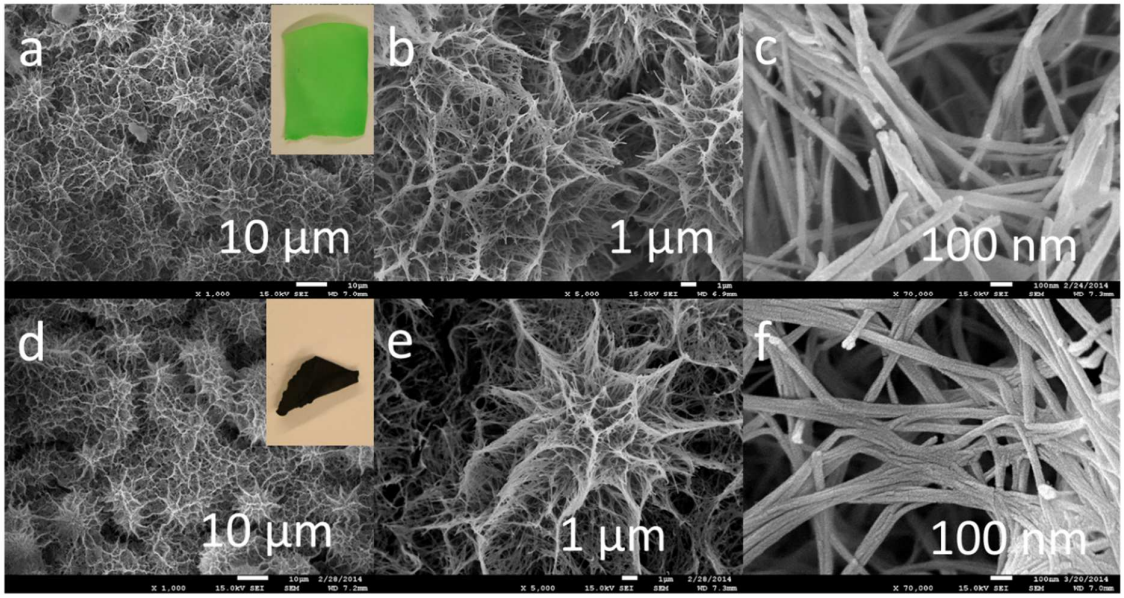

Figure 9.3. FESEM images of (a-c) α-$Ni(OH)_2$ nanowire networks on ESM after reaction for 2 days, (d-f) NiO-Ni nanowire networks on CESM after calcination at 350 °C in argon for 2 h. The insets of (a) and (d) are corresponding optical image

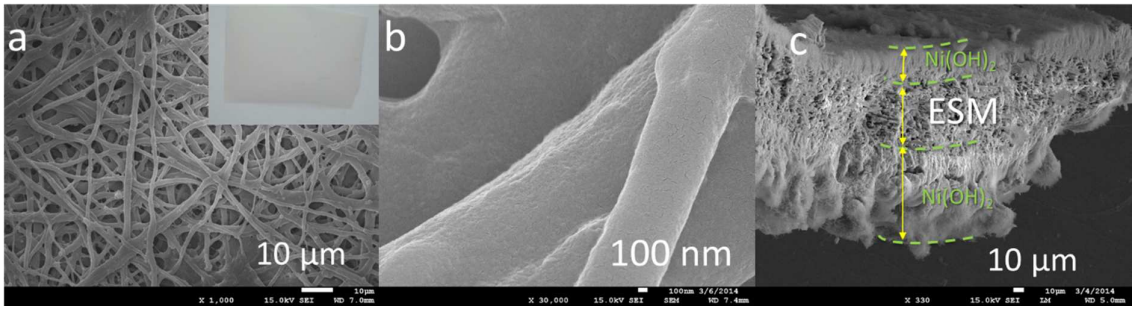

Figure 9.4. FESEM images of (a, b) pristine ESM at different magnifications, and (c) the cross-section of α-Ni(OH)$_2$@ESM after 2 days reaction The inset of (a) is the optical image of ESM

FESEM images of the Ni(OH)$_2$ precursors with ESM and the corresponding NiO-Ni@CESM are shown in Figure 9.3. After 2 days reaction, the surface of ESM was covered by nanostructured Ni(OH)$_2$ coating and the color changed to green from white in Figure 9.3a inset. In specific, 3D networks of Ni(OH)$_2$ are clearly observed in Figure 9.3a. It is interconnected by micrometer scaled flower-like structures. The size of them is ~10 µm. At higher magnification, we surprisingly notice that the flower-like structures are different from the typical flower-like structures reported based on the sheet-like structures of Ni(OH)$_2$.[156, 380-381] Instead, they are made of massive nanowires. The diameter of nanowires is less than 100 nm (Figure 9.3c). This special morphology is more like reported α-Ni(OH)$_2$,[374] in contrast of typical β-Ni(OH)$_2$ with hexagonal platelets.[380] The original fiber-like structures of ESM are presented in Figure 9.4. Its 3D networks are unique as well. After 2 days reaction, Ni(OH)$_2$ precursors had fully covered the both sides of ESM in Figure 9.4c. After calcination in argon at 350 ^{o}C for 2 h, ESM shrunk dramatically and the color turned to black (Figure 9.3d inset). In the corresponding FESEM images (Figure 9.3d-3f), the flower-like structures and nanowires both remain unchanged. However, the surface of nanowires becomes a little rough (Figure 9.3f), compared with that in Figure 9.3c. To our best knowledge, there is no this kind of hierarchical structure NiO-Ni studied before though similar nanostructures of Ni(OH)$_2$ were reported.[373, 382-383] These unique 3D networks might be related to the properties of ESM and the experimental conditions we created.

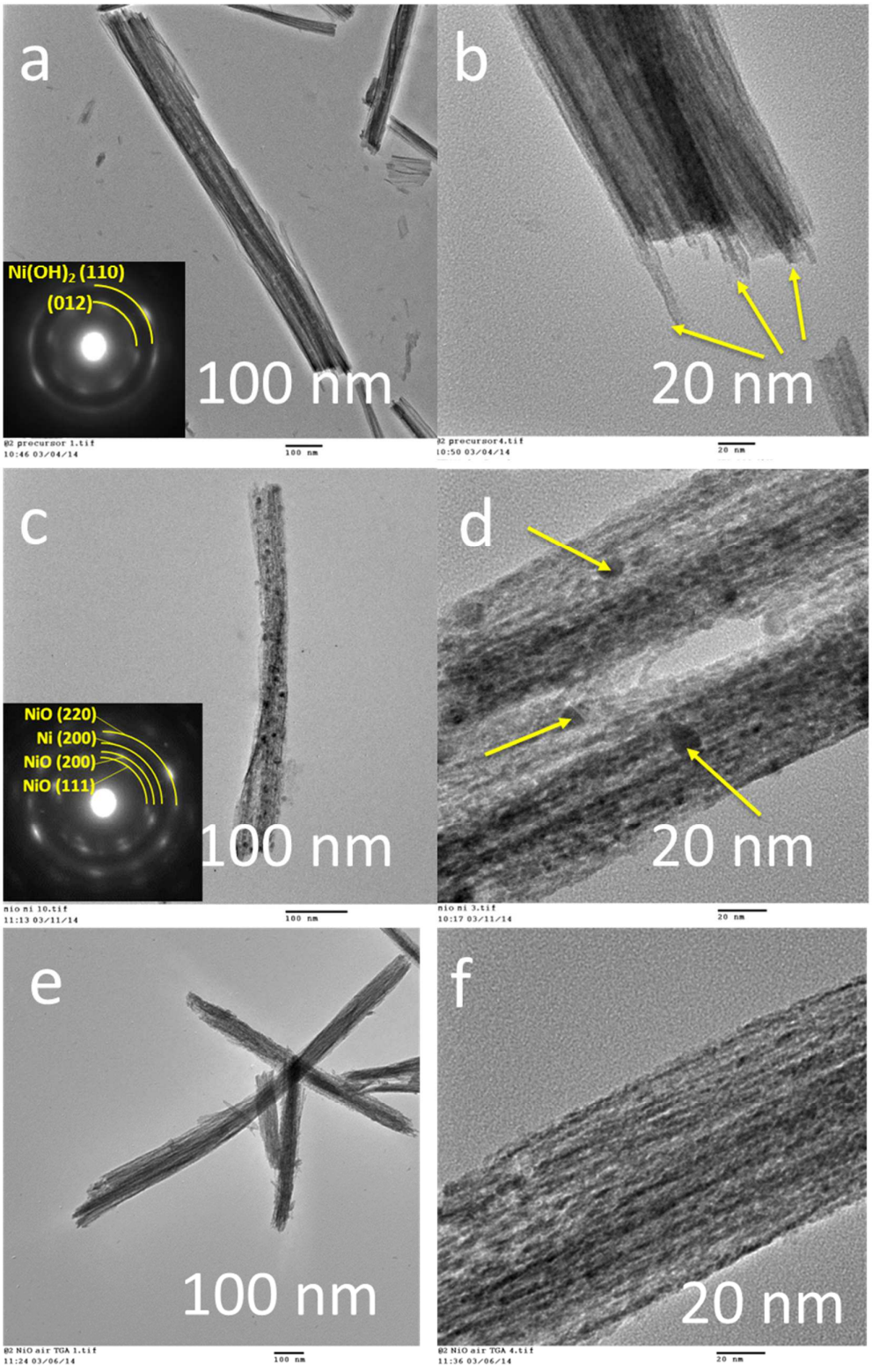

Figure 9.5. TEM images of (a, b) α-$Ni(OH)_2$ nanowires after reaction for 2 days at 50 ^oC, (c, d) NiO-Ni after calcination at 350 ^oC in argon for 2 h, and (e, f) the NiO control after calcination

at 350 ^{o}C in air for 2 h. Insets of (a) and (c) are their SAED patterns. The details of nanostructures are marked by allows.

The individual nanowires of $Ni(OH)_2$ and NiO-Ni are also revealed by an obvious contrast in the TEM images (Figure 9.5). For Figure 9.5a, a typical nanowire of $Ni(OH)_2$ precursors is presented. The diameter of it is ~100 nm. Unlike the traditional nanowires reported before,[281, 364, 384-387] it doesn't have the homogenous color, and the edge of it presents a special sheet-like structure. At higher magnification, in Figure 9.5b, the more details of the nanowire are shown. Interestingly, the nanowire is combined by a cluster of smaller nanowires in parallel. The yellow arrows marked the different tips of sub-nanowires. The different densities result in the different colors among them. The select area electron diffraction (SAED) pattern is shown in Figure 9.5a inset. The pattern is comprised of dots and blur rings, which suggests the special mixed crystalline structures. This mixed crystalline structure suggests to a metastable state of $Ni(OH)_2$ between stable crystalline. After calcination, the nanowire structure is kept, but there are a lot of black dots in it (Figure 9.5c). The SAED pattern in Figure 9.5c inset can be indexed to (111), (200), (220) planes of NiO and (200) plane of Ni, respectively.[388-389] As shown in Figure 9.5d, the rough texture of a nanowire is observed clearly and made of massive tiny particles. Except for the tiny particles of nanowires, the larger black dots related in Figure 9.5c are also shown there, the diameter of them is less than 10 nm as marked. The average size of Ni nanoparticles is 5.8 nm, which is consistent with the calculated value in Figure 9.2. To further confirm it, the NiO control after calcination in air is revealed in Figure 9.5e and Figure 9.5f. Reasonably, no black dots are observed. We would like to highlight that these Ni nanoparticles doped NiO nanowires haven’t been reported. Variable applications have to be studied in future.

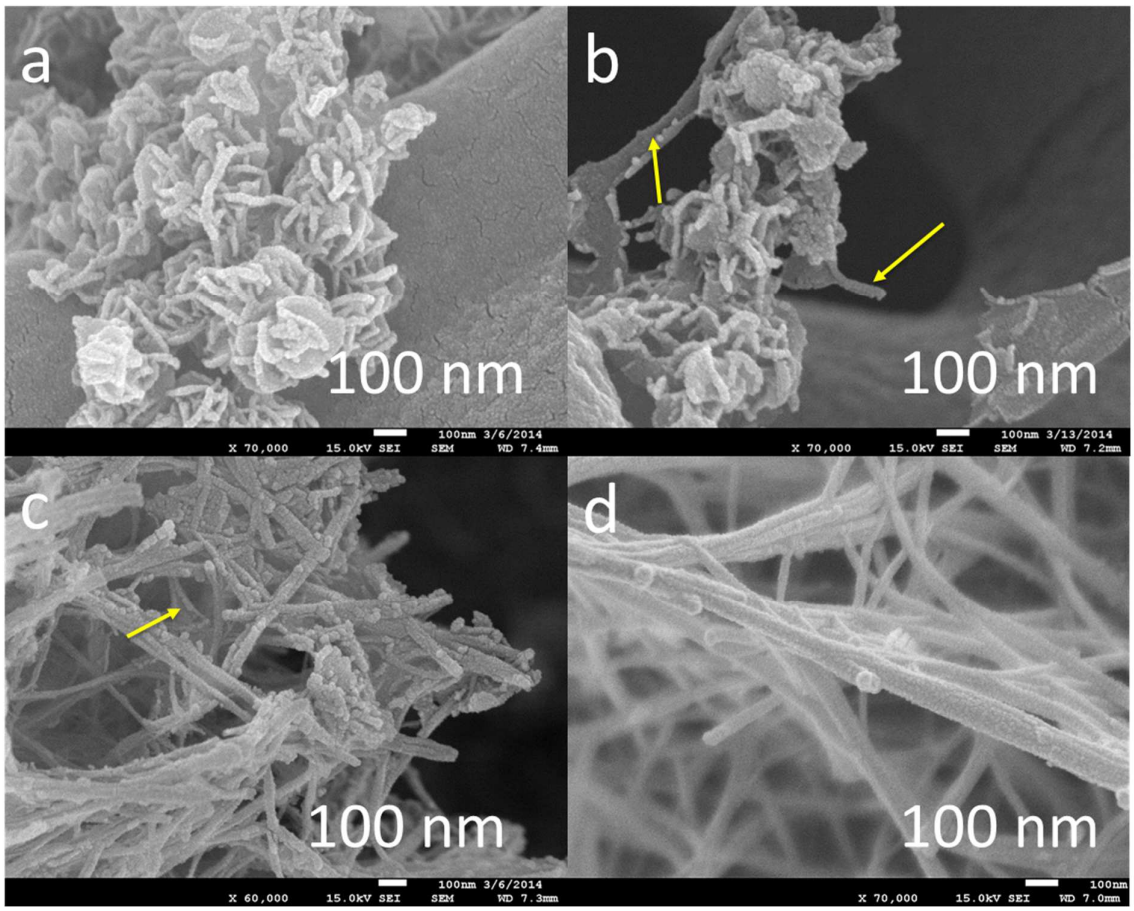

Figure 9.6. FESEM images of the evolution of α-$Ni(OH)_2$ precursors after different reaction periods for (a) 12 h, (b) 24 h, (c) 36 h and (d) 2 days.

To investigate the formation process of nanowire networks of $Ni(OH)_2$ precursors, the effect of reaction periods are recorded in Figure 9.5. During the first 12 h, common flower-like structures with nanoplatelets of $Ni(OH)_2$ are found on the local surface of ESM (Figure 9.6a). However, after 24 h, these flower-like structures partly disappear and big sheet-like structures are noticed. Dissolution and recrystallization process might be involved. At the same time, the edges of left sheet-like structures start to curl and form short wires (~ 100 nm) as marked in Figure 9.6b. With the increase of reaction time, after 36 h, nanoplatelets totally disappear and a lot of long nanowires aggregated are emerging. The surface of them is rough. The curled sheet-like structures are limited as marked. Finally, only interconnected nanowires are observed in Figure 9.6d when the reaction time is extended to 2 days. The surface of nanowires

also become smooth. Similar morphology evolution from nanoplatelets to nanowires of $Ni(OH)_2$ was studied before.[386] but the details of growth mechanism are entirely different. Besides, chrysanthemum-like $Co(CO_3)_{0.5}(OH)_{0.11}H_2O$ was reported based on the similar transformation process.[147] To our best knowledge, this is the first observation the route to form $Ni(OH)_2$ nanowires by curling the edges of sheet-like precursors. Its formation mechanism will be discussed later in this study.

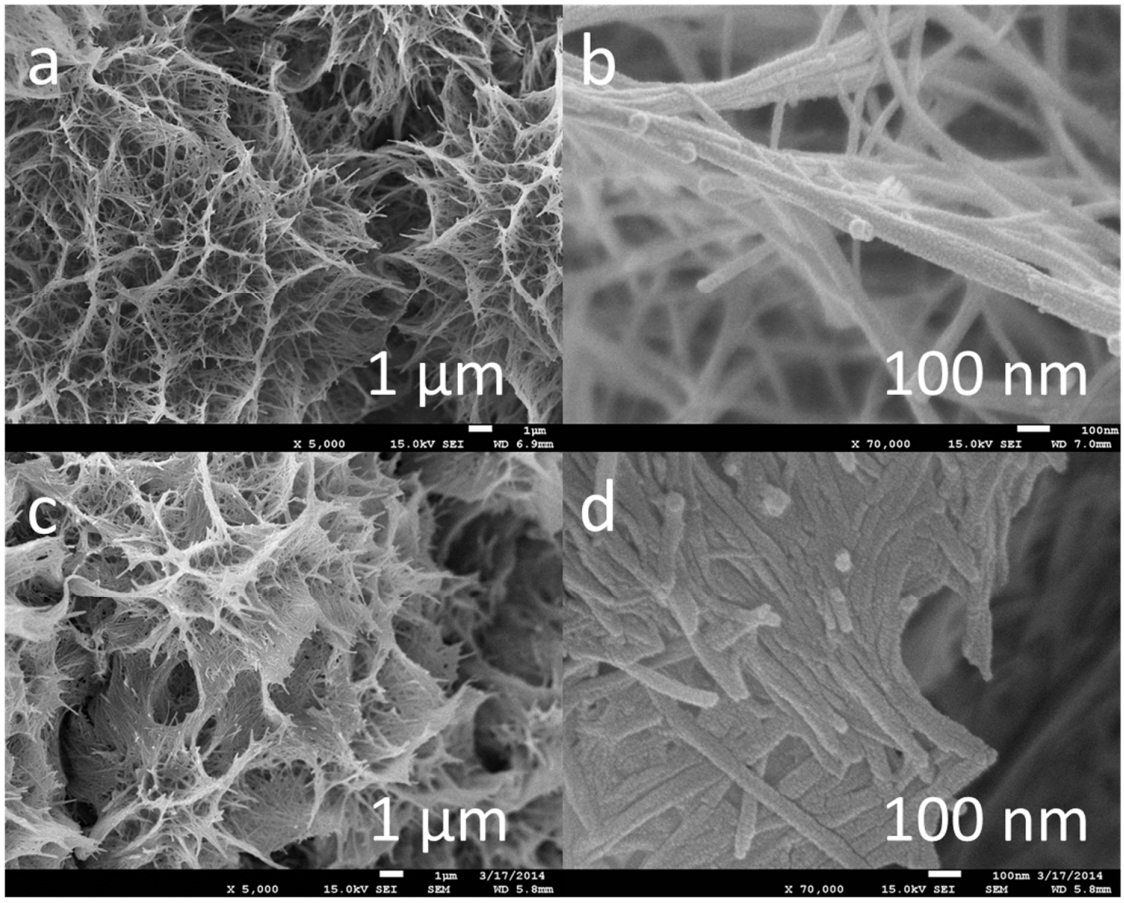

Figure 9.7. FESEM of α-$Ni(OH)_2$ precursors obtained after 2 days reaction at 50 °C: (a, b) in the presence of 5 mM CTAB, (c, d) in the absence of 5 mM CTAB.

To form distinct nanowire networks, CTAB plays a crucial part in forming these 3D structures. Figure 9.6 demonstrates the differences between two kinds of networks assembled by nanowires. In typical conditions with CTAB (Figure 9.7a and Figure 9.7b), the final nanowires are clearly independent and connect with other nanowires by crossing each other.

As a result, the whole 3D networks are highly porous. Instead, as shown in Figure 9.7c, although 3D networks are still existing, the units, nanowires, are highly compact. The clear pores are hard to observe. At higher magnification in Figure 9.7c. The details of these compact nanowires are revealed. They are prone to connect each other by attaching in parallel rather than crossing themselves. As a surfactant, CTAB can be taken as morphology-directing agent to accelerate the formation of 1D nanowires.[131, 390]

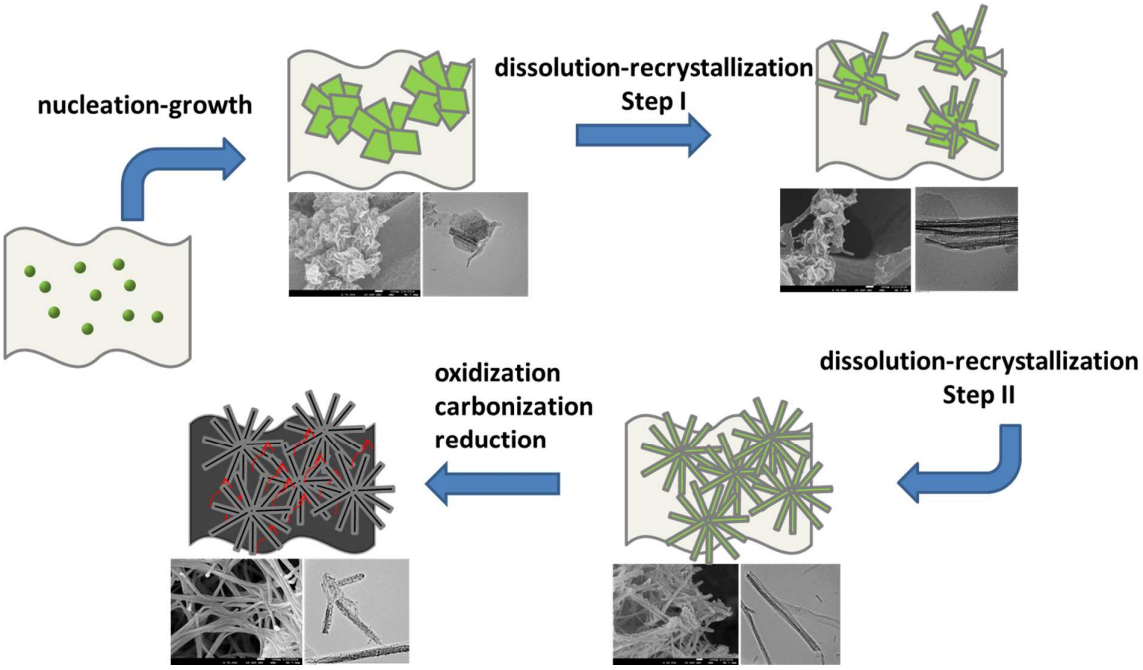

Figure 9.8. The proposed mechanism of the formation of nanostructured NiO-Ni@CESM.

Because we created unique experimental conditions via controllable diffusion method and special ESM substrate, the process of forming of $Ni(OH)_2$ nanowire networks and following NiO-Ni nanocomposites are worth studying. The proposed mechanism of it is demonstrated in Figure 9.8. On one hand, Nafion N117 is a special cation-exchange membrane, which is widely used to control the ions transportation in fuel cells and chlorine alkali industry.[391-392] It is capable of blocking most of anions due to the specific chemical structure.[260, 393] However, if the concentration of anions is high enough, they still could slightly diffuse through it at a certain rate.[291-292, 394] In this study, we creatively introduced this mechanism to

control the diffuse of OH^- ions from high concentration of NaOH solution toward $NiCl_2$ solution. In contrast Ni^{2+} ions might be trapped in Nafion N117 when they react with OH^- ions and sulfonate functional groups in Nafion N117 instead of freely transporting through it. Consequently, the decrease of concentration of $NiCl_2$ can be almost stopped and it makes sure of the relatively stable concentration of Ni^{2+} in the chamber filled with $NiCl_2$ solution. As the reaction initiated, the pH value in $NiCl_2$ solution started to elevate from initial 3.8 to 7.2 gradually due to diffusion of OH^- ions. At the same time, ESM itself possesses active surface with a large number of functional groups to attract free ions.[395] It can accelerate heterogeneous nucleation of $Ni(OH)_2$. Considering the elevated pH value, the high concentration of $NiCl_2$ solution as well as the chemical activity of ESM, local supersaturation could be easily created at 50 ^oC, providing a critical condition for forming $Ni(OH)_2$ nucleus on ESM. After that, the growth of flowers-like $Ni(OH)_2$ continued. Note that the pH value could be kinetically controlled by the formation of $Ni(OH)_2$ and diffusion of OH^- ions spontaneously. Coordination between OH^- and Ni^{2+} on the ESM's surface and slowly elevated pH value together inhibited the rapid precipitation of bulk structures of β-$Ni(OH)_2$.[396] This situation is crucial for forming special 3D networks. Since only the high enough concentration of Ni^{2+} and relatively low pH value could provide the low supersaturation of forming the nanostructures of α-$Ni(OH)_2$ rather than common β-$Ni(OH)_2$ by mixing two reagent solutions directly. By now, some researchers have prepared α-$Ni(OH)_2$ by controlling the pH value indirectly.[27, 397] Hydrolysis of specific chemicals such as urea and hexamethylenetetramine (HMT) are the conventional approaches.[287, 293] By hydrolysis, the pH value could be well controlled. Too low and too high value will affect the formation of α-$Ni(OH)_2$.[398]

On the other hand, The morphologies of $Ni(OH)_2$ is not always stable in the whole process. The special conditions affected the formation of nanostructures in solution. According to the classic principle of the growth of crystals, there are two main steps of the formation of

$Ni(OH)_2$: nucleation and growth. The second step is mainly based on the conditions in solution. Once the stage of nucleation initiates, it is easy to form specific larger structures. The morphologies of $Ni(OH)_2$ crystals were controlled kinetically and thermodynamically via lateral and longitudinal growth. Since $Ni(OH)_2$ has a hexagonal orthorhombic crystal structure, the different crystal planes of the nuclei own different surface energy.[399] At the early stage, the sudden change of the pH value and the chemical activity of ESM supported the formation of nanoplatelets. Then, due to the influence of anions and relative stable pH, large amounts of anions and water molecules might intercalate layers of 2D $Ni(OH)_{2-x}$ sheets.[148] Lateral growth could be hindered and longitudinal growth would be preferred. The change of growth directions reflected the curled trend of nanostructures, and nanowires started to form among 2D nanoplatelets. This phenomenon might also involve a crystallization-dissolution-recrystallization process.[386, 400] Besides, CTAB could promote this transformation from 2D structures to 1D structures by attaching the surface of crystals and forming 1D structured micelles.[401-402] Finally, 1D nanowires self-assembled into 3D networks. The whole process involved controllable ions diffusion (Nafion N117), active organic surface (ESM), organic molecules (CTAB), and mild conditions (reaction in aqueous solutions at 50 ^oC), which is similar to biomineralization in nature.[150] We would like to highlight that the existed methods to form long 1D nanowires of $Ni(OH)_2$ are quite limited in comparison with $Co(OH)_2$.[69, 99, 145, 399, 403-406] Our special bio-inspired method is meaningful to control the crystalline and nanostructures of $Ni(OH)_2$. Considering many factors in reaction, the mechanism behind our route is still unclear and has to be confirmed in future.

Not only are the morphologies interesting, but also the following formation of NiO-Ni composites is surprising. Firstly of all, 3D nanowire networks of $Ni(OH)_2$ precursors can be easily converted into NiO without an obvious change in morphologies after heat treatment. Secondly, unlike the conventional calcination process in preparing NiO with other carbon

sources,[354, 407] ESM was able to partly reduce NiO to Ni at relatively low temperature and carbonize itself (CESM) in order to significantly increase conductivity. Finally, the novel NiO-Ni@CESM composites were developed. The possible reason for the reducibility of ESM might be attributed to the gases from the decomposition of proteins in it as we discussed above. Using waste organic products to partly reduce nanostructured metal oxides is scarcely studied. This bio-inspired route is worth studying and further experiments such as controlling the ratio between NiO and Ni are undergoing.

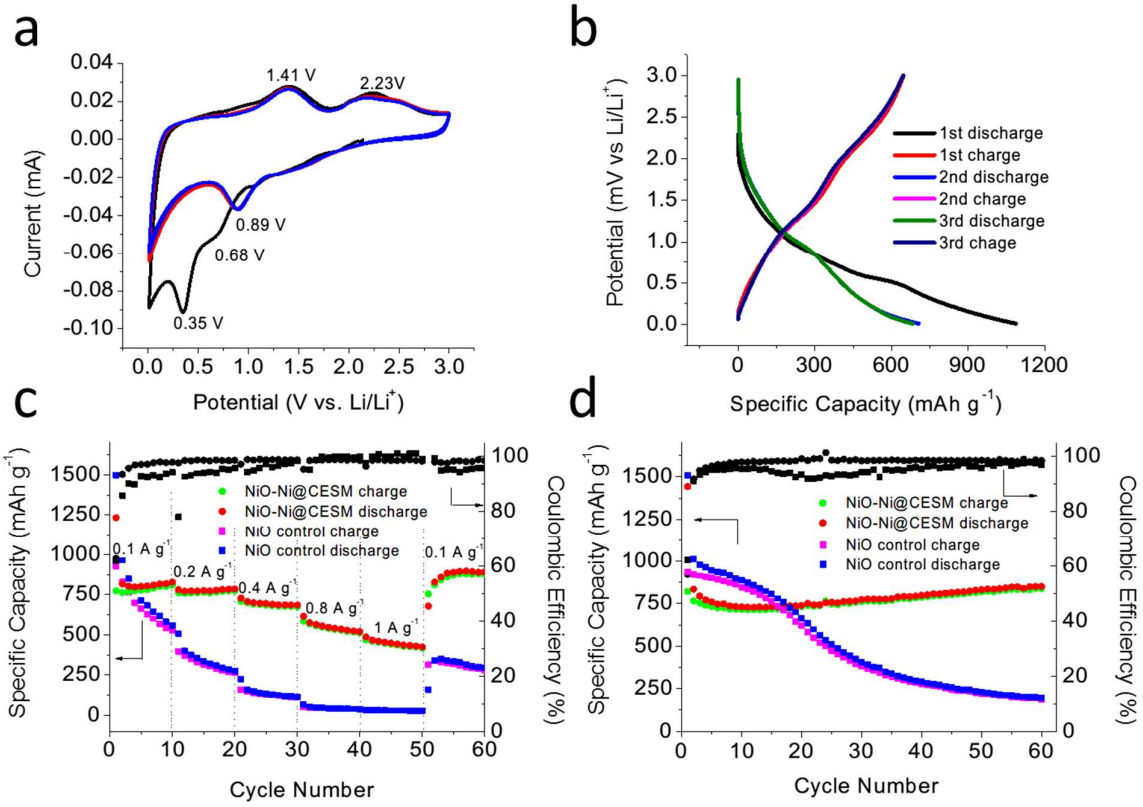

Figure 9.9. (a) Cyclic voltammetry (CV) curves of the NiO-Ni@CESM electrodes scanned at a rate of 0.2 mV s^{-1} in the voltage window of 0.01-3 V; (b) Charge-discharge profiles of NiO-Ni@CESM at 0.1 A g^{-1}; (c) Rate performance of NiO-Ni@CESM and the NiO control after calcination in argon and air at 350 ^{o}C for 2 h, respectively; (d) Cycling performance of NiO-Ni@CESM and the NiO control at 0.1 A g^{-1}. All the specific capacities are reported based on the total weight of NiO-Ni@CESM composites.

The electrochemical properties of as-prepared NiO-Ni@CESM composite materials were evaluated as anode materials for LIBs in Figure 9.9. To explore the exact redox process

in electrodes, the CV curves of initial three cycles are shown in Figure 9.9a. It can be seen that NiO-Ni@CESM electrodes have a strong peak with a weak shoulder peak at around 0.35 and 0.68 V in the first cathodic scan, corresponding to the decomposition of NiO into Ni and the formation of Li_2O and SEI.[408] For the following anodic scan, the broad peaks are located at around ~1.41 V and ~2.23 V, which may be contributed to decomposition of the SEI and oxidation of Ni.[389, 409] The proposed reaction mechanism is as follows: $NiO + 2Li + 2e^- \rightleftharpoons Ni + Li_2O$.[172] In the following cycles, the reduction peaks are found at ~0.89 V, while the oxidation peaks are seen at ~1.41 V and ~2.23 V, periodically. The well overlapped of curves of the second and third cycles indicate the good stability of the electrochemical process. The first three discharge-charge profiles of NiO-Ni@CESM are shown in Figure 9.9b. For the first discharge process, the voltage plateau located at ~0.55 V is not obvious in that in pure NiO or NiO-Ni.[389] The possible reason might be the existence of CESM. Previously, other carbon integrated NiO composites always had similar shapes of a plateau in first discharge curve.[407, 410] NiO-Ni@CESM electrodes delivered ~750 mAh g^{-1} at the end of the plateau. And then, another slow slope continues till the capacity reaches ~1200 mAh g^{-1}, which could be attributed to a polymer/gel-like film formed on the surface.[217] The first charge curve is agreed well with reported NiO electrodes.[376, 408] After that, the following charge-discharge curves are highly overlapped, which indicates the stable reversible capacity. Figure 9.9c shows the rate performance of the NiO-Ni@CESM electrodes at various current densities of 0.1-1 A g^{-1} in comparison of the NiO control. At 0.1 A g^{-1}, NiO-Ni@CESM electrodes delivered a capacity of 827 mAh g^{-1} at the 10^{th} cycle. The subsequent capacities of the composite electrodes are 784 mAh g^{-1} at the 20^{th} cycle at 0.2 A g^{-1}, 683 mAh g^{-1} at the 30^{th} cycle at 0.4 A g^{-1}, 519 mAh g^{-1} at the 40^{th} cycle at 0.8 A g^{-1}, and 424 mAh g^{-1} at the 50^{th} cycle at 1 A g^{-1}, respectively. In comparison, the rate performance of the NiO control was severely deteriorated within the first 50 cycles. When the current density went back to 0.1 A g^{-1}, the specific capacity of NiO-

Ni@CESM rapidly increased to 900 mAh g^{-1} and then kept stable. But for the NiO control, only 288 mAh g^{-1} was left at this current density at the 60th cycle. Consequently, the composites structure of NiO-Ni@CESM indeed improved the electrochemical performance of NiO. Cycling performance of NiO-Ni@CESM and the NiO control were characterized at 0. 1 A^{-1} for 60 cycles in Figure 9.9d. After an initial decrease of capacity in first 6 cycles, NiO-Ni@CESM electrodes experienced gradually increase of reversible capacity from 725 to 851 mA g^{-1}. The slight increase might be the result of decomposition of electrolyte and formation of the gel-like film.[411] In contrast, the NiO control electrodes suffered from fast decay, leaving 194 mA g^{-1} at the 60th cycle. For both rate capability and cycling stability tests, the Coulombic efficiency of NiO-Ni@CESM electrodes was more stable than that in the NiO control.

The superior electrochemical properties of NiO-Ni@CESM composites can be attributed to three main reasons: (1) integrated Ni nanoparticles, (2) hierarchical nanowire networks, and (3) carbonized substrate-CESM. Firstly of all, the distributed Ni nanoparticles inside nanowires of NiO could facilitate the decomposition of Li_2O and the SEI film during the charging process.[376, 412] This catalytic effect make sure of highly reversible capacity during charge-discharge process. Although NiO has high theoretical capacities, it is a semiconductor. The poor conductivity will affect the transportation of electrons. After compositing with Ni nanoparticles, the conductivity of nanowires might increase significantly, improving the electrochemical performance.[365, 376, 389] Secondly, NiO-Ni nanocomposites possess 3D networks with the extremely large surface area. It could enhance electrochemical activity of composites and support fast diffusion of ions/electrons. Unique 3D networks could achieve high-speed transportation of electrons among nanowires. In addition, the 3D porous structures endured the huge volume change of electrodes, resulting in a better rate capability.[61, 407] After cyclability test, most of nanowire networks were kept well (Figure 9.10a and Figure 9.10b), compared with the initial structures (Figure 9.3f). The only difference is the rough textile on

the surface, which could be attributed to the SEI layer or slight volume change in reactions. Thirdly, CESM might have special contributions. Although it only exhibited low capacity, its performance is pretty stable, which is important for the whole electrodes. It also could accommodate the volume change of NiO-Ni nanocomposites as a carbon support and stabilize the connection between active materials. Besides, its 3D porous fiber-like structure might be in favor of uniformed formation slurries and improving the electrode/electrolyte contact surface. In practice, we noticed the more uniformed slurries of NiO-Ni@CESM electrodes than that of the NiO control. All these advantages were briefly presented in Figure 9.10c.

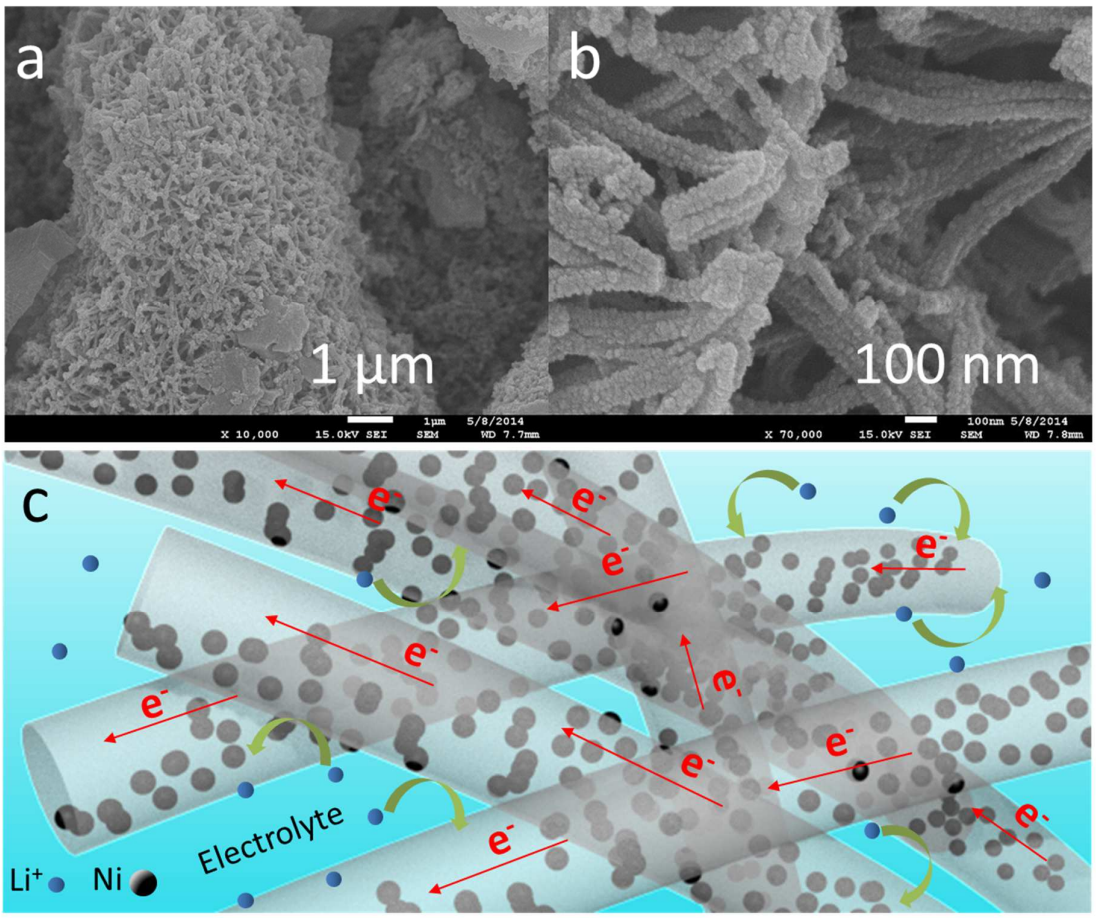

Figure 9.10. (a, b) FESEM images of NiO-Ni@CESM electrodes after cyclability test for 60 cycles, (c) schematic demonstrating the advantages of NiO-Ni@CESM composites as LIBs electrodes.

9.4 Conclusion

In summary, the present study provides a bio-inspired method for synthesis of novel NiO-Ni@CESM composite materials with hierarchical 3D networks. The 3D networks are self-assembled by nanowires via the special diffusion process and crystallization-dissolution-recrystallization process. The conditions of reactions are similar to that in biomineralization. ESM not only provides the active place for facile heterogeneous nucleation but also stable components for electrochemical reactions. Moreover, ESM is served as a natural reductant of NiO nanowires. As a result, the prepared NiO-Ni@CESM composite electrodes demonstrated remarkable stability in rate performance and excellent cycling stability in contrast to the NiO control. Under the synergistic effect of unique structures and compositions, the NiO-Ni@CESM electrodes delivered an initial discharge capacity of ~1200 mAh g^{-1} at 0.1 A g^{-1} and maintains a high reversible capacity of 851.05 mAh g^{-1} after 60 cycles. The performance was much higher than the NiO control. This novel synthesis introduces a bio-inspired path to create unique hierarchical structures with good conductivity to improve the electrochemical performance of transition-metal oxide nanowires. It could be applied to materials for various applications.

CHAPTER 10 SUMMARY AND FUTURE WORK

10.1 Summary

This dissertation focused on preparation of nanomaterials on substrates for energy and environmental applications. Through a bio-inspired strategy, two types of diaphragm-assisted system have been investigated: (1) natural eggshell system and (2) artificial Nafion system.

In the eggshell system, taking the eggshell with eggshell membrane as a bio-reactor, we explored to prepare amorphous $Co(OH)_2$ nanorods on different substrates in $CoSO_4$ solution. The controllable diffusion via eggshell was firstly introduced to develop nanomaterials. $Co(OH)_2$ could self-assembly on active eggshell membrane in eggshell. After thermal treatment at 350 ^oC, nanostructured CoO nanorods derived from $Co(OH)_2$ formed on carbonized eggshell membrane directly. These CoO nanorods were tested as anode materials for lithium-ion batteries. It demonstrated extremely stable performance in rate and cycling test. When Ni foam was used as a robust porous substrate, as-deposited $Co(OH)_2$ nanorods can be employed as additive-free electrodes for supercapacitors. The highly active nanostructures equipped with binder-free design boosted extraordinary electrochemical performance. The mechanism of this eggshell-inspired method has been carefully studied. More interestingly, during exploring eggshell system with $CoCl_2$ and NaOH solutions, it was found that eggshell membrane can be taken as reductant and carbon coating source during carbonization. As a result, we have successfully developed hierarchical pomegranate-like CoO-Co@C from as-deposited $Co_2(OH)_3Cl$ based on similar diffusion and thermal treatment. The introduction of metallic Co, carbon coating, core-shell structures as well as conductive carbon matrix made sure of excellent rate and cycling performance of CoO-Co@C composite electrodes for lithium-ion batteries.

We also have also successfully expanded this idea of controllable diffusion to artificial membrane system without eggshell. Cation-exchange membrane, Nafion N117, was chosen as

a model of semipermeable membrane to control the movement of ions and pH value in separated solutions. At the beginning, we used its cation-exchange feature to fabricate $Mn_3(PO_4)_2 \cdot 3H_2O$ nanoflake arrays on this flexible artificial membrane. The whole growth procedure has been recorded to show its controllable design of nanostructures. Interesting superoleophobicity in water was achieved, which has potential applications in environmental protection. And then, unique anion diffusion phenomena in Nafion system was introduced in synthesizing hydroxides. Similar to the eggshell system, after controlling the diffusion of OH^- ions, nanostructured α-$Ni(OH)_2$ was successfully deposited on various substrates in $NiCl_2$ solution. Superhydrophobicity in air and superoleophobicity in water were both achieved, which can be helpful for environmental protection. With 3D network assembled by nanobristle arrays, binder-free electrodes demonstrated impressive high initial capacitance and can keep stability within 1000 cycles. Therefore, it is a promising candidate for supercapacitors. After fabrication nanostructured $Ni(OH)_2$, nickel-cobalt hydroxide nanosheet arrays were studied by using mixed Co-Ni solution. After optimization, we successfully achieve highly controllable synthesis of this bimetallic hydroxide at room temperature. Its nanostructures, ratios of Ni and Co could be easily adjusted. Better electrochemical performances for supercapacitors have been achieved, compared with pure $Ni(OH)_2$.

Finally, the discovered features of eggshell membrane and Nafion system were combined to design NiO-Ni nanocomposites. The active surface of eggshell membrane and its reducibility can fast initiate the self-assembly of 3D nanowires networks of $Ni(OH)_2$, and transform them into NiO-Ni nanocomposites after simple heat treatment. The formation mechanism of special 3D network and highly improved performances for lithium-ion batteries were both demonstrated.

10.2 Future Work

Although natural and artificial diaphragm-assisted system derived from eggshell were developed, the deep insight of them is still unclear. Further investigation has to be focused on clarifying the mechanism of them. For example, the relationship between pore structures and diffusion rate is worth studying to fabricate adjustable membrane for highly controllable synthesis. Some theoretical models could be built to help us to design better artificial membrane. As a result, this study will be free from the natural eggshell structure or Nafion membrane.

The explored precursors here are mainly hydroxides since we are familiar with the pH value for initiating their nucleation and crystal growth. The further study could expand to more kinds of inorganic nanomaterials though controllable synthesis from bottom-up. There are so many combinations between cations and anions. To regulate them elaborately in solution is an exciting step towards biomimic synthesis. Therefore, this bio-inspired strategy has potential value to develop universal inorganic nanomaterials in simple solutions. In some projects, eggshell membrane could release some special gases during carbonization. Qualitatively and quantitively analysis of them are necessary. This work will be much helpful to better control conversion reaction during calcination. The components of composite materials could be tailored to meet requirements of different applications.

The potential applications involved are attractive. However, we only did some fundamental work on them. For superhydorphobic and superoleophobic behavior, more practical applications such as oil-water separation, self-cleaning can be systematically studied. For lithium-ion batteries, the performances of anode materials need to be evaluated in full cell structure. The rate performance and cycling performance can be improved after optimization. For supercapacitors, hydroxides and oxides always demonstrated much higher specific capacitance than carbon materials in the three-electrode system. Future work will be focused

on standard two-electrode system, which is closer to practice. To make use of advantages of nanomaterials with substrates, other applications are waiting for exploration.

REFERENCES

1. Cao, G.; Wang, Y., Nanostructures & Nanomaterials: Synthesis, Properties, and Applications. 2nd ed.; World Scientific: New Jersey, 2011.

2. Reddy, M. V.; Rao, G. V. S.; Chowdari, B. V. R., Metal Oxides and Oxysalts as Anode Materials for Li Ion Batteries. Chem. Rev. 2013, 113, 5364-5457.

3. Jiang, J.; Li, Y. Y.; Liu, J. P.; Huang, X. T.; Yuan, C. Z.; Lou, X. W., Recent Advances in Metal Oxide-Based Electrode Architecture Design for Electrochemical Energy Storage. Adv. Mater. 2012, 24, 5166-5180.

4. Fan, G. L.; Li, F.; Evans, D. G.; Duan, X., Catalytic Applications of Layered Double Hydroxides: Recent Advances and Perspectives. Chem. Soc. Rev. 2014, 43, 7040-7066.

5. Lu, J. G.; Chang, P.; Fan, Z., Quasi-One-Dimensional Metal Oxide Materials—Synthesis, Properties and Applications. Mater. Sci. Eng., R 2006, 52, 49-91.

6. Rao, C. N. R.; Müller, A.; Cheetham, A. K., The Chemistry of Nanomaterials: Synthesis, Properties and Applications. Wiley-VCH Weinheim Chichester, 2004.

7. Shi, W. D.; Song, S. Y.; Zhang, H. J., Hydrothermal Synthetic Strategies of Inorganic Semiconducting Nanostructures. Chem. Soc. Rev. 2013, 42, 5714-5743.

8. Adschiri, T.; Kanazawa, K.; Arai, K., Rapid and Continuous Hydrothermal Crystallization of Metal Oxide Particles in Supercritical Water. J. Am. Ceram. Soc. 1992, 75, 1019-1022.

9. Nalwa, H. S., Handbook of Nanostructured Materials and Nanotechnology. Academic Press: San Diego, 2000.

10. Bicelli, L. P.; Bozzini, B.; Mele, C.; D'Urzo, L., A Review of Nanostructural Aspects of Metal Electrodeposition. Int. J. Electrochem. Sci. 2008, 3.

11. Masuda, H.; Fukuda, K., Ordered Metal Nanohole Arrays Made by a 2-Step Replication of Honeycomb Structures of Anodic Alumina. Science 1995, 268, 1466-1468.

12. Chang, P.-C.; Fan, Z.; Wang, D.; Tseng, W.-Y.; Chiou, W.-A.; Hong, J.; Lu, J. G., Zno Nanowires Synthesized by Vapor Trapping CVD Method. Chem. Mater. 2004, 16, 5133-5137.

13. Thostenson, E. T.; Ren, Z.; Chou, T.-W., Advances in the Science and Technology of Carbon Nanotubes and Their Composites: A Review. Compos. Sci. Technol. 2001, 61, 1899-1912.

14. Dang, H.; Wang, J.; Fan, S., The Synthesis of Metal Oxide Nanowires by Directly Heating Metal Samples in Appropriate Oxygen Atmospheres. Nanotechnology 2003, 14, 738.

15. Nosonovsky, M., Biomimetics in Materials Science: Self-Healing, Self-Lubricating, and Self-Cleaning Materials. 2012 ed.; Springer: 2011.

16. Benyus, J. M., Biomimicry: Innovation Inspired by Nature. 1st ed.; Morrow: New York, 1997.

17. Bar-Cohen, Y., Biomimetics: Biologically Inspired Technologies. CRC/Taylor & Francis: Boca Raton, FL, 2006.

18. Seeman, N. C.; Belcher, A. M., Emulating Biology: Building Nanostructures from the Bottom Up. Proc. Natl. Acad. Sci. USA 2002, 99, 6451-5.

19. Zan, G.; Wu, Q., Biomimetic and Bioinspired Synthesis of Nanomaterials/Nanostructures. Adv. Mater. 2016.

20. Whaley, S. R.; English, D. S.; Hu, E. L.; Barbara, P. F.; Belcher, A. M., Selection of Peptides with Semiconductor Binding Specificity for Directed Nanocrystal Assembly. Nature 2000, 405, 665-668.

21. Woo, S.; Rothemund, P. W. K., Programmable Molecular Recognition Based on the Geometry of DNA Nanostructures Nat. Chem. 2011, 3, 829-829.

22. Green, D.; Walsh, D.; Mann, S.; Oreffo, R. O. C., The Potential of Biomimesis in Bone Tissue Engineering: Lessons from the Design and Synthesis of Invertebrate Skeletons. Bone 2002, 30, 810-815.

23. Baeuerlein, E.; Behrens, P.; Epple, M., Handbook of Biomineralization. Wiley-VCH: Weinheim, 2007.

24. Ball, P., Life's Lessons in Design. Nature 2001, 409, 413-416.

25. Lakshminarayanan, R.; Kini, R. M.; Valiyaveettil, S., Investigation of the Role of Ansocalcin in the Biomineralization in Goose Eggshell Matrix. Proc. Natl. Acad. Sci. USA 2002, 99, 5155-5159.

26. Yang, D.; Qi, L. M.; Ma, J. M., Eggshell Membrane Templating of Hierarchically Ordered Macroporous Networks Composed of TiO2 Tubes. Adv. Mater. 2002, 14, 1543-1546.

27. Deng, W. T.; Liu, Y.; Zhang, Y.; Lu, F.; Chen, Q. Y.; Ji, X. B., Enhanced Electrochemical Capacitance of Nanoporous NiO Based on an Eggshell Membrane. RSC Adv. 2012, 2, 1743-1745.

28. Lee, S. M.; Grass, G.; Kim, G. M.; Dresbach, C.; Zhang, L. B.; Gosele, U.; Knez, M., Low-Temperature Zno Atomic Layer Deposition on Biotemplates: Flexible Photocatalytic Zno Structures from Eggshell Membranes. Phys. Chem. Chem. Phys. 2009, 11, 3608-3614.

29. Kumari, T. S. D.; Kumar, T. P.; Stephan, A. M., Lithium Insertion Behavior of Nanoscopic Co3O4 Prepared with Avian Egg Membrane as a Template. Bull. Korean Chem. Soc 2011, 32, 1205.

30. Li, J.; Chiu, K. L.; Kwong, F. L.; Ng, D. H.; Chan, S. L., Conversion of Egg Shell Membrane to Inorganic Porous CexZr1-xO2 Fibrous Network. Current Applied Physics 2009, 9, 1438-1444.

31. Kokubo, T., Surface-Chemistry of Bioactive Glass-Ceramics. J. Non-Cryst. Solids 1990, 120, 138-151.

32. Alivisatos, A. P.; Johnsson, K. P.; Peng, X.; Wilson, T. E.; Loweth, C. J.; Bruchez, M. P.; Schultz, P. G., Organization Of'nanocrystal Molecules' Using DNA. Nature 1996, 382, 609-611.

33. Geng, B.; Zhan, F.; Jiang, H.; Guo, Y.; Xing, Z., Egg Albumin as a Nanoreactor for Growing Single-Crystalline Fe3o4 Nanotubes with High Yields. Chem. Commun. 2008, 5773-5775.

34. Yang, X. H.; Wu, Q. S.; Lju, J. K., Controlled Synthesis of Srcro4 Crystals with Different Morphologies. Cryst. Res. Technol. 2007, 42, 211-215.

35. Liu, J. K.; Wu, Q. S.; Ding, Y. P.; Wang, S. Y., Biomimetic Synthesis of Baso4 Nanotubes Using Eggshell Membrane as Template. J. Mater. Res. 2004, 19, 2803-2806.

36. Liu, J. K.; Wu, Q. S.; Ding, Y. P., Assembling Synthesis of Baso4 Biomimetic Nano-Superstructures through Eggshell Membrane Template. Chem Res Chinese U 2005, 21, 243-245.

37. Iijima, M.; Moriwaki, Y., Effects of Inorganic Ions on Morphology of Octacalcium Phosphate Grown on Cation Selective Membrane at Physiological Temperature and Ph in Relation to Enamel Formation. J. Cryst. Growth 1989, 96, 59-64.

38. Takiguchi, M.; Igarashi, K.; Azuma, M.; Ooshima, H., Tubular Structure Agglomerates of Calcium Carbonate Crystals Formed on a Cation-Exchange Membrane J. Cryst. Growth 2006, 6, 1611-1614.

39. Zhang, Y.; Liu, Y.; Ji, X. B.; Banks, C. E.; Zhang, W., Sea Cucumber-Like Hydroxyapatite: Cation Exchange Membrane-Assisted Synthesis and Its Application in Ultra-Sensitive Heavy Metal Detection. Chem. Commun. 2011, 47, 4126-4128.

40. Kokubu, T.; Oaki, Y.; Hosono, E.; Zhou, H. S.; Imai, H., Biomimetic Solid-Solution Precursors of Metal Carbonate for Nanostructured Metal Oxides: MnO/Co and MnO-CoO Nanostructures and Their Electrochemical Properties. Adv. Funct. Mater. 2011, 21, 3673-3680.

41. Wong, T. S.; Kang, S. H.; Tang, S. K.; Smythe, E. J.; Hatton, B. D.; Grinthal, A.; Aizenberg, J., Bioinspired Self-Repairing Slippery Surfaces with Pressure-Stable Omniphobicity. Nature 2011, 477, 443-447.

42. Bao, S.-J.; Li, C. M.; Guo, C.-X.; Qiao, Y., Biomolecule-Assisted Synthesis of Cobalt Sulfide Nanowires for Application in Supercapacitors. J. Power Sources 2008, 180, 676-681.

43. Xiao, J. W.; Yang, S. H., Bio-Inspired Synthesis of NaCl-Type Coxni1−Xo (0 ⩽ X < 1) Nanorods on Reduced Graphene Oxide Sheets and Screening for Asymmetric Electrochemical Capacitors. J. Mater. Chem. 2012, 22, 12253.

44. Shen, L. Y.; Guo, X. W.; Fang, X. P.; Wang, Z. X.; Chen, L. Q., Magnesiothermically Reduced Diatomaceous Earth as a Porous Silicon Anode Material for Lithium Ion Batteries. J. Power Sources 2012, 213, 229-232.

45. Yang, X. W.; Zhu, J. W.; Qiu, L.; Li, D., Bioinspired Effective Prevention of Restacking in Multilayered Graphene Films: Towards the Next Generation of High-Performance Supercapacitors. Adv. Mater. 2011, 23, 2833-2838.

46. Chen, X. L.; Gerasopoulos, K.; Guo, J. C.; Brown, A.; Wang, C. S.; Ghodssi, R.; Culver, J. N., Virus-Enabled Silicon Anode for Lithium-Ion Batteries. Acs Nano 2010, 4, 5366-5372.

47. Oba, M.; Oaki, Y.; Imai, H., A Microbial-Mineralization-Inspired Approach for Synthesis of Manganese Oxide Nanostructures with Controlled Oxidation States and Morphologies. Adv. Funct. Mater. 2010, 20, 4279-4286.

48. Fei, X.; Shao, Z. Z.; Chen, X., Synthesis of Hierarchical Three-Dimensional Copper Oxide Nanostructures through a Biomineralization-Inspired Approach. Nanoscale 2013, 5, 7991-7997.

49. Liu, H. J.; Wang, X. M.; Cui, W. J.; Dou, Y. Q.; Zhao, D. Y.; Xia, Y. Y., Highly Ordered Mesoporous Carbon Nanofiber Arrays from a Crab Shell Biological Template and Its Application in Supercapacitors and Fuel Cells. J. Mater. Chem. 2010, 20, 4223-4230.

50. Li, Z.; Zhang, L.; Amirkhiz, B. S.; Tan, X. H.; Xu, Z. W.; Wang, H. L.; Olsen, B. C.; Holt, C. M. B.; Mitlin, D., Carbonized Chicken Eggshell Membranes with 3D Architectures as High-Performance Electrode Materials for Supercapacitors. Adv. Energy Mater. 2012, 2, 431-437.

51. Adler-Abramovich, L.; Aronov, D.; Beker, P.; Yevnin, M.; Stempler, S.; Buzhansky, L.; Rosenman, G.; Gazit, E., Self-Assembled Arrays of Peptide Nanotubes by Vapour Deposition. Nat. Nanotechnol. 2009, 4, 849-854.

52. Chang, C. M.; Weng, C. J.; Chien, C. M.; Chuang, T. L.; Lee, T. Y.; Yeh, J. M.; Wei, Y., Polyaniline/Carbon Nanotube Nanocomposite Electrodes with Biomimetic Hierarchical Structure for Supercapacitors. J. Mater. Chem. A 2013, 1, 14719-14728.

53. Liu, L.; Yang, L. Q.; Liang, H. W.; Cong, H. P.; Jiang, J.; Yu, S. H., Bio-Inspired Fabrication of Hierarchical Feooh Nanostructure Array Films at the Air-Water Interface, Their Hydrophobicity and Application for Water Treatment. Acs Nano 2013, 7, 1368-1378.

54. Liu, M. J.; Wang, S. T.; Wei, Z. X.; Song, Y. L.; Jiang, L., Bioinspired Design of a Superoleophobic and Low Adhesive Water/Solid Interface. Adv. Mater. 2009, 21, 665-669.

55. Zhang, X.; He, W.; Yue, Y.; Liu, H.; Ma, J., Biocarbon-Coated LiFePO(4) Nucleus Nanoparticles Enhancing Electrochemical Performances. Chem. Commun. 2012, 48, 10093-10095.

56. Arico, A. S.; Bruce, P.; Scrosati, B.; Tarascon, J. M.; Van Schalkwijk, W., Nanostructured Materials for Advanced Energy Conversion and Storage Devices. Nat. Mater. 2005, 4, 366-377.

57. Wei, W.; Wang, Z. H.; Liu, Z.; Liu, Y.; He, L.; Chen, D. Z.; Umar, A.; Guo, L.; Li, J. H., Metal Oxide Hollow Nanostructures: Fabrication and Li Storage Performance. J. Power Sources 2013, 238, 376-387.

58. Zhang, Y.; Feng, H.; Wu, X. B.; Wang, L. Z.; Zhang, A. Q.; Xia, T. C.; Dong, H. C.; Li, X. F.; Zhang, L. S., Progress of Electrochemical Capacitor Electrode Materials: A Review. Int. J. Hydrogen Energy 2009, 34, 4889-4899.

59. Do, J. S.; Weng, C. H., Preparation and Characterization of CoO Used as Anodic Material of Lithium Battery. J. Power Sources 2005, 146, 482-486.

60. He, Y. S.; Bai, D. W.; Yang, X. W.; Chen, J.; Liao, X. Z.; Ma, Z. F., A Co(OH)2-Graphene Nanosheets Composite as a High Performance Anode Material for Rechargeable Lithium Batteries. Electrochem. Commun. 2010, 12, 570-573.

61. Chen, J.; Xia, X. H.; Tu, J. P.; Xiong, Q. Q.; Yu, Y. X.; Wang, X. L.; Gu, C. D., Co3O4-C Core-Shell Nanowire Array as an Advanced Anode Material for Lithium Ion Batteries. J. Mater. Chem. 2012, 22, 15056-15061.

62. Hao, F. B.; Zhang, Z. W.; Yin, L. W., Co3O4/Carbon Aerogel Hybrids as Anode Materials for Lithium-Ion Batteries with Enhanced Electrochemical Properties. ACS Appl. Mater. Interfaces 2013, 5, 8337-8344.

63. Zhang, H.; Wu, J. B.; Zhai, C. X.; Ma, X. Y.; Du, N.; Tu, J. P.; Yang, D. R., From Cobalt Nitrate Carbonate Hydroxide Hydrate Nanowires to Porous Co3O4 Nanorods for High Performance Lithium-Ion Battery Electrodes. Nanotechnology 2008, 19.

64. Liao, Q. Y.; Li, N.; Jin, S. X.; Yang, G. W.; Wang, C. X., All-Solid-State Symmetric Supercapacitor Based on Co3O4 Nanoparticles on Vertically Aligned Graphene. Acs Nano 2015, 9, 5310-5317.

65. Cao, F.; Pan, G. X.; Tang, P. S.; Chen, H. F., Hydrothermal-Synthesized Co(OH)2 Nanocone Arrays for Supercapacitor Application. J. Power Sources 2012, 216, 395-399.

66. Zhu, Y. G.; Wang, Y.; Shi, Y. M.; Wong, J. I.; Yang, H. Y., CoO Nanoflowers Woven by CNT Network for High Energy Density Flexible Micro-Supercapacitor. Nano Energy 2014, 3, 46-54.

67. Zhang, Z.; Zhang, Y.; Song, R.; Wang, M.; Yan, F.; He, L.; Feng, X.; Fang, S.; Zhao, J.; Zhang, H., Manganese (II) Phosphate Nanoflowers as Electrochemical Biosensors for the High-Sensitivity Detection of Ractopamine. Sensors and Actuators B: Chemical 2015, 211, 310-317.

68. Liang, Y. Y.; Cao, L.; Kong, L. B.; Li, H. L., Synthesis of Co(OH)(2)/USY Composite and Its Application for Electrochemical Supercapacitors. J. Power Sources 2004, 136, 197-200.

69. Yang, L.; Cheng, S.; Ding, Y.; Zhu, X. B.; Wang, Z. L.; Liu, M. L., Hierarchical Network Architectures of Carbon Fiber Paper Supported Cobalt Oxide Nanonet for High-Capacity Pseudocapacitors. Nano Lett. 2012, 12, 321-325.

70. He, T.; Chen, D. R.; Jiao, X. L.; Xu, Y. Y.; Gu, Y. X., Surfactant-Assisted Solvothermal Synthesis of Co3O4 Hollow Spheres with Oriented-Aggregation Nanostructures and Tunable Particle Size. Langmuir 2004, 20, 8404-8408.

71. Lin, C.; Ritter, J. A.; Popov, B. N., Characterization of Sol-Gel-Derived Cobalt Oxide Xerogels as Electrochemical Capacitors. J. Electrochem. Soc. 1998, 145, 4097-4103.

72. Casella, I. G.; Gatta, M., Study of the Electrochemical Deposition and Properties of Cobalt Oxide Species in Citrate Alkaline Solutions. J. Electroanal. Chem. 2002, 534, 31-38.

73. Shinde, V. R.; Mahadik, S. B.; Gujar, T. P.; Lokhande, C. D., Supercapacitive Cobalt Oxide (Co3O4) Thin Films by Spray Pyrolysis. Appl. Surf. Sci. 2006, 252, 7487-7492.

74. Swiegers, G. F., Bioinspiration and Biomimicry in Chemistry: Reverse-Engineering Nature. Wiley-VCH: Hoboken, 2013.

75. Cao, F.; Li, D. X., Biotemplate Synthesis of Monodispersed Iron Phosphate Hollow Microspheres. Bioinspiration Biomimetics 2010, 5, 16005.

76. Yang, D.; Qi, L. M.; Ma, J. M., Hierarchically Ordered Networks Comprising Crystalline ZrO2 Tubes through Sol-Gel Mineralization of Eggshell Membranes. J. Mater. Chem. 2003, 13, 1119-1123.

77. Ikeda, T.; Oaki, Y.; Imai, H., Thin Films That Consist of CuO Mesocrystal Nanosheets: An Application of Microbial-Mineralization-Inspired Approaches to Thin-Film Formation. Chem. - Asian J. 2013, 8, 2064-2069.

78. Zhang, Y.; Li, K.; Zhang, Q.; Liu, W.; Liu, Y.; Banks, C. E., Multi-Dimensional Hydroxyapatite (HAP) Nanocluster Architectures Fabricated Via Nafion-Assisted Biomineralization. New J. Chem. 2015, 39, 750-754.

79. Dorvee, J. R.; Boskey, A. L.; Estroff, L. A., Rediscovering Hydrogel-Based Double-Diffusion Systems for Studying Biomineralization. Crystengcomm 2012, 14, 5681-5700.

80. Li, H. B.; Yu, M. H.; Lu, X. H.; Liu, P.; Liang, Y.; Xiao, J.; Tong, Y. X.; Yang, G. W., Amorphous Cobalt Hydroxide with Superior Pseudocapacitive Performance. ACS Appl. Mater. Interfaces 2014, 6, 745-749.

81. Kasarda, D. D.; Black, D. R., Thermal Degradation of Proteins Studied by Mass Spectrometry. Biopolymers 1968, 6, 1001-1004.

82. Yablokov, V. A.; Vasina, Y. A.; Zelyaev, I. A.; Mitrofanova, S. V., Kinetics of Thermal Decomposition of Sulfur-Containing Amino Acids. Russ. J. Gen. Chem. 2009, 79, 1141-1145.

83. Guan, X.; Nai, J. W.; Zhang, Y. P.; Wang, P. X.; Yang, J.; Zheng, L. R.; Zhang, J.; Guo, L., CoO Hollow Cube/Reduced Graphene Oxide Composites with Enhanced Lithium Storage Capability. Chem. Mater. 2014, 26, 5958-5964.

84. Yang, J.; Liu, H. W.; Martens, W. N.; Frost, R. L., Synthesis and Characterization of Cobalt Hydroxide, Cobalt Oxyhydroxide, and Cobalt Oxide Nanodiscs. J. Phys. Chem. C 2010, 114, 111-119.

85. Biesinger, M. C.; Payne, B. P.; Grosvenor, A. P.; Lau, L. W. M.; Gerson, A. R.; Smart, R. S., Resolving Surface Chemical States in Xps Analysis of First Row Transition Metals, Oxides and Hydroxides: Cr, Mn, Fe, Co and Ni. Appl. Surf. Sci. 2011, 257, 2717-2730.

86. Burriel, M.; Garcia, G.; Santiso, J.; Abrutis, A.; Saltyte, Z.; Figueras, A., Growth Kinetics, Composition, and Morphology of Co3o4 Thin Films Prepared by Pulsed Liquid-Injection Mocvd. Chem. Vap. Deposition 2005, 11, 106-111.

87. Lu, Z. Y.; Chang, Z.; Liu, J. F.; Sun, X. M., Stable Ultrahigh Specific Capacitance of NiO Nanorod Arrays. Nano Res. 2011, 4, 658-665.

88. Wang, G. X.; Shen, X. P.; Horvat, J.; Wang, B.; Liu, H.; Wexler, D.; Yao, J., Hydrothermal Synthesis and Optical, Magnetic, and Supercapacitance Properties of Nanoporous Cobalt Oxide Nanorods. J. Phys. Chem. C 2009, 113, 4357-4361.

89. Peng, D. L.; Sumiyama, K.; Konno, T. J.; Hihara, T.; Yamamuro, S., Characteristic Transport Properties of CoO-Coated Monodispersive Co Cluster Assemblies. Phys. Rev. B 1999, 60, 2093-2100.

90. Guru, P. S.; Dash, S., Sorption on Eggshell Waste-a Review on Ultrastructure, Biomineralization and Other Applications. Adv. Colloid Interface Sci. 2014, 209, 49-67.

91. Nancollas, G. H.; Wu, W. J., Biomineralization Mechanisms: A Kinetics and Interfacial Energy Approach. J. Cryst. Growth 2000, 211, 137-142.

92. Nys, Y.; Gautron, J.; Garcia-Ruiz, J. M.; Hincke, M. T., Avian Eggshell Mineralization: Biochemical and Functional Characterization of Matrix Proteins. Comptes Rendus Palevol 2004, 3, 549-562.

93. Takiguchi, M.; Igarashi, K.; Azuma, M.; Ooshima, H., Flowerlike Agglomerates of Calcium Carbonate Crystals Formed on an Eggshell Membrane. Cryst. Growth Des. 2006, 6, 2754-2757.

94. Liu, J. C.; Xu, Y. J.; Ma, X. J.; Feng, J. K.; Qian, Y. T.; Xiong, S. L., Multifunctional CoO@C Metasequoia Arrays for Enhanced Lithium Storage. Nano Energy 2014, 7, 52-62.

95. Zhang, M.; Uchaker, E.; Hu, S.; Zhang, Q. F.; Wang, T. H.; Cao, G. Z.; Li, J. Y., CoO-Carbon Nanofiber Networks Prepared by Electrospinning as Binder-Free Anode Materials for Lithium-Ion Batteries with Enhanced Properties. Nanoscale 2013, 5, 12342-12349.

96. Zhang, M.; Jia, M. Q.; Jin, Y. H.; Shi, X. R., Synthesis and Electrochemical Performance of CoO/Graphene Nanocomposite as Anode for Lithium Ion Batteries. Appl. Surf. Sci. 2012, 263, 573-578.

97. Sun, Y.; Du, C.; Feng, X. Y.; Yu, Y.; Lieberwirth, I.; Chen, C. H., Electrostatic Spray Deposition of Nanoporous CoO/Co Composite Thin Films as Anode Materials for Lithium-Ion Batteries. Appl. Surf. Sci. 2012, 259, 769-773.

98. Deng, W.; Sun, Y. R.; Su, Q.; Xie, E. Q.; Lan, W., Porous CoO Nanobundles Composited with 3D Graphene Foams for Supercapacitors Electrodes. Mater. Lett. 2014, 137, 124-127.

99. Ji, D. L.; Li, J. H.; Chen, L. M.; Zhang, D.; Liu, T.; Zhang, N.; Ma, R. Z.; Qiu, G. Z.; Liu, X. H., Needle-Like CoO Nanowires Grown on Carbon Cloth for Enhanced Electrochemical Properties in Supercapacitors. RSC Adv. 2015, 5, 41627-41630.

100. Saravanakumar, B.; Purushothaman, K. K.; Muralidharan, G., Interconnected V2O5 Nanoporous Network for High-Performance Supercapacitors. ACS Appl. Mater. Interfaces 2012, 4, 4484-4490.

101. Kruger, M. B.; Jeanloz, R., Memory Glass - an Amorphous Material Formed from AlPO4. Science 1990, 249, 647-649.

102. Lu, Z. P.; Liu, C. T.; Thompson, J. R.; Porter, W. D., Structural Amorphous Steels. Phys. Rev. Lett. 2004, 92, 245503.

103. Yang, J. S.; Xu, J. J., Nanoporous Amorphous Manganese Oxide as Electrocatalyst for Oxygen Reduction in Alkaline Solutions. Electrochem. Commun. 2003, 5, 306-311.

104. Noll, F.; Sumper, M.; Hampp, N., Nanostructure of Diatom Silica Surfaces and of Biomimetic Analogues. Nano Lett. 2002, 2, 91-95.

105. Poulsen, N.; Kroger, N., Silica Morphogenesis by Alternative Processing of Silaffins in the Diatom Thalassiosira Pseudonana. J. Biol. Chem. 2004, 279, 42993-42999.

106. Addadi, L.; Raz, S.; Weiner, S., Taking Advantage of Disorder: Amorphous Calcium Carbonate and Its Roles in Biomineralization. Adv. Mater. 2003, 15, 959-970.

107. Cai, Y. R.; Tang, R. K., Calcium Phosphate Nanoparticles in Biomineralization and Biomaterials. J. Mater. Chem. 2008, 18, 3775-3787.

108. Nai, J.; Kang, J.; Guo, L., Tailoring the Shape of Amorphous Nanomaterials: Recent Developments and Applications. Science China Materials 2015, 58, 44-59.

109. Yin, Y. J.; Hu, Y. J.; Wu, P.; Zhang, H.; Cai, C. X., A Graphene-Amorphous FePO4 Hollow Nanosphere Hybrid as a Cathode Material for Lithium Ion Batteries. Chem. Commun. 2012, 48, 2137-2139.

110. Fang, Y. J.; Xiao, L. F.; Qian, J. F.; Ai, X. P.; Yang, H. X.; Cao, Y. L., Mesoporous Amorphous FePO4 Nanospheres as High-Performance Cathode Material for Sodium-Ion Batteries. Nano Lett. 2014, 14, 3539-3543.

111. Kim, S. W.; Ryu, J.; Park, C. B.; Kang, K., Carbon Nanotube-Amorphous FePO4 Core-Shell Nanowires as Cathode Material for Li Ion Batteries. Chem. Commun. 2010, 46, 7409-7411.

112. Wang, Q.; Li, H.; Chen, L. Q.; Huang, X. J., Monodispersed Hard Carbon Spherules with Uniform Nanopores. Carbon 2001, 39, 2211-2214.

113. Luo, W.; Schardt, J.; Bommier, C.; Wang, B.; Razink, J.; Simonsen, J.; Ji, X. L., Carbon Nanofibers Derived from Cellulose Nanofibers as a Long-Life Anode Material for Rechargeable Sodium-Ion Batteries. J. Mater. Chem. A 2013, 1, 10662-10666.

114. Xiong, H.; Slater, M. D.; Balasubramanian, M.; Johnson, C. S.; Rajh, T., Amorphous TiO2 Nanotube Anode for Rechargeable Sodium Ion Batteries. J. Phys. Chem. Lett. 2011, 2, 2560-2565.

115. Kim, Y.; Park, Y.; Choi, A.; Choi, N. S.; Kim, J.; Lee, J.; Ryu, J. H.; Oh, S. M.; Lee, K. T., An Amorphous Red Phosphorus/Carbon Composite as a Promising Anode Material for Sodium Ion Batteries. Adv. Mater. 2013, 25, 3045-3049.

116. Uchaker, E.; Zheng, Y. Z.; Li, S.; Candelaria, S. L.; Hu, S.; Cao, G. Z., Better Than Crystalline: Amorphous Vanadium Oxide for Sodium-Ion Batteries. J. Mater. Chem. A 2014, 2, 18208-18214.

117. Barranco, V.; Lillo-Rodenas, M. A.; Linares-Solano, A.; Oya, A.; Pico, F.; Ibanez, J.; Agullo-Rueda, F.; Amarilla, J. M.; Rojo, J. M., Amorphous Carbon Nanofibers and Their Activated Carbon Nanofibers as Supercapacitor Electrodes. J. Phys. Chem. C 2010, 114, 10302-10307.

118. Li, J.; Wang, X. Y.; Huang, Q. H.; Gamboa, S.; Sebastian, P. J., Studies on Preparation and Performances of Carbon Aerogel Electrodes for the Application of Supercapacitor. J. Power Sources 2006, 158, 784-788.

119. Yuan, D. S.; Zhou, T. X.; Zhou, S. L.; Zou, W. J.; Mo, S. S.; Xia, N. N., Nitrogen-Enriched Carbon Nanowires from the Direct Carbonization of Polyaniline Nanowires and Its Electrochemical Properties. Electrochem. Commun. 2011, 13, 242-246.

120. Niu, L. Y.; Li, Z. P.; Xu, Y.; Sun, J. F.; Hong, W.; Liu, X. H.; Wang, J. Q.; Yang, S. R., Simple Synthesis of Amorphous NiWO4 Nanostructure and Its Application as a Novel

Cathode Material for Asymmetric Supercapacitors. ACS Appl. Mater. Interfaces 2013, 5, 8044-8052.

121. Munaiah, Y.; Raj, B. G. S.; Kumar, T. P.; Ragupathy, P., Facile Synthesis of Hollow Sphere Amorphous Mno2: The Formation Mechanism, Morphology and Effect of a Bivalent Cation-Containing Electrolyte on Its Supercapacitive Behavior. J. Mater. Chem. A 2013, 1, 4300-4306.

122. Gujar, T. P.; Shinde, V. R.; Lokhande, C. D.; Kim, W. Y.; Jung, K. D.; Joo, O. S., Spray Deposited Amorphous RuO2 for an Effective Use in Electrochemical Supercapacitor. Electrochem. Commun. 2007, 9, 504-510.

123. Prasad, K. R.; Koga, K.; Miura, N., Electrochemical Deposition of Nanostructured Indium Oxide: High-Performance Electrode Material for Redox Supercapacitors. Chem. Mater. 2004, 16, 1845-1847.

124. Shi, F.; Li, L.; Wang, X. L.; Gu, C. D.; Tu, J. P., Metal Oxide/Hydroxide-Based Materials for Supercapacitors. RSC Adv. 2014, 4, 41910-41921.

125. Gao, S.; Sun, Y. F.; Lei, F. C.; Liang, L.; Liu, J. W.; Bi, W. T.; Pan, B. C.; Xie, Y., Ultrahigh Energy Density Realized by a Single-Layer Beta-Co(OH)2 All-Solid-State Asymmetric Supercapacitor. Angew. Chem. Int. Ed. 2014, 53, 12789-12793.

126. Cao, L.; Xu, F.; Liang, Y. Y.; Li, H. L., Preparation of the Novel Nanocomposite Co(OH)2/Ultra-Stable Y Zeolite and Its Application as a Supercapacitor with High Energy Density. Adv. Mater. 2004, 16, 1853-1857.

127. Yuan, C. Z.; Hou, L. R.; Shen, L. F.; Li, D. K.; Zhang, F.; Fan, C. G.; Li, J. M.; Zhang, X. G., A Novel Method to Synthesize Whisker-Like Co(OH)2 and Its Electrochemical Properties as an Electrochemical Capacitor Electrode. Electrochim. Acta 2010, 56, 115-121.

128. Hu, C. C.; Chen, J. C.; Chang, K. H., Cathodic Deposition of Ni(OH)2 and Co(OH)2 for Asymmetric Supercapacitors: Importance of the Electrochemical Reversibility of Redox Couples. J. Power Sources 2013, 221, 128-133.

129. Liu, C. J.; Li, Y. W., Synthesis and Characterization of Amorphous Alpha-Nickel Hydroxide. J. Alloys Compd. 2009, 478, 415-418.

130. Wang, L.; Dong, Z. H.; Wang, Z. G.; Zhang, F. X.; Jin, J., Layered -Co(OH)2 Nanocones as Electrode Materials for Pseudocapacitors: Understanding the Effect of Interlayer Space on Electrochemical Activity. Adv. Funct. Mater. 2013, 23, 2758-2764.

131. Tang, Y. F.; Liu, Y. Y.; Yu, S. X.; Mu, S. C.; Xiao, S. H.; Zhao, Y. F.; Gao, F. M., Morphology Controlled Synthesis of Monodisperse Cobalt Hydroxide for Supercapacitor with High Performance and Long Cycle Life. J. Power Sources 2014, 256, 160-169.

132. Zhou, W. J.; Xu, M. W.; Zhao, D. D.; Xu, C. L.; Li, L., Electrodeposition and Characterization of Ordered Mesoporous Cobalt Hydroxide Films on Different Substrates for Supercapacitors. Microporous Mesoporous Mater. 2009, 117, 55-60.

133. Zhou, W. J.; Zhang, J.; Xue, T.; Zhao, D. D.; Li, H. L., Electrodeposition of Ordered Mesoporous Cobalt Hydroxide Film from Lyotropic Liquid Crystal Media for Electrochemical Capacitors. J. Mater. Chem. 2008, 18, 905-910.

134. Chang, J. K.; Wu, C. M.; Sun, I. W., Nano-Architectured Co(OH)2 Electrodes Constructed Using an Easily-Manipulated Electrochemical Protocol for High-Performance Energy Storage Applications. J. Mater. Chem. 2010, 20, 3729-3735.

135. Gupta, V.; Kusahara, T.; Toyama, H.; Gupta, S.; Miura, N., Potentiostatically Deposited Nanostructured Alpha-Co(OH)2: A High Performance Electrode Material for Redox-Capacitors. Electrochem. Commun. 2007, 9, 2315-2319.

136. Zhang, F.; Zhang, W. B.; Shi, Z.; Wang, D.; Jin, J.; Jiang, L., Nanowire-Haired Inorganic Membranes with Superhydrophilicity and Underwater Ultralow Adhesive

Superoleophobicity for High-Efficiency Oil/Water Separation. Adv. Mater. 2013, 25, 4192-4198.

137. Zhao, T.; Jiang, H.; Ma, J., Surfactant-Assisted Electrochemical Deposition of Alpha-Cobalt Hydroxide for Supercapacitors. J. Power Sources 2011, 196, 860-864.

138. Zhu, Y. C.; Li, H. L.; Koltypin, Y.; Gedanken, A., Preparation of Nanosized Cobalt Hydroxides and Oxyhydroxide Assisted by Sonication. J. Mater. Chem. 2002, 12, 729-733.

139. Liu, Y. L.; Xu, Y. H.; Han, X. G.; Pellegrinelli, C.; Zhu, Y. J.; Zhu, H. L.; Wan, J. Y.; Chung, A. C.; Vaaland, O.; Wang, C. S.; Hu, L. B., Porous Amorphous FePO4 Nanoparticles Connected by Single-Wall Carbon Nanotubes for Sodium Ion Battery Cathodes. Nano Lett. 2012, 12, 5664-5668.

140. Salunkhe, R. R.; Bastakoti, B. P.; Hsu, C. T.; Suzuki, N.; Kim, J. H.; Dou, S. X.; Hu, C. C.; Yamauchi, Y., Direct Growth of Cobalt Hydroxide Rods on Nickel Foam and Its Application for Energy Storage. Chem. - Eur. J. 2014, 20, 3084-3088.

141. Xu, R.; Zeng, H. C., Dimensional Control of Cobalt-Hydroxide-Carbonate Nanorods and Their Thermal Conversion to One-Dimensional Arrays of Co3O4 Nanoparticles. J. Phys. Chem. B 2003, 107, 12643-12649.

142. Chen, Y. J.; Qu, B. H.; Hu, L. L.; Xu, Z.; Li, Q. H.; Wang, T. H., High-Performance Supercapacitor and Lithium-Ion Battery Based on 3D Hierarchical NH4F-induced Nickel Cobaltate Nanosheet-Nanowire Cluster Arrays as Self-Supported Electrodes. Nanoscale 2013, 5, 9812-9820.

143. Xie, X. W.; Shang, P. J.; Liu, Z. Q.; Lv, Y. G.; Li, Y.; Shen, W. J., Synthesis of Nanorod-Shaped Cobalt Hydroxycarbonate and Oxide with the Mediation of Ethylene Glycol. J. Phys. Chem. C 2010, 114, 2116-2123.

144. Hosono, E.; Fujihara, S.; Honma, I.; Zhou, H. S., Fabrication of Morphology and Crystal Structure Controlled Nanorod and Nanosheet Cobalt Hydroxide Based on the

Difference of Oxygen-Solubility between Water and Methanol, and Conversion into Co3O4. J. Mater. Chem. 2005, 15, 1938-1945.

145. Zhao, Z. G.; Geng, F. X.; Bai, J. B.; Cheng, H. M., Facile and Controlled Synthesis of 3D Nanorods-Based Urchinlike and Nonosheets-Based Flowerlike Cobalt Basic Salt Nanostructures. J. Phys. Chem. C 2007, 111, 3848-3852.

146. Zhang, H.; Wu, J. B.; Zhai, C. X.; Ma, X. Y.; Du, N.; Tu, J. P.; Yang, D. R., From Cobalt Nitrate Carbonate Hydroxide Hydrate Nanowires to Porous Co3O4 Nanorods for High Performance Lithium-Ion Battery Electrodes. Nanotechnology 2008, 19, 035711.

147. Xiong, S. L.; Chen, J. S.; Lou, X. W.; Zeng, H. C., Mesoporous Co3O4 and CoO@C Topotactically Transformed from Chrysanthemum-Like Co(CO3)0.5(OH)0.11H2O and Their Lithium-Storage Properties. Adv. Funct. Mater. 2012, 22, 861-871.

148. Xu, Z. P.; Zeng, H. C., Interconversion of Brucite-Like and Hydrotalcite-Like Phases in Cobalt Hydroxide Compounds. Chem. Mater. 1999, 11, 67-74.

149. Mann, S., Biomineralization : Principles and Concepts in Bioinorganic Materials Chemistry. Oxford University Press: New York, 2001.

150. Oaki, Y.; Kajiyama, S.; Nishimura, T.; Kato, T., Selective Synthesis and Thin-Film Formation of Alpha-Cobalt Hydroxide through an Approach Inspired by Biomineralization. J. Mater. Chem. 2008, 18, 4140-4142.

151. Wang, W. Z.; Feng, K.; Wang, Z.; Ma, Y. Y.; Zhang, S. Y.; Liang, Y. J., Controllable Synthesis and Growth Mechanism of Alpha-Co(OH)2 Nanorods and Nanoplates by a Facile Solution-Phase Route. J. Solid State Chem. 2011, 184, 3299-3302.

152. Wang, S. L.; Qian, L. Q.; Xu, H.; Lu, G. L.; Dong, W. J.; Tang, W. H., Synthesis and Structural Characterization of Cobalt Hydroxide Carbonate Nanorods and Nanosheets. J. Alloys Compd. 2009, 476, 739-743.

153. Hu, Z. A.; Xie, Y. L.; Wang, Y. X.; Xie, L. J.; Fu, G. R.; Jin, X. Q.; Zhang, Z. Y.; Yang, Y. Y.; Wu, H. Y., Synthesis of Alpha-Cobalt Hydroxides with Different Intercalated Anions and Effects of Intercalated Anions on Their Morphology, Basal Plane Spacing, and Capacitive Property. J. Phys. Chem. C 2009, 113, 12502-12508.

154. Jiang, J. A.; Liu, J. P.; Ding, R. M.; Zhu, J. H.; Li, Y. Y.; Hu, A. Z.; Li, X.; Huang, X. T., Large-Scale Uniform Alpha-Co(OH)2 Long Nanowire Arrays Grown on Graphite as Pseudocapacitor Electrodes. ACS Appl. Mater. Interfaces 2011, 3, 99-103.

155. Liang, Y. Y.; Cao, L.; Kong, L. B.; Li, H. L., Synthesis of Co(OH)2/USY Composite and Its Application for Electrochemical Supercapacitors. J. Power Sources 2004, 136, 197-200.

156. Yan, J.; Fan, Z. J.; Sun, W.; Ning, G. Q.; Wei, T.; Zhang, Q.; Zhang, R. F.; Zhi, L. J.; Wei, F., Advanced Asymmetric Supercapacitors Based on Ni(OH)2/Graphene and Porous Graphene Electrodes with High Energy Density. Adv. Funct. Mater. 2012, 22, 2632-2641.

157. Yan, J.; Wei, T.; Qiao, W. M.; Shao, B.; Zhao, Q. K.; Zhang, L. J.; Fan, Z. J., Rapid Microwave-Assisted Synthesis of Graphene Nanosheet/Co3O4 Composite for Supercapacitors. Electrochim. Acta 2010, 55, 6973-6978.

158. Pan, G. X.; Xia, X.; Cao, F.; Tang, P. S.; Chen, H. F., Porous Co(OH)2/Ni Composite Nanoflake Array for High Performance Supercapacitors. Electrochim. Acta 2012, 63, 335-340.

159. Guo, D.; Yu, X. Z.; Shi, W.; Luo, Y. Z.; Li, Q. H.; Wang, T. H., Facile Synthesis of Well-Ordered Manganese Oxide Nanosheet Arrays on Carbon Cloth for High-Performance Supercapacitors. J. Mater. Chem. A 2014, 2, 8833-8838.

160. Li, H. B.; Yu, M. H.; Wang, F. X.; Liu, P.; Liang, Y.; Xiao, J.; Wang, C. X.; Tong, Y. X.; Yang, G. W., Amorphous Nickel Hydroxide Nanospheres with Ultrahigh Capacitance and Energy Density as Electrochemical Pseudocapacitor Materials. Nat. Commun. 2013, 4, 1894.

161. Li, H. B.; Gao, Y. Q.; Wang, C. X.; Yang, G. W., A Simple Electrochemical Route to Access Amorphous Mixed-Metal Hydroxides for Supercapacitor Electrode Materials. Adv. Energy Mater. 2015, 5, 1401767.

162. Zhu, Y. G.; Wang, Y.; Shi, Y. M.; Huang, Z. X.; Fu, L.; Yang, H. Y., Phase Transformation Induced Capacitance Activation for 3D Graphene-CoO Nanorod Pseudocapacitor. Adv. Energy Mater. 2014, 4, 1301788.

163. Yuan, C. Z.; Zhang, X. G.; Su, L. H.; Gao, B.; Shen, L. F., Facile Synthesis and Self-Assembly of Hierarchical Porous NiO Nano/Micro Spherical Superstructures for High Performance Supercapacitors. J. Mater. Chem. 2009, 19, 5772-5777.

164. Zhang, Y. Q.; Xia, X. H.; Tu, J. P.; Mai, Y. J.; Shi, S. J.; Wang, X. L.; Gu, C. D., Self-Assembled Synthesis of Hierarchically Porous NiO Film and Its Application for Electrochemical Capacitors. J. Power Sources 2012, 199, 413-417.

165. Li, J. T.; Zhao, W.; Huang, F. Q.; Manivannan, A.; Wu, N. Q., Single-Crystalline Ni(OH)2 and NiO Nanoplatelet Arrays as Supercapacitor Electrodes. Nanoscale 2011, 3, 5103-5109.

166. Zhang, X. J.; Shi, W. H.; Zhu, J. X.; Kharistal, D. J.; Zhao, W. Y.; Lalia, B. S.; Hng, H. H.; Yan, Q. Y., High-Power and High-Energy-Density Flexible Pseudocapacitor Electrodes Made from Porous CuO Nanobelts and Single-Walled Carbon Nanotubes. Acs Nano 2011, 5, 2013-2019.

167. Patil, U. M.; Lee, S. C.; Sohn, J. S.; Kulkarni, S. B.; Gurav, K. V.; Kim, J. H.; Kim, J. H.; Lee, S.; Jun, S. C., Enhanced Symmetric Supercapacitive Performance of Co(OH)2 Nanorods Decorated Conducting Porous Graphene Foam Electrodes. Electrochim. Acta 2014, 129, 334-342.

168. Nai, J. W.; Wang, S. Q.; Bai, Y.; Guo, L., Amorphous Ni(OH)2 Nanoboxes: Fast Fabrication and Enhanced Sensing for Glucose. Small 2013, 9, 3147-3152.

169. Yang, W. L.; Gao, Z.; Ma, J.; Wang, J.; Zhang, X. M.; Liu, L. H., Two-Step Electrodeposition Construction of Flower-on-Sheet Hierarchical Cobalt Hydroxide Nano-Forest for High-Capacitance Supercapacitors. Dalton Trans. 2013, 42, 15706-15715.

170. Hosono, E.; Fujihara, S.; Honma, I.; Ichihara, M.; Zhou, H. S., Synthesis of the Coooh Fine Nanoflake Film with the High Rate Capacitance Property. J. Power Sources 2006, 158, 779-783.

171. Etacheri, V.; Marom, R.; Elazari, R.; Salitra, G.; Aurbach, D., Challenges in the Development of Advanced Li-Ion Batteries: A Review. Energy Environ. Sci. 2011, 4, 3243-3262.

172. Poizot, P.; Laruelle, S.; Grugeon, S.; Dupont, L.; Tarascon, J., Nano-Sized Transition-Metal Oxides as Negative-Electrode Materials for Lithium-Ion Batteries. Nature 2000, 407, 496-499.

173. Wang, Z. Y.; Zhou, L.; Lou, X. W., Metal Oxide Hollow Nanostructures for Lithium-Ion Batteries. Adv. Mater. 2012, 24, 1903-1911.

174. Wang, G. X.; Chen, Y.; Konstantinov, K.; Lindsay, M.; Liu, H. K.; Dou, S. X., Investigation of Cobalt Oxides as Anode Materials for Li-Ion Batteries. J. Power Sources 2002, 109, 142-147.

175. Li, F.; Zou, Q. Q.; Xia, Y. Y., CoO-Loaded Graphitable Carbon Hollow Spheres as Anode Materials for Lithium-Ion Battery. J. Power Sources 2008, 177, 546-552.

176. Sun, Y. M.; Hu, X. L.; Luo, W.; Huang, Y. H., Self-Assembled Mesoporous CoO Nanodisks as a Long-Life Anode Material for Lithium-Ion Batteries. J. Mater. Chem. 2012, 22, 13826-13831.

177. Zhang, L. J.; Hu, P.; Zhao, X. Y.; Tian, R. L.; Zou, R. Q.; Xia, D. G., Controllable Synthesis of Core-Shell Co@CoO Nanocomposites with a Superior Performance as an Anode Material for Lithium-Ion Batteries. J. Mater. Chem. 2011, 21, 18279-18283.

178. Zhu, W. J.; Huang, H.; Gan, Y. P.; Tao, X. Y.; Xia, Y.; Zhang, W. K., Mesoporous Cobalt Monoxide Nanorods Grown on Reduced Graphene Oxide Nanosheets with High Lithium Storage Performance. Electrochim. Acta 2014, 138, 376-382.

179. Qiao, H.; Xiao, L. F.; Zheng, Z.; Liu, H. W.; Jia, F. L.; Zhang, L. Z., One-Pot Synthesis of CoO/C Hybrid Microspheres as Anode Materials for Lithium-Ion Batteries. J. Power Sources 2008, 185, 486-491.

180. Li, D. D.; Ding, L. X.; Wang, S. Q.; Cai, D. D.; Wang, H. H., Ultrathin and Highly-Ordered CoO Nanosheet Arrays for Lithium-Ion Batteries with High Cycle Stability and Rate Capability. J. Mater. Chem. A 2014, 2, 5625-5630.

181. Guo, Y. G.; Hu, J. S.; Wan, L. J., Nanostructured Materials for Electrochemical Energy Conversion and Storage Devices Adv. Mater. 2008, 20, 4384-4384.

182. Yuan, W. W.; Zhang, J.; Xie, D.; Dong, Z. M.; Su, Q. M.; Du, G. H., Porous CoO/C Polyhedra as Anode Material for Li-Ion Batteries. Electrochim. Acta 2013, 108, 506-511.

183. Wu, F. D.; Wang, Y., Self-Assembled Echinus-Like Nanostructures of Mesoporous CoO Nanorod@CNT for Lithium-Ion Batteries. J. Mater. Chem. 2011, 21, 6636-6641.

184. King'ori, A., A Review of the Uses of Poultry Eggshells and Shell Membranes. Int. J. poult. sci 2011, 10, 908-912.

185. Balaz, M., Eggshell Membrane Biomaterial as a Platform for Applications in Materials Science. Acta Biomater. 2014, 10, 3827-3843.

186. Boro, J.; Deka, D.; Thakur, A. J., A Review on Solid Oxide Derived from Waste Shells as Catalyst for Biodiesel Production. Renewable Sustainable Energy Rev. 2012, 16, 904-910.

187. Ruff, K. J.; Winkler, A.; Jackson, R. W.; DeVore, D. P.; Ritz, B. W., Eggshell Membrane in the Treatment of Pain and Stiffness from Osteoarthritis of the Knee: A Randomized, Multicenter, Double-Blind, Placebo-Controlled Clinical Study. Clin. Rheumatol. 2009, 28, 907-914.

188. Dodson, J. R.; Parker, H. L.; Garcia, A. M.; Hicken, A.; Asemave, K.; Farmer, T. J.; He, H.; Clark, J. H.; Hunt, A. J., Bio-Derived Materials as a Green Route for Precious & Critical Metal Recovery and Re-Use. Green Chem. 2015, 17, 1951-1965.

189. Wang, Z. T.; Shao, X.; Hu, X.; Parkinson, G.; Xie, K.; Dong, D. H.; Li, C. Z., Hierarchically Structured NiO/CeO2 Nanocatalysts Templated by Eggshell Membranes for Methane Steam Reforming. Catal. Today 2014, 228, 199-205.

190. Mallampati, R.; Valiyaveettil, S., Biomimetic Metal Oxides for the Extraction of Nanoparticles from Water. Nanoscale 2013, 5, 3395-3399.

191. Meng, X.; Deng, D., Bio-Inspired Synthesis of A-Ni(OH)2 Nanobristles on Various Substrates and Their Applications. J. Mater. Chem. A 2016.

192. Zheng, X. G.; Hagihala, M.; Fujihala, M.; Kawae, T., Recent Developments in the Magnetic Study of the Deformed Pyrochlore Lattice M(2)(OH)(3)X (M=3d Magnetic Ions, X = Cl, Br) - Exotic Magnetic Order in Ni(2)(OH)(3)Cl and Controlled Spin-Spin Interactions in Co(2)(OH)(3)Cl(1-X)Br(X) and (Co(1-X)Fe(X))(2)(OH)(3)Cl. J. Phys.: Conf. Ser. 2009, 145.

193. Zheng, X. G.; Kawae, T.; Yamada, H.; Nishiyama, K.; Xu, C. N., Coexisting Ferromagnetic Order and Disorder in a Uniform System of Hydroxyhalide Co2(OH)3Cl. Phys. Rev. Lett. 2006, 97.

194. Zheng, X. G.; Hagihala, M.; Kawae, T.; Xu, C. N., Defect-Induced Short-Range-Order from a Spin-Ice Related State in Deformed Pyrochlore Co2(OH)3Cl. Phys. Rev. B 2008, 77.

195. Ma, J. J.; Yuan, T.; He, Y. S.; Wang, J. L.; Zhang, W. M.; Yang, D. Z.; Liao, X. Z.; Ma, Z. F., A Novel Graphene Sheet-Wrapped Co2(OH)3Cl Composite as a Long-Life Anode Material for Lithium Ion Batteries. J. Mater. Chem. A 2014, 2, 16925-16930.

196. J. Mater. Chem. A 2014Peterson, G. R.; Hung-Low, F.; Gumeci, C.; Bassett, W. P.; Korzeniewski, C.; Hope-Weeks, L. J., Preparation-Morphology-Performance Relationships in Cobalt Aerogels as Supercapacitors. ACS Appl. Mater. Interfaces 2014, 6, 1796-1803.

197. Zhang, Z.; Yin, L., Mn-Doped Co2(OH)3Cl Xerogels with 3D Interconnected Mesoporous Structures as Lithium Ion Battery Anodes with Improved Electrochemical Performance. J. Mater. Chem. A 2015.

198. Lee, J. W.; Ko, J. M.; Kim, J. D., Hierarchical Microspheres Based on Alpha-Ni(OH)2 Nanosheets Intercalated with Different Anions: Synthesis, Anion Exchange, and Effect of Intercalated Anions on Electrochemical Capacitance. J. Phys. Chem. C 2011, 115, 19445-19454.

199. Dewolff, P. M., The Crystal Structure of Co2(OH)3Cl. Acta Crystallographica 1953, 6, 359-360.

200. Hagihala, M.; Zheng, X. G.; Kawae, T., Drastic Anion Substitution Effect in Deformed Pyrochlore Lattice Co2(OH)3Cl1-xBrx. Phys. B 2009, 404, 671-673.

201. Yoon, T. J.; Lee, H.; Shao, H. L.; Hilderbrand, S. A.; Weissleder, R., Multicore Assemblies Potentiate Magnetic Properties of Biomagnetic Nanoparticles. Adv. Mater. 2011, 23, 4793-4797.

202. Jeong, G.; Kim, J. G.; Park, M. S.; Seo, M.; Hwang, S. M.; Kim, Y. U.; Kim, Y. J.; Kim, J. H.; Dou, S. X., Core-Shell Structured Silicon Nanoparticles@TiO2-X/Carbon Mesoporous Microfiber Composite as a Safe and High-Performance Lithium-Ion Battery Anode. Acs Nano 2014, 8, 2977-2985.

203. Hwang, T. H.; Lee, Y. M.; Kong, B. S.; Seo, J. S.; Choi, J. W., Electrospun Core-Shell Fibers for Robust Silicon Nanoparticle-Based Lithium Ion Battery Anodes. Nano Lett. 2012, 12, 802-807.

204. Zhang, H. R.; Qin, X. Y.; Wu, J. X.; He, Y. B.; Du, H. D.; Li, B. H.; Kang, F. Y., Electrospun Core-Shell Silicon/Carbon Fibers with an Internal Honeycomb-Like Conductive Carbon Framework as an Anode for Lithium Ion Batteries. J. Mater. Chem. A 2015, 3, 7112-7120.

205. Zhou, J.; Wang, S. T.; Nie, F. Q.; Feng, L.; Zhu, G. S.; Jiang, L., Elaborate Architecture of the Hierarchical Hen's Eggshell. Nano Res. 2011, 4, 171-179.

206. Lakshminarayanan, R.; Kini, R. M.; Valiyaveettil, S., Investigation of the Role of Ansocalcin in the Biomineralization in Goose Eggshell Matrix. Proc. Natl. Acad. Sci. U. S. A. 2002, 99, 5155-5159.

207. Germs, A., Hydrogen Sulphide Production in Eggs and Egg Products as a Result of Heating. J. Sci. Food Agric. 1973, 24, 7-16.

208. Kodali, V. K.; Gannon, S. A.; Paramasivam, S.; Raje, S.; Polenova, T.; Thorpe, C., A Novel Disulfide-Rich Protein Motif from Avian Eggshell Membranes. Plos One 2011, 6.

209. Dravid, V. P.; Host, J. J.; Teng, M. H.; Elliot, B.; Hwang, J. H.; Johnson, D. L.; Mason, T. O.; Weertman, J. R., Controlled-Size Nanocapsules. Nature 1995, 374, 602-602.

210. Sun, X. M.; Li, Y. D., Colloidal Carbon Spheres and Their Core/Shell Structures with Noble-Metal Nanoparticles. Angew. Chem. Int. Ed. 2004, 43, 597-601.

211. Wang, Z. H.; Zhang, Z. D.; Choi, C. J.; Kim, B. K., Structure and Magnetic Properties of Fe(C) and Co(C) Nanocapsules Prepared by Chemical Vapor Condensation. J. Alloys Compd. 2003, 361, 289-293.

212. Zhu, G. X.; Wei, X. W.; Jiang, S., A Facile Route to Carbon-Coated Nickel-Based Metal Nanoparticles. J. Mater. Chem. 2007, 17, 2301-2306.

213. Chen, C.; Hwang, B.; Do, J.; Weng, J.; Venkateswarlu, M.; Cheng, M.; Santhanam, R.; Ragavendran, K.; Lee, J.; Chen, J., An Understanding of Anomalous Capacity of Nano-Sized CoO Anode Materials for Advanced Li-Ion Battery. Electrochem. Commun. 2010, 12, 496-498.

214. Peng, C. X.; Chen, B. D.; Qin, Y.; Yang, S. H.; Li, C. Z.; Zuo, Y. H.; Liu, S. Y.; Yang, J. H., Facile Ultrasonic Synthesis of CoO Quantum Dot/Graphene Nanosheet Composites with High Lithium Storage Capacity. Acs Nano 2012, 6, 1074-1081.

215. Stevens, D. A.; Dahn, J. R., The Mechanisms of Lithium and Sodium Insertion in Carbon Materials. J. Electrochem. Soc. 2001, 148, A803-A811.

216. Ponrouch, A.; Taberna, P. L.; Simon, P.; Palacin, M. R., On the Origin of the Extra Capacity at Low Potential in Materials for Li Batteries Reacting through Conversion Reaction. Electrochim. Acta 2012, 61, 13-18.

217. Laruelle, S.; Grugeon, S.; Poizot, P.; Dolle, M.; Dupont, L.; Tarascon, J. M., On the Origin of the Extra Electrochemical Capacity Displayed by Mo/Li Cells at Low Potential. J. Electrochem. Soc. 2002, 149, A627-A634.

218. Zhang, M.; Wang, Y.; Jia, M. Q., Three-Dimensional Reduced Graphene Oxides Hydrogel Anchored with Ultrafine CoO Nanoparticles as Anode for Lithium Ion Batteries. Electrochim. Acta 2014, 129, 425-432.

219. Kang, Y. M.; Song, M. S.; Kim, J. H.; Kim, H. S.; Park, M. S.; Lee, J. Y.; Liu, H. K.; Dou, S. X., A Study on the Charge-Discharge Mechanism of Co3O4 as an Anode for the Li Ion Secondary Battery. Electrochim. Acta 2005, 50, 3667-3673.

220. Zhou, Z. Y.; Tian, N.; Li, J. T.; Broadwell, I.; Sun, S. G., Nanomaterials of High Surface Energy with Exceptional Properties in Catalysis and Energy Storage. Chem. Soc. Rev. 2011, 40, 4167-4185.

221. Sun, Z. Y.; Yuan, H. Q.; Liu, Z. M.; Han, B. X.; Zhang, X. R., A Highly Efficient Chemical Sensor Material for H2S: Alpha-Fe2O3 Nanotubes Fabricated Using Carbon Nanotube Templates. Adv. Mater. 2005, 17, 2993-2997.

222. Jiang, H. J., Chemical Preparation of Graphene-Based Nanomaterials and Their Applications in Chemical and Biological Sensors. Small 2011, 7, 2413-2427.

223. Bhushan, B.; Jung, Y. C., Natural and Biomimetic Artificial Surfaces for Superhydrophobicity, Self-Cleaning, Low Adhesion, and Drag Reduction. Prog. Mater Sci. 2011, 56, 1-108.

224. Farokhzad, O. C.; Langer, R., Impact of Nanotechnology on Drug Delivery. Acs Nano 2009, 3, 16-20.

225. Osterloh, F. E., Inorganic Nanostructures for Photoelectrochemical and Photocatalytic Water Splitting. Chem. Soc. Rev. 2013, 42, 2294-2320.

226. Zhang, Q. F.; Cao, G. Z., Nanostructured Photoelectrodes for Dye-Sensitized Solar Cells. Nano Today 2011, 6, 91-109.

227. Lak, A.; Mazloumi, M.; Mohajerani, M.; Kajbafvala, A.; Zanganeh, S.; Arami, H.; Sadrnezhaad, S. K., Self-Assembly of Dandelion-Like Hydroxyapatite Nanostructures Via Hydrothermal Method. J. Am. Ceram. Soc. 2008, 91, 3292-3297.

228. Chang, Y.; Zeng, H. C., Controlled Synthesis And. Self-Assembly of Single-Crystalline CuO Nanorods and Nanoribbons. Cryst. Growth Des. 2004, 4, 397-402.

229. Kamins, T. I.; Williams, R. S.; Chen, Y.; Chang, Y. L.; Chang, Y. A., Chemical Vapor Deposition of Si Nanowires Nucleated by TiSi2 Islands on Si. Applied Physics Letters 2000, 76, 562-564.

230. Byrappa, K.; Adschiri, T., Hydrothermal Technology for Nanotechnology. Prog. Cryst. Growth Charact. Mater. 2007, 53, 117-166.

231. Cassell, A. M.; Raymakers, J. A.; Kong, J.; Dai, H. J., Large Scale CVD Synthesis of Single-Walled Carbon Nanotubes. J. Phys. Chem. B 1999, 103, 6484-6492.

232. Obraztsov, A. N.; Obraztsova, E. A.; Tyurnina, A. V.; Zolotukhin, A. A., Chemical Vapor Deposition of Thin Graphite Films of Nanometer Thickness. Carbon 2007, 45, 2017-2021.

233. Singh, K. V.; Martinez-Morales, A. A.; Andavan, G. T. S.; Bozhilov, K. N.; Ozkan, M., A Simple Way of Synthesizing Single-Crystalline Semiconducting Copper Sulfide Nanorods by Using Ultrasonication During Template-Assisted Electrodeposition. Chem. Mater. 2007, 19, 2446-2454.

234. Xia, X. H.; Tu, J. P.; Zhang, Y. Q.; Chen, J.; Wang, X. L.; Gu, C. D.; Guan, C.; Luo, J. S.; Fan, H. J., Porous Hydroxide Nanosheets on Preformed Nanowires by Electrodeposition: Branched Nanoarrays for Electrochemical Energy Storage. Chem. Mater. 2012, 24, 3793-3799.

235. Cheng, Y. T.; Rodak, D. E.; Wong, C. A.; Hayden, C. A., Effects of Micro- and Nano-Structures on the Self-Cleaning Behaviour of Lotus Leaves. Nanotechnology 2006, 17, 1359-1362.

236. Huang, J. Y.; Wang, X. D.; Wang, Z. L., Bio-Inspired Fabrication of Antireflection Nanostructures by Replicating Fly Eyes. Nanotechnology 2008, 19.

237. Vukusic, P.; Sambles, J. R.; Lawrence, C. R.; Wootton, R. J., Quantified Interference and Diffraction in Single Morpho Butterfly Scales. Proceedings of the Royal Society B: Biological Sciences 1999, 266, 1403-1411.

238. Bixler, G. D.; Bhushan, B., Fluid Drag Reduction with Shark-Skin Riblet Inspired Microstructured Surfaces. Adv. Funct. Mater. 2013, 23, 4507-4528.

239. Imai, H.; Oaki, Y., Bioinspired Hierarchical Crystals. MRS Bull. 2010, 35, 138-144.

240. Autumn, K.; Peattie, A. M., Mechanisms of Adhesion in Geckos. Integr. Comp. Biol. 2002, 42, 1081-1090.

241. Epstein, A. K.; Pokroy, B.; Seminara, A.; Aizenberg, J., Bacterial Biofilm Shows Persistent Resistance to Liquid Wetting and Gas Penetration. Proceedings of the National Academy of Sciences of the United States of America 2011, 108, 995-1000.

242. Zhai, L.; Berg, M. C.; Cebeci, F. C.; Kim, Y.; Milwid, J. M.; Rubner, M. F.; Cohen, R. E., Patterned Superhydrophobic Surfaces: Toward a Synthetic Mimic of the Namib Desert Beetle. Nano Lett. 2006, 6, 1213-1217.

243. Gao, X. F.; Yan, X.; Yao, X.; Xu, L.; Zhang, K.; Zhang, J. H.; Yang, B.; Jiang, L., The Dry-Style Antifogging Properties of Mosquito Compound Eyes and Artificial Analogues Prepared by Soft Lithography. Adv. Mater. 2007, 19, 2213-2217.

244. Toro, P.; Quijada, R.; Yazdani-Pedram, M.; Arias, J. L., Eggshell, a New Bio-Filler for Polypropylene Composites. Mater. Lett. 2007, 61, 4347-4350.

245. Arias, J. L.; Fernandez, M. S., Biomimetic Processes through the Study of Mineralized Shells. Mater. Charact. 2003, 50, 189-195.

246. Waghmare, P. R.; Gunda, N. S. K.; Mitra, S. K., Under-Water Superoleophobicity of Fish Scales. Sci. Rep. 2014, 4.

247. Takiguchi, M.; Igarashi, K.; Azuma, M.; Ooshima, H., Tubular Structure Agglomerates of Calcium Carbonate Crystals Formed on a Cation-Exchange Membrane. Cryst. Growth Des. 2006, 6, 1611-1614.

248. Shi, W. K.; Jiang, H. W.; Qin, D. T.; Chen, Y., Friction and Wear Performance of Superfine Manganous Phosphate Conversion Coating. Tribology 2009, 29, 267-271.

249. Zhu, H. J.; Zhai, W.; Yang, M.; Liu, X. M.; Chen, Y. C.; Yang, H.; Shen, X. D., Synthesis and Characterization of Limnpo4/C Nano-Composites from Manganese(II) Phosphate Trihydrate Precipitated from a Micro-Channel Reactor Approach. RSC Adv. 2014, 4, 25625-25632.

250. Su, K.; Liu, F.; Chen, J. T., Preparation of High Performance Carbon-Coated Limnpo4 Nanocomposite by an Acetate-Assisted Antisolvent Precipitation Method. J. Power Sources 2013, 232, 234-239.

251. Zhang, P.; Song, L.; Lu, H. D.; Hu, Y.; Xing, W. Y.; Ni, J. X.; Wang, J., Synergistic Effect of Nanoflaky Manganese Phosphate on Thermal Degradation and Flame Retardant Properties of Intumescent Flame Retardant Polypropylene System. Polym. Degrad. Stab. 2009, 94, 201-207.

252. Peng, S.; Huang, J. W.; Wu, W. W.; Wu, X. H.; Liao, S.; Fan, Y. J., Synthesis Via Solid-State Reaction at Room Temperature and Characterization of Layered Nanocrystalline Mn3(PO4)2·3H2O. Applied Chemical Industry 2009, 12, 8.

253. Jin, K.; Park, J.; Lee, J.; Yang, K. D.; Pradhan, G. K.; Sim, U.; Jeong, D.; Jang, H. L.; Park, S.; Kim, D.; Sung, N. E.; Kim, S. H.; Han, S.; Nam, K. T., Hydrated Manganese(II) Phosphate (Mn-3(PO4)(2)Center Dot 3H(2)O) as a Water Oxidation Catalyst. J. Am. Chem. Soc. 2014, 136, 7435-7443.

254. Mauritz, K. A.; Moore, R. B., State of Understanding of Nafion. Chem. Rev. 2004, 104, 4535-4585.

255. Rozendal, R. A.; Hamelers, H. V. M.; Buisman, C. J. N., Effects of Membrane Cation Transport on Ph and Microbial Fuel Cell Performance. Environ. Sci. Technol. 2006, 40, 5206-5211.

256. Okada, T.; Xie, G.; Gorseth, O.; Kjelstrup, S.; Nakamura, N.; Arimura, T., Ion and Water Transport Characteristics of Nafion Membranes as Electrolytes. Electrochim. Acta 1998, 43, 3741-3747.

257. Wu, Y. S.; Chen, L.; Xie, K. W.; Li, J. P.; Chen, Y.; Tang, Y. W.; Zhou, Y. M.; Lu, T. H., Synthesis and Characterization of Multi-Wall Carbon Nanotubes Supported-Hydrated Iron Phosphate Cathode Material for Lithium-Ion Cells by a Novel Homogeneous Precipitation Method. Ionics 2012, 18, 721-729.

258. Miyazaki, T.; Sivaprakasam, K.; Tantry, J.; Suryanarayanan, R., Physical Characterization of Dibasic Calcium Phosphate Dihydrate and Anhydrate. J. Pharm. Sci. 2009, 98, 905-916.

259. Wullschleger, L.; Ghazi Wakili, K., Numerical Parameter Study of the Thermal Behaviour of a Gypsum Plaster Board at Fire Temperatures. Fire Mater. 2008, 32, 103-119.

260. Schmidt-Rohr, K.; Chen, Q., Parallel Cylindrical Water Nanochannels in Nafion Fuel-Cell Membranes. Nat. Mater. 2008, 7, 75-83.

261. Mann, S., Molecular Recognition in Biomineralization. Nature 1988, 332, 119-124.

262. Nasef, M. M.; Yahaya, A. H., Adsorption of Some Heavy Metal Ions from Aqueous Solutions on Nafion 117 Membrane. Desalination 2009, 249, 677-681.

263. Tian, D. L.; Zhang, X. F.; Tian, Y.; Wu, Y.; Wang, X.; Zhai, J.; Jiang, L., Photo-Induced Water-Oil Separation Based on Switchable Superhydrophobicity-Superhydrophilicity and Underwater Superoleophobicity of the Aligned Zno Nanorod Array-Coated Mesh Films. J. Mater. Chem. 2012, 22, 19652-19657.

264. Wang, B.; Guo, Z. G., Ph-Responsive Bidirectional Oil-Water Separation Material. Chem. Commun. 2013, 49, 9416-9418.

265. Xue, Z. X.; Wang, S. T.; Lin, L.; Chen, L.; Liu, M. J.; Feng, L.; Jiang, L., A Novel Superhydrophilic and Underwater Superoleophobic Hydrogel-Coated Mesh for Oil/Water Separation. Adv. Mater. 2011, 23, 4270-4273.

266. Brimblecombe, R.; Koo, A.; Dismukes, G. C.; Swiegers, G. F.; Spiccia, L., Solar Driven Water Oxidation by a Bioinspired Manganese Molecular Catalyst. J. Am. Chem. Soc. 2010, 132, 2892-2894.

267. Yang, C.; Dong, L.; Chen, Z. X.; Lu, H. B., High-Performance All-Solid-State Supercapacitor Based on the Assembly of Graphene and Manganese(II) Phosphate Nanosheets. J. Phys. Chem. C 2014, 118, 18884-18891.

268. Gao, H.; Lian, K., Proton-Conducting Polymer Electrolytes and Their Applications in Solid Supercapacitors: A Review. RSC Adv. 2014, 4, 33091-33113.

269. Kamath, P. V.; Dixit, M.; Indira, L.; Shukla, A. K.; Kumar, V. G.; Munichandraiah, N., Stabilized Alpha-Ni(OH)2 as Electrode Material for Alkaline Secondary Cells. J. Electrochem. Soc. 1994, 141, 2956-2959.

270. Gao, M. R.; Sheng, W. C.; Zhuang, Z. B.; Fang, Q. R.; Gu, S.; Jiang, J.; Yan, Y. S., Efficient Water Oxidation Using Nanostructured Alpha-Nickel-Hydroxide as an Electrocatalyst. J. Am. Chem. Soc. 2014, 136, 7077-7084.

271. Wu, H.; Xu, M.; Wu, H. Y.; Xu, J. J.; Wang, Y. L.; Peng, Z.; Zheng, G. F., Aligned NiO Nanoflake Arrays Grown on Copper as High Capacity Lithium-Ion Battery Anodes. J. Mater. Chem. 2012, 22, 19821-19825.

272. Ji, J. Y.; Zhang, L. L.; Ji, H. X.; Li, Y.; Zhao, X.; Bai, X.; Fan, X. B.; Zhang, F. B.; Ruoff, R. S., Nanoporous Ni(OH) Thin Film on 3D Ultrathin-Graphite Foam for Asymmetric Supercapacitor. Acs Nano 2013, 7, 6237-6243.

273. Li, G. H.; Wang, X. W.; Liu, L.; Liu, R.; Shen, F. P.; Cui, Z.; Chen, W.; Zhang, T., Controllable Synthesis of 3D Ni(OH)(2) and NiO Nanowalls on Various Substrates for High-Performance Nanosensors. Small 2015, 11, 731-739.

274. Xu, L. P.; Ding, Y. S.; Chen, C. H.; Zhao, L. L.; Rimkus, C.; Joesten, R.; Suib, S. L., 3D Flowerlike Alpha-Nickel Hydroxide with Enhanced Electrochemical Activity Synthesized by Microwave-Assisted Hydrothermal Method. Chem. Mater. 2008, 20, 308-316.

275. Jeevanandam, P.; Koltypin, Y.; Gedanken, A., Synthesis of Nanosized Alpha-Nickel Hydroxide by a Sonochemical Method. Nano Lett. 2001, 1, 263-266.

276. Du, H. M.; Jiao, L. F.; Cao, K. Z.; Wang, Y. J.; Yuan, H. T., Polyol-Mediated Synthesis of Mesoporous Alpha-Ni(OH)(2) with Enhanced Supercapacitance. ACS Appl. Mater. Interfaces 2013, 5, 6643-6648.

277. Wang, H. J.; Gao, J.; Li, Z. G.; Ge, Y. L.; Kan, K.; Shi, K. Y., One-Step Synthesis of Hierarchical Alpha-Ni(OH)(2) Flowerlike Architectures and Their Gas Sensing Properties for Nox at Room Temperature. Crystengcomm 2012, 14, 6843-6852.

278. Meng, X. H.; Deng, D., Bio-Inspired Formation of Nanostructured Arrays on Flexible Substrates with Superoleophobicity. Crystengcomm 2015, 17, 8441-8448.

279. Hu, G.; Li, C.; Gong, H., Capacitance Decay of Nanoporous Nickel Hydroxide. J. Power Sources 2010, 195, 6977-6981.

280. Zhao, D. D.; Bao, S. J.; Zhou, W. H.; Li, H. L., Preparation of Hexagonal Nanoporous Nickel Hydroxide Film and Its Application for Electrochemical Capacitor. Electrochem. Commun. 2007, 9, 869-874.

281. Gao, T.; Jelle, B. P., Paraotwayite-Type Alpha-Ni(OH)(2) Nanowires: Structural, Optical, and Electrochemical Properties. J. Phys. Chem. C 2013, 117, 17294-17302.

282. Cheng, B.; Le, Y.; Cai, W. Q.; Yu, J. G., Synthesis of Hierarchical Ni(OH)(2) and NiO Nanosheets and Their Adsorption Kinetics and Isotherms to Congo Red in Water. J. Hazard. Mater. 2011, 185, 889-897.

283. Aghazadeh, M.; Ghaemi, M.; Sabour, B.; Dalvand, S., Electrochemical Preparation of Alpha-Ni(OH)(2) Ultrafine Nanoparticles for High-Performance Supercapacitors. J. Solid State Electrochem. 2014, 18, 1569-1584.

284. Chen, S.; Zhu, J. W.; Zhou, H.; Wang, X., One-Step Synthesis of Low Defect Density Carbon Nanotube-Doped Ni(OH)(2) Nanosheets with Improved Electrochemical Performances. RSC Adv. 2011, 1, 484-489.

285. Wang, R. T.; Lang, J. W.; Liu, Y. H.; Lin, Z. Y.; Yan, X. B., Ultra-Small, Size-Controlled Ni(OH)(2) Nanoparticles: Elucidating the Relationship between Particle Size and Electrochemical Performance for Advanced Energy Storage Devices. NPG Asia Mater. 2015, 7.

286. Hu, W. K.; Noreus, D., Alpha Nickel Hydroxides as Lightweight Nickel Electrode Materials for Alkaline Rechargeable Cells. Chem. Mater. 2003, 15, 974-978.

287. Liu, B. H.; Yu, S. H.; Chen, S. F.; Wu, C. Y., Hexamethylenetetramine Directed Synthesis and Properties of a New Family of Alpha-Nickel Hydroxide Organic-Inorganic Hybrid Materials with High Chemical Stability. J. Phys. Chem. B 2006, 110, 4039-4046.

288. Li, Y. M.; Li, W. Y.; Chou, S. L.; Chen, J., Synthesis, Characterization and Electrochemical Properties of Aluminum-Substituted Alpha-Ni(OH)(2) Hollow Spheres. J. Alloys Compd. 2008, 456, 339-343.

289. Kamath, P. V.; Dixit, M.; Indira, L.; Shukla, A.; Kumar, V. G.; Munichandraiah, N., Stabilized A - Ni (OH) 2 as Electrode Material for Alkaline Secondary Cells. J. Electrochem. Soc. 1994, 141, 2956-2959.

290. Pokroy, B.; Kang, S. H.; Mahadevan, L.; Aizenberg, J., Self-Organization of a Mesoscale Bristle into Ordered, Hierarchical Helical Assemblies. Science 2009, 323, 237-240.

291. Yeo, R. S., Ion Clustering and Proton Transport in Nafion Membranes and Its Applications as Solid Polymer Electrolyte. J. Electrochem. Soc. 1983, 130, 533-538.

292. Koh, W. H.; Silverman, H. P., Anion Transport in Thin-Channel Cation-Exchange Membranes. J. Membr. Sci. 1983, 13, 279-290.

293. Jayalakshmi, M.; Venugopal, N.; Reddy, B. R.; Rao, M. M., Optimum Conditions to Prepare High Yield, Phase Pure Alpha-Ni(OH)(2) Nanoparticles by Urea Hydrolysis and Electrochemical Ageing in Alkali Solutions. J. Power Sources 2005, 150, 272-275.

294. Wang, X.; Li, Y. D., Solution-Based Synthetic Strategies for 1-D Nanostructures. Inorg. Chem. 2006, 45, 7522-7534.

295. Zhang, J.; Zhang, S. Y.; Chen, H. Y., Ctab-Controlled Synthesis of One-Dimensional Selenium Nanostructures. Chem. Lett. 2004, 33, 1054-1055.

296. Jana, N. R.; Gearheart, L.; Murphy, C. J., Wet Chemical Synthesis of Silver Nanorods and Nanowires of Controllable Aspect Ratio. Chem. Commun. 2001, 617-618.

297. Liu, B.; Zeng, H. C., Room Temperature Solution Synthesis of Monodispersed Single-Crystalline Zno Nanorods and Derived Hierarchical Nanostructures. Langmuir 2004, 20, 4196-4204.

298. Yuan, J. K.; Liu, X. G.; Akbulut, O.; Hu, J. Q.; Suib, S. L.; Kong, J.; Stellacci, F., Superwetting Nanowire Membranes for Selective Absorption. Nat. Nanotechnol. 2008, 3, 332-336.

299. Marmur, A., Wetting on Hydrophobic Rough Surfaces: To Be Heterogeneous or Not to Be? Langmuir 2003, 19, 8343-8348.

300. He, Z. K.; Ma, M.; Lan, X. R.; Chen, F.; Wang, K.; Deng, H.; Zhang, Q.; Fu, Q., Fabrication of a Transparent Superamphiphobic Coating with Improved Stability. Soft Matter 2011, 7, 6435-6443.

301. Hu, B. L.; Qin, X. Y.; Asiri, A. M.; Alamry, K. A.; Al-Youbi, A. O.; Sun, X. P., Fabrication of Ni(OH)(2) Nanoflakes Array on Ni Foam as a Binder-Free Electrode Material for High Performance Supercapacitors. Electrochim. Acta 2013, 107, 339-342.

302. Gund, G. S.; Dubal, D. P.; Jambure, S. B.; Shinde, S. S.; Lokhande, C. D., Temperature Influence on Morphological Progress of Ni(OH)(2) Thin Films and Its Subsequent Effect on Electrochemical Supercapacitive Properties. J. Mater. Chem. A 2013, 1, 4793-4803.

303. Huang, W.; Li, Z. I.; Peng, Y. D.; Chen, S.; Zheng, J. F.; Niu, Z. J., Oscillatory Electrocatalytic Oxidation of Methanol on an Ni(OH)(2) Film Electrode. J. Solid State Electrochem. 2005, 9, 284-289.

304. Zhang, G. G.; Li, W. F.; Xie, K. Y.; Yu, F.; Huang, H. T., A One-Step and Binder-Free Method to Fabricate Hierarchical Nickel-Based Supercapacitor Electrodes with Excellent Performance. Adv. Funct. Mater. 2013, 23, 3675-3681.

305. Zhang, L. S.; Ding, Q. W.; Huang, Y. P.; Gu, H. H.; Miao, Y. E.; Liu, T. X., Flexible Hybrid Membranes with Ni(OH)(2) Nanoplatelets Vertically Grown on Electrospun Carbon Nanofibers for High-Performance Supercapacitors. ACS Appl. Mater. Interfaces 2015, 7, 22669-22677.

306. Liang, J. B.; Ma, R. Z.; Iyi, N. B. O.; Ebina, Y.; Takada, K.; Sasaki, T., Topochemical Synthesis, Anion Exchange, and Exfoliation of Co-Ni Layered Double Hydroxides: A Route to Positively Charged Co-Ni Hydroxide Nanosheets with Tunable Composition. Chem. Mater. 2010, 22, 371-378.

307. Liu, X. H.; Ma, R. Z.; Bando, Y.; Sasaki, T., A General Strategy to Layered Transition-Metal Hydroxide Nanocones: Tuning the Composition for High Electrochemical Performance. Adv. Mater. 2012, 24, 2148-2153.

308. Li, Z. C.; Han, J.; Fan, L.; Wang, M. G.; Tao, S. Y.; Guo, R., The Anion Exchange Strategy Towards Mesoporous Alpha-Ni(OH)(2) Nanowires with Multinanocavities for High-Performance Supercapacitors. Chem. Commun. 2015, 51, 3053-3056.

309. Cao, L.; Xu, F.; Liang, Y. Y.; Li, H. L., Preparation of the Novel Nanocomposite Co(OH)(2)/Ultra-Stable Y Zeolite and Its Application as a Supercapacitor with High Energy Density. Adv. Mater. 2004, 16, 1853-1857.

310. Xiong, X. H.; Ding, D.; Chen, D. C.; Waller, G.; Bu, Y. F.; Wang, Z. X.; Liu, M. L., Three-Dimensional Ultrathin Ni(OH)(2) Nanosheets Grown on Nickel Foam for High-Performance Supercapacitors. Nano Energy 2015, 11, 154-161.

311. Hu, C. C.; Chen, J. C.; Chang, K. H., Cathodic Deposition of Ni(OH)(2) and Co(OH)(2) for Asymmetric Supercapacitors: Importance of the Electrochemical Reversibility of Redox Couples. J. Power Sources 2013, 221, 128-133.

312. Song, F.; Hu, X. L., Ultrathin Cobalt-Manganese Layered Double Hydroxide Is an Efficient Oxygen Evolution Catalyst. J. Am. Chem. Soc. 2014, 136, 16481-16484.

313. Swierk, J. R.; Klaus, S.; Trotochaud, L.; Bell, A. T.; Tilley, T. D., Electrochemical Study of the Energetics of the Oxygen Evolution Reaction at Nickel Iron (Oxy)Hydroxide Catalysts. J. Phys. Chem. C 2015, 119, 19022-19029.

314. Drenkova-Tuhtan, A.; Schneider, M.; Mandel, K.; Meyer, C.; Gellermann, C.; Sextl, G.; Steinmetz, H., Influence of Cation Building Blocks of Metal Hydroxide Precipitates on Their Adsorption and Desorption Capacity for Phosphate in Wastewater—a Screening Study. Colloids and Surfaces A: Physicochemical and Engineering Aspects 2016, 488, 145-153.

315. Qi, Y. J.; Qi, H. Y.; Lu, C. J.; Yang, Y.; Zhao, Y., Photoluminescence and Magnetic Properties of Beta-Ni(OH)(2) Nanoplates and NiO Nanostructures. Journal of Materials Science-Materials in Electronics 2009, 20, 479-483.

316. Xu, Q.; Li, J.; Tian, J.; Zhu, J.; Gao, X. F., Energy-Effective Frost-Free Coatings Based on Superhydrophobic Aligned Nanocones. ACS Appl. Mater. Interfaces 2014, 6, 8976-8980.

317. Chang, Y. H.; Hau, N. Y.; Liu, C.; Huang, Y. T.; Li, C. C.; Shih, K.; Feng, S. P., A Short-Range Ordered-Disordered Transition of a Niooh/Ni(OH)(2) Pair Induces Switchable Wettability. Nanoscale 2014, 6, 15309-15315.

318. Lu, Z. Y.; Chang, Z.; Zhu, W.; Sun, X. M., Beta-Phased Ni(OH)(2) Nanowall Film with Reversible Capacitance Higher Than Theoretical Faradic Capacitance. Chem. Commun. 2011, 47, 9651-9653.

319. Cheng, Y. W.; Zhang, H. B.; Varanasi, C. V.; Liu, J., Improving the Performance of Cobalt-Nickel Hydroxidebased Self-Supporting Electrodes for Supercapacitors Using Accumulative Approaches. Energy Environ. Sci. 2013, 6, 3314-3321.

320. Ghosh, D.; Mandal, M.; Das, C. K., Solid State Flexible Asymmetric Supercapacitor Based on Carbon Fiber Supported Hierarchical Co(OH)(X)CO3 and Ni(OH)(2). Langmuir 2015, 31, 7835-7843.

321. Chen, G.; Liaw, S. S.; Li, B. S.; Xu, Y.; Dunwell, M.; Deng, S. G.; Fan, H. Y.; Luo, H. M., Microwave-Assisted Synthesis of Hybrid CoxNi1-x(OH)(2) Nanosheets: Tuning the Composition for High Performance Supercapacitor. J. Power Sources 2014, 251, 338-343.

322. Li, R. C.; Hu, Z. X.; Shao, X. F.; Cheng, P. P.; Li, S. S.; Yu, W. D.; Lin, W. R.; Yuan, D. S., Large Scale Synthesis of Nico Layered Double Hydroxides for Superior Asymmetric Electrochemical Capacitor. Sci. Rep. 2016, 6.

323. Yan, W.; Wang, D.; Botte, G. G., Nickel and Cobalt Bimetallic Hydroxide Catalysts for Urea Electro-Oxidation. Electrochim. Acta 2012, 61, 25-30.

324. Jiang, J.; Zhang, A. L.; Li, L. L.; Ai, L. H., Nickel-Cobalt Layered Double Hydroxide Nanosheets as High-Performance Electrocatalyst for Oxygen Evolution Reaction. J. Power Sources 2015, 278, 445-451.

325. Chen, H.; Hu, L. F.; Chen, M.; Yan, Y.; Wu, L. M., Nickel- Cobalt Layered Double Hydroxide Nanosheets for High- Performance Supercapacitor Electrode Materials. Adv. Funct. Mater. 2014, 24, 934-942.

326. Gong, X. F.; Cheng, J. P.; Liu, F.; Zhang, L.; Zhang, X. B., Nickel-Cobalt Hydroxide Microspheres Electrodepositioned on Nickel Cobaltite Nanowires Grown on Ni Foam for High-Performance Pseudocapacitors. J. Power Sources 2014, 267, 610-616.

327. Martins, P. R.; Parussulo, A. L. A.; Toma, S. H.; Rocha, M. A.; Toma, H. E.; Araki, K., Highly Stabilized Alpha-Nico(OH)(2) Nanomaterials for High Performance Device Application. J. Power Sources 2012, 218, 1-4.

328. Salunkhe, R. R.; Jang, K.; Lee, S. W.; Ahn, H., Aligned Nickel-Cobalt Hydroxide Nanorod Arrays for Electrochemical Pseudocapacitor Applications. RSC Adv. 2012, 2, 3190-3193.

329. Grote, F.; Yu, Z. Y.; Wang, J. L.; Yu, S. H.; Lei, Y., Self-Stacked Reduced Graphene Oxide Nanosheets Coated with Cobalt-Nickel Hydroxide by One-Step Electrochemical Deposition toward Flexible Electrochromic Supercapacitors. Small 2015, 11, 4666-4672.

330. Meng, X.; Deng, D., Bio-Inspired Synthesis of A-Ni (OH) 2 Nanobristles on Various Substrates and Their Applications. J. Mater. Chem. A 2016.

331. Nethravathi, C.; Harichandran, G.; Shivakumara, C.; Ravishankar, N.; Rajamathi, M., Surfactant Intercalated Alpha-Hydroxides of Cobalt and Nickel and Their Delamination-Restacking Behavior in Organic Media. J. Colloid Interface Sci. 2005, 288, 629-633.

332. Cressent, A.; Pralong, V.; Audemer, A.; Leriche, J. B.; Delahaye-Vidal, A.; Tarascon, J. M., Electrochemical Performance Comparison between Beta-Type Mixed Nickel Cobalt Hydroxides Prepared by Various Synthesis Routes. Solid State Sci. 2001, 3, 65-80.

333. Liu, Z. P.; Ma, R. Z.; Osada, M.; Takada, K.; Sasaki, T., Selective and Controlled Synthesis of Alpha- and Beta-Cobalt Hydroxides in Highly Developed Hexagonal Platelets. J. Am. Chem. Soc. 2005, 127, 13869-13874.

334. Yan, T.; Li, Z. J.; Li, R. Y.; Ning, Q.; Kong, H.; Niu, Y. L.; Liu, J. K., Nickel-Cobalt Double Hydroxides Microspheres with Hollow Interior and Hedgehog-Like Exterior Structures for Supercapacitors. J. Mater. Chem. 2012, 22, 23587-23592.

335. Bai, Y.; Wang, W. Q.; Wang, R. R.; Sun, J.; Gao, L., Controllable Synthesis of 3D Binary Nickel-Cobalt Hydroxide/Graphene/Nickel Foam as a Binder-Free Electrode for High-Performance Supercapacitors. J. Mater. Chem. A 2015, 3, 12530-12538.

336. Guan, C.; Liu, J. P.; Cheng, C. W.; Li, H. X.; Li, X. L.; Zhou, W. W.; Zhang, H.; Fan, H. J., Hybrid Structure of Cobalt Monoxide Nanowire @ Nickel Hydroxidenitrate Nanoflake Aligned on Nickel Foam for High-Rate Supercapacitor. Energy Environ. Sci. 2011, 4, 4496-4499.

337. Pu, J.; Tong, Y.; Wang, S. B.; Sheng, E. H.; Wang, Z. H., Nickel-Cobalt Hydroxide Nanosheets Arrays on Ni Foam for Pseudocapacitor Applications. J. Power Sources 2014, 250, 250-256.

338. Xu, Y. Z.; Wei, J. C.; Tan, L. C.; Yu, J.; Chen, Y. W., A Facile Approach to Nicoo2 Intimately Standing on Nitrogen Doped Graphene Sheets by One-Step Hydrothermal Synthesis for Supercapacitors. J. Mater. Chem. A 2015, 3, 7121-7131.

339. Chen, H. C.; Jiang, J. J.; Zhang, L.; Zhao, Y. D.; Guo, D. Q.; Ruan, Y. J.; Xia, D. D., One-Pot Fabrication of Layered Alpha-Phase Nickel-Cobalt Hydroxides as Advanced Electrode Materials for Pseudocapacitors. Chempluschem 2015, 80, 181-187.

340. Xing, J. H.; Wu, S. Y.; Ng, K. Y. S., Electrodeposition of Ultrathin Nickel-Cobalt Double Hydroxide Nanosheets on Nickel Foam as High-Performance Supercapacitor Electrodes. RSC Adv. 2015, 5, 88780-88786.

341. Patil, U. M.; Sohn, J. S.; Kulkarni, S. B.; Lee, S. C.; Park, H. G.; Gurav, K. V.; Kim, J. H.; Jun, S. C., Enhanced Supercapacitive Performance of Chemically Grown Cobalt-Nickel Hydroxides on Three-Dimensional Graphene Foam Electrodes. ACS Appl. Mater. Interfaces 2014, 6, 2450-2458.

342. Lu, X. H.; Huang, X.; Xie, S. L.; Zhai, T.; Wang, C. S.; Zhang, P.; Yu, M. H.; Li, W.; Liang, C. L.; Tong, Y. X., Controllable Synthesis of Porous Nickel-Cobalt Oxide Nanosheets for Supercapacitors. J. Mater. Chem. 2012, 22, 13357-13364.

343. Deng, F. Z.; Yu, L.; Cheng, G.; Lin, T.; Sun, M.; Ye, F.; Li, Y. F., Synthesis of Ultrathin Mesoporous NiCo2O4 Nanosheets on Carbon Fiber Paper as Integrated High-Performance Electrodes for Supercapacitors. J. Power Sources 2014, 251, 202-207.

344. Xiao, J. W.; Wan, L.; Yang, S. H.; Xiao, F.; Wang, S., Design Hierarchical Electrodes with Highly Conductive NiCo2S4 Nanotube Arrays Grown on Carbon Fiber Paper for High-Performance Pseudocapacitors. Nano Lett. 2014, 14, 831-838.

345. Pu, J.; Wang, T. T.; Wang, H. Y.; Tong, Y.; Lu, C. C.; Kong, W.; Wang, Z. H., Direct Growth of NiCo2S4 Nanotube Arrays on Nickel Foam as High-Performance Binder-Free Electrodes for Supercapacitors. Chempluschem 2014, 79, 577-583.

346. Park, J.; Kang, E.; Son, S. U.; Park, H. M.; Lee, M. K.; Kim, J.; Kim, K. W.; Noh, H. J.; Park, J. H.; Bae, C. J.; Park, J. G.; Hyeon, T., Monodisperse Nanoparticles of Ni and NiO:

Synthesis, Characterization, Self-Assembled Superlattices, and Catalytic Applications in the Suzuki Coupling Reaction. Adv. Mater. 2005, 17, 429-434.

347. Davar, F.; Fereshteh, Z.; Salavati-Niasari, M., Nanoparticles Ni and NiO: Synthesis, Characterization and Magnetic Properties. J. Alloys Compd. 2009, 476, 797-801.

348. Dirksen, J. A.; Duval, K.; Ring, T. A., NiO Thin-Film Formaldehyde Gas Sensor. Sensors and Actuators, B: Chemical 2001, 80, 106-115.

349. Gibson, E. A.; Smeigh, A. L.; Le Pleux, L.; Fortage, J.; Boschloo, G.; Blart, E.; Pellegrin, Y.; Odobel, F.; Hagfeldt, A.; Hammarstrom, L., A P-Type NiO-Based Dye-Sensitized Solar Cell with an Open-Circuit Voltage of 0.35 V. Angew. Chem. Int. Ed. 2009, 48, 4402-4405.

350. deSouza, S.; Visco, S. J.; DeJonghe, L. C., Thin-Film Solid Oxide Fuel Cell with High Performance at Low-Temperature. Solid State Ionics 1997, 98, 57-61.

351. Wang, H. L.; Casalongue, H. S.; Liang, Y. Y.; Dai, H. J., Ni(OH)(2) Nanoplates Grown on Graphene as Advanced Electrochemical Pseudocapacitor Materials. J. Am. Chem. Soc. 2010, 132, 7472-7477.

352. Varghese, B.; Reddy, M. V.; Yanwu, Z.; Lit, C. S.; Hoong, T. C.; Rao, G. V. S.; Chowdari, B. V. R.; Wee, A. T. S.; Lim, C. T.; Sow, C. H., Fabrication of NiO Nanowall Electrodes for High Performance Lithium Ion Battery. Chem. Mater. 2008, 20, 3360-3367.

353. Mai, Y. J.; Tu, J. P.; Xia, X. H.; Gu, C. D.; Wang, X. L., Co-Doped NiO Nanoflake Arrays toward Superior Anode Materials for Lithium Ion Batteries. J. Power Sources 2011, 196, 6388-6393.

354. Rahman, M. M.; Chou, S. L.; Zhong, C.; Wang, J. Z.; Wexler, D.; Liu, H. K., Spray Pyrolyzed NiO-C Nanocomposite as an Anode Material for the Lithium-Ion Battery with Enhanced Capacity Retention. Solid State Ionics 2010, 180, 1646-1651.

355. Bai, Z. C.; Ju, Z. C.; Guo, C. L.; Qian, Y. T.; Tang, B.; Xiong, S. L., Direct Large-Scale Synthesis of 3D Hierarchical Mesoporous NiO Microspheres as High-Performance Anode Materials for Lithium Ion Batteries. Nanoscale 2014, 6, 3268-3273.

356. Liu, L. X.; Guo, Y. Y.; Wang, Y. P.; Yang, X. J.; Wang, S. X.; Guo, H., Hollow NiO Nanotubes Synthesized by Bio-Templates as the High Performance Anode Materials of Lithium-Ion Batteries. Electrochim. Acta 2013, 114, 42-47.

357. Mondal, A. K.; Su, D. W.; Wang, Y.; Chen, S. Q.; Liu, Q.; Wang, G. X., Microwave Hydrothermal Synthesis of Urchin-Like NiO Nanospheres as Electrode Materials for Lithium-Ion Batteries and Supercapacitors with Enhanced Electrochemical Performances. J. Alloys Compd. 2014, 582, 522-527.

358. Huang, X. H.; Tu, J. P.; Xia, X. H.; Wang, X. L.; Xiang, J. Y.; Zhang, L.; Zhou, Y., Morphology Effect on the Electrochemical Performance of NiO Films as Anodes for Lithium Ion Batteries. J. Power Sources 2009, 188, 588-591.

359. Bruce, P. G.; Scrosati, B.; Tarascon, J. M., Nanomaterials for Rechargeable Lithium Batteries. Angew. Chem. Int. Ed. 2008, 47, 2930-2946.

360. Xia, Y. N.; Yang, P. D.; Sun, Y. G.; Wu, Y. Y.; Mayers, B.; Gates, B.; Yin, Y. D.; Kim, F.; Yan, Y. Q., One-Dimensional Nanostructures: Synthesis, Characterization, and Applications. Adv. Mater. 2003, 15, 353-389.

361. Liu, J. H.; Liu, X. W., Two-Dimensional Nanoarchitectures for Lithium Storage. Adv. Mater. 2012, 24, 4097-4111.

362. Magasinski, A.; Dixon, P.; Hertzberg, B.; Kvit, A.; Ayala, J.; Yushin, G., High-Performance Lithium-Ion Anodes Using a Hierarchical Bottom-up Approach. Nat. Mater. 2010, 9, 353-358.

363. Nam, K. T.; Kim, D. W.; Yoo, P. J.; Chiang, C. Y.; Meethong, N.; Hammond, P. T.; Chiang, Y. M.; Belcher, A. M., Virus-Enabled Synthesis and Assembly of Nanowires for Lithium Ion Battery Electrodes. Science 2006, 312, 885-888.

364. Liang, H.; Liu, L.; Yang, Z. J.; Yang, Y. Z., Hydrothermal Synthesis of Ultralong Single-Crystalline Alpha-Ni(OH)(2) Nanobelts and Corresponding Porous NiO Nanobelts. Cryst. Res. Technol. 2010, 45, 661-666.

365. Li, X. F.; Dhanabalan, A.; Wang, C. L., Enhanced Electrochemical Performance of Porous NiO-Ni Nanocomposite Anode for Lithium Ion Batteries. J. Power Sources 2011, 196, 9625-9630.

366. Needham, S. A.; Wang, G. X.; Liu, H. K., Synthesis of NiO Nanotubes for Use as Negative Electrodes in Lithium Ion Batteries. J. Power Sources 2006, 159, 254-257.

367. Cheng, J.; Cao, G. P.; Yang, Y. S., Characterization of Sol-Gel-Derived Niox Xerogels as Supercapacitors. J. Power Sources 2006, 159, 734-741.

368. Lang, J. W.; Kong, L. B.; Wu, W. J.; Luo, Y. C.; Kang, L., Facile Approach to Prepare Loose-Packed NiO Nano-Flakes Materials for Supercapacitors. Chem. Commun. 2008, 4213-4215.

369. Gazit, E., An Introduction to Bionanotechnology. World Scientific: 2007.

370. Kim, S.; Park, C. B., Bio-Inspired Synthesis of Minerals for Energy, Environment, and Medicinal Applications. Adv. Funct. Mater. 2013, 23, 10-25.

371. Kong, C. S.; Zhang, H. L.; Somodi, F.; Morse, D. E., Bio-Inspired Synthesis of High-Performance Nanocomposite Catalysts for Hydrogen Oxidation. Adv. Funct. Mater. 2013, 23, 4585-4592.

372. Miot, J.; Recham, N.; Larcher, D.; Guyot, F.; Brest, J.; Tarascon, J. M., Biomineralized Alpha-Fe2O3: Texture and Electrochemical Reaction with Li. Energy Environ. Sci. 2014, 7, 451-460.

373. Meng, X.; Deng, D., Bio-Inspired Synthesis of Alpha-Ni(OH)(2) Nanobristles on Various Substrates and Their Applications. J. Mater. Chem. A 2016.

374. Li, X. W.; Xiong, S. L.; Li, J. F.; Bai, J.; Qian, Y. T., Mesoporous NiO Ultrathin Nanowire Networks Topotactically Transformed from Alpha-Ni(OH)(2) Hierarchical Microspheres and Their Superior Electrochemical Capacitance Properties and Excellent Capability for Water Treatment. J. Mater. Chem. 2012, 22, 14276-14283.

375. Tong, G. X.; Liu, F. T.; Wu, W. H.; Shen, J. P.; Hu, X.; Liang, Y., Polymorphous Alpha- and Beta-Ni(OH)(2) Complex Architectures: Morphological and Phasal Evolution Mechanisms and Enhanced Catalytic Activity as Non-Enzymatic Glucose Sensors. Crystengcomm 2012, 14, 5963-5973.

376. Yue, G. H.; Zhao, Y. C.; Wang, C. G.; Zhang, X. X.; Zhang, X. Q.; Xie, Q. S., Flower-Like Nickel Oxide Nanocomposites Anode Materials for Excellent Performance Lithium-Ion Batteries. Electrochim. Acta 2015, 152, 315-322.

377. Li, J. T.; Zhao, W.; Huang, F. Q.; Manivannan, A.; Wu, N. Q., Single-Crystalline Ni(OH)(2) and NiO Nanoplatelet Arrays as Supercapacitor Electrodes. Nanoscale 2011, 3, 5103-5109.

378. Wang, M. M.; Ren, W. Z.; Zhao, Y. N.; Liu, Y.; Cui, H. T., One-Pot Synthesis of Powder-Form Beta-Ni(OH)(2) Monolayer Nanosheets with High Electrochemical Performance. J. Nanopart. Res. 2013, 15.

379. Dixit, M.; Subbanna, G. N.; Kamath, P. V., Homogeneous Precipitation from Solution by Urea Hydrolysis: A Novel Chemical Route to the Alpha-Hydroxides of Nickel and Cobalt. J. Mater. Chem. 1996, 6, 1429-1432.

380. Zhu, L. P.; Liao, G. H.; Yang, Y.; Xiao, H. M.; Wang, J. F.; Fu, S. Y., Self-Assembled 3D Flower-Like Hierarchical Beta-Ni(OH)(2) Hollow Architectures and Their in Situ Thermal Conversion to NiO. Nanoscale Res Lett 2009, 4, 550-557.

381. Ren, Y.; Gao, L. A., From Three-Dimensional Flower-Like Alpha-Ni(OH)(2) Nanostructures to Hierarchical Porous NiO Nanoflowers: Microwave-Assisted Fabrication and Supercapacitor Properties. J. Am. Ceram. Soc. 2010, 93, 3560-3564.

382. Li, W.; Yang, L.-L.; Lin, B.; Isimjan, T. T.; Yang, D.-Q.; Hu, Y.; Hu, Z.; Sacher, E., Large-Scale Synthesis of 3D Sphere-Like Hierarchical Ni(OH)2 Nanofibers for High-Performance Electrochemical Supercapacitors. Mater. Res. Express 2015, 2, 095008.

383. Cao, M. H.; He, X. Y.; Chen, J.; Hu, C. W., Self-Assembled Nickel Hydroxide Three-Dimensional Nanostructures: A Nanomaterial for Alkaline Rechargeable Batteries. Cryst. Growth Des. 2007, 7, 170-174.

384. Luo, Z. J.; Wang, K.; Li, H. M.; Yin, S.; Guan, Q. F.; Wang, L. G., One-Dimensional Beta-Ni(OH)(2) Nanostructures: Ionic Liquid Etching Synthesis, Formation Mechanism, and Application for Electrochemical Capacitors. Crystengcomm 2011, 13, 7108-7113.

385. Zhang, K.; Wang, J. B.; Lu, X. L.; Li, L. Y.; Tang, Y. W.; Jia, Z. Y., Structural Evolution of Hydrothermal-Synthesized Ni(SO4)(0.3)(OH)(1.4) Nanobelts During Ex Situ Heat Treatment and in Situ Electron Irradiation. J. Phys. Chem. C 2009, 113, 142-147.

386. Luo, Z.; Yin, S.; Wang, K.; Li, H.; Wang, L.; Xu, H.; Xia, J., Synthesis of One-Dimensional B-Ni(OH)2 Nanostructure and Their Application as Nonenzymatic Glucose Sensors. Mater. Chem. Phys. 2012, 132, 387-394.

387. Liu, B.; Yang, H. Q.; Zhao, H.; An, L. J.; Zhang, L. H.; Shi, R. Y.; Wang, L.; Bao, L.; Chen, Y., Synthesis and Enhanced Gas-Sensing Properties of Ultralong NiO Nanowires Assembled with NiO Nanocrystals. Sensors and Actuators, B: Chemical 2011, 156, 251-262.

388. Wen, W.; Wu, J. M.; Cao, M. H., NiO/Ni Powders with Effective Architectures as Anode Materials in Li-Ion Batteries. J. Mater. Chem. A 2013, 1, 3881-3885.

389. Huang, X. H.; Tu, J. P.; Zhang, B.; Zhang, C. Q.; Li, Y.; Yuan, Y. F.; Wu, H. M., Electrochemical Properties of NiO-Ni Nanocomposite as Anode Material for Lithium Ion Batteries. J. Power Sources 2006, 161, 541-544.

390. Lian, S. Y.; Wang, E. B.; Gao, L.; Xu, L., Fabrication of Single-Crystalline Co3O4 Nanorods Via a Low-Temperature Solvothermal Process. Mater. Lett. 2007, 61, 3893-3896.

391. Alberti, G.; Casciola, M.; Massinelli, L.; Bauer, B., Polymeric Proton Conducting Membranes for Medium Temperature Fuel Cells (110-160 Degrees C). J. Membr. Sci. 2001, 185, 73-81.

392. Goswami, A.; Acharya, A.; Pandey, A. K., Study of Self-Diffusion of Monovalent and Divalent Cations in Nafion-117 Ion-Exchange Membrane. J. Phys. Chem. B 2001, 105, 9196-9201.

393. Haubold, H. G.; Vad, T.; Jungbluth, H.; Hiller, P., Nano Structure of Nafion: A SAXS Study. Electrochim. Acta 2001, 46, 1559-1563.

394. Rhee, Y. W.; Ha, S. Y.; Masel, R. I., Crossover of Formic Acid through Nafion Membranes. J. Power Sources 2003, 117, 35-38.

395. Song, N. N.; Jiang, H. X.; Cui, T. L.; Chang, L. L.; Wang, X. J., Synthesis and Enhanced Gas-Sensing Properties of Mesoporous Hierarchical Alpha-Fe2O3 Architectures from an Eggshell Membrane. Micro & Nano Letters 2012, 7, 943-946.

396. Li, Q. Y.; Wang, R. N.; Nie, Z. R.; Wang, Z. H.; Wei, Q., Preparation and Characterization of Nanostructured Ni(OH)(2) and NiO Thin Films by a Simple Solution Growth Process. J. Colloid Interface Sci. 2008, 320, 254-258.

397. Song, X. F.; Gao, L., Facile Route to Nanoporous NiO Structures from the Alpha-Ni(OH)(2)/EG Precursor and Application in Water Treatment. J. Am. Ceram. Soc. 2008, 91, 4105-4108.

398. Luo, Y. Y.; Li, G. H.; Duan, G. T.; Zhang, L. D., One-Step Synthesis of Spherical Alpha-Ni(OH)(2) Nanoarchitectures. Nanotechnology 2006, 17, 4278-4283.

399. Yu, L.; Chen, Y. J.; Feng, D. D.; Li, Q. H., Controllable Synthesis of Co3O4 Nanostructures with Good Cycling Performance and Rate Capacity in Lithium-Ion Batteries. J. Nanopart. Res. 2013, 15.

400. Tang, B.; Zhuo, L. H.; Ge, J. C.; Niu, J. Y.; Shi, Z. Q., Hydrothermal Synthesis of Ultralong and Single-Crystalline Cd(OH)(2) Nanowires Using Alkali Salts as Mineralizers. Inorg. Chem. 2005, 44, 2568-2569.

401. Bai, G. M.; Dai, H. X.; Deng, J. G.; Liu, Y. X.; Wang, F.; Zhao, Z. X.; Qiu, W. G.; Au, C. T., Porous Co3O4 Nanowires and Nanorods: Highly Active Catalysts for the Combustion of Toluene. Applied Catalysis, A: General 2013, 450, 42-49.

402. Kundu, S.; Mukadam, M. D.; Yusuf, S. M.; Jayachandran, M., Formation of Shape-Selective Magnetic Cobalt Oxide Nanowires: Environmental Application in Catalysis Studies. Crystengcomm 2013, 15, 482-497.

403. Xiong, S. L.; Chen, J. S.; Lou, X. W.; Zeng, H. C., Mesoporous Co3O4 and CoO@C Topotactically Transformed from Chrysanthemum-Like Co(CO3)0.5(OH)·0.11H2O and Their Lithium-Storage Properties. Adv. Funct. Mater. 2012, 22, 861-871.

404. Du, J.; Chai, L. L.; Wang, G. M.; Li, K.; Qian, Y. T., Controlled Synthesis of One-Dimensional Single-Crystal Co3O4 Nanowires. Aust. J. Chem. 2008, 61, 153-158.

405. Wang, W. Z.; Feng, K.; Wang, Z.; Ma, Y. Y.; Zhang, S. Y.; Liang, Y. J., Controllable Synthesis and Growth Mechanism of Alpha-Co(OH)(2) Nanorods and Nanoplates by a Facile Solution-Phase Route. J. Solid State Chem. 2011, 184, 3299-3302.

406. Zhang, H.; Wu, J. B.; Zhai, C. X.; Ma, X. Y.; Du, N.; Tu, J. P.; Yang, D. R., From Cobalt Nitrate Carbonate Hydroxide Hydrate Nanowires to Porous Co(3)O(4) Nanorods for High Performance Lithium-Ion Battery Electrodes. Nanotechnology 2008, 19.

407. Liu, X. G.; Or, S. W.; Jin, C. G.; Lv, Y. H.; Feng, C.; Sun, Y. P., NiO/C Nanocapsules with Onion-Like Carbon Shell as Anode Material for Lithium Ion Batteries. Carbon 2013, 60, 215-220.

408. Sun, X. L.; Si, W. P.; Liu, X. H.; Deng, J. W.; Xi, L. X.; Liu, L. F.; Yan, C. L.; Schmidt, O. G., Multifunctional Ni/NiO Hybrid Nanomembranes as Anode Materials for High-Rate Li-Ion Batteries. Nano Energy 2014, 9, 168-175.

409. Liu, H.; Wang, G. X.; Liu, J.; Qiao, S. Z.; Ahn, H. J., Highly Ordered Mesoporous NiO Anode Material for Lithium Ion Batteries with an Excellent Electrochemical Performance. J. Mater. Chem. 2011, 21, 3046-3052.

410. Zai, J. T.; Yu, C.; Tao, L. Q.; Xu, M.; Xiao, Y. L.; Li, B.; Han, Q. Y.; Wang, K. X.; Qian, X. F., Synthesis of Ni-Doped NiO/RGONS Nanocomposites with Enhanced Rate Capabilities as Anode Materials for Li Ion Batteries. Crystengcomm 2013, 15, 6663-6671.

411. Wang, X. H.; Li, X. W.; Sun, X. L.; Li, F.; Liu, Q. M.; Wang, Q.; He, D. Y., Nanostructured NiO Electrode for High Rate Li-Ion Batteries. J. Mater. Chem. 2011, 21, 3571-3573.

412. Zhang, C. Q.; Tu, J. P.; Yuan, Y. F.; Huang, X. H.; Chen, X. T.; Mao, F., Electrochemical Performances of Ni-Coated Zno as an Anode Material for Lithium-Ion Batteries. J. Electrochem. Soc. 2007, 154, A65-A69.

ABSTRACT

BIO-INSPIRED SYNTHESIS OF NANOSTRUCTURED MATERIALS ON SUBSTRATES FOR ENVIRONMENTAL AND ENERGY APPLICATIONS

by

XINGHUA MENG

August 2016

Advisor: Dr. Da Deng

Major: Materials Sciences and Engineering

Degree: Doctor of Philosophy

It is still a challenging task to develop simple methods for facile synthesis of functional nanostructures on substrates under mild conditions without using expensive instruments. We have successfully developed a bio-inspired method using simple diaphragm-assisted system to synthesize functional nanostructures on various substrates under mild conditions. We have systematically studied the effects of experimental parameters on the formation of nanostructures under controlled conditions. The fundamental mechanism involved has been systematically studied and revealed. By growing the unique networks of nanostructures on a piece of substrate, a double-rough surface, with structures at both nanoscale and microscale, has been achieved, showing interesting roughness-induced superhydrophobicity in air and superoleophobicity in water. The double rough substrates will find important environmental applications. Additionally, nanostructures formed on substrates have been used as integrated and binder-free electrodes for energy storage. The unique structures with a large exposed surface enable the electrodes to demonstrate dramatically improved performances. Moreover, some chemically active substrates were used to build up composite materials to enhance their applications. The method and ideas outlined in the dissertation, based on diaphragm-assisted

systems, will have impacts, in principle, on the synthesis of numerous functional materials or precursors under mild conditions.

AUTOBIOGRAPHICAL STATEMENT

Xinghua Meng was born in Changzhou, China in 1985 and grew up at the same city. He received his B.S. degree in Materials Science and Engineering from Nanjing University Aeronautics and Astronautics, Nanjing, China, in 2008 and M.S. degree in Materials Science and Engineering from Donghua University, Shanghai, China, in 2011. In August 2011, he enrolled in the Materials Science and Engineering (MSE) Program at Wayne State University. He joined Dr. Deng's research group in January 2012. His research is focused on novel materials for energy and environmental applications.

List of Peer-Reviewed Journal Publications:

1. Meng, X.; Deng, D.*, Trash to Treasure: Waste Eggshells Used as Reactor and Template for Synthesis of Co9S8 Nanorod Arrays on Carbon Fibers for Energy Storage, Chemistry of Materials, under revision, 2016

2. Meng, X.; Deng, D.*, Bio-inspired synthesis of α-$Ni(OH)_2$ nanobristles on various substrates and their applications. Journal of Materials Chemistry A, DOI: 10.1039/C5TA09329E, 2016

3. Meng, X.; Deng, D.*, Bio-Inspired Formation of Single-Crystalline Nanoflake Arrays on Flexible Substrates with Superoleophobicity. CrystEngComm, DOI: 10.1039/C5CE01506E, 2015.

4. Meng, X.; Savage, P. E.; Deng, D.*, Trash to Treasure: From Harmful Algal Blooms to High-Performance Electrodes for Sodium Ion Batteries. Environmental Science & Technology, DOI: 10.1021/acs.est.5b03882, 2015.

5. Fonseca, W. S.; Meng, X.; Deng, D.*, Trash to Treasure: Transforming Waste Polystyrene Cups into Negative Electrode Materials for Sodium Ion Batteries. ACS Sustainable Chemistry & Engineering, 3, 2153-2159, 2015.

6. Meng, X.; Deng, D.*, "Core-Shell Ti@Si Coaxial Nanorod Arrays Formed Directly on Current Collectors for Lithium-Ion Batteries", ACS Applied Materials & Interfaces, 7, 6867-6874, 2015.